Distribution Agreement

In presenting this thesis or dissertation as a partial fulfillment of the requirements for an advanced degree from Emory University, I hereby grant to Emory University and its agents the non-exclusive license to archive, make accessible, and display my thesis or dissertation in whole or in part in all forms of media, now or hereafter known, including display on the world wide web. I understand that I may select some access restrictions as part of the online submission of this thesis or dissertation. I retain all ownership rights to the copyright of the thesis or dissertation. I also retain the right to use in future works (such as articles or books) all or part of this thesis or dissertation

Signature:

_____ _____

Kaifeng Wu Date

Charge Separation and Transport Dynamics in One-Dimensional Colloidal Nanostructures for Solar Energy Conversion

By

Kaifeng Wu

Doctor of Philosophy

Chemistry

_____

Dr. Tianquan Lian

Advisor

_____

Dr. Michael C. Heaven

Committee Member

_____

Dr. Craig L. Hill

Committee Member

Accepted:

_____

Lisa A. Tedesco. Ph.D.

Dean of the James T. Laney School of Graduate Studies

_____

Date

Charge Separation and Transport Dynamics in One-Dimensional Colloidal Nanostructures for Solar Energy Conversion

By

Kaifeng Wu
B.S., University of Science and Technology of China, P.R. China, 2010

Advisor: Tianquan Lian, Ph.D.

An abstract of
A dissertation submitted to the Faculty of the
James T. Laney School of Graduate Studies of Emory University
in partial fulfillment of the requirements for the degree of
Doctor of Philosophy
in Chemistry
2015

Abstract

Charge Separation and Transport Dynamics in One-Dimensional Colloidal Nanostructures for Solar Energy Conversion

By Kaifeng Wu

Colloidal one-dimensional (1D) semiconductor nanocrystals offer the opportunity to maintain quantum confinement in two dimensions and to tune their light absorption and charge separation capabilities in the remaining dimension. For this reason, they can be implemented into various solar energy conversion applications, such as photocatalysis, which utilizes long distance charge separations, and luminescent solar concentrators, where strong light absorptions are needed. In this dissertation, we investigated carrier separation and transport dynamics in 1D colloidal nanostructures which are crucial for those applications.

We first demonstrated efficient and long-lived photoinduced electron transfer from CdS and CdSe/CdS Nanorods (NRs) to Pt tips, enabled by ultrafast hole trapping in the former and hole localization to CdSe seed in the later. These studies reveal that hole immobilization is the key factor for efficient charge separation in 1D NRs. In addition, we showed that when using CdS-Pt and CdSe/CdS-Pt NRs for light-driven H_2 evolution, hole removal was the efficiency limiting step, providing guidance for rational improvement of these NRs for solar-to-fuel conversion.

We then studied plasmon induced hot electron transfer from metal to semiconductor in Au tipped NRs. Electron transfer in CdS-Au NRs was found to follow a low-efficiency conventional mechanism where the excited plasmon in Au decayed into a hot electron-hole pair and hot electron transfer into CdS competed with ultrafast electron relaxation within Au. In contrast, in CdSe-Au NRs the plasmon band was strongly damped and highly efficient charge separation was observed. For this, we proposed a new plasmon induced charge transfer transition mechanism. These findings suggest an exciting possibility of using plasmons as the light harvesting component for solar energy conversion.

Finally, we studied exciton transport dynamics in CdSe/CdS NRs as a model system for luminescent solar concentrators (LSCs). We revealed a competition between band offset driven exciton transport and trap states induced exciton localization processes, which resulted in a universal length dependence of rod-to-seed exciton localization efficiency. We also showed that exciton trapping can be overcome in 2D CdSe/CdTe hetero-nanosheets where unity exciton localization efficiency was realized, showing great potentials for efficient LSCs.

Charge Separation and Transport Dynamics in One-Dimensional Colloidal Nanostructures for Solar Energy Conversion

By

Kaifeng Wu
B.S., University of Science and Technology of China, P.R. China, 2010

Advisor: Tianquan Lian, Ph.D.

A dissertation submitted to the Faculty of the
James T. Laney School of Graduate Studies of Emory University
in partial fulfillment of the requirements for the degree of
Doctor of Philosophy
in Chemistry
2015

ACKNOWLEDGEMENT

First, I would like to express my deepest gratitude to my advisor, Dr. Tianquan Lian, for his guidance and support throughout my graduate study and research at Emory University. The profundity of his knowledge has helped me overcome many difficulties in my research and his critical thinking as a physical chemist often provides value insights into scientific problems. His willingness to collaborate with scientists in and outside the department also taught me how to work fruitfully with others. He will be the model for my future independent research career. I also wish to extend my sincere thanks to my graduate committee professors, Dr. Michael C. Heaven and Dr. Craig L. Hill, for their insightful questions, helpful comments and valuable support to my graduate research.

It is my pleasure to acknowledge my lab colleagues and my friends for their support in my research and personal life. Dr. Haiming Zhu and Dr. Ye Yang introduced me laser spectroscopy and synthesis and optical properties of nanocrystals during my first year in the lab. I have been working closely with them for most of my graduate research and the discussions with them often lead to wonderful scientific ideas. Dr. William Rodr ́guez, Dr. Jinquan Chen, and Dr. Zheyuan Chen have been responsible for the laser set-ups in the lab and it is their excellent job that guarantees my fruitful research outputs. Mr. Hongjin Lv from Dr. Hill group has provided me helps on light-driven reactions and many other experiments. I am also grateful to other colleagues and friends: Dr. Zhuangqun Huang, Dr. Nianhui Song, Dr. Chantelle Anfuso, Dr. Allen Ricks, Dr. Zheng Liu, Dr. Xu Xiang, Dr. Aimin Ge, Dr. Guijie Liang, Dr. Yongling Du, Dr. Degui Kong, Dr. Hua Tang, Dr. Yueping Ren, Lewen Yang, Nannan Han, Yanyan Jia, Qiuyang Li, Zihao Xu, Arshad Karumbamkandathil, Qiongyi Shang, Li Yu, Jia Song, and Xinhe Shan. They brought lots of happiness to me in and outside the lab.

Last but not least, I would like to thank my family, my father, mother, and brother, for their unconditional and continuous support over the years. Sharing happiness and sadness with them has always been an important part of my life and they always give me enormous encouragements for my future. To them, I am eternally thankful.

Table of Content

List of Figures

List of Tables

Chapter 1. Introduction

1.1. Low-Dimensional Nanostructures beyond QDs for Solar Energy Conversion

One of current society's most daunting challenges is the search for sustainable supplies of clean energy.[1] Solar energy conversion is one of the most promising approaches to addressing this problem, considering that energy of sunlight striking the earth's surface in one hour ($4.3 \cdot 10^{20}$ J) is as much as the current world total energy consumption in one year (~$4.7 \cdot 10^{20}$ J).[1] Therefore, the challenge is transformed to developing efficient and cost-effective solar energy conversion techniques.[2] Generally, there are two ways to utilize solar energy:[2] solar energy conversion into electricity through photovoltaic devices (solar cells) and solar energy conversion into chemical fuels (solar-to-fuel conversion). However, until 2013, solar cells provided less than 0.9% of the world's energy and solar-to-fuel conversion is in its infantry stage, far from mass production.[3] The two major factors that hinder widespread solar energy use are low conversion efficiencies and high manufacturing costs. These limitations often result from the light absorber component, which plays the role for both light harvesting and charge separation in solar energy conversion devices. Two

representative examples are the *p*-*n* junction in traditional silicon solar cells[4] and molecular chromophores in dye sensitized solar cells (DSSCs) [5] or organic heterojunction solar cells.[6] The former usually has relatively high power conversion efficiencies but expensive high temperature and vacuum conditions are required to manufacture defect-free and controllably-doped semiconductor materials. In contrast, the latter utilizes solution-processable low-cost organic materials but suffers from low power conversion efficiencies because of inefficient light absorption and charge separation and transport in organic materials.

Solution-processed colloidal semiconductor nanocrystals or quantum dots (QDs) have the potential to combine the advantage of cost-effective productions of organic materials with strong and broad light absorption properties of inorganic semiconductor materials.[7,8] In addition, the quantum confinement effect in QDs gives rise to new properties that are unachievable in traditional materials.[9-13] For example, the electron and hole energy levels and therefore band gaps can be tuned through their sizes.[14-17] Confinement induced strong carrier-carrier interactions lead to enhanced efficiency of multi-exciton generation (MEG) in QDs,[18-27] a process of generating multiple excitons by absorbing one high energy photon. Efficient MEG may potentially be used to develop third-generation solar cells that can exceed Shockley-Queisser limit.[28,29] For these reasons, QDs have been extensively studied for solar conversion related applications.[17,30-37] To date, however, the solar energy conversion efficiencies of QD based devices remain low,[8,38] due to intrinsic limitations of these zero-dimensional (0D) materials. The small size in all three dimensions limits the light absorption cross sections of QDs (scaled with their volume)

and the distance and therefore lifetime of charge separations.[10,39] These limitations motivate us to seek better low-dimensional materials for solar energy conversion.

Recent advances in nanocrystal shape control have led to the synthesis of colloidal quantum-confined one-dimensional (1D) semiconductor nanostructures, such as nanorods (NRs) and tetrapods.[40-43] Unlike 0D QDs,[44] in which the exciton is quantum confined in all three dimensions, exciton motions in 1D NRs (with diameters of a few nanometers and lengths of 10-100 nanometers) are quantum confined in the radial direction but are bulk like along the axial direction.[45-47] Thus NRs can simultaneously possess the properties of quantum confined QDs (such as size-tunable band gaps and strong carrier-carrier interactions) and bulk crystals (such as large absorption cross sections and long distance charge transport and separation),[48] as shown in Figure 1.1. In addition to single component 1D nanostructures, advances in compositional control of colloidal synthesis have led to various 1D heterostructures,[49] such as dot-in-rod NRs,[50-52] tetrapods[50,51] and nanobarbells.[53,54] In these 1D heterostructures, the concept of "wavefunction engineering" can be applied. The spatial distribution of conduction band (CB) electrons and valence band (VB) holes in excitonic states can be tuned by the sizes and compositions of the constituent materials to control their photo-physical properties, including the lifetimes of single and multiple excitons and the rates of charge separation and recombination in the presence of charge acceptors.[55]

The diameter-tunable energetics and length-tunable light absorptions and charge separations, combined with the capability of wavefunction engineering through heterostructure formation, make 1D colloidal NRs a family of functional materials

with strong potentials for various solar energy conversion applications. The research presented in this dissertation is motivated by these potentials. In our study, we apply ultrafast spectroscopic techniques, mostly pump-probe transient absorption spectroscopy, to investigate the light absorption and emission and charge transport, separation and recombination dynamics in a series of NRs and hetero-NRs. The understanding of these processes provides valuable insights for two general ways of solar energy conversion using 1D nanostructures (Figure 1.1). The first one utilizes the dimensions of NRs to set up long-distance charge separations for photocatalysis[56-61] and the other one uses NRs as light-harvesting antennas to absorb light and transport excitations into engineered emitting centers for luminescent solar concentrations.[62-65]

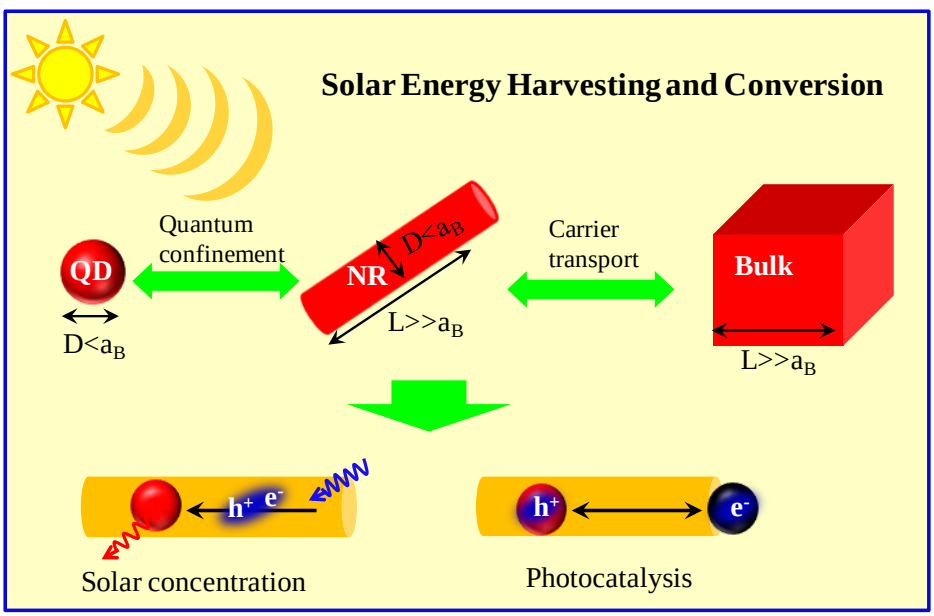

Figure 1.1. The scheme of solar energy harvesting and conversion using 1D semiconductor Nanorods (NRs) and related heterostructures. NRs bridge the gap between QDs and bulk semiconductors: they simultaneously maintain QD like quantum confinement effect in the radial direction and bulk like transport properties in the axial direction. This leads to tunable light absorption and charge separation capabilities using NRs. Various heterostructures of NRs further enrich their functionalities. Here we show two ways of utilizing hetero NRs for solar energy conversion: one uses CdSe/CdS dot-in-rod NRs for luminescent solar concentrations and the other efficiently separate charges using triadic Pt tipped CdSe/CdS dot-in-rod NRs for photocatalysis.

1.2. Electronic structure of NRs

To understand the spectroscopy of 1D NRs, it is necessary to present a brief introduction of their electronic structure. The static absorption spectra of three CdS NRs with similar diameter but different lengths are displayed in Figure 1.2.a.[66] It illustrates that when the length of NR is much larger than exciton Bohr diameter (~5.5 nm in bulk CdS[67,68]), the excitonic transition energies are determined by the rod diameter. In NRs with cylindrical symmetry, quantum confinement in the radial direction leads to discrete electron and hole levels labeled as 1σ, 1π,……[47,69] Because the carrier motion in the radial direction is much faster than the axial direction, electron-hole interaction ($V_{e\text{-}h}$) can be described by an effective 1D Coulomb potential

that depends on their separation along the long axis of the NR (Figure 1.2.b). This 1D potential between the 1σ (π) electron and hole forms a manifold of bound $1\Sigma(\Pi)$ exciton states with the oscillator strength largely concentrated on the lowest energy exciton state, $1\Sigma_0(1\Pi_0)$.[47,69] Following this model, the peaks at ~390 nm and 450 nm can be attributed to the lowest energy $1\Pi_0$ and $1\Sigma_0$ transitions, respectively, as shown in Figure 1.2.a.[47,70] It is also important to note that as a general property of 1-D materials, the exciton binding energy in NRs (on the order of hundreds of meV[47]) is much larger than that in QDs, as a result of reduced dielectric screening and dimensionality effect . [71] [72,73]

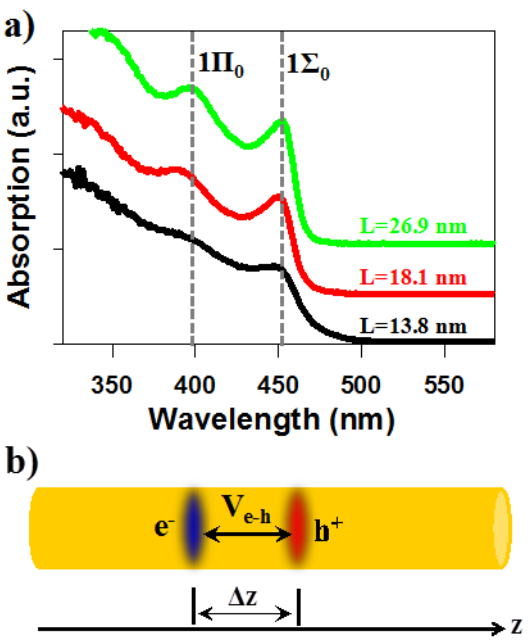

Figure 1.2. Electronic structure and optical property of NRs. a) Static absorption spectra of three CdS NRs with similar diameters (3.8 nm) and different lengths (L). b) Illustration of fast electron and hole motions in the quantum confined radial direction and the effective 1D coulomb interaction, $V_{e\text{-}h}(\Delta z)$, that gives rise to 1D bound

exciton states in NRs. The center of mass of this bound exciton is free to move along the axial direction.

1.3. Charge Separation and Recombination Dynamics in Photocatalytic Pt-tipped Nanorods

Because the tips of NRs with wurtzite crystal structures are often associated with high-energy facets,[74] selective growth of metal nanoparticles (such as platinum and gold[74,75]) at the tip can be readily achieved. It is well known that these metal nanoparticles can act as electron acceptors and catalytic centers, such as Pt for H_2 evolution. Thus, in principle, these integrated semiconductor/metal NR heterostructures, consisted of well positioned light absorbing, charge separating and catalytic components, can be ideal materials for solar-to-fuel conversion.[56,57,70,76]

The overall light driven catalytic conversion reaction involves many forward and backward elementary steps. Here we use Pt tipped CdSe/CdS dot-in-rod (CdSe/CdS-Pt) NRs as a model system to illustrate these steps, as depicted in Figure 1.3.[77] In this triadic structure, CdS domain acts as light absorbers due to its large absorption cross section, CdSe acts as hole acceptors due to the valence band offset between CdSe and CdS,[62,78] and Pt acts as electron acceptors as well as catalytic centers for H_2 generation.[56]

Ideally, photogenerated holes in CdS are driven to the CdSe core (with a time constant of τ_{HL}) by valence band offset[62,78] while electrons can be dissociated from holes and transported to the Pt domain (τ_{ET}). This long distance spatial separation of electrons and holes in the axial direction over three domains prolongs the lifetime of the charge-separated states (CS). The strong quantum confinement in the radial direction also facilitates fast hole removal by electron donor (τ_{HT}), which enables the accumulation of electrons in the Pt tip to carry out reduction of two protons to form H_2 (τ_{CAT}). These forward charge separation steps compete with backward recombination processes, including the intrinsic electron-hole recombination within the NR (τ_{IN}), the loss of electrons in the Pt by recombination with the holes in the CdSe (τ_{CR}) and with the oxidized donor (τ_{L}). Furthermore, due to large surface to volume ratio, photo-generated carriers are susceptible to trapping along the rod, [70,79] which can localize excitons at the trap sites through the large electron-hole binding energy in NRs.[47,78,79] Thus, rational improvement of the photocatalytic efficiencies in such triadic nanoheterostructures requires a detailed understanding of the rates of these competing processes and their dependences on the constituent materials, dimensions and surface properties..

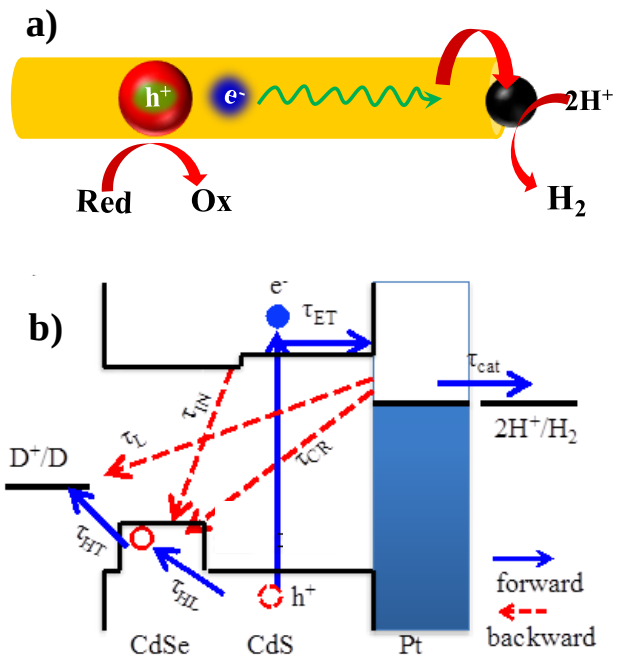

Figure 1.3. Photo-generation of H_2 in CdSe/CdS-Pt triadic NRs. a) Schematic illustration of a triadic NR: a CdSe core embedded in a CdS NR with a Pt nanoparticle at one tip. Upon photoexcitation, electrons are transferred to Pt tip for the catalytic reduction of $2H^+$ to H_2, while holes are transferred to CdSe core and then removed by external electron donors. b) Schematic diagram showing relative energy levels in CdSe, CdS and Pt and charge separation (forward) and recombination (backward) processes relevant to photo-catalytic H_2 generation.

1.4. Plasmon Induced Charge Separation in Au-tipped NRs

The light absorption and charge separation behaviors of 1D semiconductor/metal NR heterostructures become more interesting than simply using metallic domains as

electron acceptors and catalytic centers if the metallic domains can support Surface Plasmon Resonance (SPR).[80-83] SPR is the collective oscillation of conduction band electrons driven by light and has long been a subject of intense research interests.[84-89] The SPR bands are tunable from UV to near-IR, depending sensitively on the nanostructure (materials, size and shape) and the dielectric properties of the surrounding environment. [87] For these reasons, plasmonic nanostructures have been used to enhance the efficiency of semiconductors based solar energy conversion devices.[90-96] One of the most interesting enhancing mechanisms is recently reported plasmon induced hot electron transfer from excited metal nanostructures into semiconductors.[97,98] This novel plasmon-exciton interaction mechanism suggests that plasmonic nanostructures can potentially function as a new class of widely tunable and robust light harvesting materials for photo-detection or solar energy conversion.[97-104]

So far, most reported efficiencies of plasmon-induced hot electron injection from metal to semiconductor are low because hot electrons can quickly relax to lower energy levels via ultrafast electron-electron and electron-phonon scatterings, [105-107] losing the energy needed to overcome the electron transfer barrier between metal and semiconductor. Because the electron-electron scattering process takes place on the tens to hundreds of femtoseconds time scale,[107] electron transfer on this or faster time scales is required for the efficient utilization of plasmons. This requirement is difficult to meet in many semiconductor-metal hybrid materials in which these two domains are connected by molecular linkers[108] or insulating layers.[109,110]

1D semiconductor/metal NR heterostructures are an ideal system for exploring the plasmon-induced hot electron injection phenomenon. [74,75,111] First, the direct contact between semiconductor and metal domains can lead to strong electronic couplings for ultrafast interfacial electron transfer.[112-114] Second, similar to the strategy for long-lived charge separations in triadic CdSe/CdS-Pt NRs, engineered NR heterostructures with efficient charge transport and separation offer opportunities for long-lived plasmon induced charge separation. Last but not the least, the well-defined electronic structure of semiconductor NRs provides direct spectroscopic signatures for following plasmon induced hot electrons. In our study, we use transient absorption spectroscopy to directly probe plasmon induced hot electron transfer processes in Au tipped CdS or CdSe NRs (CdS-Au or CdSe-Au, respectively),[115] as shown in Figure 1.4. Charge separation and recombination dynamics as well as charge separation efficiencies are directly measured. This fundamental study reveals the mechanisms and efficiency limiting factors of plasmon induced hot electron transfer and provides directions for further improving this process for possible applications in solar energy conversion systems.

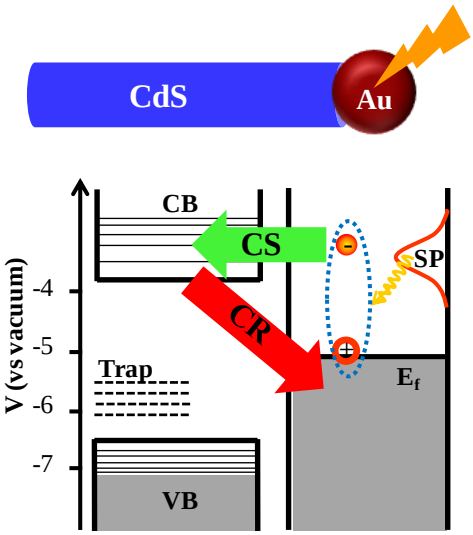

Figure 1.4. A scheme for plasmon induced charge separation in Au tipped CdS NRs. An excited surface plasmon in the Au tip (SP, red peak) can decay non-radiatively (yellow arrow) into a hot electron-hole pair (blue dashed line), which can lead to hot electron injection into the CB of the CdS NR (green arrow) and charge recombination with the Au tip (red arrow).

1.5. Exciton Transport Dynamics in Hetero NRs for Luminescent Solar Concentration

In most nanocrystal based solar energy conversion devices, the nanocrystals function as both light absorption and charge separation components.[55] However, charge separation processes are usually complicated due to many competing forward charge transfer and backward charge recombination steps,[48] as we illustrated above. Long-term experimental and theoretic studies are required to reach rational control

over these steps before the implementation of these colloidal nanostructures. An alternative way to utilize nanocrystals for solar energy conversion is to harness their excellent light emitting properties.[63-65,116-119] Unlike the complicated nature of charge separation, light emission from nanocrystals is relatively easy to control and improve. Indeed, near unity photoluminescence (PL) quantum yields (QYs) have been achieved using, for example, core/shell QDs.[120,121] Therefore, it is possible to use nanocrystals to absorb light and then efficiently re-emit light in a controllable manner into a high-performance solar energy conversion device such as Si or GaAs solar cells. The control over charge separation in the latter has been much more well-established compared with nanocrystals. This is the idea of luminescent solar concentrators (LSCs) for enhanced solar energy conversion efficiencies.[122-127]

A LSC typically consists of a lumophore embedded in a polymer sheet, in which sunlight is absorbed by the lumophore and emitted into the waveguide modes of the polymer sheet and directed to the place where a high-performance solar cell is attached, as shown in Figure 1.5.b.[122,123,128,129] Since the area of the polymer sheet is much larger than that of the solar cell, concentration of the solar photon flux can be achieved. Thermodynamically, LSCs rely on the Stokes shift of lumophores.[128,130,131] Without sufficiently large Stokes shift, an emitted photon can be reabsorbed by other lumophores when travelling through the LSC. Every reabsorption event presents an opportunity for luminescence concentration loss for two reasons.[63,64] The first one is nonradiative decay due to none unity PL QYs of most lumophores and the second one arises from isotropic nature of light emission process which creates the possibility of photon emission into the escape cone. For this reason, single-component QDs cannot

be used for efficient LSCs because of their small Stokes shifts and therefore strong re-absorption of emitted photons.[119] Reabsorption can be partially mitigated in core/shell QDs such CdSe/CdS by increasing the CdS shell size. However, limited by current colloidal synthesis, the shell thicknesses have so far been limited to around 10 nm and also the PL QYs of CdSe/CdS QDs decrease with shell thickness.[64]

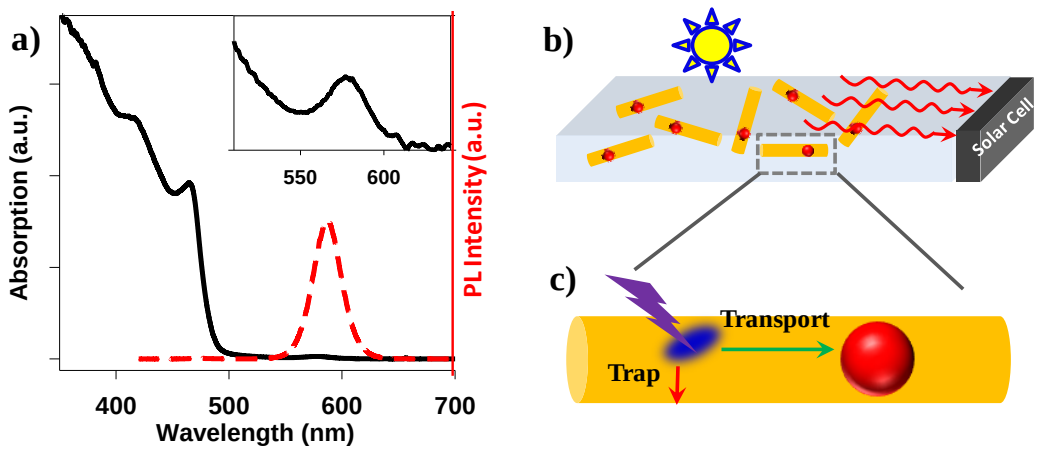

Figure 1.5. CdSe/CdS dot-in-rod NRs for solar concentration. a) Absorption (black solid line) and PL (red dashed line) spectra of a typical CdSe/CdS NRs (~5.6 nm in diameter and 120 nm in length). The inset shows that absorption from the CdSe seed. b) The minimized re-absorption of emitted light makes this structure highly desirable for building luminescent solar concentrators (LSCs) where the emitted lights travels with little re-absorption loss to the attached solar cell. c) Microscopically, there exists a possible competition between exciton transport from CdS rod to CdSe seed and exciton trapping on CdS rod, which is important in determining LSC performances.

1D hetero NRs, such as CdSe/CdS dot-in-rod NRs, offer unique designs to overcome the limits of core and core/shell QDs for efficient LSCs. First, it is possible to grow much larger volumes of CdS in the NR geometry than in the core/shell geometry by simply increasing the NR length, resulting in diminishing re-absorption of emitted photons, as shown in Figure 1.5.a.[50,51,63] Second, unlike in core/shell QDs, the CdSe/CdS interface is not perturbed with continuously growing NR length and therefore PL QY decrease can in principle be avoided during volume increase. Therefore, these CdSe/CdS NRs should be excellent candidates for efficient LSCs. However, transfer of photo-excited excitons from the CdS rod to CdSe seed in these hetero NRs involves not only energy relaxation from higher to lower energy states but also charge transport over a length scale of 10-1000 nm.[78,132] Such long distance exciton transport is susceptible to energetic disorder along the length of the rod caused by diameter variations and trap states.[62] In our study, we investigate the competition between band offset driven exciton transport and trap states induced exciton localization processes in CdSe/CdS NRs, a shown in Figure 1.5.c . CdS rod length dependent rod-to-seed exciton transport efficiencies are measured to obtain a universal scaling law that can provide directions for designing highly efficient 1D hetero NRs based LSCs.

1.6. Conclusion

In conclusion, we have conducted comprehensive spectroscopic studies of charge transport, trapping, and separation dynamics in a series of colloidal 1D semiconductor NRs, semiconductor/semiconductor hetero NRs, and semiconductor/metal hetero NRs, aiming at providing mechanistic insights for the application of 1D nanostructures in solar energy conversion. Our studies reveal two general directions to utilize 1D NRs. The first one harnesses the physical dimensions of these NRs for long-distance and therefore long-lived charge separations in solar-to-fuel conversion. The second one takes advantages of excellent light absorption and emission properties of hetero NRs for luminescent solar concentrations. Under the first category, we measured charge separation and recombination dynamics in photocatalytic Pt tipped CdS (CdS-Pt) and CdSe/CdS (CdSe/CdS-Pt) NRs . Hole trapping in CdS NRs or localization to an engineered site (CdSe seed) in CdSe/CdS NRs was identified as the key contribution to efficient and long-lived charge separations. When applying these structures to light-driven H_2 generation reactions, efficiencies were limited by hole removal from these trapping or localization sites. As to the application of hetero NRs for luminescent solar concentrations, we found a competition between band offset driven exciton transport and trap states induced exciton localization processes in CdSe/CdS NRs. We also illustrated how this competition led to saturation of solar concentration capability as a function of NR length, raising a key issue when designing 1D hetero NRs based LSCs.

The rest of this dissertation is organized as follows: Chapter 2 summarizes the experimental procedures, including the preparation of samples and experimental techniques. Chapter 3 studies the exciton quenching mechanism in CdS-Pt NRs and

shows that electron transfer from CB of CdS NRs to Pt is the dominant quenching channel due to ultrafast hole trapping and for the same reason the charge separated states are long-lived. Chapter 4 further illustrates this principle using Pt tipped 2D CdSe nanosheets in which energy transfer from CdSe nanosheets to Pt becomes dominant quench pathway for lack of efficient hole trapping. Chapter 5 studies charge separation and recombination dynamics in CdSe/CdS-Pt NRs with engineering hole localization sites (CdSe seeds) and compares CdS-Pt and CdSe/CdS-Pt NRs for light-driven H_2 evolution. Chapter 6 and 7 study plasmon induced hot electron transfer from metal to semiconductor using Au tipped CdS (CdS-Au) and CdSe NRs (CdSe-Au) as model systems. Electron transfer in CdS-Au NRs follows a low-efficiency conventional mechanism where the excited plasmon in Au decays into a hot electron-hole pair and then injects the hot electron into CdS. In contrast, highly efficient electron transfer is observed in CdSe-Au NRs with strongly coupled interfaces, which we attribute to a new plasmon induced charge transfer transition mechanism. Chapter 8 examines the competition between band offset driven exciton transport and trap states induced exciton localization processes in CdSe/CdS NRs and reveals multiple exciton species existing on the NRs as a result of this competition. Chapter 9 systematically studies the dependence of this competition on rod lengths and shows a universal length-dependent rod-to-seed exciton localization efficiency. This dependence is discussed under the context of luminescent solar concentrations. Chapter 10 presents 2D CdSe/CdTe hetero nanosheets where this size-dependence can be overcome and unity exciton localization efficiency can be realized, showing great potential for luminescent solar concentrations.

References

(1) Lewis, N. S.; Nocera, D. G. *Proc. Natl. Acad. Sci.* **2006**, *103*, 15729.

(2) Blankenship, R. E.; Tiede, D. M.; Barber, J.; Brudvig, G. W.; Fleming, G.; Ghirardi, M.; Gunner, M. R.; Junge, W.; Kramer, D. M.; Melis, A.; Moore, T. A.; Moser, C. C.; Nocera, D. G.; Nozik, A. J.; Ort, D. R.; Parson, W. W.; Prince, R. C.; Sayre, R. T. *Science* **2011**, *332*, 805.

(3) BP Statistical Review of World Energy 2014, *June*.

(4) Zhao, J. H.; Wang, A. H.; Green, M. A.; Ferrazza, F. *Appl. Phys. Lett.* **1998**, *73*, 1991.

(5) O'regan, B.; Gratzel, M. *nature* **1991**, *353*, 737.

(6) Dennler, G.; Scharber, M. C.; Brabec, C. J. *Adv. Mater.* **2009**, *21*, 1323.

(7) Talapin, D. V.; Lee, J.-S.; Kovalenko, M. V.; Shevchenko, E. V. *Chem. Rev.* **2009**, *110*, 389.

(8) Kramer, I. J.; Sargent, E. H. *Chem. Rev.* **2013**.

(9) Brus, L. E. *J. Chem. Phys.* **1983**, *79*, 5566.

(10) Brus, L. E. *J. Chem. Phys.* **1984**, *80*, 4403.

(11) Alivisatos, A. P. *Science* **1996**, *271*, 933.

(12) Klimov, V. I.; Mikhailovsky, A. A.; Xu, S.; Malko, A.; Hollingsworth, J. A.; Leatherdale, C. A.; Eisler, H. J.; Bawendi, M. G. *Science* **2000**, *290*, 314.

(13) Klimov, V. I. *Annu. Rev. Phys. Chem.* **2007**, *58*, 635.

(14) Zhu, H.; Song, N.; Lian, T. *J. Am. Chem. Soc.* **2010**, *132*, 15038.

(15) Zhu, H.; Song, N.; Lian, T. *J. Am. Chem. Soc.* **2011**, *133*, 8762.

(16) Zhu, H.; Yang, Y.; Song, N.; Rodr ́guez-Cordoba, W.; Lian, T. *Proc. SPIE* **2011**, *8098*, 809802.

(17) Zhu, H.; Song, N.; Rodr ́guez-C ́ordoba, W.; Lian, T. *J. Am. Chem. Soc.* **2012**, *134*, 4250.

(18) Ben-Lulu, M.; Mocatta, D.; Bonn, M.; Banin, U.; Ruhman, S. *Nano Lett.* **2008**, *8*, 1207.

(19) Pijpers, J. J. H.; Ulbricht, R.; Tielrooij, K. J.; Osherov, A.; Golan, Y.; Delerue, C.; Allan, G.; Bonn, M. *Nat Phys* **2009**, *5*, 811.

(20) Midgett, A. G.; Hillhouse, H. W.; Hughes, B. K.; Nozik, A. J.; Beard, M. C. *J. Phys. Chem. C* **2010**, *114*, 17486.

(21) Nair, G.; Chang, L.-Y.; Geyer, S. M.; Bawendi, M. G. *Nano Lett.* **2011**, *11*, 2145.

(22) Schaller, R. D.; Sykora, M.; Jeong, S.; Klimov, V. I. *J. Phys. Chem. B* **2006**, *110*, 25332.

(23) McGuire, J. A.; Joo, J.; Pietryga, J. M.; Schaller, R. D.; Klimov, V. I. *Acc. Chem. Res.* **2008**, *41*, 1810.

(24) Trinh, M. T.; Houtepen, A. J.; Schins, J. M.; Hanrath, T.; Piris, J.; Knulst, W.; Goossens, A. P. L. M.; Siebbeles, L. D. A. *Nano Lett.* **2008**, *8*, 1713.

(25) Beard, M. C.; Midgett, A. G.; Hanna, M. C.; Luther, J. M.; Hughes, B. K.; Nozik, A. J. *Nano Lett.* **2010**, *10*, 3019.

(26) Allan, G.; Delerue, C. *ACS Nano* **2011**, *5*, 7318.
(27) Cunningham, P. D.; Boercker, J. E.; Foos, E. E.; Lumb, M. P.; Smith, A. R.; Tischler, J. G.; Melinger, J. S. *Nano Lett.* **2011**, *11*, 3476.
(28) Nozik, A. J. *Physica E* **2002**, *14*, 115.
(29) Nozik, A. J.; Beard, M. C.; Luther, J. M.; Law, M.; Ellingson, R. J.; Johnson, J. C. *Chem. Rev.* **2010**, *110*, 6873.
(30) Sambur, J. B.; Novet, T.; Parkinson, B. A. *Science* **2010**, *330*, 63.
(31) Semonin, O. E.; Luther, J. M.; Choi, S.; Chen, H.-Y.; Gao, J.; Nozik, A. J.; Beard, M. C. *Science* **2011**, *334*, 1530.
(32) Matylitsky, V. V.; Dworak, L.; Breus, V. V.; Basche, T.; Wachtveitl, J. *J. Am. Chem. Soc.* **2009**, *131*, 2424.
(33) Huang, J.; Huang, Z.; Yang, Y.; Zhu, H.; Lian, T. *J. Am. Chem. Soc.* **2010**, *132*, 4858.
(34) Keuleyan, S.; Lhuillier, E.; Brajuskovic, V.; Guyot-Sionnest, P. *Nat Photon* **2011**, *5*, 489.
(35) Burai, T. N.; Panay, A. J.; Zhu, H.; Lian, T.; Lutz, S. *ACS Catalysis* **2012**, *2*, 667.
(36) Brown, K. A.; Dayal, S.; Ai, X.; Rumbles, G.; King, P. W. *J. Am. Chem. Soc.* **2010**, *132*, 9672.
(37) Sato, S.; Arai, T.; Morikawa, T.; Uemura, K.; Suzuki, T. M.; Tanaka, H.; Kajino, T. *J. Am. Chem. Soc.* **2011**, *133*, 15240.
(38) Kamat, P. V. *J. Phys. Chem. C* **2008**, *112*, 18737.
(39) Bawendi, M. G.; Steigerwald, M. L.; Brus, L. E. *Annu. Rev. Phys. Chem.* **1990**, *41*, 477.
(40) Peng, X. G.; Manna, L.; Yang, W. D.; Wickham, J.; Scher, E.; Kadavanich, A.; Alivisatos, A. P. *Nature* **2000**, *404*, 59.
(41) Milliron, D. J.; Hughes, S. M.; Cui, Y.; Manna, L.; Li, J.; Wang, L.-W.; Paul Alivisatos, A. *Nature* **2004**, *430*, 190.
(42) Li, H.; Kanaras, A. G.; Manna, L. *Acc. Chem. Res.* **2013**, *46*, 1387.
(43) Shieh, F.; Saunders, A. E.; Korgel, B. A. *J. Phys. Chem. B* **2005**, *109*, 8538.
(44) Steigerwald, M. L.; Brus, L. E. *Acc. Chem. Res.* **1990**, *23*, 183.
(45) Katz, D.; Wizansky, T.; Millo, O.; Rothenberg, E.; Mokari, T.; Banin, U. *Phys. Rev. Lett.* **2002**, *89*, 0868011.
(46) Li, L.-s.; Hu, J.; Yang, W.; Alivisatos, A. P. *Nano Lett.* **2001**, *1*, 349.
(47) Shabaev, A.; Efros, A. L. *Nano Lett.* **2004**, *4*, 1821.
(48) Wu, K.; Zhu, H.; Lian, T. *Acc. Chem. Res.* **2015**, *48*, 851.
(49) Sitt, A.; Hadar, I.; Banin, U. *Nano Today* **2013**, *8*, 494.
(50) Talapin, D. V.; Nelson, J. H.; Shevchenko, E. V.; Aloni, S.; Sadtler, B.; Alivisatos, A. P. *Nano Lett.* **2007**, *7*, 2951.
(51) Carbone, L.; Nobile, C.; De Giorgi, M.; Sala, F. D.; Morello, G.; Pompa, P.; Hytch, M.; Snoeck, E.; Fiore, A.; Franchini, I. R.; et al *Nano Lett.* **2007**, *7*, 2942.
(52) Talapin, D. V.; Koeppe, R.; Götzinger, S.; Kornowski, A.; Lupton, J. M.; Rogach, A. L.; Benson, O.; Feldmann, J.; Weller, H. *Nano Lett.* **2003**, *3*, 1677.
(53) Halpert, J. E.; Porter, V. J.; Zimmer, J. P.; Bawendi, M. G. *J. Am. Chem. Soc.* **2006**, *128*, 12590.

(54) Kirsanova, M.; Nemchinov, A.; Hewa-Kasakarage, N. N.; Schmall, N.; Zamkov, M. *Chem. Mat.* **2009**, *21*, 4305.

(55) Zhu, H.; Lian, T. *Energy & Environ. Sci.* **2012**, *5*, 9406.

(56) Amirav, L.; Alivisatos, A. P. *J. Phys. Chem. Lett.* **2010**, *1*, 1051.

(57) Acharya, K. P.; Khnayzer, R. S.; O'Connor, T.; Diederich, G.; Kirsanova, M.; Klinkova, A.; Roth, D.; Kinder, E.; Imboden, M.; Zamkov, M. *Nano Lett.* **2011**, *11*, 2919.

(58) Simon, T.; Bouchonville, N.; Berr, M. J.; Vaneski, A.; Adrović, A.; Volbers, D.; Wyrwich, R.; Döblinger, M.; Susha, A. S.; Rogach, A. L.; Jäckel, F.; Stolarczyk, J. K.; Feldmann, J. *Nat Mater* **2014**, *doi:10.1038/nmat4049*.

(59) Berr, M.; Vaneski, A.; Susha, A. S.; Rodriguez-Fernandez, J.; Doblinger, M.; Jackel, F.; Rogach, A. L.; Feldmann, J. *Appl. Phys. Lett.* **2010**, *97*, 0931081.

(60) Tongying, P.; Vietmeyer, F.; Aleksiuk, D.; Ferraudi, G. J.; Krylova, G.; Kuno, M. *Nanoscale* **2014**, *6*, 4117.

(61) Tongying, P.; Plashnitsa, V. V.; Petchsang, N.; Vietmeyer, F.; Ferraudi, G. J.; Krylova, G.; Kuno, M. *J. Phys. Chem. Lett.* **2012**, *3*, 3234.

(62) Borys, N. J.; Walter, M. J.; Huang, J.; Talapin, D. V.; Lupton, J. M. *Science* **2010**, *330*, 1371.

(63) Bronstein, N. D.; Li, L.; Xu, L.; Yao, Y.; Ferry, V. E.; Alivisatos, A. P.; Nuzzo, R. G. *ACS Nano* **2013**, *8*, 44.

(64) Meinardi, F.; Colombo, A.; Velizhanin, K. A.; Simonutti, R.; Lorenzon, M.; Beverina, L.; Viswanatha, R.; Klimov, V. I.; Brovelli, S. *Nat Photon* **2014**, *8*, 392.

(65) Coropceanu, I.; Bawendi, M. G. *Nano Lett.* **2014**, *14*, 4097.

(66) Wu, K.; Rodríguez-Córdoba, W.; Lian, T. *J. Phys. Chem. B* **2014**, *118*, 14062.

(67) Puthussery, J.; Lan, A.; Kosel, T. H.; Kuno, M. *ACS Nano* **2008**, *2*, 357.

(68) Hoang, T. B.; Titova, L. V.; Jackson, H. E.; Smith, L. M.; Yarrison-Rice, J. M.; Lensch, J. L.; Lauhon, L. J. *Appl. Phys. Lett.* **2006**, *89*, 1231231.

(69) Bartnik, A. C.; Efros, A. L.; Koh, W. K.; Murray, C. B.; Wise, F. W. *Phys. Rev. B* **2010**, *82*, 19531301.

(70) Wu, K.; Zhu, H.; Liu, Z.; Rodríguez-Córdoba, W.; Lian, T. *J. Am. Chem. Soc.* **2012**, *134*, 10337.

(71) Vietmeyer, F.; McDonald, M. P.; Kuno, M. *J. Phys. Chem. C* **2012**, *116*, 12379.

(72) Brus, L. *Acc. Chem. Res.* **2014**, *47*, 2951.

(73) Brus, L. *Nano Lett.* **2010**, *10*, 363.

(74) Mokari, T.; Rothenberg, E.; Popov, I.; Costi, R.; Banin, U. *Science* **2004**, *304*, 1787.

(75) Habas, S. E.; Yang, P.; Mokari, T. *J. Am. Chem. Soc.* **2008**, *130*, 3294.

(76) Berr, M. J.; Vaneski, A.; Mauser, C.; Fischbach, S.; Susha, A. S.; Rogach, A. L.; Jäckel, F.; Feldmann, J. *Small* **2012**, *8*, 291.

(77) Wu, K.; Chen, Z.; Lv, H.; Zhu, H.; Hill, C. L.; Lian, T. *J. Am. Chem. Soc.* **2014**, *136*, 7708.

(78) Wu, K.; Rodríguez-Córdoba, W. E.; Liu, Z.; Zhu, H.; Lian, T. *ACS Nano* **2013**, *7*, 7173.

(79) Mauser, C.; Da Como, E.; Baldauf, J.; Rogach, A. L.; Huang, J.; Talapin, D. V.; Feldmann, J. *Phys. Rev. B* **2010**, *82*, 0813061.

(80) Brongersma, M. L.; Halas, N. J.; Nordlander, P. *Nat Nano* **2015**, *10*, 25.

(81) Mubeen, S.; Lee, J.; Lee, W.-r.; Singh, N.; Stucky, G. D.; Moskovits, M. *ACS Nano* **2014**.

(82) Manjavacas, A.; Liu, J. G.; Kulkarni, V.; Nordlander, P. *ACS Nano* **2014**.

(83) Clavero, C. *Nat Photon* **2014**, *8*, 95.

(84) Hartland, G. V. *Chem. Rev.* **2011**, *111*, 3858.

(85) Giannini, V.; Fernández-Domínguez, A. I.; Heck, S. C.; Maier, S. A. *Chem. Rev.* **2011**, *111*, 3888.

(86) Eustis, S.; El-Sayed, M. A. *Chem. Soc. Rev.* **2006**, *35*, 209.

(87) Kelly, K. L.; Coronado, E.; Zhao, L. L.; Schatz, G. C. *J. Phys. Chem. B* **2002**, *107*, 668.

(88) Kamat, P. V. *J. Phys. Chem. B* **2002**, *106*, 7729.

(89) Halas, N. J. *Nano Lett.* **2010**, *10*, 3816.

(90) Li, P.; Wei, Z.; Wu, T.; Peng, Q.; Li, Y. *J. Am. Chem. Soc.* **2011**, *133*, 5660.

(91) Hirakawa, T.; Kamat, P. V. *J. Am. Chem. Soc.* **2005**, *127*, 3928.

(92) Thomann, I.; Pinaud, B. A.; Chen, Z.; Clemens, B. M.; Jaramillo, T. F.; Brongersma, M. L. *Nano Lett.* **2011**, *11*, 3440.

(93) Liu, Z.; Hou, W.; Pavaskar, P.; Aykol, M.; Cronin, S. B. *Nano Lett.* **2011**, *11*, 1111.

(94) Gao, H.; Liu, C.; Jeong, H. E.; Yang, P. *ACS Nano* **2011**, *6*, 234.

(95) Thimsen, E.; Le Formal, F.; Grätzel, M.; Warren, S. C. *Nano Lett.* **2010**, *11*, 35.

(96) Gomes Silva, C. u.; Juárez, R.; Marino, T.; Molinari, R.; García, H. *J. Am. Chem. Soc.* **2010**, *133*, 595.

(97) Furube, A.; Du, L.; Hara, K.; Katoh, R.; Tachiya, M. *J. Am. Chem. Soc.* **2007**, *129*, 14852.

(98) Tian, Y.; Tatsuma, T. *J. Am. Chem. Soc.* **2005**, *127*, 7632.

(99) Lee, J.; Mubeen, S.; Ji, X.; Stucky, G. D.; Moskovits, M. *Nano Lett.* **2012**, *12*, 5014.

(100) Chen, H. M.; Chen, C. K.; Chen, C.-J.; Cheng, L.-C.; Wu, P. C.; Cheng, B. H.; Ho, Y. Z.; Tseng, M. L.; Hsu, Y.-Y.; Chan, T.-S.; Lee, J.-F.; Liu, R.-S.; Tsai, D. P. *ACS Nano* **2012**, *6*, 7362.

(101) Mubeen, S.; Hernandez-Sosa, G.; Moses, D.; Lee, J.; Moskovits, M. *Nano Lett.* **2011**, *11*, 5548.

(102) Lee, Y. K.; Jung, C. H.; Park, J.; Seo, H.; Somorjai, G. A.; Park, J. Y. *Nano Lett.* **2011**, *11*, 4251.

(103) Knight, M. W.; Sobhani, H.; Nordlander, P.; Halas, N. J. *Science* **2011**, *332*, 702.

(104) Wu, X.; Thrall, E. S.; Liu, H.; Steigerwald, M.; Brus, L. *J. Phys. Chem. C* **2010**, *114*, 12896.

(105) Fann, W. S.; Storz, R.; Tom, H. W. K.; Bokor, J. *Phys. Rev. B* **1992**, *46*, 13592.

(106) Hertel, T.; Knoesel, E.; Wolf, M.; Ertl, G. *Phys. Rev. Lett.* **1996**, *76*, 535.

(107) Hodak, J. H.; Martini, I.; Hartland, G. V. *J. Phys. Chem. B* **1998**, *102*, 6958.

(108) Li, M.; Cushing, S. K.; Wang, Q.; Shi, X.; Hornak, L. A.; Hong, Z.; Wu, N. *J. Phys. Chem. Lett.* **2011**, *2*, 2125.

(109) Liu, N.; Prall, B. S.; Klimov, V. I. *J. Am. Chem. Soc.* **2006**, *128*, 15362.

(110) Khanal, B. P.; Pandey, A.; Li, L.; Lin, Q.; Bae, W. K.; Luo, H.; Klimov, V. I.; Pietryga, J. M. *ACS Nano* **2012**, *6*, 3832.

(111) Menagen, G.; Macdonald, J. E.; Shemesh, Y.; Popov, I.; Banin, U. *J. Am. Chem. Soc.* **2009**, *131*, 17406.

(112) Yu, P.; Wen, X.; Lee, Y.-C.; Lee, W.-C.; Kang, C.-C.; Tang, J. *J. Phys. Chem. Lett.* **2013**, *4*, 3596.

(113) Sagarzazu, G.; Inoue, K.; Saruyama, M.; Sakamoto, M.; Teranishi, T.; Masuo, S.; Tamai, N. *Phys. Chem. Chem. Phys.* **2013**, *15*, 2141.

(114) Mongin, D.; Shaviv, E.; Maioli, P.; Crut, A.; Banin, U.; Del Fatti, N.; Vallée, F. *ACS Nano* **2012**, *6*, 7034.

(115) Wu, K.; Rodríguez-Córdoba, W. E.; Yang, Y.; Lian, T. *Nano Lett.* **2013**, *13*, 5255.

(116) Bradshaw, L. R.; Knowles, K. E.; McDowall, S.; Gamelin, D. R. *Nano Lett.* **2015**, *DOI: 10.1021/nl504510t*.

(117) Erickson, C. S.; Bradshaw, L. R.; McDowall, S.; Gilbertson, J. D.; Gamelin, D. R.; Patrick, D. L. *ACS Nano* **2014**, *8*, 3461.

(118) Fisher, M.; Farrell, D.; Zanella, M.; Lupi, A.; Stavrinou, P. N.; Chatten, A. J. *Appl. Phys. Lett.* **2015**, *106*, 041110.

(119) Bomm, J.; Büchtemann, A.; Chatten, A. J.; Bose, R.; Farrell, D. J.; Chan, N. L. A.; Xiao, Y.; Slooff, L. H.; Meyer, T.; Meyer, A.; van Sark, W. G. J. H. M.; Koole, R. *Sol. Energy Mater. Sol. Cells* **2011**, *95*, 2087.

(120) Chen, O.; Zhao, J.; Chauhan, V. P.; Cui, J.; Wong, C.; Harris, D. K.; Wei, H.; Han, H.-S.; Fukumura, D.; Jain, R. K.; Bawendi, M. G. *Nat Mater* **2013**, *12*, 445.

(121) Qin, H.; Niu, Y.; Meng, R.; Lin, X.; Lai, R.; Fang, W.; Peng, X. *J. Am. Chem. Soc.* **2013**.

(122) Weber, W. H.; Lambe, J. *Applied Optics* **1976**, *15*, 2299.

(123) Goetzberger, A.; Greube, W. *Appl. Phys.* **1977**, *14*, 123.

(124) Currie, M. J.; Mapel, J. K.; Heidel, T. D.; Goffri, S.; Baldo, M. A. *Science* **2008**, *321*, 226.

(125) Yoon, J.; Li, L.; Semichaevsky, A. V.; Ryu, J. H.; Johnson, H. T.; Nuzzo, R. G.; Rogers, J. A. *Nat Commun* **2011**, *2*, 343.

(126) Debije, M. G.; Verbunt, P. P. C. *Advanced Energy Materials* **2012**, *2*, 12.

(127) Sheng, X.; Shen, L.; Kim, T.; Li, L.; Wang, X.; Dowdy, R.; Froeter, P.; Shigeta, K.; Li, X.; Nuzzo, R. G.; Giebink, N. C.; Rogers, J. A. *Advanced Energy Materials* **2013**, *3*, 991.

(128) Batchelder, J. S.; Zewai, A. H.; Cole, T. *Applied Optics* **1979**, *18*, 3090.

(129) Batchelder, J. S.; Zewail, A. H.; Cole, T. *Applied Optics* **1981**, *20*, 3733.

(130) Yablonovitch, E. *J. Opt. Soc. Am.* **1980**, *70*, 1362.

(131) Smestad, G.; Ries, H.; Winston, R.; Yablonovitch, E. *Solar Energy Materials* **1990**, *21*, 99.

(132) Wu, K.; Hill, L. J.; Chen, J.; McBride, J. R.; Pavlopolous, N. G.; Richey, N. E.; Pyun, J.; Lian, T. *ACS Nano* **2015**, *9*, 4591.

Chapter 2. Experimental Methods

2.1. Sample Preparation

2.1.1. Synthesis of CdSe and CdS Quantum Dots

CdSe quantum dots (QDs). CdSe QDs capped with Trioctylphosphine oxide (TOPO), Trioctylphosphine (TOP), and Octadecylphosphonic acid (ODPA) were synthesized according to a literature procedure. [1] Typically, 0.06 g Cadmium Oxide (CdO), 3 g TOPO, and 0.3 g ODPA were degassed under vacuum for 1 hour at 150 ℃. After heating to 350 ^{o}C under nitrogen for half an hour, the mixture turned into clear solution, indicating the dissolution of CdO. At this point, 1.8 mL TOP was injected to the solution. After TOP injection, the temperature was raised to 370 ^{o}C. 0.75 mL Se/TOP stock solution, prepared by dissolving 1.16 g Selenium (Se) powders in 15 mL TOP by sonication, was swiftly injected into. The solution turned orange in 5s and was instantaneously cooled by removing the heating mantle. In this way, small CdSe QDs (with the first exciton peak at 500 nm) were obtained, corresponding to a diameter of 2.4 nm.[2] CdSe QDs of other sizes can be tuned through the reaction temperature and time. These QDs were precipitated out of the reaction crudes by addition of ethanol and followed by centrifuge. The precipitation processes were repeated for several times.

CdS quantum dots (QDs). CdS QDs with oleic acids (OA) were synthesized according to a literature procedure.[3] In a typical synthesis, 0.077 g Cadmium Oxide (CdO), 0.5 mL Oleic acid (OA) and 15 mL 1-octadecene (ODE) were heated to 280 ^{o}C under nitrogen until complete dissolution of CdO. After the temperature stabilized, 3 mL of sulfur stock solution (0.1 M of S in ODE) were injected. The reaction was stopped after 30 s by injection of 10 mL ODE solution and removing the heating mantle. The CdS QDs were precipitated out by addition of ethanol followed by centrifuge at 4000 rpm for 10 min. The precipitation processes were repeated for several times. As-prepared CdS QDs have the first exciton peak at 375 nm, corresponding to a diameter of 2.6 nm.[2] QDs of other sizes can be prepared by varying the amount of OA used, with higher OA concentration facilitating formation of larger QDs.

2.1.2. Synthesis of CdSe, CdS and CdSe/CdS Nanorods

CdSe Nanorods (NRs) CdSe NRs were synthesized by previously-reported procedures with slight modifications.[4,5] Briefly, a mixture of 0.104 g Cadmium Oxide (CdO), 0.401 g octadecylphosphonic acid (ODPA), 0.07 g hexylphosphonic acid (ODPA), and 1.43 g tri-n-octylphosphine oxide (TOPO) was degassed at 150 ℃ for 1 h and then heated to 320 ℃ under argon atmosphere until it turned clear. 0.136 g Se powder was dissolved in a mixture of 0.5 mL tri-n-butylphosphine (TBP) and 2.85 mL tri-n-octylphosphine (TOP) as the Se stock solution. At 320 ℃, 1 mL of Se stock was swiftly injected, which brought the temperature down to 290 ℃. The reaction

was kept at 290 ℃ for 7 min for growth of CdSe NRs before it was stopped by removing the heating mantle. The resulting NRs have their first excitonic absorption peak at ~582 nm. NRs of other diameters can be obtained by tuning the growth temperature and time, with higher temperature and longer time favoring formation of thicker NRs. Products were precipitated out of the reaction crudes by addition of toluene and ethanol. The precipitation processes were repeated for several times to remove excessive surfactants. Final products were dispersed in chloroform for optical measurements.

CdS Nanorods (NRs) CdS NRs were synthesized following a seeded-growth procedure reported in the literature.[6-8] In a typical synthesis, 0.06 g O Cadmium Oxide (CdO), 3 g Trioctylphosphine oxide (TOPO), 0.29 g Octadecylphosphonic acid (ODPA), and 0.08 g hexylphosphonic acid (HPA) were degassed under vacuum for 1 hour at 150 ℃. After heating to 350 ºC under argon for half an hour, the mixture turned into clear solution, indicating the dissolution of CdO. At this point, 1.8 ml Trioctylphosphine (TOP) was injected to the solution. In a separated container, sulfur injection solution (0.12g S in 1.8 mL TOP) was mixed with CdS quantum dot seeds with first excitonic transition at 370 nm. The amount of seeds in a typical synthesis was 4×10^{-8} mol. When the temperature of the CdO-containing solution was stabilized at 350 ℃, the seed-containing Sulfur injection solution was quickly injected. The temperature dropped down upon the injection and recovers to 350 ℃ in ~1 min. The solution was allowed to grow for 3-8 min. Nanorod with different lengths and diameters could be achieved by tuning the growth temperature and time. Reactions

were stopped by removing the heating mantle. Products were precipitated out of the reaction crudes by addition of ethanol. The precipitation processes were repeated for several times. Final products are dispersed in chloroform.

CdSe/CdS Nanorods (NRs) To synthesize CdSe/CdS dot -in-rod hetero NRs, 0.06 g CdO, 3 g TOPO, 0.29 g ODPA, and 0.08 g HPA were degassed under vacuum for 1 hour at 150 ℃. After heating to 350 ºC under nitrogen for half an hour, the mixture turned into clear solution, indicating the dissolution of CdO. At this point, 1.8 ml Trioctylphosphine (TOP) was injected into the solution. In a separated container, sulfur injection solution (0.12g S in 1.8 mL TOP) was mixed with CdS or CdSe QDs. The amount of seeds in a typical synthesis was 8×10^{-8} mol. When the temperature of the Cd-containing solution was stabilized at 350 ℃, the seed-containing Sulfur injection solution was quickly injected. The temperature dropped down upon the injection and recovered to 350 ℃ in ~1 min. The solution was allowed to grow for 8 min. Products were precipitated out of the reaction crudes by addition of ethanol. The precipitation processes were repeated for several times. Final DIRs were dispersed in chloroform.

2.1.3. Synthesis of Metal Tipped Nanorods

CdS-Pt NRs CdS NRs with Pt nanoparticle at one tip were synthesized according to a reported procedure with slight modifications.[9] Briefly, a mixture of 0.2 mL oleic acid, 0.2 mL oleylamine, 43 mg 1,2-hexadecanediol and 10 mL diphenyl ether was

degassed under vacuum for 1h at 80 ℃. Then the temperature of the solution was raised to 190 ℃ under argon. 10 mg Pt acetylacetonate was added to a suspension of NRs in dichlorobenzene and sonicated for 5 minutes to dissolve the Pt precursor. This solution was injected into the diphenyl ether solution. The reaction was allowed to proceed for 9 min and quenched by water bath. The products were washed twice by precipitation with ethanol followed by centrifugation, and finally dispersed in chloroform. Platinum nanoparticles for control experiments were synthesized under similar conditions without the addition of NRs. The growth time was slightly longer, typically 15 minutes, because the homogeneous nucleation of platinum nanoparticles was slower than the heterogeneous nucleation on the surfaces of CdS NRs.

CdS-Au NRs CdS NRs with Au nanoparticle at one tip were synthesized using the method developed by Banin et al, with slight modifications.[10] Briefly, ~1×10^{-8} mol of CdS NRs were dispersed in 3 mL toluene in a sealed vial and purged with Argon gas. The gold stock solution was made by dissolution of 10 mg gold(III) chloride ($AuCl_3$), 15 mg of didodecyldimethylammonium bromide (DDAB, 98%) and 40 mg of dodecylamine (DDA) in 6 mL toluene in another sealed vial. After sonication for about 1h, $AuCl_3$ was completely dissolved and formed a pale yellow solution. The NR-containing vial was placed in an ice bath, which was critical for suppression of Au growth along the sides of NRs.[10] 2 mL of Au stock solution was injected into this vial under vigorous stirring. The vial was irradiated with a Xeon lamp (20 W) to deposit Au tips on one end of NRs. The reason why Au tip only grows on one end of CdS NR is not clear. It is proposed that the intrinsic electrical dipole moment of the

wurtzite structure may drive photogenerated electrons exclusively to one end of NR or there is a preferential crystal matching between gold and certain facets of CdS NR.[11] After 1 hour, the reaction was stopped and ethanol was added to precipitate CdS-Au NRs. The precipitation process was repeated for several times to remove excessive surfactants. Final products were dispersed in chloroform for optical measurements. Au NPs for control experiments were synthesized by thermal reduction of gold(III) chloride ($AuCl_3$).[12] Briefly, 4 mL of oleylamine was degassed at 120 ℃ for about 30 minutes and cooled down to 50 ℃. 20 mg of $AuCl_3$ was added and the temperature was raised to 90 ℃. After reaction of 1 h, it was stopped by addition of toluene. Spherical Au NPs with diameter ~7 nm were produced. The Au NPs were precipitated out by addition of ethanol.

CdSe-Au NRs. Au tipped CdSe NRs were synthesized using the method of Banin and coworkers with slight modifications.[10] Briefly, 1 mL of CdSe NRs with optical density (OD) of 2 at 582 nm (1mm light pathlength) in chloroform was dried and re-dispersed in 4 mL toluene in a sealed vial and purged with Argon gas. The gold stock solution was prepared by dissolution of 33 mg gold(III) chloride ($AuCl_3$), 30 mg of didodecyldimethylammonium bromide (DDAB, 98%) and 115 mg of dodecylamine (DDA) in 9 mL toluene in another sealed vial. It was also purged with Argon before use. The Au deposition reaction was initiated by adding 3 mL of Au stock solution drop-wise to the CdSe NR solution over a period of 3 min in an ice bath. The ice bath was found to effectively suppress Au growth along the wall of NRs and preserve the well-defined exciton properties of NRs.[10] After another 10 min, the reaction was stopped and ethanol was added to precipitate CdSe-Au NRs. Final

products were dispersed in chloroform for optical measurements. Similar procedures were applied to synthesize QD-Au dimmers and CdSe-Au NRs with different NR diameters.

2.1.4. Synthesis of CdSe, Pt tipped CdSe, and core/crown CdSe/CdTe Nanosheets

CdSe nanosheets (NSs) CdSe NSs were synthesized following procedures reported in the literature, with slight modifications.[13-15] In a typical synthesis, 170mg of Cadmium myristate ($Cd(myr)_2$) and 15ml of 1-Octadecene (ODE) were mixed in a three-neck flask and degassed under vacuum for 1 hour at 100 ^oC. The mixture was then heated under argon flow at 240 ^oC and injected swiftly with 1ml of Selenium (Se) solution (0.15 M in ODE). After 10 seconds, 80mg of Cadmium acetate dihydrate ($Cd(Ac)_2 \cdot 2H_2O$) dispersed in ODE (in a slurry form) were introduced to initiate nanosheet formation. The reaction continued for 10 minutes at 240 ^oC before quenching by water bath. At room temperature, 1mL of oleic acid (OA) was added to the mixture for better dispersion of NSs. The product was a mixture of quantum dots (QDs) and NSs. NSs were separated from the QDs using centrifugation at 3000 rpm for 10 minutes. Final NSs were dispersed in chloroform for optical studies.

CdSe NS-Pt Pt nanoparticle tipped CdSe NSs were synthesized in a similar way to a reported synthesis procedure for Pt tipped CdS nanorods.[9] Briefly, a mixture of 0.2 mL oleic acid (OA), 0.4 mL oleylamine (OLAm), 40 mg 1,2-hexadecanediol (HDT) and 10 mL diphenyl ether (DPE) was degassed under vacuum for 1 hour at 100 ^oC. After that, the temperature of the solution was raised to 195 ^oC under argon flow. 15

mg Pt acetylacetonate was added to a suspension of NSs in dichlorobenzene and sonicated for 5 minutes to dissolve the Pt precursor. This solution was swiftly injected into the DPE solution at 195 ^{o}C. The reaction was allowed to proceed for 3.5 min before quenched by water bath. The product was washed by precipitation with ethanol followed by centrifugation, and finally dispersed in chloroform. To independently obtain the absorption spectrum of Pt nanoparticles, free Pt nanoparticles were also synthesized under similar conditions without the addition of CdSe NSs. The growth time was longer, typically 15 minutes because the homogeneous nucleation of Pt nanoparticles was slower than the heterogeneous nucleation on the surfaces of CdSe NSs.

Core/crown CdSe/CdTe nanosheets (NSs) 80mg $Cd(Ac)_2$ $2H_2O$, 50 uL of OA, and 10ml of ODE were introduced into a 25mL three-neck flask and degassed under vacuum for 1 hour at 100 ^{o}C. The Te precursor was made by sonicating a mixture of 12.7 mg Te powder, 400 uL Trioctylphosphine (TOP), and 5ml ODE. 3 mL CdSe NSs (with optical density of 1 at 512 nm in 1 mm cuvette) in chloroform were dried and then dispersed in 1 mL ODE or dichlorobenzene. At 200 ^{o}C, the CdSe NSs were swiftly injected. The temperature was then set at 190 ^{o}C. After 5 seconds, the Te precursor was slowly injected using a syringe pump at a rate of 1 ml/hour. Aliquots of colloidal solution were withdrawn using a syringe to monitor the CdTe crown growth. The reaction was quenched after ~ 1 hour and the product was washed by precipitation with ethanol followed by centrifugation, and finally dispersed in chloroform for optical characterizations.

2.1.5. Preparation of Water Soluble Nanorods

The original ligands on DIRs and NRs were replaced by 11-mercaptoundecanoic acid (MUA) molecules through a reported procedure. [16,17] Typically, 10 mg of MUA and 8 mL of 0.1 M aqueous solution of KOH were added to 10 mL chloroform solution of DIRs or NRs. The mixture was vigorously shaken and then left stirring for ~2h to transfer the DIRs or NRs into the aqueous phase. The upper layer was taken out and 10 mL of methanol was added to precipitate out the MUA-capped DIRs or NRs. The precipitates were re-dissolved water. The DIR-Pt and NR-Pt are transferred to water phase using the same method.

2.1.6. Representative Sample Images

Figure 2.1 shows a “stamp collection” of Transmission Electron Microscopy (TEM) and Energy Dispersive X-ray Spectroscopy (EDX) images of some representative nanocrystals, including QDs, NRs, NSs, and hetero-NRs. TEM is the most straightforward technique for morphologic characterizations of various nanocrystals whereas EDX is powerful for element mappings and heterostructure identifications. These nanocrystals and heterostructures are building blocks for various solar energy conversion applications and their ultrafast carrier dynamics is the focus of the rest chapters of this dissertation.

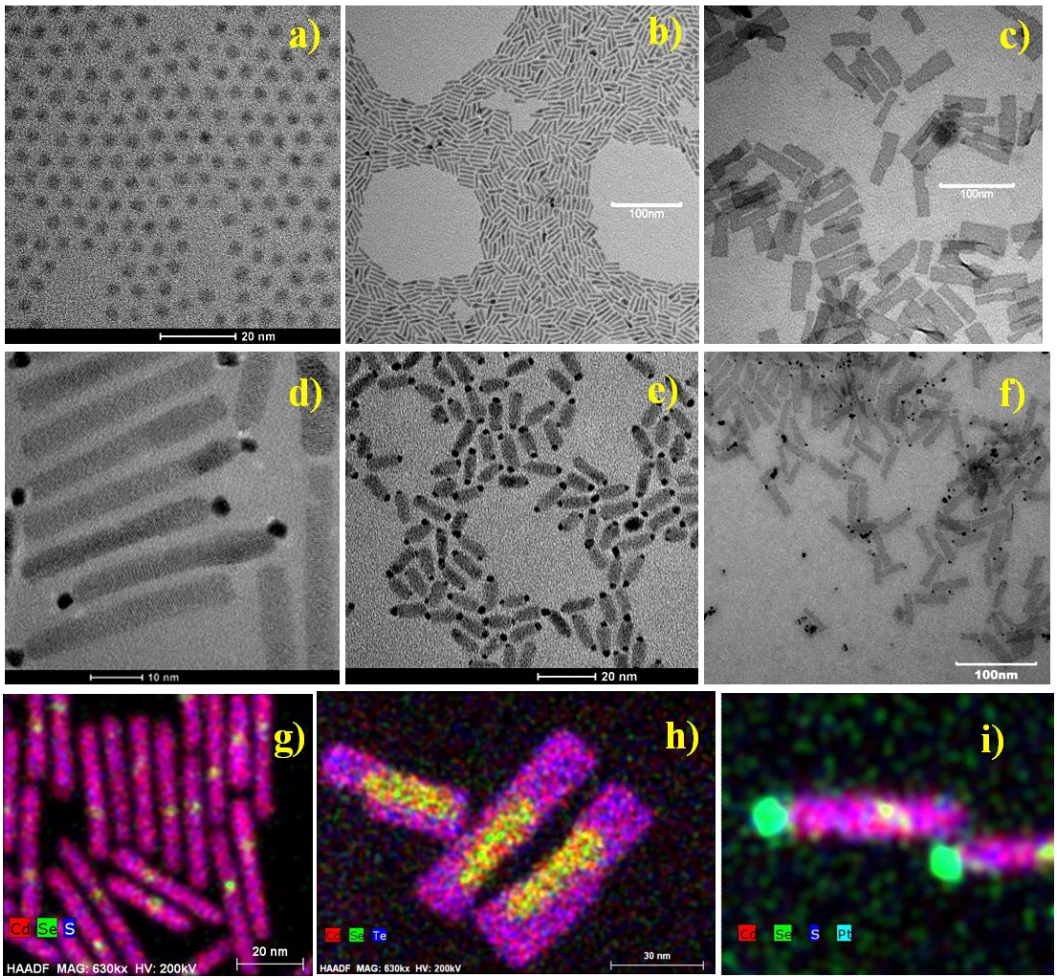

Figure 2.1. A "stamp collection" of TEM and EDX images of some representative nanocrystals and heterostructures. a-f) TEM images of a) CdSe QDs, b) CdS NRs, c) CdSe NSs, d) Pt tipped CdS NRs, e) Au tipped CdSe NRs, and f) Pt tipped CdSe NSs. g-i) EDX elemental maps of a) CdSe/CdS seeded NRs, b) CdSe/CdTe core/crown NSs, and i) Pt tipped CdSe/CdS NRs.

2.2. Time Resolved Spectroscopy Setup

2.2.1. Femtosecond Transient Absorption Setup

Visible Transient Absorption Spectrometer Our tunable femtosecond transient absorption setup is based on a regenerative amplified Ti:sapphire laser system from Coherent (800 nm, 130 fs, 3 mJ/pulse, and 1 kHz repetition rate), nonlinear frequency mixing techniques and the Helios spectrometer (Ultrafast Systems LLC). Briefly, the 800 nm output pulse from the regenerative amplifier was split in two parts with a 10% beamsplitter. One part, with 0.3 μJ/pulse was used to pump a Coherent Opera Optical Parametric Amplifier (OPA) which generates two tunable near-IR pulses from 1.1 to 2.5 μm. This signal and idler beams were separated with a dichroic mirror, and used separately to generate the 495 and 565 nm excitation beam by sum frequency mixing with the 800 nm fundamental beam in a type I β-BBO crystal. The transmitted 800 nm beam, with pulse energy of about 2.7 μJ, was split again into two parts. One part, with ~ 2.4 μJ/pulse, was frequency doubled in a β-BBO crystal to generate the 400 nm excitation pulses at 400 nm. The remaining 800 nm beam was used to generate a white light continuum (WLC) in a sapphire window, which were split into a probe and a reference beams. The probe beam was focused with an Al parabolic reflector onto the sample (with a beam diameter of ~150 μm at the sample). The reference and probe beams were focused into a fiber optics coupled multichannel spectrometer with CMOS sensors and detected at a frequency of 1 KHz. The intensity of the pump pulse used in the experiment was controlled by a variable neutral-density filter wheel. The pump beam diameter at the sample was ~360 μm.

The delay between the pump and probe pulses was controlled by a motorized delay stage. The pump pulses were chopped by a synchronized chopper to 500 Hz and the change in optical density at the sample resulted from the pump pulse was calculated. For all spectroscopy measurements, the samples were kept in a 1 mm cuvette and constantly stirred by a magnetic stirrer to avoid photodegradation.

Mid-IR Transient Absorption Spectrometer A Clark-MXR IR optical parametric amplifier was pumped with 1 mJ/pulse of the 800 nm fundamental beam to generate two tunable near-IR pulses from 1.1 to 2.5 μm (signal and idler, respectively). They were combined in a 1-mm-thick $AgGaS_2$ crystal to generate the mid-infrared probe pulses from 3 to 10 μm by difference frequency generation (DFG). The DFG signal was collimated with a 50 cm CaF_2 lens before it was focused into a 1mm path length cell containing the sample, and at the focal point, it overlapped with the temporally delayed 400 nm or 590 nm excitation pulse. The waist of the probe beam at the sample was 83 μm and the waists of the 400 nm and 590 nm pump beams were 107 and 102 μm, respectively. The mid-IR probe was then dispersed in a monochromator and the intensity change of the IR light induced by photoexcitation was monitored as a function of time with a 32-element HgCdTe array detector. The pump beam was chopped by a New Focus Model 3501 Chopper at 500 Hz. The IRF of this spectrometer was determined to be 210 fs using a thin silicon wafer.

2.2.2. Nanosecond Transient Absorption Setup

Nanosecond (0.5 ns to 1 μs) transient absorption was performed with the EOS spectrometer (Ultrafast Systems LLC). The pump pulses at 400 nm were generated in the regenerative amplified Ti:sapphire laser system as described above. The white light continuum pulse (380 -1700 nm, 0.5 ns pulse width, 20 KHz repetition rate) was generated by focusing a Nd:YAG laser into a photonic crystal fiber. The delay time between the pump and probe pulses was controlled by a digital delay generator (CNT-90, Pendulum Instruments). The probe and reference beams were detected by the same multichannel spectrometers used in the femtosecond setup. To correct for slight difference of excitation intensity of the data acquired by fs and ns instruments under the single exciton conditions, the signal size of the ns kinetics was slightly scaled such that these transient kinetics overlap at the 0.6-1.4 ns.

2.2.3. Time Resolved Fluorescence Setup

Time–resolved fluorescence measurements were performed in the time-correlated single photon counting (TCSPC) mode under right-angle sample geometry.11 A modelocked Ti:Sapphire laser (Tsunami oscillator pumped by a 10 W Millennia Pro, Spectra- Physics) was used to generate femtosecond laser pulses (~100 fs) with a repetition rate of 80 MHz. Pump pulses at 400 nm were produced by doubling the output centered at 800 nm in a BBO crystal. The emission was detected

by a micro-channel-platephotomultiplier tube (Hamamatsu R3809U-51), the output of which was amplified and analyzed by a TCSPC board (Becker & Hickel SPC 600).

2.3. Light Driven H_2 Evolution

The H_2 generation reaction was performed in a cylindrical cuvette (NSG, 32UV10) with a total volume of ~2.5 mL and light path of 1cm. The reaction solutions are MUA capped NR-Pt or DIR-Pt in 1:10 volume ratio of methanol/water or in 0.1 M sodium sulfite water solution. The optical densities of all the samples are adjusted to~1.5 at 455 nm. The reaction solution was constantly stirred and illuminated by a 455 nm monochromatic LED light (15 mW). H_2 generated in the reaction headspace was detected using a HP5890A model gas chromatograph equipped with a thermal conductivity detector and a HP-MOLESIEVE capillary GC column (30m x 0.535 mm x 25.00 μm) packed with 5Å molecular sieves. Argon was used as a carrier gas.

Typically, the H_2 amount was quantified by withdrawing a gas sample from the headspace at certain intervals without stopping the reaction. Two independent measurements were performed for each sample to ensure the reproducibility. Quantum efficiency (QE) for H_2 generation is calculated using: $QE = 2\Delta(H_2)/ \Delta(\hbar\nu)$, where $\Delta(H_2)$ is the H_2 generation rates (number of generated H_2 molecules per second) extracted from the H_2 evolution slope and $\Delta(\hbar\nu)$ is the number of absorbed photons per second calculated from the excitation power and sample optical density. To obtain

the internal QE, number of absorbed photons by DIR or NR is used as Δ(ħν), which is obtained by excluding the light absorbed or scattered by the cuvette and Pt particles from the total number of absorbed photons.

References

(1) Carbone, L.; Nobile, C.; De Giorgi, M.; Sala, F. D.; Morello, G.; Pompa, P.; Hytch, M.; Snoeck, E.; Fiore, A.; Franchini, I. R.; et al *Nano Lett.* **2007**, *7*, 2942.

(2) Yu, W. W.; Qu, L. H.; Guo, W. Z.; Peng, X. G. *Chem. Mat.* **2003**, *15*, 2854.

(3) Yu, W. W.; Peng, X. G. *Angew. Chem. Int. Ed.* **2002**, *41*, 2368.

(4) Peng, Z. A.; Peng, X. G. *J. Am. Chem. Soc.* **2002**, *124*, 3343.

(5) Tice, D. B.; Weinberg, D. J.; Mathew, N.; Chang, R. P. H.; Weiss, E. A. *J. Phys. Chem. C* **2013**, *117*, 13289.

(6) Talapin, D. V.; Nelson, J. H.; Shevchenko, E. V.; Aloni, S.; Sadtler, B.; Alivisatos, A. P. *Nano Lett.* **2007**, *7*, 2951.

(7) Carbone, L.; Nobile, C.; De Giorgi, M.; Sala, F. D.; Morello, G.; Pompa, P.; Hytch, M.; Snoeck, E.; Fiore, A.; Franchini, I. R.; Nadasan, M.; Silvestre, A. F.; Chiodo, L.; Kudera, S.; Cingolani, R.; Krahne, R.; Manna, L. *Nano Lett.* **2007**, *7*, 2942.

(8) Müller, J.; Lupton, J. M.; Lagoudakis, P. G.; Schindler, F.; Koeppe, R.; Rogach, A. L.; Feldmann, J.; Talapin, D. V.; Weller, H. *Nano Lett.* **2005**, *5*, 2044.

(9) Habas, S. E.; Yang, P.; Mokari, T. *J. Am. Chem. Soc.* **2008**, *130*, 3294.

(10) Menagen, G.; Macdonald, J. E.; Shemesh, Y.; Popov, I.; Banin, U. *J. Am. Chem. Soc.* **2009**, *131*, 17406.

(11) Carbone, L.; Jakab, A.; Khalavka, Y.; Sönnichsen, C. *Nano Lett.* **2009**, *9*, 3710.

(12) Khon, E.; Mereshchenko, A.; Tarnovsky, A. N.; Acharya, K.; Klinkova, A.; Hewa-Kasakarage, N. N.; Nemitz, I.; Zamkov, M. *Nano Lett.* **2011**, *11*, 1792.

(13) Ithurria, S.; Dubertret, B. *J. Am. Chem. Soc.* **2008**, *130*, 16504.

(14) Ithurria, S.; Bousquet, G.; Dubertret, B. *J. Am. Chem. Soc.* **2011**, *133*, 3070.

(15) Ithurria, S.; Tessier, M. D.; Mahler, B.; Lobo, R. P. S. M.; Dubertret, B.; Efros, A. L. *Nat Mater* **2011**, *10*, 936.

(16) Amirav, L.; Alivisatos, A. P. *J. Phys. Chem. Lett.* **2010**, *1*, 1051.

(17) Acharya, K. P.; Khnayzer, R. S.; O'Connor, T.; Diederich, G.; Kirsanova, M.; Klinkova, A.; Roth, D.; Kinder, E.; Imboden, M.; Zamkov, M. *Nano Lett.* **2011**, *11*, 2919.

Chapter 3. Ultrafast Charge Separation and Long-lived Charge Separated State in Photocatalytic CdS-Pt Nanorod Heterostructures

3.1. Introduction

In recent years, a new class of colloidal nanoheterostructures containing both semiconductor nanorods and metallic domains has been prepared.[1-10] These materials, combining the size tunable light harvesting ability of quantum-confined semiconductor nanocrystals with the catalytic activities of small metal nanoparticles, show promising applications for photocatalysis, including light-driven H_2 production. For examples, CdS-Pt nanorod (NR) heterostructures, in which a Pt nanoparticle is grown selectively at one end of a CdS nanorod, can generate H_2 under illumination in the presence sacrificial electron donors.[11-14] Upon absorption of light, excitons are generated in the semiconductor NR. As shown in Figure 3.1.a, the excitons can decay by electron, hole and energy transfer to the metallic domain. The generation of H_2 requires the selective transfer of electrons from the semiconductor to the metal while suppressing the charge recombination, hole transfer and energy transfer pathways. The competition between these pathways determines the photo-catalytic quantum

efficiency of these heterostructures. To date, the rates of these processes in strongly-coupled semiconductor-metal heterostructures have not been determined and the mechanism for their photocatalytic activity remains unclear. Furthermore, in heterostructures with plasmonic metallic domains, the exciton and Plasmon interaction provides additional mechanism to control the properties of these "plexcitonic" nanomaterials.[15-17]

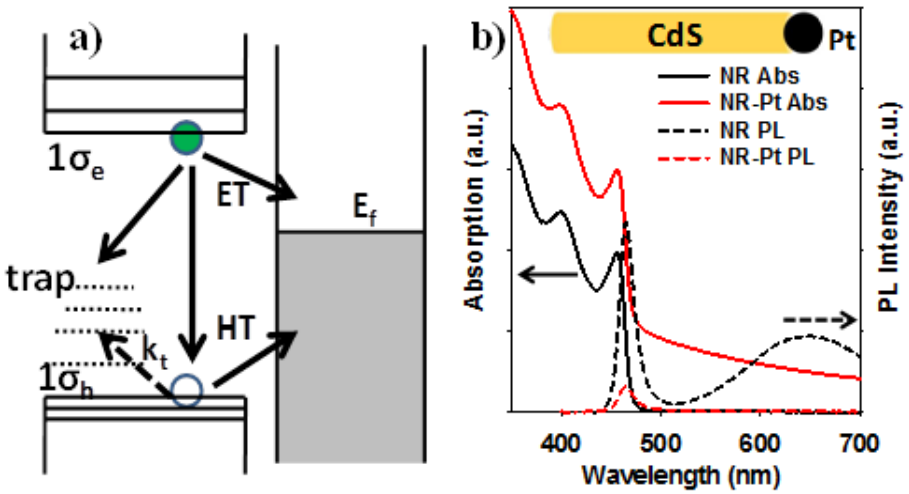

Figure 3.1. a) Schematic energy level and exciton quenching pathways in CdS-Pt NR heterostructures. In addition to the intrinsic exciton decay within CdS NRs, the presence of Pt introduces interfacial electron transfer (ET), hole transfer (HT) and energy transfer (not shown) pathways. b) Absorption (solid lines, left axis) and emission (dashed lines, right axis) spectra of CdS NRs (black) and CdS-Pt NR heterostructures(red). CdS-Pt shows absorption features of both the platinum nanoparticle and CdS NR and significant quenching of band edge and trap state emissions. Inset: schematic structure of CdS-Pt.

In this Chapter, we choose CdS-Pt NRs as a model system to investigate the competition of electron, hole and energy transfer processes in semiconductor-metal heterostructures. Using transient absorption (TA) spectroscopy in conjunction with known molecular electron acceptors, we first identify spectral signatures for electrons, holes and charge separated state in CdS NRs. Following these spectral signatures, we show that electron transfer from excited CdS to Pt is the main exciton quenching pathway in CdS-Pt. We find that the electron transfer process is ultrafast (~3.4 ps) and the charge separated state is surprisingly long-lived (~0.6 μs). This slow charge recombination is attributed to ultrafast hole trapping (~0.7 ps) in CdS NRs. This finding reveals the mechanism of photodriven H_2 generation in these CdS-Pt NRs and provides insight into the design of NR heterostructures for efficient photocatalysis.

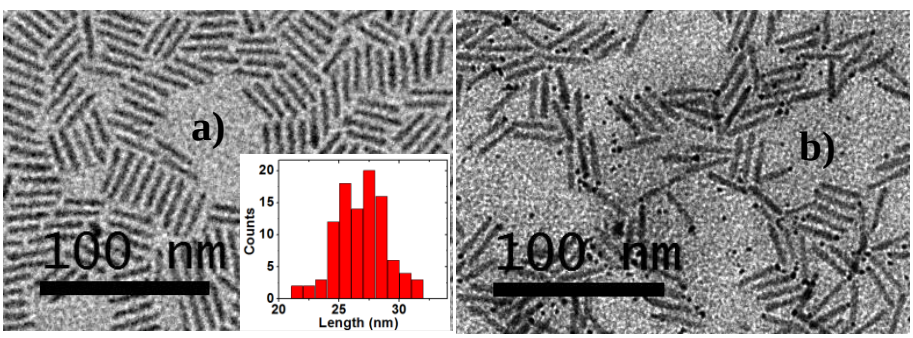

Figure 3.2. TEM images of CdS NRs a) and platinum tipped CdS NRs b), inset in a) is the length distribution for NRs.

3.2. Results and Discussion

3.2.1. Sample synthesis and characterizations

CdS-Pt heterostructures, in which a Pt nanoparticle is grown at one end of a CdS nanorod, were synthesized according to a literature procedure.[6] TEM images of CdS NRs before and after platinum tips growth (Figure 3.2.) indicates an average length of 26.9±2.1 nm and diameter of 3.8±0.3 nm for the CdS NR and diameter of 2.3±0.2 nm for the Pt tip. The absorption and photoluminescence (PL) spectra CdS NRs and CdS-Pt are compared in Figure 3.1.b. The CdS NR exhibits discrete transitions arising from quantum confinement in the radial direction.[18-21] The first absorption peak centered at 456 nm can be attributed to the 1Σ exciton band. In CdS-Pt, the CdS exciton bands remain unchanged (no obvious broadening or shifting), while additional broad absorption features, extending from the UV to near IR, is also observed. The latter can be attributed to the strong d-sp interband transition of platinum nanoparticles.[22] PL of CdS NRs shows two distinct emission bands, with a narrow band-edge emission at 463 nm and a broad trap-state emission centered at 650 nm.[23] In CdS-Pt, the trap-state emission is completely quenched while the band-edge emission is also significantly reduced, indicating a faster decay of electron and/or holes in the excited NR.

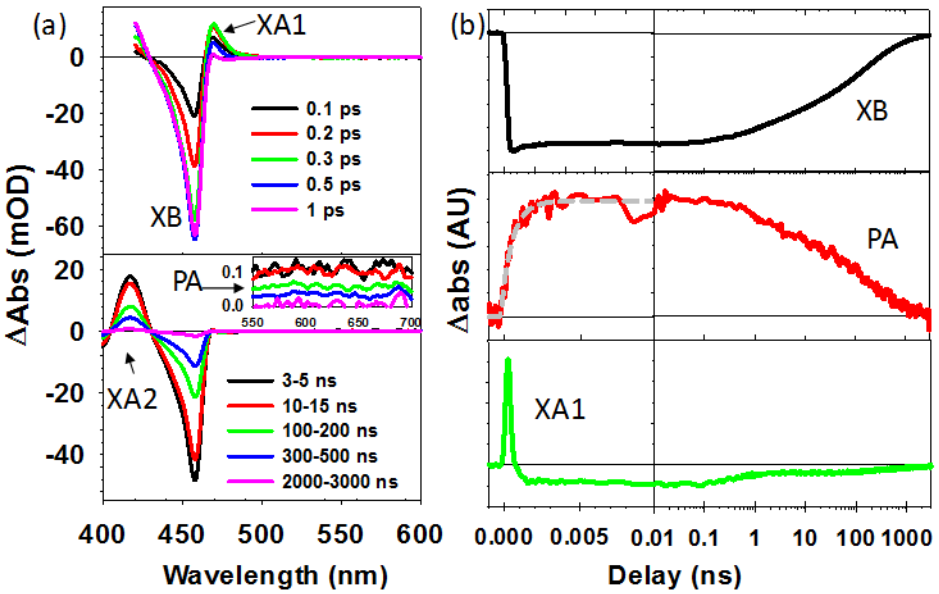

Figure 3.3. a) TA spectra of CdS NRs at indicated time delays after 400 nm excitation: 0 – 1 ps (top) and 3-3000 ns (bottom). Inset: expanded view of the broad photo-induced absorption (PA) spectra. b) TA kinetics for three spectral features: exciton bleach (XB at ~ 456 nm, black line, top), photoinduced aborption (PA from 550 to 700 nm, red line, middle), and hot-exciton induced shift (XA1 at ~470 nm, green line, bottom). A fit to the rise of the PA signal (with a single exponential time constant of 0.7 ps) is also shown in the middle panel (grey dashed line).

3.2.2. Carrier dynamics in free CdS NRs and NR-molecular acceptor complexes

In order to reveal the exciton quenching mechanism in CdS-Pt NRs, we use transient absorption (TA) spectroscopy to follow the carrier dynamics in CdS and CdS-Pt NRs. The details of instrument set-up are described in Chapter 2.2.[24,25] We first identify the spectral signatures of electron, hole, and charge separation in CdS

NRs. Unlike the well-studied quantum dots (QDs),[26-32] these spectral signatures in the one-dimensional NRs have yet to be unambiguously assigned.[11,33,34] Previous studied CdSe NR- methyl viologen complexes is a less complicated system than CdS-Pt because electron transfer is the only interaction mechanism and the generation of reduced formation of the $MV^{+\bullet}$ radical can be used to unambiguously determine electron transfer rate.[34] Previous work on CdS-Pt relied on exciton bleach feature alone to measure electron transfer rate from CdS to Pt, which is problematic since various channels can lead to exciton bleach recovery.[11] In fact, to our best knowledge, all the previous works on metal tipped semiconductor NR mentioned electron transfer from semiconductor NR to metal tips, but none of them provide unambiguous evidence for it.[11-14,33,35] Therefore, identifications of electron, hole and charge separated state signals on TA spectra are necessary. The TA spectra of CdS NRs after 400 nm excitation (Figure 3.3.a) shows a red-shifted absorption feature (XA1) at early delay time that decays rapidly (with a time constant of 70 fs) to form a bleach of the 1Σ band (XB) and a derivative-like feature of higher energy exciton bands (XA2). In addition to these exciton band features, a broad photoinduced absorption band (PA) at wavelength longer than 500 nm is also formed with a rise time of 0.7 ps (Figure 3.3.b, middle panel). These spectral features are remarkably similar to those observed in CdS[36-38] and CdSe[28,39-41] QDs and are assigned in the same manner. The XA1 feature at 470 nm can be attributed to hot excitons in the NR, whose presence shifts the 1Σ exciton band to lower energy. The decay of hot carriers to the 1 σ orbitals gives rise to the state filling induced bleach of 1 Σ exciton band (XB). Because of the state-specific biexciton interaction energy, this exciton relaxation process also affects

the higher energy exciton transitions, giving rise to the growth of the higher energy XA2 feature and the decrease of XA1 feature. The XA2 features reflects the interaction of the 1Σ exciton with other exciton bands and can be well described by a red-shift of these transitions (see Fig. A.3.1).[42] The XB feature shows only slight decay (~16%) within 1 ns (Fig. 3.3.b), indicating the dominance of long-lived single exciton state at this excitation intensity (Fig. 3.3.b).

In CdSe and CdS QDs the XB signal is attributed to the state filling of the electron level with negligible contribution from the hole due to a higher degeneracy of the hole levels.[30]-[32] The assignment of the broad PA signal is less clear and has been attributed to both the electron[41] and hole.[28,36-38] In order to identify the carrier contribution to both XB and PA signals in CdS NRs, known electron acceptors, methyl viologen (MV^{2+}) and benzoquinone (BQ) molecules, are used to selectively remove the excited electrons by interfacial electron transfer. The TA spectra of NR-MV^{2+} complexes (Figure 3.4.) show an ultrafast recovery of the 1 Σ XB signal within 100 ps and a corresponding formation of the $MV^{+\bullet}$ radicals absorption band centered at 620 nm and a derivative like feature of the 1 Σ exciton band.[41] These spectral features confirm the ultrafast transfer of electrons from the NR and support the assignment of the XB feature in the CdS NR to the state filling of the 1 σ electron level.

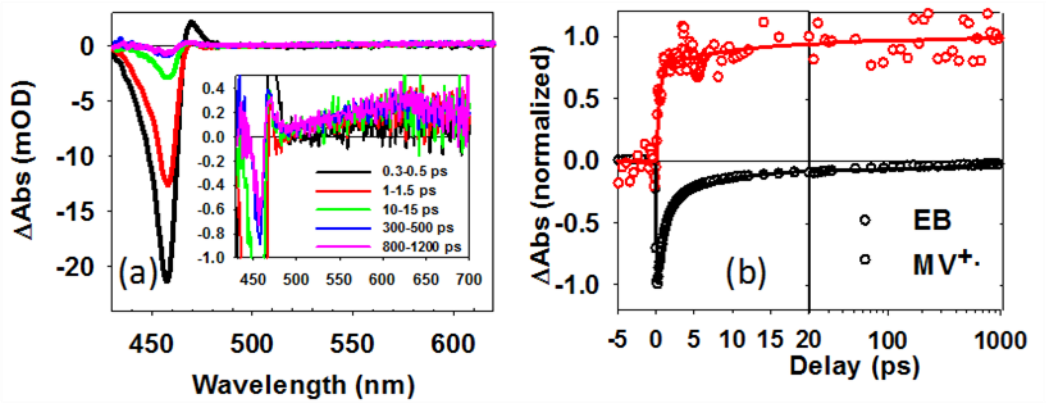

Figure 3.4. a) TA spectrum of CdS NR-methyl viologen complexes at indicated time delays. Inset: expanded view of the spectra at later delay times, showing the methyl viologen radical absorption band at ~ 620 nm and the derivative like SE feature of the NR. b) Normalized kinetics for CdS NR exciton bleach recovery (black circles) and methyl viologen radical formation (red circles)

The overlap of the $MV^{+\bullet}$ radical absorption with the PA signal hinders an unambiguous assignment of the latter. For this reason, we also studied CdS-BQ complexes, in which the reduced BQ anion has negligible absorption in the visible region.[43] As shown in Figure 3.5., the electron transfer process in CdS-BQ complexes leads to a faster recovery of the XB compared to free NRs. However, the ET process does not affect the PA signal, suggesting that the PA signal can be attributed to holes in the NR. The PA signal in NR-BQ complexes decays more slowly than that in free NRs (in the 100-10000 ns time scale, Figure 3.5.b inset), which can be attributed to slow charge recombination in this system. It is interesting to note that the ~0.7 ps rise time of PA signal (Fig. 3.3.b, middle panel) is similar to the hole trapping time in CdS

QDs determined by fluorescence up-conversion measurement,[44] suggesting the PA signal in the NR is likely due to the trapped holes.[36-38] Time-resolved PL measurement (Fig. 3.6.b) shows an ultrafast decay (<< 25ps) of the band-edge emission and ultrafast formation (<<25ps) of the trap-state emission, consistent with the ultrafast trapping of the valence band hole and the small band edge emission quantum yield (0.1%,). Furthermore, the decay of trap-state emission and the XB and PA TA signals follow the same kinetics (Fig. 3.6.c), suggesting that the main decay pathway of the 1σ electron is through recombination with the trapped holes in the CdS NR.

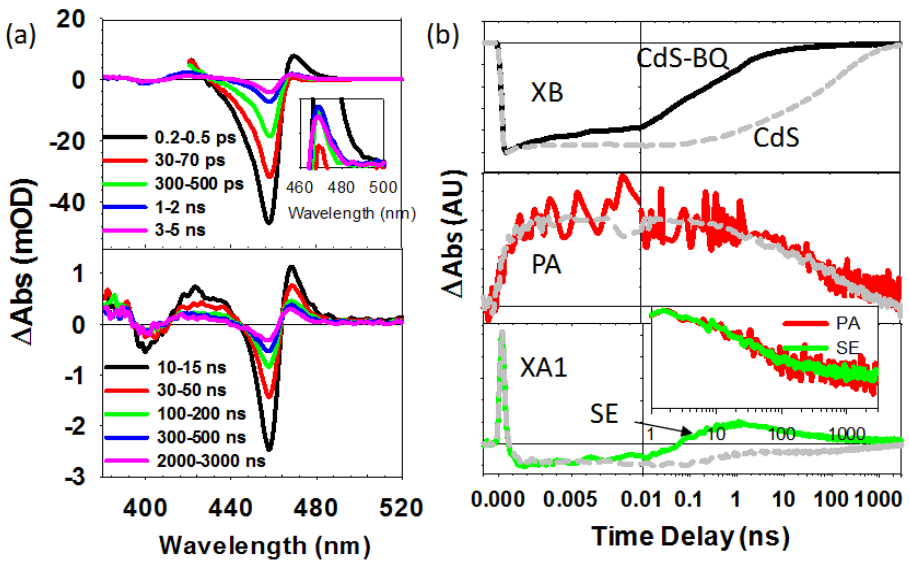

Figure 3.5. a) TA spectra of CdS-BQ complexes at indicated delay time windows after 400 nm excitation: 0.2-5 ns (upper panel) and 10-3000ns (lower panel). Inset in the upper panel shows the formation of charge separation induced Stark effect signal (SE). b) TA kinetics for the XB (black solid line, top), PA (red solid line, middle), and XA1 and SE (green solid line, bottom) features in CdS-BQ complexes. In each panel,

the kinetics of free CdS NRs (grey dashed line) is also included for comparison. Inset: kinetics for PA and SE signals from 10-3000 ns, reflecting the charge recombination process.

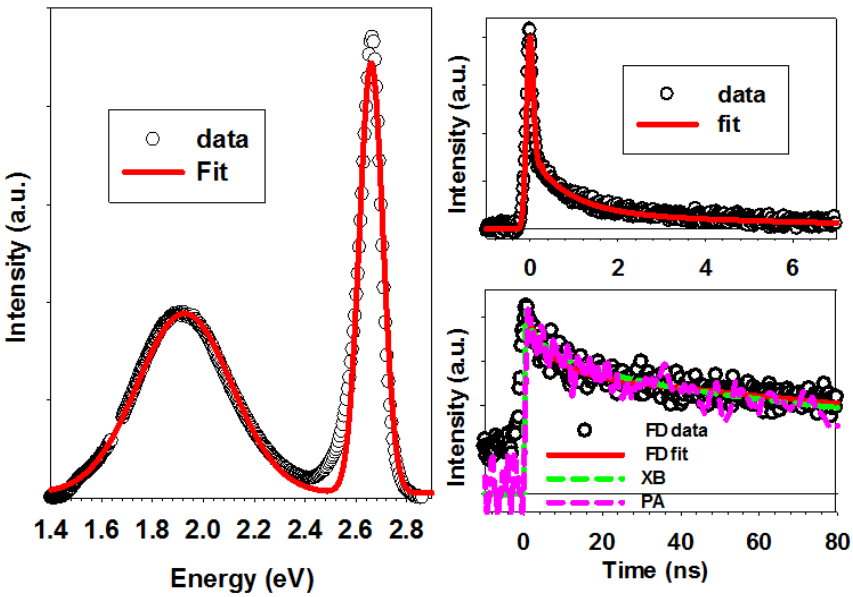

Figure 3.6. a) Photoluminescence spectrum of CdS NRs (black circles) and a fit by the sum of two Gaussian functions (red lines), showing a sharp band edge emission and a broad trap-state emission. Photoluminescence decay (black circles) and multi-exponential fit (red line) of band-edge b) and trap-state (c) emission. Also shown in c) is the exciton bleach recovery (green line) and PA decay (pink dashed line) shown in Figure 2b in the main text.

In addition to the small PA feature, the TA spectra of the charge separated state of the NR-BQ complexes (> 1 ns) show pronounced derivative-like features of the exciton bands that are similar to those observed in the charge separated state of QD-acceptor complexes and can be assigned to the Stark-effect (SE) induced exciton

band shift in the presence of the charge separated pair (NR^{+}-BQ^{-}).[24,25] This feature leads to the reappearance of the red-shifted 1Σ and higher energy exciton bands (SE, Figure 3.5.b, bottom panel) at ~1 ns. Although similar to the bi-exciton induced shift (XA), the SE feature is much weaker in comparison. The kinetics of the formation of the SE signal and XB recovery agrees with each other, supporting the assignment of the SE feature. After 1 ns, the SE signal decays with the same kinetics as the PA feature (inset of Figure 3b) due to the charge recombination process. This suggests that both the PA and SE spectral features can be used to follow the charge recombination kinetics, although the latter will be used in the NR-Pt complexes due to its larger signal amplitude.

3.2.3. Charge separation and recombination dynamics in CdS-Pt NRs

After the assignment of TA signals of the electron, hole and charge separated state in CdS NRs, we investigated the exciton quenching mechanism in CdS-Pt NRs. A control experiment of Pt nanoparticles shows negligible TA spectral signatures in the visible region after 400 nm excitation. Therefore all TA features in CdS-Pt (Fig. 3.7.a) can be attributed to the excitation of the CdS domain. However, due to the absorption of Pt, their amplitudes are reduced by a factor of two compared to free CdS NRs under the same conditions. The TA spectra of CdS-Pt NRs shows that, in the first 100 ps, the XB feature decays by ~ 90% while the PA signal displays negligible change, indicating the depopulation of 1σ electrons without the removal of the trapped holes. This suggests that ultrafast electron transfer (with a half-life time of

~3.4 ps) from the excited CdS NR to the Pt tip is the main exciton quenching pathway.

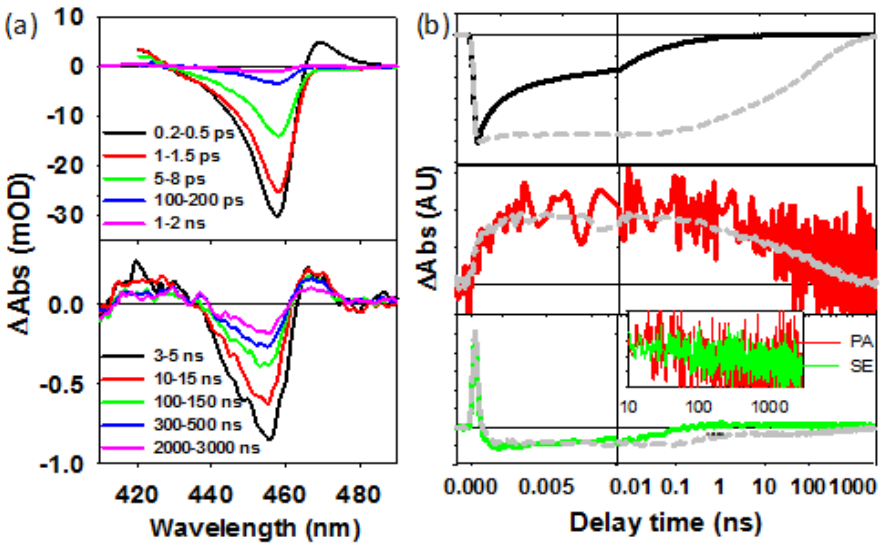

Figure 3.7. a) TA spectra of CdS-Pt NRs at indicated time delays: 0.2 ps -2 ns (upper panel) and 3 – 3000 ns (lower panel). b) TA kinetics of XB (black solid line, top), PA (red solid line, middle) and XA1 and SE (green solid line, bottom) spectral features for CdS-Pt NRs. Also shown for comparison are kinetics for CdS NRs (grey dashed lines) at the same wavelengths, whose amplitudes are a factor of two larger compared to CdS-Pt. Inset: comparison of SE and PA kinetics in CdS-Pt after 10 ns.

The 1σ exciton bleach recovery is accompanied by the formation of a derivative-like feature of exciton bands similar to that observed previously in CdS-BQ complexes. The TA spectra can be simulated as a sum of the SE and XB features (Fig. A.3.2). The SE signal amplitude is smaller in CdS-Pt, likely reflecting the different dipolar field strength of the charge separated state in these complexes. The simulation

also shows that at ~3-5 ns, the charge separation efficiency in CdS-Pt is near unity. The charge recombination process can be monitored by the decay of the SE signal (Figure 3.7.b), which has a half life time of 600 ns and is 10^5-fold slower than the charge separation time. The large difference in the charge separation and recombination rates are surprising because, as shown in Figure 3.1.a, there exist continua of empty and filled states (above and below the Pt Fermi level, respectively) for both electron and hole transfer from CdS to Pt. The 1σ electron is delocalized in the rod and has considerable overlap with the empty accepting levels in Pt, leading to a fast ET process. The ultrafast trapping of the hole in the CdS reduces its overlap with the filled Pt levels, slowing down the hole transfer process (in the initial exciton state and in the charge separated state). This large difference in the charge separation and recombination rates enables the removal of the trapped hole in the presence of hole acceptors, leading to the accumulation of electrons in the Pt tip and photocatalytic H_2 production.[13,14] Thus, the hole trapping induced asymmetry in the electron and hole transfer times is essential for efficient photoinduced charge separation and photocatalysis in these NR-Pt heterostructures.

3.3. Conclusion

In conclusion, the mechanism of exciton quenching and charge separation in the CdS-Pt NR heterostructure has been investigated by transient absorption spectroscopy. The dominant exciton quenching pathway is ultrafast interfacial electron transfer

(~3.4 ps) from the CdS NR to the Pt tip. The charge recombination process is surprisingly slow (~0.6 μs). The asymmetry in the electron and hole transfer rates across the CdS-Pt interface can be attributed to the efficient trapping of the hole in the NR. This asymmetry is essential for efficient accumulation of the transferred electrons in the Pt tip and photocatalysis.

References

(1) Mokari, T.; Rothenberg, E.; Popov, I.; Costi, R.; Banin, U. *Science* **2004**, *304*, 1787.

(2) Mokari, T.; Costi, R.; Sztrum, C. G.; Rabani, E.; Banin, U. *phys. sta. sol. (b)* **2006**, *243*, 3952.

(3) Saunders, A. E.; Popov, I.; Banin, U. *The Journal of Physical Chemistry B* **2006**, *110*, 25421.

(4) Shi, W.; Zeng, H.; Sahoo, Y.; Ohulchanskyy, T. Y.; Ding, Y.; Wang, Z. L.; Swihart, M.; Prasad, P. N. *Nano Lett.* **2006**, *6*, 875.

(5) Yang, J.; Elim, H. I.; Zhang, Q.; Lee, J. Y.; Ji, W. *J. Am. Chem. Soc.* **2006**, *128*, 11921.

(6) Habas, S. E.; Yang, P.; Mokari, T. *J. Am. Chem. Soc.* **2008**, *130*, 3294.

(7) Carbone, L.; Jakab, A.; Khalavka, Y.; Sönnichsen, C. *Nano Lett.* **2009**, *9*, 3710.

(8) Menagen, G.; Macdonald, J. E.; Shemesh, Y.; Popov, I.; Banin, U. *J. Am. Chem. Soc.* **2009**, *131*, 17406.

(9) Khon, E.; Hewa-Kasakarage, N. N.; Nemitz, I.; Acharya, K.; Zamkov, M. *Chem. Mat.* **2010**, *22*, 5929.

(10) Li, X.; Lian, J.; Lin, M.; Chan, Y. *J. Am. Chem. Soc.* **2010**, *133*, 672.

(11) Berr, M. J.; Vaneski, A.; Mauser, C.; Fischbach, S.; Susha, A. S.; Rogach, A. L.; Jäckel, F.; Feldmann, J. *Small* **2012**, *8*, 291.

(12) Acharya, K. P.; Khnayzer, R. S.; O'Connor, T.; Diederich, G.; Kirsanova, M.; Klinkova, A.; Roth, D.; Kinder, E.; Imboden, M.; Zamkov, M. *Nano Lett.* **2011**, *11*, 2919.

(13) Berr, M.; Vaneski, A.; Susha, A. S.; Rodriguez-Fernandez, J.; Doblinger, M.; Jackel, F.; Rogach, A. L.; Feldmann, J. *Applied Physics Letters* **2010**, *97*, 093108.

(14) Amirav, L.; Alivisatos, A. P. *J. Phys. Chem. Lett.* **2010**, *1*, 1051.

(15) Manjavacas, A.; Abajo, F. J. G. a. d.; Nordlander, P. *Nano Lett.* **2011**, *11*, 2318.

(16) Fofang, N. T.; Grady, N. K.; Fan, Z.; Govorov, A. O.; Halas, N. J. *Nano Lett.* **2011**, *11*, 1556.

(17) Fofang, N. T.; Park, T.-H.; Neumann, O.; Mirin, N. A.; Nordlander, P.; Halas, N. J. *Nano Lett.* **2008**, *8*, 3481.

(18) Shabaev, A.; Efros, A. L. *Nano Lett.* **2004**, *4*, 1821.

(19) Hu, J.; Wang; Li, L.-s.; Yang, W.; Alivisatos, A. P. *J. Phys. Chem. B* **2002**, *106*, 2447.

(20) Katz, D.; Wizansky, T.; Millo, O.; Rothenberg, E.; Mokari, T.; Banin, U. *Physical Review Letters* **2002**, *89*, 086801.

(21) Giblin, J.; Vietmeyer, F.; McDonald, M. P.; Kuno, M. *Nano Letters* **2011**, *11*, 3307.

(22) Johnson, R. C.; Li, J.; Hupp, J. T.; Schatz, G. C. *Chem. Phys. Lett.* **2002**, *356*, 534.

(23) Saunders, A. E.; Ghezelbash, A.; Sood, P.; Korgel, B. A. *Langmuir* **2008**, *24*, 9043.

(24) Zhu, H.; Song, N.; Lian, T. *J. Am. Chem. Soc.* **2011**, *133*, 8762.

(25) Zhu, H.; Song, N.; Lian, T. *Journal of the American Chemical Society* **2010**, *132*, 15038.

(26) Yang, Y.; Rodríguez-Córdoba, W.; Lian, T. *Journal of the American Chemical Society* **2011**, *133*, 9246.

(27) Huang, J.; Huang, Z. Q.; Yang, Y.; Zhu, H. M.; Lian, T. Q. *J. Am. Chem. Soc.* **2010**, *132*, 4858.

(28) Huang, J. E.; Huang, Z. Q.; Jin, S. Y.; Lian, T. Q. *J. Phys. Chem. C* **2008**, *112*, 19734.

(29) Huang, J.; Stockwell, D.; Huang, Z. Q.; Mohler, D. L.; Lian, T. Q. *J. Am. Chem. Soc.* **2008**, *130*, 5632.

(30) Klimov, V. I. *Annu. Rev. Phys. Chem.* **2007**, *58*, 635.

(31) Boulesbaa, A.; Issac, A.; Stockwell, D.; Huang, Z.; Huang, J.; Guo, J.; Lian, T. *J. Am. Chem. Soc.* **2007**, *129*, 15132.

(32) Klimov, V. I. *J. Phys. Chem. B* **2000**, *104*, 6112.

(33) Khon, E.; Mereshchenko, A.; Tarnovsky, A. N.; Acharya, K.; Klinkova, A.; Hewa-Kasakarage, N. N.; Nemitz, I.; Zamkov, M. *Nano Lett.* **2011**, *11*, 1792.

(34) Jiang, Z.-J.; Kelley, D. F. *J. Phys. Chem. C* **2011**, *115*, 4594.

(35) Costi, R.; Saunders, A. E.; Elmalem, E.; Salant, A.; Banin, U. *Nano Lett.* **2008**, *8*, 637.

(36) Baral, S.; Fojtik, A.; Weller, H.; Henglein, A. *J. Am. Chem. Soc.* **1986**, *108*, 375.

(37) Haase, M.; Weller, H.; Henglein, A. *J. Phys. Chem.* **1988**, *92*, 4706.

(38) Gopidas, K. R.; Bohorquez, M.; Kamat, P. V. *J. Phys. Chem.* **1990**, *94*, 6435.

(39) Tyagi, P.; Kambhampati, P. *J. Chem. Phys.* **2011**, *134*, 094706.

(40) Burda, C.; Link, S.; Mohamed, M.; El-Sayed, M. *J. Phys. Chem. B* **2001**, *105*, 12286.

(41) McArthur, E. A.; Morris-Cohen, A. J.; Knowles, K. E.; Weiss, E. A. *J. Phys. Chem. B* **2010**, *114*, 14514.

(42) Sacra, A.; Norris, D. J.; Murray, C. B.; Bawendi, M. G. *J. Chem. Phys.* **1995**, *103*, 5236.

(43) Burda, C.; Green, T. C.; Link, S.; El-Sayed, M. A. *J. Phys. Chem. B* **1999**, *103*, 1783.
(44) Klimov, V.; Bolivar, P. H.; Kurz, H. *Phys. Rev. B* **1996**, *53*, 1463.

Appendix 1.

Simulation of TA spectrum of CdS NRs

The TA spectra can be modeled by the sum of state filling induced exciton bleach (XB) and the shift of exciton band due to exciton-exciton interaction. State-filling results from the Pauli exclusion principle ---the occupancy of the photo-excited electrons in the 1σ electron level inhibits transition to this level, thus leading to a decrease of absorption (bleach) of the 1Σ exciton. Bi-exciton effect results from the coulomb interaction between the first exciton prepared by the pump pulse and the second exciton prepared by the probe pulse. This interaction usually lowers the energy of the second exciton thus red-shift the absorption spectrum, giving rise to a derivative-like feature in the difference spectrum.

The ground state absorption spectrum of NRs can be fitted by a sum of exciton bands, each represented by a Gaussian function G_i (with area of b_i, center energy of E_i and width of Γ_i), and a broad background function (*bg*). To account for the heterogeneity in diameter distribution of the NRs, the width of the Gaussian functions is assumed to correlate with the center energy E_i through :

$$\Gamma_i = 2\frac{\Delta R}{R}(E_i - E_g) \qquad \text{(A.1)}$$

where ΔR and R are the standard deviation and average of the NR diameters and E_g is the bulk band gap. The ground state absorption spectrum is :

$$Abs_g(\omega) = bg(\omega) + \sum_{i=1}^{4} \frac{b_i}{\sqrt{2\pi}\Gamma_i} \exp\left[-\frac{(\hbar\omega - E_i)^2}{2\Gamma_i^{\,2}} \right] \qquad \text{(A.2)}$$

Accounting for state filling and bi-exciton effects, the excited spectrum is given by:

$$Abs_e(\omega) = bg(\omega) + \sum_{i=1}^{4} \alpha_i \frac{b_i}{\sqrt{2\pi}\Gamma_i} \exp\left[-\frac{[\hbar\omega - (E_i - \delta_{BX,i})]^2}{2\Gamma_i^{\,2}} \right] \qquad \text{(A.3)}$$

α_i is 0.5 for i=1,2 and 1 for i=3,4 in equation (A.3), accounting for bleach of only the $1\sigma_{1/2h}$-$1\sigma_e$ and $1\sigma_{3/2h}$-$1\sigma_e$ transitions by the occupation of the two-fold degenerate $1\sigma_e$ electron level. $\delta_{BX,i}$ is bi-exciton interaction energy. The transient absorption spectrum is the difference between the excited and ground state absorption spectra:

$$NRTA(\omega) = C \bullet (Abs_e - Abs_g) \qquad \text{(A.4)}$$

where C is a scaling factor that is proportional to the number excited NRs.

As shown in Figure A.3.1, the ground state absorption spectrum can be well fit by equation (A.2). The fitting parameters are tabulated in Table A.3.1. A quadratic background function gives the best fit to the data. Similarly, in an early work on CdSe quantum dots, a cubic background function was included to fit the absorption spectrum. Figure S3b shows that the TA difference spectrum simulated using equation (A.4), which agrees qualitatively with the experimental spectrum. The discrepancy may arise from the 1-D exciton band structure of NRs, with each exciton band in the absorption spectrum consisting of a manifold of exciton transitions. We also note that a reasonable fit with this model requires different bi-exciton interaction energies for different exciton bands, consistent with the state-specific bi-exciton interaction energy

reported for QDs. These values (δ_i), the binding energies between the $1\sigma_{1/2h}$-$1\sigma_e$ exciton and the first four excitons, are also listed in Table A.3.1.

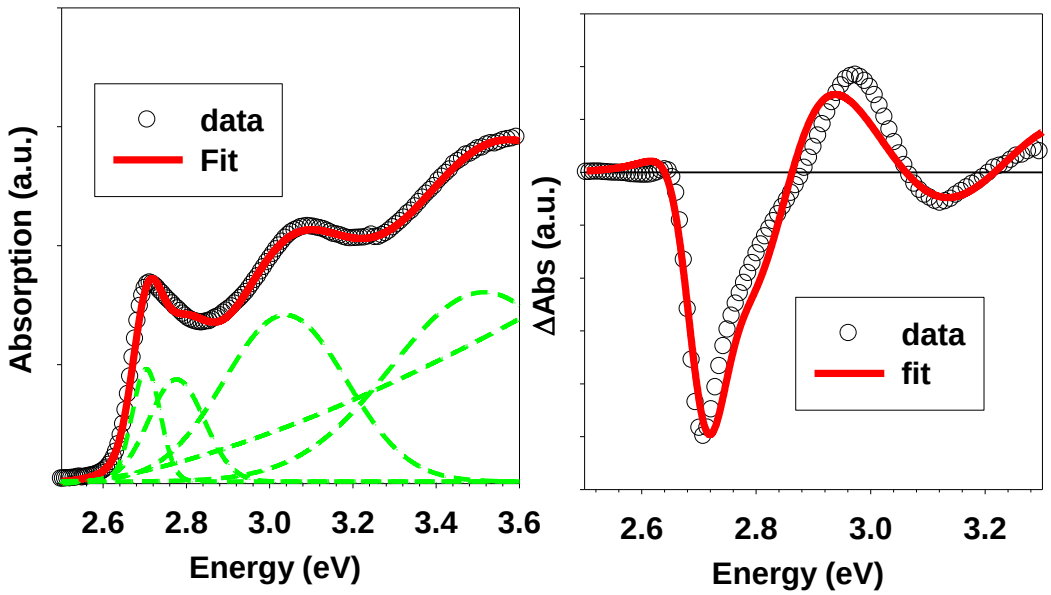

Figure A.3.1 a) CdS NR absorption spectrum (open circles) and fit (red solid line) by a sum of Gaussian bands and a background function. The individual components of the fit function are also shown (green dashed line). b) Transient absorption spectrum of CdS NRs (open circles) and best fit (red solid line) according to the model described in the text.

Table A.3.1. Fitting parameters for CdS NR absorption spectrum

	G1	G2	G3	G4
b_i (a.u.)	0.040	0.071	0.258	0.444
E_i (eV)	2.70	2.78	3.04	3.52

Γ_i (eV)	0.034	0.066	0.147	0.223
$\delta_{BX,i}$ (eV)	0.01	0.02	0.04	0.05

Appendix 2.

Simulation of TA spectrum of charge separated states in CdS-BQ and CdS-Pt

The TA spectrum of NR-electron acceptor complexes contains two parts: the excited and charge separated state. The excited complexes can be represented by the TA spectrum of free NRs (equation (A.4)). In the charge separated state, the electric field of the charge separated pair leads to shifts of the NR exciton bands ($\delta_{CS,i}$). This Stark-effect induced shift can be represented by a red-shift of absorption spectrum. We thus can represent the absorption spectrum of charge separated state as:

$$Abs_{CS} = bg(\omega) + \sum_{i=1}^{4} \frac{b_i}{\sqrt{2\pi}\Gamma_i} \exp\left[-\frac{[\hbar\omega - (E_i - \delta_{C,S\ i})]^2}{2\Gamma_i^2}\right] \quad \text{(A.5)}$$

The TA difference spectrum due to the charge separated state is:

$$CS(\omega) = C \bullet (Abs_{CS} - Abs_g) \quad \text{(A.6)}$$

The total TA difference spectrum in NR-A complexes is then:

$$ComTA(\omega) = A_1 \bullet NRTA(\omega) + A_2 \bullet CS(\omega) \quad \text{(A.7)}$$

where $A_1(t)$ and $A_2(t)$ reflects the population of excited and charge separated species in the sample.

Fits to the average TA spectra of CdS-BQ and CdS-Pt at 3-5 ns using equations (A.5)-(A.7) are shown in Figure A.3.2. At this delay time the charge separation has

nearly completed and the extent of charge recombination is small. The fitting parameters are listed in Table A.3.2. There are several interesting findings in the fitting results. Firstly, the charge separation induced exciton peak shifts in both CdS-BQ and CdS-Pt are on the order of 0.1- 0.7 meV, much smaller than the bi-exciton binding energy in free NRs. One possible reason is the dipolar electric field of the charge separated pair is much weaker than the field of electron-hole pair inside the NRs. Secondly, the peak shifts in CdS-Pt is about half the values in CdS-BQ. This difference may be caused by the larger charge separation distance and the image charge effects in CdS-Pt. Finally, we can use the amplitudes of state filling and charge separation signal to estimate charge accumulation efficiency in these systems. In CdS-BQ, at 3-5 ns, 93% of the excitons has decayed and 80% of the excited complexes are in the charge separated state. For CdS-Pt at the same delay time, 98% of the excitons has decayed and 97% of the excited complexes are in the charge separated state, which corresponds to a near unity charge separation efficiency.

Table A.3.2. Fitting parameters for charge separated states spectrum

	$\delta_{CS,1}$ (meV)	$\delta_{CS,2}$ (meV)	$\delta_{CS,3}$ (meV)	$\delta_{CS,4}$ (meV)	A_1	A_2
CdS-BQ	0. 7	0. 2	0. 2	0. 2	0.07	0.80
CdS-Pt	0. 3	0. 1	0. 1	0. 1	0.02	0.97

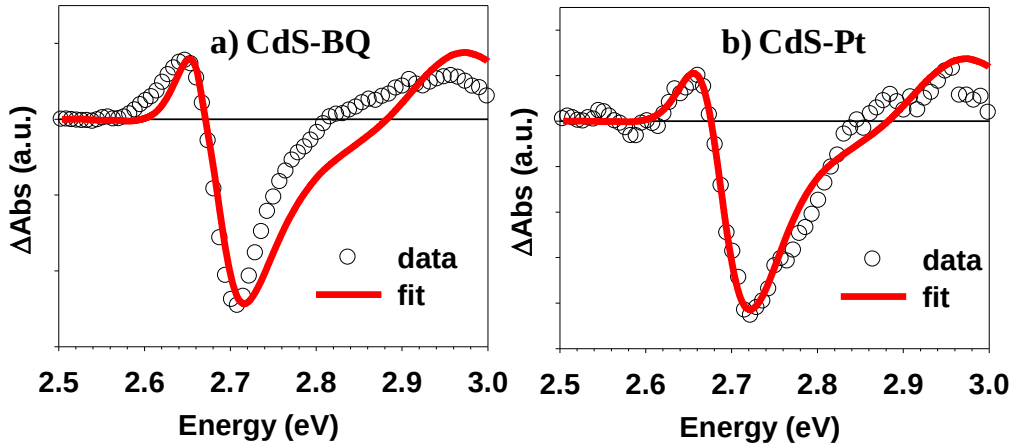

Figure A.3.2. Measured (open black circles) and simulated (solid red lines) TA spectrum of a) CdS-BQ and b) CdS-Pt complexes at 3-5 ns.

Chapter 4. Ultrafast Exciton Quenching by Energy and Electron Transfer in Colloidal CdSe Nanosheet-Pt Heterostructures

4.1. Introduction

Colloidal quantum confined semiconductor-metal nanoheterostructures that combine tunable light absorption of the semiconductor domain and catalytic activity of metal nanoparticles, are promising materials for solar energy conversion. [1-4] To date, heterostructures of 0D (QDs) and 1D NRs semiconductors have been prepared and studied.[5-20] Our previous Chapter examined exciton quenching mechanism and charge separation and recombination dynamics in 1D Pt tipped CdS NRs. More recently, 2-dimensional (2-D) semiconductor nanomaterials are receiving tremendous interests due to their attractive light absorption and charge transport properties.[21,22] Among them are colloidal CdSe nanosheets (NSs) with atomically precise thickness of only a few CdSe layers.[23-28] CdSe nanosheets (NSs) have atomically precise thickness of only a few CdSe layers.[23-28] In addition to strong quantum confinement in the thickness direction, these nanosheets have large absorption cross sections[29], high photoluminescence (PL) quantum yield,[25,30] and fast in-plane carrier transport,[30-32]

making them a promising light-absorbing material for photocatalysis. As shown by the energy level scheme in Figure 4.1.a, the band alignment between CdSe NSs and Pt nanoparticles also allows exciton quenching through electron, hole and energy transfers to the Pt domain.[20] Unlike CdS NRs, the atomically precise thickness of CdSe NSs may lead to ultrafast in-plane exciton motion and alter the exciton quenching mechanisms. For this reason, these NS-Pt heterostructures serve as an interesting model system for fundamental understanding of the interaction between excitons in 2-D nanomaterials with metal nanoparticles.

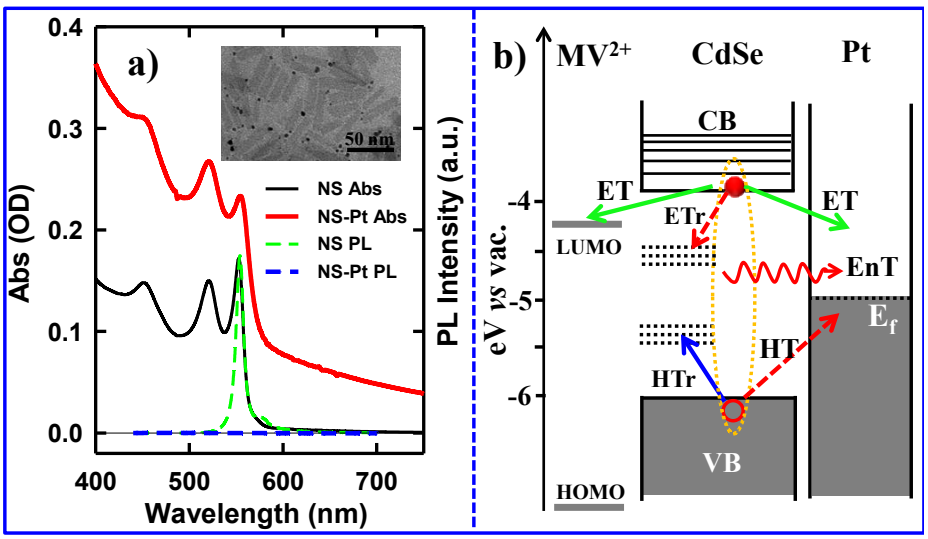

Figure 4.1. a) Absorption and photoluminescence (PL) spectra of CdSe NS (black solid line, green dashed line) and CdSe NS-Pt heterostructures (red solid line and blue dashed line). Inset: a representative TEM image of NS-Pt. b) Schematic energy levels and possible exciton quenching pathways in NS-Pt and NS-MV^{2+} complexes. In addition to radiative e-h recombination, electron trapping (ETr) and hole trapping (HTr) pathways within the CdSe NS, excitons can be quenched through interfacial

electron transfer (ET), hole transfer (HT) and energy transfer (EnT) to Pt. In contrast, ET is the only quenching pathway in NS-MV^{2+} complexes.

4.2. Results and Discussion

4.2.1. Sample synthesis and characterizations

CdSe NSs were synthesized according to literature procedures.[23-25] Pt deposition on nanosheets was achieved by thermal reduction of Pt(II) acetylacetonate in the presence of oleic acid and oleylamine as both reducing reagents and capping ligands, similar to the reported procedure of Pt deposition on CdS nanorods.[7] These NSs typically exhibited rectangular morphology with average dimensions of 39. 2 (±4.9) nm×11. 3 (±2.0) nm. Their thickness was estimated to be ~1.52 nm from their absorption spectrum (see below). The average dimensions of NSs with Pt nanoparticle (3.1±1.2 nm in diameter) were 39. 9 (±5.8) nm×10. 9 (±1.6) nm, showing negligible etching of NSs during the Pt deposition process. Interestingly, instead of the highly-exposed (001) basal plane,[24] the procedure selectively deposited only one Pt tip at either the edge or vertex of the rectangular NS(Figure 4.1.a inset), which likely resulted from high surface energies or sparse ligand coverage at these sites. [30] Similar preferential deposition of Au nanoparticles at the edge over the basal plane of CdSe nanobelts has been observed in a previous study. [30] However, in that system, many Au nanoparticles were deposited on the edges of each nanobelt. The reason for

this difference is not clear, but likely due to different metal precursor concentrations used in the synthesis. There existed a broad size distribution of the Pt nanoparticles deposited on our NSs, which, in principle, can lead to a large heterogeneity in quenching kinetics of NSs by Pt nanoparticles, as will be discussed later.

The absorption and photoluminescence (PL) spectra of CdSe NS and CdSe NS-Pt are compared in Figure 4.1a. The CdSe NS exhibited sharp and discrete transitions arising from quantum confinement in the thickness direction.[23-25] The two lowest energy peaks at 553 nm and 521 nm can be attributed to transitions to n=1 conduction band (CB) electron level from n=1 valence band (VB) heavy hole (hh→e) and n=1 light hole (lh→e) levels, respectively.[23] The width of (lh→e) absorption band was only ~35 meV (Figure A.4.1), indicating a uniform thickness. These transition energies corresponded to a thickness of ~1.52 nm (2.5 times Zinc Blende CdSe lattice constant or 5 monolayers of CdSe).[33] The absorption spectrum of CdSe NS-Pt showed a broad feature extending from UV to the near IR in addition to the CdSe exciton bands. This feature was the same as free Pt particles and could be attributed to the strong d-sp interband transition of Pt nanoparticles.[34] In addition, the sharp CdSe exciton peaks were slightly red-shifted and broadened compared to free CdSe Ns. PL of CdSe NSs was dominated by a sharp band edge emission centered at 554 nm with a small Stokes shift of ~ 4meV and a quantum yield (QY) of 36%, consistent with previous reports.[25] In CdSe NS-Pt, the PL of NS was completely quenched, indicative of strong electronic interaction between the CdSe NS and Pt

particle. It also indicates that all the NSs are in contact with Pt particles, although some of these particles are too small to be clearly observed under TEM. In addition, there exists a possibility of PL quenching by surfaced adsorbed Pt(0) or Pt(II) species, similar to previously observed CdSe/CdS nanorods quenching by Au precursors used for Au nanoparticle deposition.[35]

4.2.2. Carrier dynamics in free CdSe NSs and NS-molecular acceptor complexes

To examine the potential of this NS-Pt heterostructure as a photocatalyst, we investigated the quenching mechanisms using pump-probe transient absorption (TA) spectroscopy. As a comparison and to facilitate spectroscopic assignment, we also studied the exciton quenching in NS-methyl-viologen (MV^{2+}) complexes, in which only the ET pathway is energetically allowed (Figure 4.1.b). We first examine carrier dynamics and their transient spectral signatures in free CdSe NSs. The transient absorption (TA) spectra of CdSe NSs (Figure 4.2.a) measured with 400 nm excitation show an exciton bleach (XB) feature at ~552 nm and an exciton absorption (XA) feature at ~560 nm. In this measurement we have used low excitation flux to ensure that the signal is dominated by NSs with single excitons (Figure A.4.2), excluding the complications of multi-exciton annihilation dynamics. Detailed assignments of these TA features in NSs have yet to be reported, although XA and XB features have been observed in a previous study of multiple exciton dynamics of NSs,[36] and are well understood in QDs and NRs.[37-41] As will be discussed below (Figure 4.3.), the XB feature in CdSe NSs is dominated by CB electron state filling induced bleach of the

lowest energy exciton band and can be used to follow the dynamics of in the CB electron level. The XB feature in free NSs (Figure 4.2.c) grew in with a time constant of 80±27 fs, corresponding to the time scale of hot electron relaxation from the excited level to the CB n=1 level. Fitting the XB decay by multiple exponential functions requires four components (see Table 4.1).

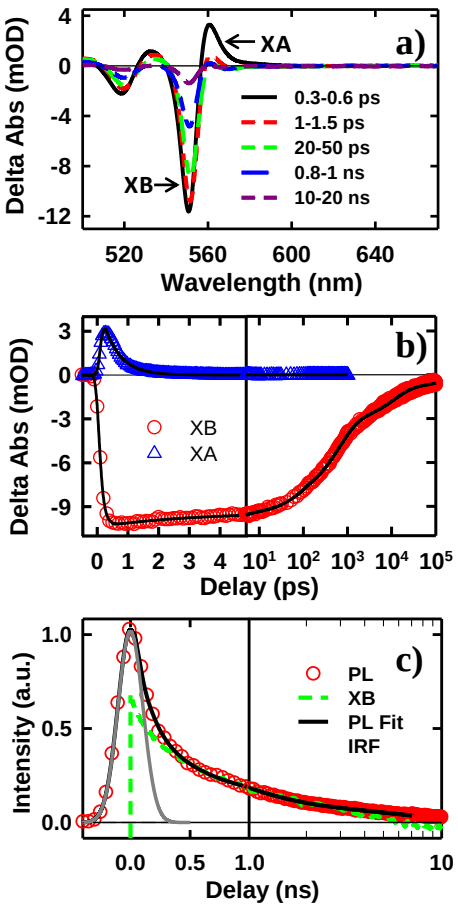

Figure 4.2. TA spectra and kinetics of CdSe NSs measured with 400 nm excitation. a) TA spectra of NSs at indicated time. b) Kinetics of XA (blue triangles) and XB (red circles) in NSs and their fits (black solid lines) c) Comparison of XB bleach (green dashed line) and PL decay of NSs (red circles). XB is scaled and vertically shifted for

comparison. Also shown are the IRF of PL decay experiment (gray line) and a fit to the PL decay (black solid line).

Table 4.1 Fitting parameters for XB and PL of free NS[a]

	$\tau_{f,1}$/fs	τ_1/ns (a_1)	τ_2/ns (a_2)	τ_3 /ns (a_3)	τ_4 /ns (a_4)	$\tau_{1/2}$ /ns
XB	80 ±27	0.108 ±0.009 (16.8 ±0.4%)	0.617 ±0.012 (50.9 ±0.5%)	10.9 ±0.3 (23.4 ±0.3%)	220 ±8 (8.9 ±0.2%)	0.63 ±0.03
	$\tau_{f,PL}$/ns	A_1	τ_{Htr}/ns	A_2	τ_{QD} /ns	$\tau_{1/2}$ /ns
PL	<<0.24	91.9 ±0.7%	<<0.24 ns	8.1 ±0.4%	6.0 ±0.2	0.18 ±0.02

[a] The kinetics was fitted to the following equation: $XB(t) = A_{XB}\left[\sum_{i=1}^{4} a_i e^{-t/\tau_i} - e^{-t/\tau_f}\right]$, where τ_f is the formation rate of XB and a_i and τ_i are the amplitude and time constant for i^{th} component of XB decay, respectively.

In addition to state-filling XB signals, the presence of an exciton also shifts the energy of all exciton transitions due to exciton-exciton interaction, giving rise to the XA feature in TA spectra.[37] Because state-specific exciton-exciton interaction strength, the XA feature provides a sensitive probe of the initial exciton relaxation dynamics.[41,42] The XA feature in free CdSe NS forms instantaneously (<<150 fs, IRF) and decays with a time constant of 0.41 ±0.12 ps (Figure 4.2.c). In QDs and NRs, this decay leads to the growth of XB formation, and can be attributed to cooling of electrons from the higher levels to the band edge.[37,43,44] In contrast, in CdSe NSs, the decay of XA signal is much slower than the growth of the XB signal (80 ±27 fs).

Furthermore, the TA spectra at early-time (Figure 4.3.) showed a red shift of XA and XB features during XA decay, indicting a decrease of bi-exciton interaction but not the population of electrons at the lowest energy (n=1) CB level. We tentatively attribute this XA decay to in-plane exciton localization (i.e. the loss of extra kinetic energy of in-plane motion) and trapping process. [37,43,44]

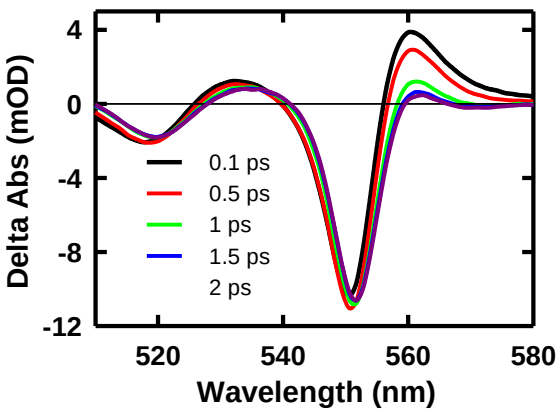

Figure 4.3. Spectral evolution (red-shifting) of 400 nm excited CdSe NSs within 2 ps.

While the XB recovery probes the electron decay dynamics from the n=1 CB level, band edge PL decay depends on both the CB electron and VB hole. The XB recovery and band-edge PL decay agree well on the ~300 ps to 3 ns time scale (Figure 4.2d), consistent with previously-reported lifetime of band edge excitons in related NSs.[25] The slower electron (XB) decay components (10.9±0.3 ns and 220±8 ns with 32.4±0.5% of the total XB amplitude, Table 4.1.) are much longer than the band edge PL decay, suggesting an electron decay process that does not lead to band edge PL.

This can be attributed to electron recombination with trapped holes, which are typically slower due to reduced electron-hole overlap.[20] The PL decay shows an instrument response (~240 ps) limited fast decay component with an amplitude that is much larger than XB recovery on the same time scale, suggesting the presence of ultrafast hole decay (Table 4.1.). The comparison of the TA and PL results suggests that in the NS ensemble, 32.4±0.5% of excitons undergo fast hole trapping, which leads to the long-lived (>3ns) XB (CB electron) signal and the fast decay (< 240 ps) in the PL signal. The remaining 67.6±0.5% excitons decay *via* fast radiative and nonradiative recombination on the < 3 ns time scale.

To help assign XB spectral signature and to identify TA spectral signature of charge separated state, we have also examined the charge separation and recombination processes in CdSe NS-MV^{2+} complexes, in which photo-reduction of MV^{2+} forms $MV^{+\bullet}$ radicals with distinct absorption band at ~610 nm. In the TA spectrum of CdSe NS-MV^{2+} complexes (Figure 4.4.a), the XB feature, generated upon 400 nm excitation of the NS, completely recovered in 200 ps and the resultant spectrum contained derivative-like signals of NS exciton bands and a positive absorption band of $MV^{+\bullet}$ radicals at ~610 nm. The decay kinetics of XB (Figure 4.4.b) agrees well with the formation kinetics of $MV^{+\bullet}$ radicals, suggesting that excitons in CdSe NS decay by electron transfer to MV^{2+}. It also confirms that XB feature is due solely to the state filling of the CB electron level with negligible contribution of the VB holes, consistent with previous observations in 0D (QD)[37,45,46] and 1D (NR)[20,43,44]

II-VI nanocrystals. The derivative-like feature of NS exciton bands can be attributed to the effect of charge separation on the exciton, caused by either the hole in the CdSe NS and/or the electric field of the separated charges (NS^{+}- $MV^{+\bullet}$). As shown in Figure 4.4.b, the CS formation kinetics follows that of $MV^{+\bullet}$ radical formation and XB bleach recovery. The subsequent decay of the CS and $MV^{+\bullet}$ radical signals can be attributed to the charge recombination process. Therefore, the CS signal provides a convenient probe for the formation and decay of the charge separated state, especially in systems where the reduced electron acceptors lack clear spectral signatures (such as NS-Pt complexes to be described below). It should be noted that the CS signal resembles the XA feature because both result from the shift of exciton bands caused by interaction with additional charges/excitons. However, as shown in Figure 4.4, these features have different red-shift amplitudes (due to different interaction strengths) and different formation and decay kinetics (the XA signal decays within the first ps).

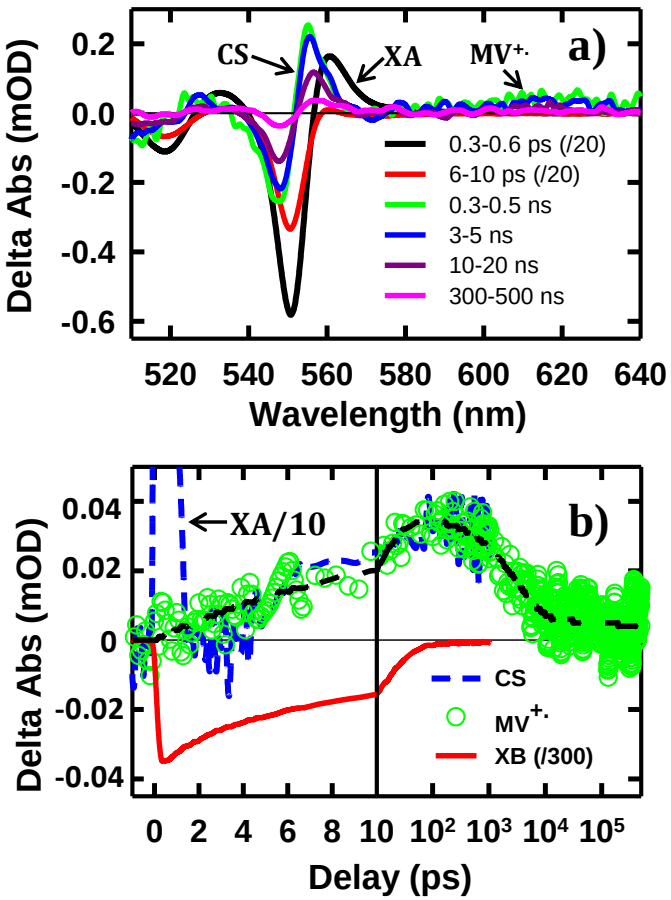

Figure 4.4. TA spectra and kinetics of CdSe NS-MV^{2+} complexes measured with 400 nm excitation. a) TA spectra evolution from 0.3 ps to 500 ns. The first two spectra have been reduced by a factor of 20 for better comparison. b) Kinetics of $MV^{+\bullet}$ radical (green circles) and the complementary NS XB (red solid line) and XA/CS signal (blue dashed line). The latter have been scaled for better comparison. The black dashed line is a multi-exponential fit to the formation and decay kinetics of $MV^{+\bullet}$ radical signal.

4.2.3. Exciton quenching mechanism in Pt tipped CdSe NSs

The TA spectra of NS-Pt after 400 nm excitation are shown in Figure 4.5.a. Our previous study on NR-Pt heterostructures shows that Pt nanoparticles can absorb 400 nm light and reduce the number of photons absorbed by the NSs, although the excited Pt do not show any TA spectral signatures in the visible region.[20] To account for this effect, we scaled the TA signal of NS-Pt to correspond to the same number of absorbed photons by the NS in both samples. After this correction, the initial XA and XB signal amplitudes in NS-Pt are only 36% those of free NSs (Figure 4.5.b), indicating ultrafast electron decay that is faster than the instrument response time of our TA measurement (<<150 fs). This initial loss was followed by a XB recovery (much faster than free NSs) and a concomitant spectral evolution from the XB feature to a derivative-like feature within 300 ps (Figure 4.5.a upper panel). The derivative-like feature (Figure 4.5.a lower panel) can be attributed to the CS state (NS^{+}-Pt^{-}) generated by ET from the NS to the Pt nanoparticle, similar to the CS features observed in CdSe NS-MV^{2+} (Figure 4.4.a) and in CdS NR-Pt heterostructures.[20]

The formation and decay kinetics of the CS state was monitored at 577 nm (Figure 4.5.b). The signal at this wavelength in free NSs (Figure 4.2.b) showed a fast XA decay (0.41 ± 0.12 ps) and negligible TA signals afterwards. As shown in Figure 4.5.b, in NS-Pt, the XA feature shows a faster decay (0.18 ± 0.06 ps), consistent with ultrafast exciton quenching process. After the ultrafast decay of the XA signal, the CS

signal grew in at <300ps due to charge separation and decayed at longer delay times due to charge recombination. Multiple exponential fit of the kinetics (Figure 4.5.b) revealed half-lives of 9.4±0.7 ps and 75±14 ns for charge separation and charge-recombination, respectively. Further support of the above assignment is provided by comparing the kinetics at 577 and 553 nm. Because the latter contains the contributions of XB bleach and CS signals, its decay kinetics should be identical to that at 577 nm after the completion of the charge separation process. Indeed, these signals decay with the same kinetics after 300 ps, reflecting the charge recombination processes. During the charge separation process, XB recovery should agree with the formation of CS, which is also shown in Figure 4.5.c. Here, we have scaled the kinetics at 577 nm and displaced it vertically to allow better comparison with the bleach recovery at 533 nm. Indeed, these two kinetics agree from ~1.5 to ~ 300 ps, indicating that exciton quenching after 1.5 ps is purely due to electron transfer. The amplitude of ~553 nm at 1.5 ps is 13.4±0.5% that of free NS (Figure 4.5.c). Since charge separation has negligible contribution within 1.5 ps, this ratio is approximately the charge separation yield in NS-Pt. The time-dependent populations of electron (XB) in NSs and CS states are shown in Figure 4.5.d.

The comparison above reveals that 87% of the excitons undergo ultrafast quenching (before 1.5 ps) without forming CS states. We attribute this pathway to rapid energy transfer from free excitons in the NS to Pt. As described in Appendix 2, due to its large transition dipole, the energy transfer time of a free exciton in contact

with the Pt particle (separated by ~2.0 nm, the sum of the radii of the Pt nanoparticle and exciton in the CdSe NS) is estimated to be ~ 29 fs. For excitons generated far away from the Pt, their quenching is limited by exciton transport rate. Due to large in-plane exciton mobility, the average exciton quenching time is estimated to be ~ 200 fs, which is in qualitative agreement with the observed half-life of the fast XB recovery component of < 150 fs.

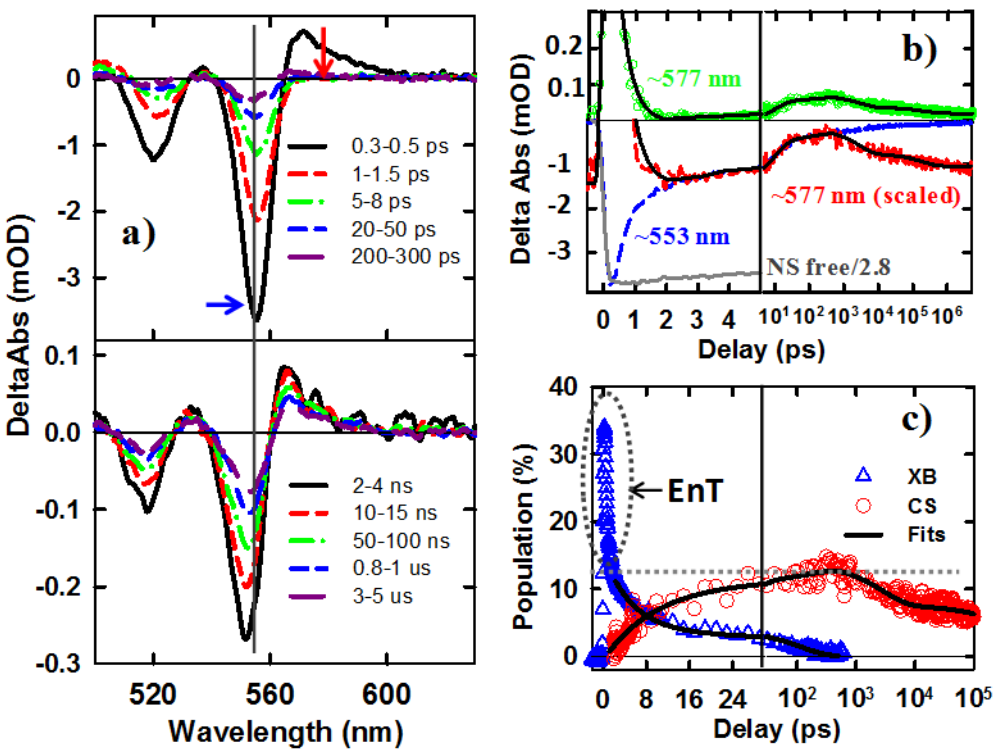

Figure 4.5. TA spectra and kinetics of CdSe NS-Pt measured with 400 nm excitation. a) TA spectra at indicated time delays from 0.3 ps to 300 ps (upper panel) and from 2 ns to 5 us (lower panel). b) Comparison of TA kinetics at ~553 nm (XB, averaged between 551-555nm, blue dashed line) and ~577 nm (average between 573-580 nm,

green circles). Also shown is the kinetics at 577nm that has been scaled and displaced vertically (red dashed line). Kinetics at ~553 nm in free NS (gray solid line) has been reduced by a factor of 2.8 for better comparison. The black solid line is a fit to kinetics at ~577 nm. c) Time-dependent population of XB (blue triangles) and charge separated states (CS, red circles). The black solid lines are multi-exponential fits to them. The gray dashed line indicates the efficiency of exciton dissociation (13.4±0.5%). The gray dashed circle indicates ultrafast exciton quenching by energy transfer pathways. In b and c, the delay time axes are in linear scale at early delay times and in logarithmic scale at longer decay time.

The remaining 13.4±0.5% of excitons was dissociated by ET to Pt, as shown in Figure 4.6. We attribute this to ultrafast hole trapping, which reduced the mobility of excitons and enabled effective competition of electron transfer with ultrafast energy transfer. The trapping of hole also leads to long-lived charge separated state (75±14 ns). This assignment is supported by the presence of ultrafast hole trapping and long-lived conduction band electrons in free CdSe NSs. Similar hole-trapping induced long-lived charge separation has also been observed in CdS NR-Pt and CdS NR-Au.[20,47] In the presence of hole acceptors, these long-lived charge separated states allow removal of trapped holes and accumulation of electrons in the Pt tip for H_2 production.[16,17] The key differences between CdSe NSs and CdS NRs are that in the latter, exciton quenching through diffusion and energy transfer is slow compared to hole trapping, leading to near unity yield of charge separation in CdS NR-Pt[20]. This difference can be attributed to atomically precise thickness in the quantum-confined dimension in NSs, which minimizes energy disorder and enables ultrafast exciton diffusion. This insight suggests that a possible way to improve the charge separation yield in NSs is to use nanosheet heterostructures with efficient hole localization at selective domains, such as the recently reported CdSe NS/CdS crown heterostructure where holes are confined in CdSe NS.[33,48] Similar strategies have been successfully demonstrated in CdSe/CdS dot-in-rod nanorod heterostructures. [17,18]

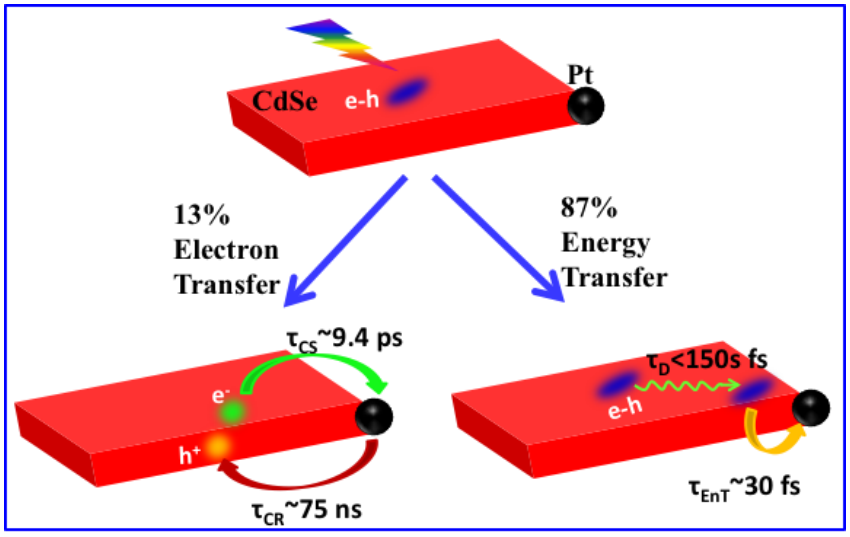

Figure 4.6. Competition between energy and electron transfer pathways in CdSe NS-Pt. Fast in-plane exciton mobility leads to fast energy transfer quenching. Trapped excitons can be dissociated by electron transfer to Pt.

4.3. Conclusion

In conclusion, in this Chapter we have prepared Pt tipped CdSe nanosheets with well-defined morphology and strong interaction between the semiconductor and metal domains. The mechanisms of efficient exciton quenching in these heterostructures have been investigated by TA spectroscopy. The result revealed ultrafast quenching of 86.6% excitons (half-life <150 fs) by fast exciton transport to the NS/Pt interface followed by rapid energy transfer. The remaining 13.4% of excitons were first localized due to hole trapping and then dissociated through interfacial electron transfer (~9.4 ps) from the CdSe NS to the Pt tip. The charge-separated state was

long-lived (~75 ns) as a result of the hole trapping, which provides potentials for charge accumulation. The comparison with unity efficient charge separation yield achieved in Pt tipped CdS NRs studied in last Chapter emphasizes the importance of immobilize holes for efficient and long-lived charge separation in these 1D and 2D semiconductor/metal nanostructures. To apply the NS-Pt heterostructures in solar driven H_2 generation, the exciton dissociation yield needs to be improved, which can potentially be achieved by using nanosheet heterostructures with engineered hole localization sites, such as CdSe/CdS hetero nanosheets.

References

(1) Banin, U.; Ben-Shahar, Y.; Vinokurov, K. *Chem. Mat.* **2013**, *26*, 97.

(2) Costi, R.; Saunders, A. E.; Banin, U. *Angew. Chem. Int. Ed.* **2010**, *49*, 4878.

(3) Vaneski, A.; Susha, A. S.; Rodríguez-Fernández, J.; Berr, M.; Jäckel, F.; Feldmann, J.; Rogach, A. L. *Adv. Funct. Mater.* **2011**, *21*, 1547.

(4) Hirakawa, T.; Kamat, P. V. *J. Am. Chem. Soc.* **2005**, *127*, 3928.

(5) Mokari, T.; Rothenberg, E.; Popov, I.; Costi, R.; Banin, U. *Science* **2004**, *304*, 1787.

(6) Shi, W.; Zeng, H.; Sahoo, Y.; Ohulchanskyy, T. Y.; Ding, Y.; Wang, Z. L.; Swihart, M.; Prasad, P. N. *Nano Lett.* **2006**, *6*, 875.

(7) Habas, S. E.; Yang, P.; Mokari, T. *J. Am. Chem. Soc.* **2008**, *130*, 3294.

(8) Carbone, L.; Jakab, A.; Khalavka, Y.; Sönnichsen, C. *Nano Lett.* **2009**, *9*, 3710.

(9) Li, X.; Lian, J.; Lin, M.; Chan, Y. *J. Am. Chem. Soc.* **2010**, *133*, 672.

(10) Costi, R.; Saunders, A. E.; Elmalem, E.; Salant, A.; Banin, U. *Nano Lett.* **2008**, *8*, 637.

(11) Dukovic, G.; Merkle, M. G.; Nelson, J. H.; Hughes, S. M.; Alivisatos, A. P. *Adv. Mater.* **2008**, *20*, 4306.

(12) Tongying, P.; Vietmeyer, F.; Aleksiuk, D.; Ferraudi, G. J.; Krylova, G.; Kuno, M. *Nanoscale* **2014**, *6*, 4117.

(13)Tongying, P.; Plashnitsa, V. V.; Petchsang, N.; Vietmeyer, F.; Ferraudi, G. J.; Krylova, G.; Kuno, M. *J. Phys. Chem. Lett.* **2012**, *3*, 3234.

(14)Berr, M. J.; Vaneski, A.; Mauser, C.; Fischbach, S.; Susha, A. S.; Rogach, A. L.; Jäckel, F.; Feldmann, J. *Small* **2012**, *8*, 291.

(15)Acharya, K. P.; Khnayzer, R. S.; O'Connor, T.; Diederich, G.; Kirsanova, M.; Klinkova, A.; Roth, D.; Kinder, E.; Imboden, M.; Zamkov, M. *Nano Lett.* **2011**, *11*, 2919.

(16)Berr, M.; Vaneski, A.; Susha, A. S.; Rodriguez-Fernandez, J.; Doblinger, M.; Jackel, F.; Rogach, A. L.; Feldmann, J. *Appl. Phys. Lett.* **2010**, *97*, 0931081.

(17)Amirav, L.; Alivisatos, A. P. *J. Phys. Chem. Lett.* **2010**, *1*, 1051.

(18)Wu, K.; Chen, Z.; Lv, H.; Zhu, H.; Hill, C. L.; Lian, T. *J. Am. Chem. Soc.* **2014**, *136*, 7708.

(19)O'Connor, T.; Panov, M. S.; Mereshchenko, A.; Tarnovsky, A. N.; Lorek, R.; Perera, D.; Diederich, G.; Lambright, S.; Moroz, P.; Zamkov, M. *ACS Nano* **2012**, *6*, 8156.

(20)Wu, K.; Zhu, H.; Liu, Z.; Rodríguez-Córdoba, W.; Lian, T. *J. Am. Chem. Soc.* **2012**, *134*, 10337.

(21)Butler, S. Z.; Hollen, S. M.; Cao, L.; Cui, Y.; Gupta, J. A.; Gutiérrez, H. R.; Heinz, T. F.; Hong, S. S.; Huang, J.; Ismach, A. F.; Johnston-Halperin, E.; Kuno, M.; Plashnitsa, V. V.; Robinson, R. D.; Ruoff, R. S.; Salahuddin, S.; Shan, J.; Shi, L.; Spencer, M. G.; Terrones, M.; Windl, W.; Goldberger, J. E. *ACS Nano* **2013**, *7*, 2898.

(22)Wang, Q. H.; Kalantar-Zadeh, K.; Kis, A.; Coleman, J. N.; Strano, M. S. *Nat Nano* **2012**, *7*, 699.

(23)Ithurria, S.; Dubertret, B. *J. Am. Chem. Soc.* **2008**, *130*, 16504.

(24)Ithurria, S.; Bousquet, G.; Dubertret, B. *J. Am. Chem. Soc.* **2011**, *133*, 3070.

(25)Ithurria, S.; Tessier, M. D.; Mahler, B.; Lobo, R. P. S. M.; Dubertret, B.; Efros, A. L. *Nat Mater* **2011**, *10*, 936.

(26)Joo, J.; Son, J. S.; Kwon, S. G.; Yu, J. H.; Hyeon, T. *J. Am. Chem. Soc.* **2006**, *128*, 5632.

(27)Son, J. S.; Wen, X.-D.; Joo, J.; Chae, J.; Baek, S.-i.; Park, K.; Kim, J. H.; An, K.; Yu, J. H.; Kwon, S. G.; Choi, S.-H.; Wang, Z.; Kim, Y.-W.; Kuk, Y.; Hoffmann, R.; Hyeon, T. *Angew. Chem. Int. Ed.* **2009**, *48*, 6861.

(28)Son, J. S.; Yu, J. H.; Kwon, S. G.; Lee, J.; Joo, J.; Hyeon, T. *Adv. Mater.* **2011**, *23*, 3214.

(29)She, C.; Fedin, I.; Dolzhnikov, D. S.; Demortière, A.; Schaller, R. D.; Pelton, M.; Talapin, D. V. *Nano Lett.* **2014**, *14*, 2772.

(30)Liu, Y.-H.; Wayman, V. L.; Gibbons, P. C.; Loomis, R. A.; Buhro, W. E. *Nano Lett.* **2009**, *10*, 352.

(31)Zhao, H.; Dal Don, B.; Moehl, S.; Kalt, H.; Ohkawa, K.; Hommel, D. *Phys. Rev. B* **2003**, *67*, 035306.

(32) Kalt, H.; Zhao, H.; Don, B. D.; Schwartz, G.; Bradford, C.; Prior, K. *J. Lumin.* **2005**, *112*, 136.

(33) Tessier, M. D.; Spinicelli, P.; Dupont, D.; Patriarche, G.; Ithurria, S.; Dubertret, B. *Nano Lett.* **2013**, *14*, 207.

(34) Johnson, R. C.; Li, J.; Hupp, J. T.; Schatz, G. C. *Chem. Phys. Lett.* **2002**, *356*, 534.

(35) Demortière, A.; Schaller, R. D.; Li, T.; Chattopadhyay, S.; Krylova, G.; Shibata, T.; dos Santos Claro, P. C.; Rowland, C. E.; Miller, J. T.; Cook, R.; Lee, B.; Shevchenko, E. V. *J. Am. Chem. Soc.* **2014**, *136*, 2342.

(36) Pelton, M.; Ithurria, S.; Schaller, R. D.; Dolzhnikov, D. S.; Talapin, D. V. *Nano Lett.* **2012**, *12*, 6158.

(37) Klimov, V. I. *J. Phys. Chem. B* **2000**, *104*, 6112.

(38) Zhu, H.; Yang, Y.; Lian, T. *Acc. Chem. Res.* **2012**, *46*, 1270.

(39) Kambhampati, P. *Acc. Chem. Res.* **2010**, *44*, 1.

(40) Kambhampati, P. *J. Phys. Chem. C* **2011**, *115*, 22089.

(41) Sewall, S. L.; Cooney, R. R.; Dias, E. A.; Tyagi, P.; Kambhampati, P. *Phys. Rev. B* **2011**, *84*, 235304.

(42) Sewall, S. L.; Cooney, R. R.; Anderson, K. E. H.; Dias, E. A.; Sagar, D. M.; Kambhampati, P. *J. Chem. Phys.* **2008**, *129*, 084701.

(43) Zhu, H.; Lian, T. *J. Am. Chem. Soc.* **2012**, *134*, 11289.

(44) Jiang, Z.-J.; Kelley, D. F. *J. Phys. Chem. C* **2011**, *115*, 4594.

(45) Huang, J. E.; Huang, Z. Q.; Jin, S. Y.; Lian, T. Q. *J. Phys. Chem. C* **2008**, *112*, 19734.

(46) Huang, J.; Stockwell, D.; Huang, Z. Q.; Mohler, D. L.; Lian, T. Q. *J. Am. Chem. Soc.* **2008**, *130*, 5632.

(47) Wu, K.; Rodríguez-Córdoba, W. E.; Yang, Y.; Lian, T. *Nano Lett.* **2013**, *13*, 5255.

(48) Prudnikau, A.; Chuvilin, A.; Artemyev, M. *J. Am. Chem. Soc.* **2013**, *135*, 14476.

(49) Curutchet, C.; Franceschetti, A.; Zunger, A.; Scholes, G. D. *J. Phys. Chem. C* **2008**, *112*, 13336.

(50) Li, M.; Cushing, S. K.; Wang, Q.; Shi, X.; Hornak, L. A.; Hong, Z.; Wu, N. *J. Phys. Chem. Lett.* **2011**, *2*, 2125.

(51) Stryer, L. *Annu. Rev. Biochem.* **1978**, *47*, 819.

(52) Clegg, R. M. *Curr. Opin. Chem. Biol.* **1995**, *6*, 103.

(53) Wu, K.; Liu, Z.; Zhu, H.; Lian, T. *J. Phys. Chem. A* **2013**, *117*, 6362.

(54) Yang, Y.; Rodríguez-Córdoba, W. E.; Lian, T. *J. Am. Chem. Soc.* **2011**, *133*, 9246.

(55) Meulenberg, R. W.; Lee, J. R. I.; Wolcott, A.; Zhang, J. Z.; Terminello, L. J.; van Buuren, T. *ACS Nano* **2009**, *3*, 325.

(56) Canali, C.; Nava, F.; Ottaviani, G.; Paorici, C. *Solid State Communications* **1972**, *11*, 105.

(57) Luer, L.; Hoseinkhani, S.; Polli, D.; Crochet, J.; Hertel, T.; Lanzani, G. *Nat Phys* **2009**, *5*, 54.

Appendix 1.

Absorption spectrum fitting for CdSe and CdSe-Pt Nanosheets

The ground state absorption spectrum of CdSe NSs can be fitted by a sum of multiple exciton bands, each represented by a Lorentzian function L_i (with peak height of H_i, center energy of E_i and half width of Γ_i), and a broad background function (*bg*). The use of Lorentzian instead of Gaussian is due to negligible inhomogeneous broadening in NS thicknesses. The origin of the background function is unclear but it could be Rayleigh scattering or unresolved transitions. The ground state absorption spectrum of NS can be fit to the following function :

$$Abs_{NS}(\omega) = bg(\omega) + \sum_{i=1}^{4} \frac{H_i}{(\hbar\omega - E_i)^2 + \Gamma_i^{\,2}} \qquad \text{(A.4.1).}$$

The fitting curve is shown in Figure A.4.1.a and the fitting parameters are listed in Table A.4.1. The fitted background function is:

$$bg(\omega) = C \bullet (\hbar\omega - E_g)^{1/2}, \qquad \text{(A.4.2)}$$

where Eg is the band gap of NS (2.2 eV) and C is a pre-factor.

The ground state absorption spectrum of CdSe NS-Pt can be approximately treated as superposition of NS absorption with Pt absorption $Abs_{Pt}(\omega)$. The latter was

obtained from free Pt nanoparticles in chloroform. Therefore, we fit NS-Pt absorption spectrum according to the following equation:

$$Abs_{NS-Pt}(\omega) = Abs_{NS}(\omega) + Abs_{Pt}(\omega) = \left[bg(\omega) + \sum_{i=1}^{4} \frac{H_i}{(\hbar\omega - E_i)^2 + \Gamma_i^2} \right] + Abs_{Pt}(\omega)$$

(A.4.3).

The fitting curve is shown in Figure A.4.1.b and the fitting parameters are listed in Table A.4.1. Comparison of the fitting parameters in CdSe NS and CdSe NS-Pt reveals that the exciton bands are red-shifted and broadened in the latter. The broadening is more prominent for lowest energy exciton band, which implies that the broadening results more likely from energy level dependent electronic interaction between the NS and Pt than dielectric environment change caused by the Pt.

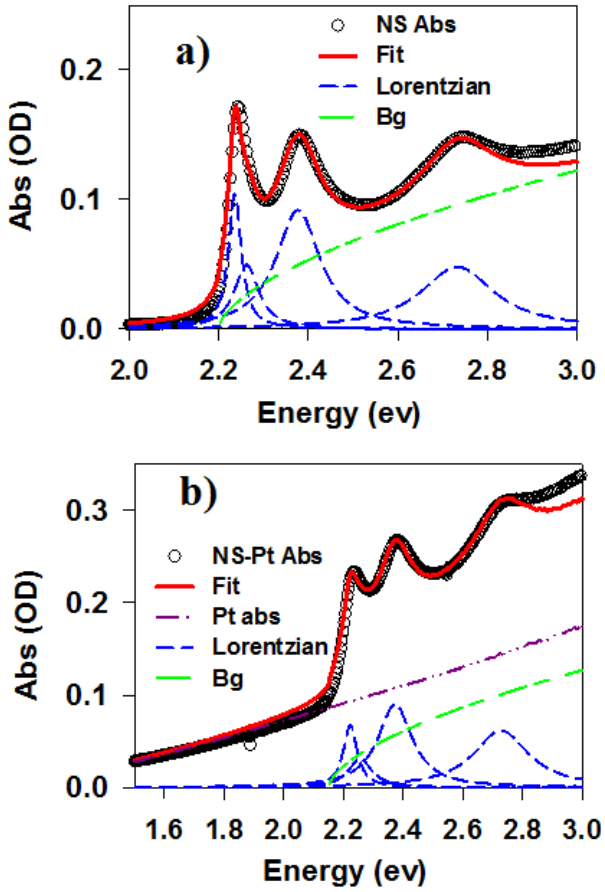

Figure A.4.1. Fitting of the absorption spectra of a) CdSe NSs and b) CdSe NS-Pt, showing the absorption spectra (black open circles) and their fits (red solid line) by a sum of Lorentzian bands (blue dashed lines) and a background function (green dashed line) and Pt absorption (purple dashed line, in b only).

Table A.4.1. Fitting parameters absorption spectra of CdSe and CdSe-Pt NSs

	CdSe NS		CdSe NS-Pt	
	Center (eV)	Width (eV)	Center (eV)	Width (eV)

L1	2.236	0.035	2.223	0.056
L2	2.262	0.066	2.256	0.096
L3	2.377	0.120	2.373	0.140
L4	2.733	0.200	2.728	0.225

Appendix 2.

Single exciton experimental condition

Estimating average number of photo-generated excitons on each CdSe NS requires absorption cross section of these NSs, which is not measured in this work. However, to ensure that our experiments were performed under single exciton conditions, i.e. each NS has either one or zero exciton, we measured power-dependent exciton kinetics for these NSs. As shown in Figure A.4.2, the kinetics at three indicated powers agree well with each other after scaling. Also, the initial signal amplitudes are proportional to excitation powers (inset). Therefore, these experiments were in the linear regime, or single exciton excitation conditions. All of our experiments shown in the main text correspond to excitation power of 19 uW.

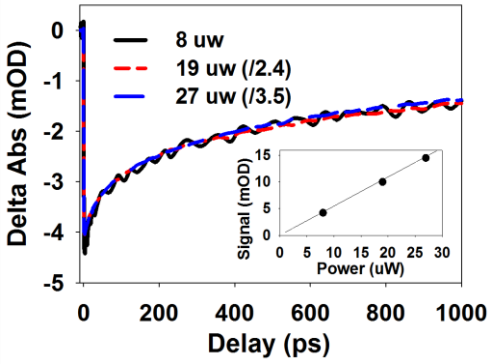

Figure A.4.2. XB recovery kinetics at different excitation powers. They are scaled for better comparison and the scaling factors are labeled. The inset is a plot of initial signal amplitudes as a function of excitation power.

Appendix 3.

Exciton quenching by diffusion and energy transfer in CdSe NS-Pt

We assume that excitons in CdSe NS can be quenched by Pt through Forster Resonant Energy Transfer (FRET) mechanism. Previous studies have confirmed the applicability of this model to these nanoscale objects even though the donor and/or acceptor dimensions are similar to their separations. The Forster radius, the distance between donor and acceptor at which the fluorescence quenching efficiency is 50%, is given by the following equation:

$$R = 0.211[\kappa^2 \Phi_D J(\lambda)/n^4]^{1/6} \quad \text{(A.4.4)},$$

in which κ^2 is dipole orientation factor. The general expression for κ^2 is given by:

$$\kappa^2 = \langle(\cos\alpha - 3\cos\beta\cos\gamma)^2\rangle \quad \text{(A.4.5)},$$

where α is the angle between the donor and acceptor transition moments, β is the angle between the donor moment and the line joining the centers of the donor and acceptor, and is the angle between the acceptor moment and the line joining the centers of the donor and acceptor. The transition dipoles in the spherical Pt nanoparticle can be assumed to be isotropic. The emission dipole in the NS is likely randomly-distributed in the plane, as demonstrated by the 2-D polarized emission in

NSs. In this case, α, β, and γ are all allowed to range from 0 to π. and the κ^2 in equation S15 is averaged to 2/3 .

Φ_D is emission quantum yield of donor, $J(\lambda)$ is the overlap integral between donor emission and acceptor absorption spectra, and n is the refractive index of the medium. The overlap integral can be calculated using:

$$J(\lambda) = \frac{\int d\lambda I_D(\lambda)\varepsilon_A(\lambda)(\lambda)^4}{\int d\lambda I_D(\lambda)}$$

(A.4.6),

where $I_D(\lambda)$ and $\varepsilon_A(\lambda)$ are donor emission spectrum and acceptor molar absorptivity, respectively. The molar absorptivity of Pt nanoparticles are estimated from the molar absorptivity of NS and the absorption spectrum of NS-Pt, by assuming 1:1 molar ratio of NS to Pt. The molar absorptivity of NS is estimated from NS-MV^{2+} electron transfer experiments where we assume that one electron in NS bleaches half of NS transition and after transfer the electron generates one $MV^{+\cdot}$ radical.

With the Foster radius, the energy transfer time constant can be calculated as:

$$\tau_{EnT} = \tau_0(\frac{r}{R})^6$$

(A.4.7),

Where τ_0 is the donor excited state lifetime in the absence of the acceptor and r is the donor-acceptor distance. The overlap integral between CdSe NS emission and Pt absorption is calculated to be 8.7×10^{17} $M^{-1}cm^{-1}nm^4$.

According to Table 4.1, we have 50.9% band edge electron-hole pairs undergo radiative and non-radiative recombination with a time constant of 617 ps. Since the QY of these NSs is 38%, the QY of these band edge electron-hole pairs is ~74.7%. The radiative life-time of band-edge exciton is then estimated to be ~826 ps. Therefore, the Forster radius calculated from equation A.4.4 is 14.1 nm, using the refractive index of chloroform (1.49).

Since energy transfer rate is sensitive to donor-acceptor distance, we calculate two cases when the excitons are near the NS/Pt interface and at the center of NS, respectively, as shown in Figure S8. In the former case, accounting for the bulk Bohr radius for CdSe (4.9 nm) and the diameter of Pt tip (3.1 nm), the approximate energy transfer distance is 6.45 nm. Using e equation A.4.4, the energy transfer time constant at this distance is calculated to be ~7.65 ps. This time changes drastically with used Bohr radius value. For example, if we assume a Bohr radius of 1 nm, the energy transfer time is 29 fs. Recognizing the tightly-bound nature of e-h pair in NS, a Bohr radius smaller than bulk value should be used. Based on these estimations, the energy transfer occurs on 10s of fs time scale at the NS/Pt interface. If the exciton is located at the center of NS, the energy transfer distance is 20.7 nm, corresponding to an energy transfer time constant of 8.4 ns.

The above estimate suggests that exciton quenching via energy transfer is likely limited by the transport excitons to the NS/Pt interface, as shown in Figure A.4.3. The

exciton transport time can be estimated by assuming that exciton in-plane motion can be described by diffusion. The drift mobility of electron μ_e and hole μ_h in bulk CdSe is reported to be ~720 cm^2/V.s and ~75cm^2/V.s, respectively. Due to strong e-h binding in NS, coupled e-h pair (i.e. exciton) diffusion is expected. We calculate the center of mass drift mobility of exciton according to:

$$\mu_X = \frac{m_e\mu_e + m_h\mu_h}{m_e + m_h} = 220 \text{ cm}^2/\text{V.s} \qquad \text{(A.4.8)},$$

where m_e (0.13 m_0) and m_h (0.45 m_0)are effective mass of electron and hole in bulk CdSe, respectively. The exciton diffusion constant D_X is related to its mobility via:

$$D_X = \frac{\mu_X kT}{e} = 5.5 \quad \text{cm}^2/\text{s} \qquad \text{(A.4.9)},$$

where k is Boltzmann constant, T is temperature and e is electron charge. Due to randomly-distributed exciton positions on NS upon photon absorption, numerical simulations are required to reproduce the diffusion times of excitons in NS. Here we provide a qualitatively estimate of time scale of this process. We assume the exciton is at the center of NS with the distance between exciton and Pt being 20.7 nm. In the case of 2-D diffusion, $t_D \sim \frac{L^2}{4D} = 195$ fs. This estimated time scale qualitatively agrees with the value calculated from equation A.4.7. Therefore, it is a reasonable model for exciton quenching in NS-Pt. From this model, the ultrafast exciton

quenching can be attributed to both giant emission dipole induced fast energy transfer rate and fast in-plane exciton transport in NS.

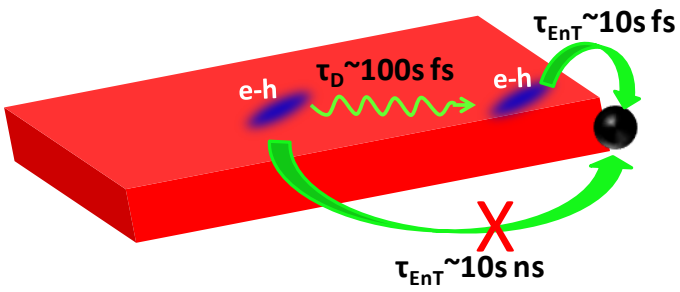

Figure A.4.3. A scheme showing the mechanism of *exciton diffusion controlled energy transfer*. Energy transfer from exciton near the nanosheet/Pt interface is fast. The overall exciton quenching rate is limited by in-plane diffusion, which is still on the ultrafast time scale due to large in-plane exciton mobility.

Chapter 5. Hole Removal Rate Limits Photo-driven H_2 Generation Efficiency in CdS-Pt and CdSe/CdS-Pt Semiconductor Nanorod-metal tip Heterostructures

5.1. Introduction

Efficient artificial photosynthesis requires optimal integration of multiple functional components, including light absorbers, electron and hole acceptors, and catalysts.[1,2] It has been well demonstrated that in donor-light absorber-acceptor molecular triads, the spatial separation of electron donors and acceptors can lengthen the lifetime of charge separated states and facilitate their coupling with catalysts for efficient selective light driven oxidation or reduction reactions.[3-5] Recent advances in colloidal nanostructure synthesis have led to the development of triadic nanoheterostructures, in which multiple functional components are integrated in single all-inorganic structures and their spatial and energetics arrangements can be systematically optimized.[6-12] Compared to molecular systems, these all-inorganic nanostructures have superior long-term stability that is hard to achieve with molecular systems [13] and the energetics of the components can be readily tuned by their size

through the quantum confinement effect.[14] For these reasons, a series of semiconductor-metal nanoheterostructures, especially platinum or gold nanoparticle decorated semiconductor nanorods (NRs) and nanowires have been successfully synthesized and investigated for photo-catalysis applications.[11,12,15-22] Among them, CdSe/CdS dot-in-rod (DIR) nanorods with a platinum nanoparticle at one end (CdSe/CdS-Pt) serve as an ideal model system for examining the design principle of these triadic photo-catalytic nanoheterostructures.[11] From the relative energetics of CdSe, CdS and Pt, photo-excitation in these triads can, in principle, lead to a long-lived charge separated state with the electron at the Pt tip and the hole confined in the CdSe core that is tens of nanometers away. Indeed, in the presence of electron donors, these structures have been shown to carry out photoreduction of protons to form hydrogen molecules with a conversion quantum efficiency (QE) of as high as 20%.[11] Interestingly, the conversion QE appears to depend on the CdSe seed size and CdS rod length, suggesting the possibility of further optimization. Despite these reported promising performances, it is unclear what factors limit the overall QE of photo-reduction and how QE depends on the chemical nature and dimension of the components.[23-25]

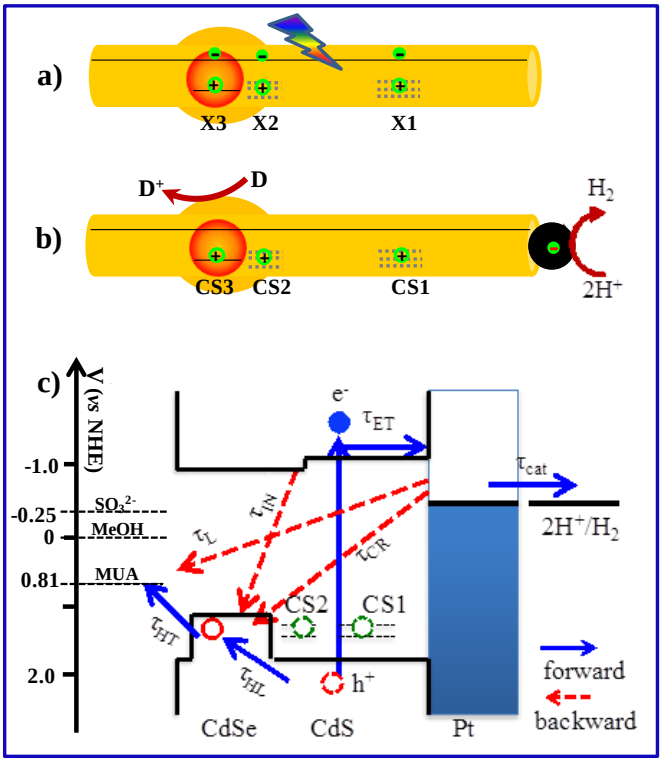

Figure 5.1. Photo-generation of H_2 using CdSe/CdS-Pt NRs. Schematic illustration of a) three distinct exciton states (X1, X2, X3) in CdSe/CdS NRs and b) three charge separated states (CS1, CS2, CS3) in CdSe/CdS-Pt triadic nanoheterostructures with the hole localized in the CdS rod (X1 and CS1), CdS bulb region surrounding the seed (X2, CS2) and CdSe seed (CX3, CS3). Also shown in b) is the photo-catalytic generation of H_2 from protons in the presence of electron donors D. c) Simplified schematic energy levels and charge separation and recombination processes relevant to photo-catalytic H_2 generation. The figure corresponds to the initial formation of CS3. The hole location for CS1 and CS2 are also labeled (dashed green circles) for comparison. See the main text for details. All band edge positions and redox

potentials correspond to aqueous solution at PH=7, the condition for the photo-catalytic experiments.

The photo-generation of H_2 in triadic nanoheterostructures such as CdSe/CdS DIR-Pt involves a series of desirable forward charge transfer and efficiency-reducing recombination processes, as shown in Figure 5.1. Because of the quasi-type II band alignment between the CdSe seed and CdS rod, it is often thought that in the excited CdSe/CdS NRs, the valence band (VB) hole should localize to the CdSe seed (with a time constant of τ_{HL}) while the conduction band (CB) electron can delocalize among the CdS rod and CdSe seed, forming the lowest energy exciton state in the heterostructure (labeled as X3 in Figure 5.1.a).[26-29] However, the carrier relaxation dynamics and final locations of carriers in CdSe/CdS NRs are recently found to be excitation-energy dependent.[30,31] As shown in Figure 5.1.a, our recent study reveals that after the rod excitation, in addition to X3, there exist two other distinct long lived exciton states in CdSe/CdS NRs with the hole localized in the CdS rod (X1) and CdS bulb region surrounding the seed (X2).[30] As a result, further transfer of the electron to the Pt tip (with a time constant of τ_{ET}) should form three different charge separated states with holes localized in the CdS rod (CS1), CdS bulb region (CS2) and CdSe core (CS3), as shown in Figure 5.1.b. This is likely a common feature in CdSe/CdS-Pt nanorods, although the branching ratio for forming X1, X2 and X3 excitons, which is

dependent on trap state density and morphology of the CdS rod, can vary among samples. For simplicity, we have only depicted the relevant processes for CS3 in Figure 5.1.c. Hole removal by electron donor D (with a time constant of τ_{HT}) enables the accumulation of electrons in the Pt tip to carry out reduction of two protons to form H_2 (with a time constant of τ_{CAT}). These forward processes compete with the recombination of electrons and holes within the NR (with an intrinsic lifetime of τ_{IN}), the loss of electrons in the Pt by charge recombination with the holes in the CdSe (with a time constant of τ_{CR}) and with the oxidized donor, D^+ (with a time constant of τ_L) and *via* other pathways. Thus, rational improvement of the photo-driven hydrogen generation efficiency in these materials requires a detailed understanding of the rates of these competing processes.

In this Chapter, we examine the factors that limit the photo-catalytic H_2 generation QE of CdSe/CdS-Pt and CdS-Pt NRs. The latter was included as a comparison to investigate the effect of quasi-type II band alignment in CdSe/CdS-Pt. We observed that the steady state H_2 generation QE using these nanorods depended on the nature of the electron donor. With methanol as an electron donor, higher QE was observed for CdSe/CdS-Pt than CdS-Pt. Using sulfite as an electron donor, the QEs were improved for both, but the QE for CdS-Pt became higher than CdSe/CdS-Pt. To investigate the mechanism of the observed electron donor dependent QE, we used transient absorption spectroscopy and time resolved fluorescence decay to measure

the charge separation, recombination and hole removal rates in these systems. In all cases, the initial charge separation efficiency (electron transfer from NRs to Pt) was nearly 100% in these materials. The hole transfer rates were dependent on the nature of the electron donor and the NR, and correlated with the steady state H_2 generation QEs. Thus, these results suggest that hole removal is the main efficiency limiting factor in these systems. We discuss how these insights provide possible approaches for improving the photo-catalytic H_2 generation properties of these nanoheterostructures.

5.2. Results and Discussion

5.2.1 Absorption and emission properties of CdSe/CdS-Pt

CdSe/CdS dot-in-rod NRs were prepared by a seeded-growth procedure.[32,33] These CdSe/CdS NRs have an average length of 16.5 (±1.0) nm and diameter of 3.5 (±0.3) nm, as well as a bulb region surrounding the CdSe seed with slightly larger diameter than rest of the rod. The static absorption and emission spectra of CdSe/CdS NRs are displayed in Figure 5.2. The lowest absorption peak at ~540 nm (B3) can be assigned to the X3 exciton transition (from the top of valance band in CdSe core to

the lowest energy conduction band level); the pronounced peaks at ~450 nm (B1) and 400 nm, can be attributed to the 1D excitonic transitions of the CdS rod region; and a small shoulder at 470 nm (B2) can be attributed to the transition from the VB top to the CB bottom of CdS in the bulb region surrounding the CdSe seed.[23,30] It is shown that the B2 and B3 transitions share the same CB electron level, reflecting the quasi-type II band alignment in this heterostructure. The photoluminescence (PL) spectrum of CdSe/CdS NRs measured with 400 nm excitation (Figure 5.2) was dominated by the emission of the X3 exciton state.

Platinum deposition on the CdSe/CdS NRs was done by thermal reduction of Pt(II) acetylacetonate.[6] These as-prepared CdSe/CdS-Pt heterostructures showed well-defined morphology, containing ~2%, 93% and 5% NRs with 0, 1 and 2 Pt tips, respectively. The absorption spectrum of CdSe/CdS-Pt can be well modeled by a linear combination of CdSe/CdS and Pt contributions (Figure A.5.1). The latter is a broad featureless absorption tail extending to the near IR.[34] The PL of CdSe/CdS was completely quenched after the attachment of the Pt tips. We have also prepared CdS and CdS-Pt NR samples with similar dimensions (average rod length of 18.1 ±1.8 nm and rod diameter of 3.5 ±0.3 nm) according to previously published procedures.[6,33]

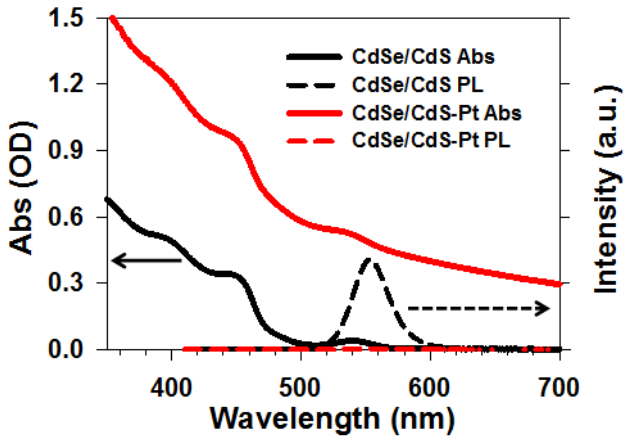

Figure 5.2. Static absorption (solid lines) and photoluminescence (PL, dashed lines) spectra of CdSe/CdS NRs (black lines) and CdSe/CdS-Pt NRs (red lines).

5.2.2. Effect of electron donors on H_2 generation efficiency

We first compare the photo-catalytic H_2 generation efficiencies of CdS-Pt and CdSe/CdS-Pt heterostructures. The as-prepared NRs samples were capped by phosphonate ligands and dispersed in chloroform solutions. They were transferred to aqueous solutions by replacing the phosphonate ligands with 11-mercaptoundecanoic acid (MUA) according to ligand exchange procedures.[11,12] The steady-state H_2 generation measurements were carried out in reaction solutions of MUA capped CdS-Pt or CdSe/CdS-Pt NRs in 1:10 volume ratio of methanol/water (methanol/MUA as electron donor) or in 0.1 M sodium sulfite water (sulfite/MUA as electron donor). As shown in Figure 5.1.c, although the redox potential becomes more

positive from sodium sulfite (-0.25 V *vs* NHE[36]) to methanol (~0 V *vs* NHE[35]) to MUA (~0.81 V *vs* NHE[36]), hole transfer from the CdSe and CdS valence bands to these molecules are energetically allowed. The optical densities of all the samples were adjusted to ~1.5 at 455 nm to ensure the same photon absorption rates in all solutions. The samples were illuminated by 455 nm LED light (15 mW) and H_2 was detected by gas chromatograph. We first repeated previously-reported experiments in which methanol was used as a sacrificial donor.[11] Figure 5.3.a shows the H_2 evolution kinetics measured in the first 40 min of light illumination. The induction period, in the first 10 min, can be attributed to the solubility of H_2 in the aqueous solution[37] or remaining O_2 due to imperfect purge of the system with Argon[38]. After this period, the amounts of H_2 increase linearly with time, the slope of which indicates H_2 generation rate. From the ratio of H_2 generation and photon absorption rates, the photo-driven H_2 generation QE can be calculated. After correcting for light absorption and scattering loss due to the cuvette and Pt particles, the internal QE is determined, as shown in Figure 5.3.b. Using methanol as electron donors, the H_2 generation QEs of CdS-Pt and CdSe/CdS-Pt are $0.78 \pm 0.03\%$ and $1.8 \pm 0.4\%$, respectively. These values are in good agreement with previous reports for NRs of similar lengths.[11]

Previous comparison of photo-reduction between CdSe/CdS-Pt and CdS-Pt [11] and between CdSe/CdS and CdS[39] have also reported higher efficiencies in CdSe/CdS NRs. The better performances in CdSe/CdS NRs have often been attributed to the

quasi-type II band alignment between CdSe and CdS, which promotes internal electron-hole separation between the CdSe and CdS domains. If this was indeed the efficiency-limiting factor for these heterostructures, CdSe/CdS-Pt should have better performance than CdS-Pt under the same conditions regardless of the electron donors used. To test this hypothesis, we performed the same comparison of photo-catalytic H_2 generation efficiencies of CdS-Pt and CdSe/CdS-Pt NRs using sodium sulfite/MUA as the electron donors. Their H_2 generation kinetics traces and the calculated internal QEs are shown in Figure 5.3.a and 5.3.b, respectively. Compared to values measured with methanol/MUA as electron donors, the internal QE for both samples are considerably higher and, more surprisingly, the QE of CdS-Pt (9.6$\pm$ 0.5%) become 3 times higher than CdSe/CdS-Pt (3.2$\pm$0.1%). This result indicates that H_2 generation efficiencies of CdS-Pt and CdSe/CdS-Pt depends strongly and in different ways on the electron donors. We notice that the higher H_2 generation efficiency from CdS-Pt NRs with sulfite as sacrificial donor than with methanol has been reported by Berr et al.[40] In addition, they investigated a series of donors with different redox potentials and constructed a positive correlation between H_2 generation efficiency and the reductivity of donor.[40] Nonetheless, the comparison between CdS-Pt and CdSe/CdS-Pt NRs under different donors is studied here for the first time.

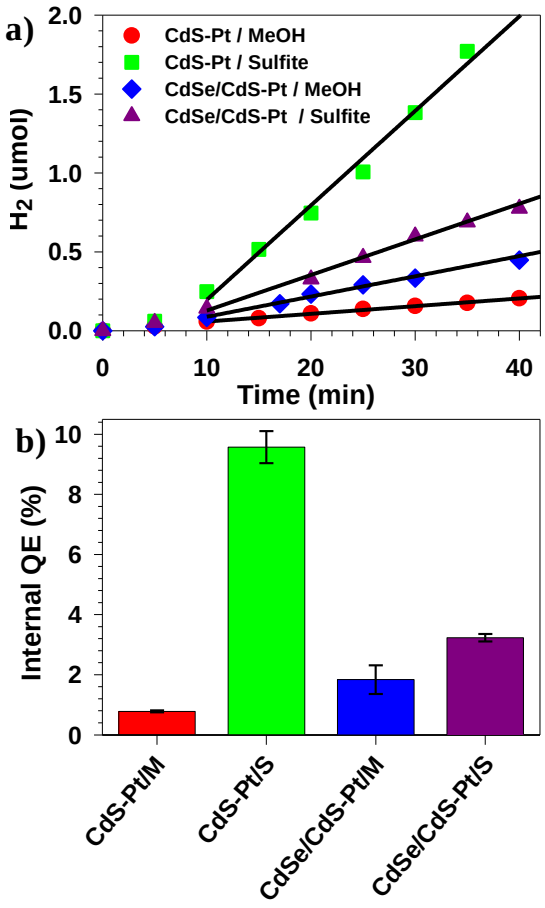

Figure 5.3. Steady state H_2 photo-generation using MUA-capped CdSe/CdS-Pt and CdS-Pt NRs. a) H_2 evolution kinetics traces for CdS-Pt with methanol (red circles) and sulfite (green squares), and CdSe/CdS-Pt with methanol (blue diamonds) and sulfite (purple triangles) as electron donors. The black solid lines are linear fits to the traces from 10 to 40 min, from which the H_2 generation rates were determined. b) Calculated H_2 generation internal QEs for CdS-Pt and CdSe/CdS-Pt with methanol or sulfite electron donors.

5.2.3. Charge separation and recombination in CdSe/CdS-Pt and CdS-Pt

To unveil the mechanism for the observed nanorod and electron donor dependent steady-state H_2 generation efficiencies, we carried out transient absorption and time-resolved fluorescence decay measurement of CdSe/CdS-Pt and CdS-Pt NRs to determine the rates of various competing processes shown in Figure 5.1.c. We first measured the rates of electron transfer (τ_{ET}) from these nanorods to the Pt tip and the subsequent charge recombination(τ_{CR}) processes in the absence of a hole acceptor. Because thiol is a hole acceptor, for this experiment, we used NRs capped by phosphonate and dispersed in chloroform solution. By comparing with intrinsic exciton lifetime measured in CdSe/CdS and CdS nanorods without Pt tips, we determined the QE for the initial charge separation (i.e. electron transfer from to Pt) process.

As illustrated in Figure 5.1.a, optical excitation of CdSe/CdS at 455 nm creates an electron-hole pair in the CdS rod region that can decay by three pathways to form X1, X2 and X3 excitons.[30] To simplify the data analysis, we first measure TA spectra with 540 nm pump pulse, which selectively excite the lowest energy exciton band and generates only the X3 exciton state in the NR.[30] X3 in free CdSe/CdS NRs is long-lived with a half-life of ~8.3 ns.[30]. Figure 5.4.a shows the TA spectra of CdSe/CdS-Pt at indicated time delays after 540 nm excitation. The TA spectrum at early delay time (< 1 ps) shows two pronounced bleach of B3 (540 nm) and B2 (475

nm) transitions, similar to free CdSe/CdS NRs. These features have been attributed to CB electron state filling induced bleaches, which provide a convenient probe of the lifetime of the X3 excitons.[30,41] The presence of X3 exciton also leads to the bleach of B2 transition, indicating that the lowest energy CB electron level extends into the CdS bulb region, consistent with the quasi-type II band alignment in this heterostructure. Compared to free CdSe/CdS NRs, these bleach features recover with a much faster rate, indicating shorter-lived CB electrons. Accompanying the decay of X3 signals, derivative-like features formed in the range of 430-500 nm. Similar features are commonly observed in the TA spectra of quantum dot-acceptor complexes and are attributed to charge separation induced Stark effect signals (CS).[30,42,43] Therefore, both the fast bleach recovery and CS spectral signatures confirm photo-induced electron transfer from the CdSe/CdS NR to the Pt tip. The lower panel of Figure 5.4.a shows that the CS features decay from 1 ns to 3000 ns due to the recombination of the electron in the Pt tip with the VB hole in the CdSe core.

The rates of charge separation and recombination processes were measured by following the decay kinetics of X3 exciton bleach and CS signals, respectively. Due to spectral and temporal overlaps of these two signals, we fit the TA spectra as a linear combination of X3 and CS signals to obtain the time-dependent X3 and CS coefficients, which were used to construct the charge separation and recombination kinetics, respectively.[30] The TA spectrum of DIR-Pt at 1ps was taken as the pure X3

spectrum and the TA spectrum averaged from 30 to 50 ns the pure CS spectrum. This is justified by the fact that charge separation is completed at 30 ns, after which all the spectral features decay in the same way, as shown in Figure 5.4.b. The time-dependent population coefficients for X3 and CS signals obtained from the fit are displayed in Figure 5.4.c. Note that the coefficients for CS after 30 ns were directly taken from TA kinetics at 453 nm which were scaled and connected with the fitted coefficients. The X3 and CS kinetics were fitted with multi-exponentials, from which half-lives of 43.5 ± 4.7 ps and 211 ± 38 ns for charge separation and recombination, respectively, were obtained.

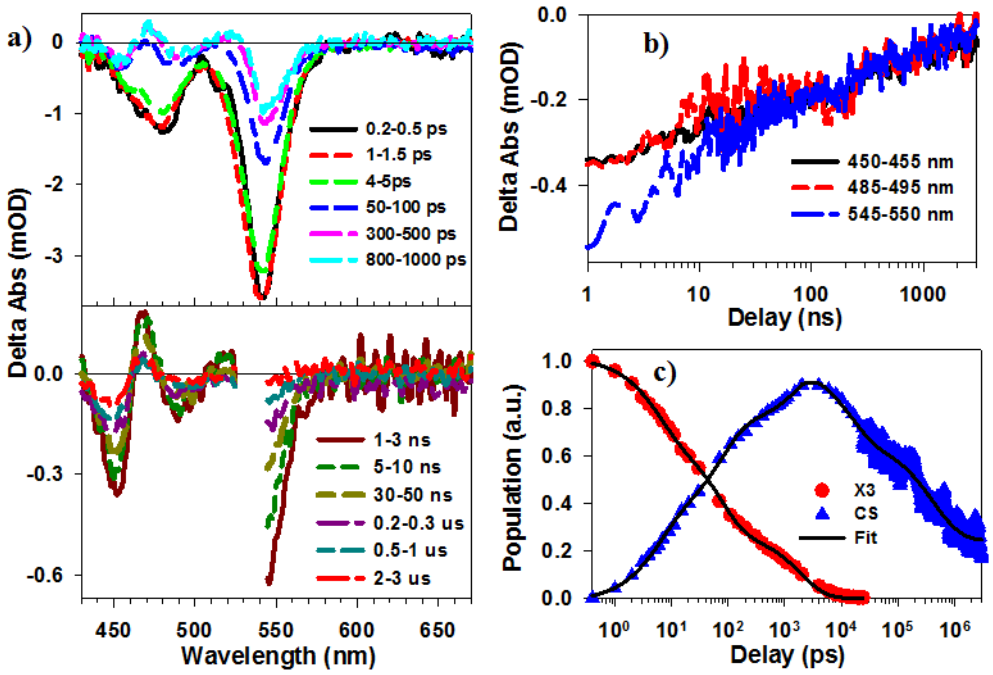

Figure 5.4. Transient absorption spectra and kinetics of CdSe/CdS-Pt measured at 540 nm excitation. a) Transient absorption spectra of CdSe/CdS-Pt at indicated time delays: 0.2 ps to 1000 ps (upper panel) and 1 ns to 3000 ns (lower panel). b) Kinetics

probed at indicated wavelength ranges from 1 to 3000 ns. c) Time-dependent populations for X3 (red circles) and charge separated states (CS, blue triangles) from 0.4 ps to 3000 ns extracted from fitting the TA spectra (see main text) and their fits to multi-exponential functions (black solid lines).

For CdSe/CdS NRs, absorption at wavelengths shorter than 460 nm is dominated by transitions within the CdS rod due to its large volume and absorption cross section.[27] To mimic the initial absorption conditions created by 455 nm excitation used in the steady state H_2 generation experiment, we measured transient absorption spectra of phosphonate capped CdSe/CdS and CdSe/CdS-Pt NRs at 400 nm excitation. We have previously shown that the e-h pairs generated with 400 nm excitation of CdS rods relax into three spatially separated excitons: X1, X2 and X3, as shown in Figure 5.1a, with formation probabilities and half-lives of (~46%, 22.5 ns), (7%, 32.1 ns) and (47%, 8.3 ns), respectively. [30] The formation of X1, X2 and X3 is driven by hole localization from the CdS rod valence band to trap states at the CdS rod (with a time constant of τ_{HL1}=0.48 ps), the CdS bulb (τ_{HL2}=0.42 ps) and CdSe seed (τ_{HL3}=0.42 ps), respectively.

The TA spectra of CdSe/CdS-Pt at indicated delay times following 400 nm excitation are shown in Figure 5.5.a. The bleaches at the B1, B2 and B3 transitions recovered quickly with concomitant formation of derivative-like charge separated

state (CS) signals. The initial signal amplitudes of B2 and B3 were only 67% of those in free DIRs (Figure 5.5.b), suggesting ultrafast electron transfer to Pt prior to the formation of X2 and X3. From the signal amplitudes of B2 and B3 and the kinetics of B1 the time constant of fast electron transfer process from these free excitons was determined to be τ_{ET}=0.47 ps

After 2 ps, all the exciton localization processes were completed and the TA spectra could be fitted to a linear combination of exciton state filling and CS signals for X1, X2 and X3 excitons. Briefly, the spectra of X1, X2, and X3 were first identified (Figure A5.5.a). The charge separation and recombination rates as well as charge separated state spectra (CS3) of X3 excitons have been independently determined in the measurement with 540 nm excitation (Figure 5.4). Because exciton X2 and X3 share the same conduction band electron level (due to quasi-type II band alignment.) and have holes localized in the bulb region, we assume that the dissociation of these excitons generate charge separated states, CS2 and CS3, respectively, with similar Stark effect TA spectra and lifetimes. Subtracting their contribution from the TA spectrum at 30 ns (measured with 400 nm excitation), consisting of the CS states (CS1+CS2+CS3) only, yields CS1 TA spectrum. The time-dependent population coefficients for X1, X2, X3 and CS1, CS2 and CS3 signals obtained from fitting the TA spectra are displayed in Figure 5.5.c. These kinetics were fitted to multi-exponential functions and the fitting parameters are listed in Table S2.

From the fit, we obtained half-lives of 1.75±0.22 ps, 30.1±3.5, and 43.5±4.7 ps for charge separation and 102 ± 29 ns, 211 ± 38 ns and 211 ± 38 ns for charge recombination for X1, X2 and X3 excitons, respectively. Further details of the fitting procedure are discussed in the Supporting Information.

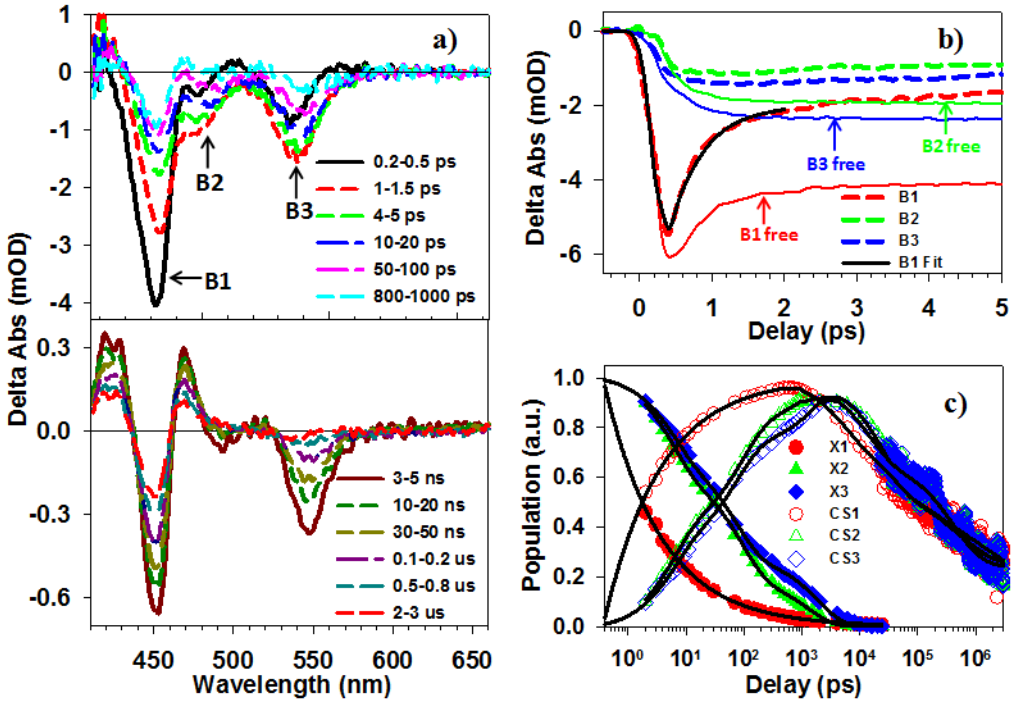

Figure 5.5. Transient absorption spectra and kinetics of CdSe/CdS-Pt measured with 400 nm excitation. a) TA spectra of CdSe/CdS-Pt at indicated delay times: (upper panel) 0.2 ps to 1000 ps, showing charge separation process, and (lower panel) 3 ns to 3000 ns, showing mostly the charge recombination process. b) Kinetics of B1 (~450 nm, red lines), B2 (~480 nm, green line) and B3 (~540 nm, blue line) of CdSe/CdS-Pt (dashed lines) and CdSe/CdS (solid lines) within 5 ps. The black solid line is a fit to

B1 kinetics within 2 ps. c) Time-dependent populations for X1 (red filled circles), X2 (green filled triangles), X3 (blue filled diamonds) excitons and their charge separated states CS1(red open circles), CS2 (green open triangles), and CS3 (blue open diamonds) from 0.4 ps to 3000 ns. The black solid lines are multi-exponential fits to these kinetics.

5.2.4. Comparing charge separation and recombination in CdS-Pt and CdSe/CdS NRs

As a comparison, we have also measured TA spectra of CdS-Pt of similar geometries (length and diameter) with 400 nm excitation. The assignment of spectral signatures in CdS-Pt nanorods and the extraction of charge separation and recombination rates from the TA spectra have been reported previously.[23] The half-lives for charge separation and recombination in CdS-Pt were determined to be 2.15 ± 0.35 ps and 149 ± 52 ns, respectively.

Due to significant spectral overlap between CdSe/CdS emission and Pt absorption (Figure 5.2), the possibility of energy transfer should be considered.[44,45] We have estimated the energy transfer rate from the X3 exciton state, the main emissive state in CdSe/CdS NRs, to the Pt tip based on the Forster resonant energy transfer (FRET) model.[46] As shown in the Appendix 2, the estimated upper limit of

energy transfer rate is ~1/38.7 ns^{-1}, which is too slow to compete with electron transfer from X3 to Pt. In addition, we have previously shown that energy transfer from CdS NR to Pt tip cannot compete with electron transfer either, due to an ultrafast hole trapping process.[23,47]

Listed in Table 5.1 are the charge separation and recombination rates for CdSe/CdS-Pt and CdS-Pt measured at 400 nm excitations, along with the intrinsic exciton lifetimes in free CdSe/CdS and CdS NRs. We define the charge separation yield (Φ) as: $\Phi = (\frac{1}{\tau_{CS}} - \frac{1}{\tau_{IN}})/(\frac{1}{\tau_{CS}}) = (\tau_{IN} - \tau_{CS})/\tau_{IN}$, where τ_{IN} and τ_{CS} are the conduction band electron half lives in NRs without and with Pt tips respectively. τ_{IN} depends on the "intrinsic" radiative and nonradiative decay processes within the semiconductor domain (in the absence of Pt tip). We have assumed that the growth of the Pt tip adds an electron transfer pathway ($1/\tau_{ET}$) and does not affect the rate of the intrinsic decay processes ($1/\tau_{CS} = 1/\tau_{ET} + 1/\tau_{IN}$). For CdSe/CdS NRs, three types of excitons have their individual charge separation yields. Therefore, the population weighted charge separation yield is taken as the effective yield: $\Phi_{eff} = \sum_{i=1}^{3} a_i \Phi_i$, where a_i and Φ_i are the population percentage and charge separation yield for exciton Xi (i=1,2,3) in CdSe/CdS-Pt NRs. The calculated Φ values for both CdS-Pt and CdSe/CdS-Pt (listed in Table 1) are nearly 100%, indicating that all excitons in the semiconductor domain dissociate by electron transfer to the Pt tip. Therefore, the

charge separation efficiencies in DIR-Pt and NR-Pt are not the factor that limits the photo-catalytic efficiency.

Table 5.1. Comparison of charge separation (τ_{CS}), charge recombination (τ_{CR}) and intrinsic half lifetimes (τ_{IN}) in CdSe/CdS-Pt and CdS-Pt

	CdSe/CdS -Pt			CdS -Pt
	X1	X2	X3	
τ_{CS} (ps)	1.75±0.22	30.1±3.5	43.5±4.7	2.15±0.35
τ_{CR} (ns)	102±29 ns	211±38 ns	211±38 ns	149±52 ns
τ_{IN} (ns)	22.5±1.7*	32.1±2.2*	8.34±0.31*	24.7±0.9
Φ (%)	99.99	99.91	99.47	99.99
Φ_{eff}(%)	99.82			99.99

* Taken from Ref. 25.

Although efficient charge separation and long-lived charge separated states are achieved in both CdSe/CdS-Pt and CdS-Pt NRs, there are interesting differences in

their mechanisms. In CdS-Pt NRs, rapid trapping of holes on CdS NR surface generates a charge separated state with long lifetime. In CdSe/CdS-Pt NRs, there exist three excitons. The charge separated states resulted from X1 and X2 (53% of the total population) excitons are similar to CdS-Pt nanorods. It should be noted that the X2 exciton is not explicitly considered in our analysis of the TA spectra of CdS-Pt NRs because its contribution, dependent on sample growth conditions, is too small to be accurately determined. The X3 exciton leads to long-lived charge separated state by localizing the hole at the CdSe seed far away from the Pt tip. In comparison, instead of the poorly understood surface traps on CdS rod, localization of hole on CdSe seed may provide a better path towards rational control of the distance (and lifetime) of charge separation in CdSe/CdS-Pt and other dot-in-rod NRs.

5.2.5. Hole filling of CdSe/CdS and CdS NRs by electron donor

As shown in Figure 5.1.b, in addition to efficient charge separation, charge accumulation and turn-over on the Pt catalyst requires fast hole removal to suppress the charge recombination processes.[12,39,40] Hole transfer rates to electron donors can be measured by time-resolved photoluminescence (PL) decay of CdS and CdSe/CdS NRs (without Pt tip) in the presence of electron donors. These experiments were performed in aqueous solutions using MUA-capped NRs under conditions used for the steady-state photo-catalytic H_2 generation measurements. In addition to methanol

and sodium sulfite, the native ligand, MUA (~0.81 V *vs* NHE[36]), is an efficient donor itself and the hole filling rate by MUA can be extracted by comparing the PL decay rates of MUA capped NRs in aqueous solution and phosphonate capped NRs in organic solvents.[12,39,48] Figure 5.6a and 5.6b show the static PL spectra of CdS and CdSe/CdS NRs, respectively, in the presence of different electron donors after 400 nm excitation. The PL intensities of CdS and CdSe/CdS NRs were quenched by 22 and 45 folds, respectively, upon exchanging the phosphonate by MUA ligands, indicating that MUA is an effective hole acceptor. Adding methanol into the aqueous solution of MUA-capped CdS and CdSe/CdS NRs had negligible effects on the PL intensities. In contrast, in the presence of 0.1 M of sodium sulfite, the PL of NRs and DIRs were further quenched to ~25% and ~63% of MUA capped NRs, respectively.

To determine the hole transfer (HT) rates, we also measured the PL decay kinetics for these samples between 532 and 675 nm after 400 nm excitation. For CdS NRs, PL in this spectral region is dominated by the broad trap-mediated emission band (Figure 5.6a), which is shown to be the main recombination channel because of the fast trapping of photo-generated holes.[23] For CdSe/CdS NRs, it probes the emission from the X3 exciton, which accounts for 47% of the excited NRs. The remaining 53% of excitons are localized on the CdS rod, whose emission quantum yield (~0.2%) is too small to be accurately measured in the presence of the much stronger X3 exciton emission (QE ~48%). The PL intensities of NRs with and

without electron donors were measured under the same conditions (excitation power and sample absorbance), such that both the absolute intensities and decay times can be compared. Compared to phosphonate capped NRs (Figure 5.6c and 5.6d), the PL of MUA-capped NRs shows a smaller initial amplitude and faster decay. The former indicates a PL decay component that is faster than the instrument response (~240 ps). PL decay kinetics of MUA-capped NRs was not affected by the addition of methanol, but was affected by sulfite, consistent with the effect of this electron donors on the steady emission intensity (Figure 5.6a and 5.6b). To quantify the hole transfer rates, these kinetics were fitted to multi-exponential decay functions. From the fitting parameters, we calculated the amplitude-weighted average PL decay rate for NRs ($k_{ave,NR}$), NRs with MUA ($k_{ave,NR-MUA}$) and NRs with MUA and sulfite ($k_{ave,NR-MUA+sulfite}$). The hole transfer rates to MUA and sulfite were then calculated according to equations (5.1) and (5.2).[49,50]

$$k_{HT,MUA} = k_{ave,NR-MUA} - k_{ave,NR} \quad (5.1)$$

$$k_{HT,sulfite} = k_{ave,NR-MUA+sulfite} - k_{ave,NR-MUA} \quad (5.2)$$

The calculated average hole transfer times ($\tau_{HT,i} = 1/k_{HT,i}$) are listed in Table 5.2. Hole transfer times from both CdS and CdSe/CdS NRs to methanol were too slow to be determined (>>100 ns). Hole transfer rate from CdSe/CdS to MUA was ~4.9 times faster than CdS while hole transfer from CdS to sulfite was ~2.5 times faster than CdSe/CdS. We speculate that the differences in hole transfer rates can be

qualitatively understood from the nature and location of the holes in CdS and CdSe/CdS NRs. The broad trap-mediated emission in CdS NRs was previously attributed to a broad distribution of trapping states,[51] but a recent model suggests that it is more likely due to localized holes with strong coupling to phonons.[52,53] The fact that the observed emission quenching is the same for the whole broad band (Figure 5.6a) agrees better with the later model. In this model, the strong coupling between holes and phonons requires a larger reorganization energy and driving force for fast hole transfer.[52-54] As for the CdSe/CdS NRs, the exclusive and high quantum yield (Figure 5.6b) emission form X3 indicates well-passivated holes in the CdSe core due to large valence band offset (~0.45 eV) between CdSe and CdS.[32,33] Therefore, in the case of using weakly reductive MUA (~0.81 V *vs* NHE[36]), the rate for transferring the surface-trapped holes in CdS NRs is slower than the VB holes from the CdSe seed. In contrast, the more strongly reductive sulfite (-0.25 V *vs* NHE[36]) provides a larger driving force for removing the surface-trapped holes in CdS NRs.[36] In this case, the hole transfer rate becomes slower in CdSe/CdS due to its confinement within the CdSe core that is harder to access by the electron donor. The increase of hole transfer rates from CdS NRs to donors with driving force also explains Berr et al's observations.[40]

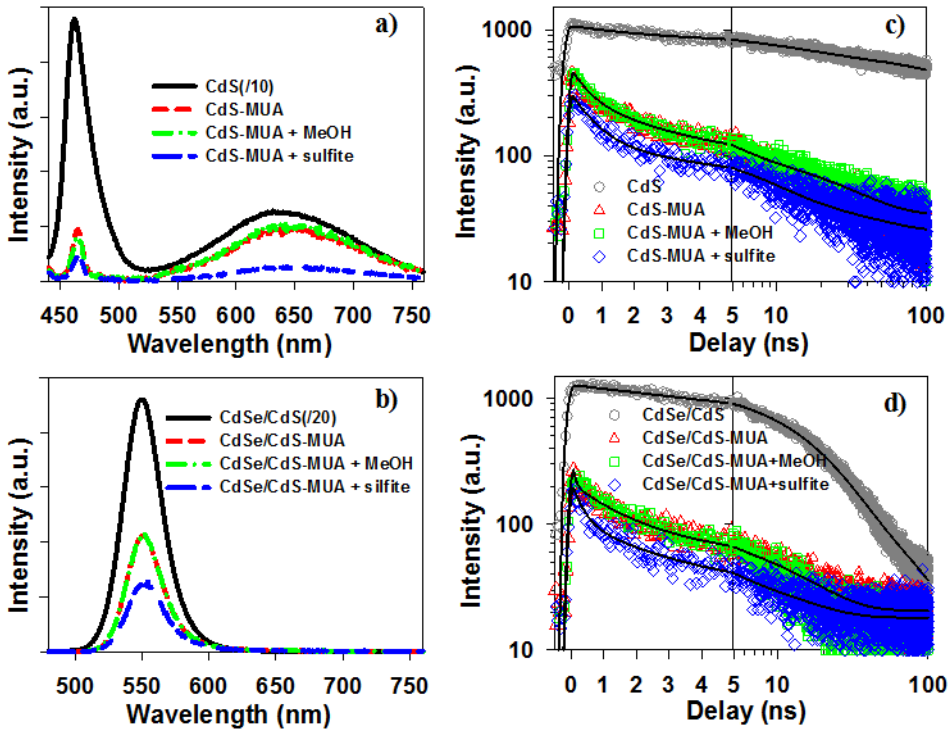

Figure 5.6. Static PL spectra (a,b) and PL decay kinetics (c, d) of CdS (a,c) and CdSe/CdS (b,d) NRs. Four samples are compared in each panel: phosphonate capped NRs in chloroform (black solid line or circles) and MUA capped NRs in in water (red dashed line, triangles), in 1:10 volume ratio of methanol/water (green dashed-dotted line or squares), and in 0.1 M sodium sulfite water solution (blue dashed line or diamonds). All samples were excited at 400 nm. The PL kinetics were measured between 532 and 675 nm. The black solid lines in c) and d) are multi-exponential fits.

Table 5.2. Apparent hole transfer times and H_2 generation quantum efficiency (QE)

	CdS-Pt+MeOH		CdS-Pt+sulfite		CdSe/CdS-Pt +MeOH		CdSe/CdS-Pt +sulfite	
Apparent	MUA	MeOH	MUA	sulfite	MUA	MeOH	MUA	sulfite
HT (ns)	0.218 ±0.003	>>100	0.218 ±0.003	0.0607 ±0.018	0.0441 ±0.008	>>100	0.0441 ±0.008	0.154 ±0.022
QE (H_2)	0.78 ±0.03%		9.6 ±0.5%		1.8 ±0.4%		3.2 ±0.1%	

The measured average hole transfer times and H_2 generation QEs for CdS and CdSe/CdS NRs are compared in Table 5.2, which shows a positive correlation between the hole transfer rate and H_2 generation QE. Specifically, i) The H_2 generation QEs and hole transfer rates are higher with sulfite than methanol for both NRs. And ii) the relative QE follows the trend of hole transfer rates when comparing CdS-Pt with CdSe/CdS-Pt NRs. Furthermore, a control experiment showed that methanol has negligible effects on the H_2 generation QEs of MUA capped NR-Pt, which is consistent with its negligible effects on the hole transfer rates (from both PL decay and static PL quenching of NRs). The positive correlation between hole transfer

rate and H_2 generation QE and the observed unity quantum yield for the initial charge separation suggests that hole removal is an efficiency-limiting step in photo-catalytic H_2 generation using these NR heterostructures. Indeed, previous studies of CdS nanoparticles show that using a mixture of sulfite and sulfide (S^{2-}/SO_3^{2-}) as electron donors can lead to H_2 generation efficiencies higher than 50%.[55-58] This may be attributed to the higher reduction power of S^{2-}(-0.45 V *vs* NHE[59]), which should give rise to faster hole removal rates. We have avoided using sulfide in this study because it can lead to charging of nanocrystals and complicate the assignment of measured PL intensities and lifetimes.[60] It should be noted that sulfite appears to have negligible effect on the absorption spectra of the QD, suggesting negligible degree of QD charging.[60]

The H_2 generation QE of CdS-Pt obtained with sulfite electron donor (9.6%) is comparable to the highest reported values for these colloidal heterostructures.[18,36,39,61] However, the steady state H_2 generation efficiency is still far from unity, despite the unity initial quantum yield of electron transfer to Pt. According to Table 5.1 and 5.2, the removal rates of holes in CdSe core or on CdS surface traps by electron donors are considerably faster than the rates of their recombination with the electrons in Pt. This result may suggest that the holes that are transferred to MUA or to sulfite (i.e. the one-electron oxidized sulfite and MUA intermediate) can still recombine with electrons in Pt, reducing the H_2 generation efficiency.[38]

The findings of this study suggest possible pathways for designing more efficient solar-to-fuel conversion systems using semiconductor-metal nanostructures. The first approach is to use hole scavengers with faster hole transfer rates. While using more reductive donors such as S^{2-} and SO_3^{2-} can achieve the goal by providing a large drive forces for hole transfer,[38,55-57,62] it reduces the net energy gain in (and hence the solar-to-fuel energy conversion efficiency of) the fuel forming reaction. Another way to improve hole transfer rates is to utilize electron donors that can more readily access the NR surface. The morphology of the nanorod can be optimized to expose the hole trapping domains to the electron donor. For example, a recent study showed that etching the lateral dimension of CdSe/CdS NRs could significantly increase the H_2 generation rate because it exposed the hole-containing CdSe core to the electron donors.[17] Alternatively, NR growth methods that can locate the CdSe seed (or other hole containing seed) at one end of the rod structure should also improve the hole transfer rate.

5.3. Conclusion

In conclusion, we have observed electron donor and nanorod structure dependent photo-catalytic H_2 generation performances of MUA capped CdSe/CdS-Pt and

CdS-Pt NRs. Compared to methanol, using sulfite as electron donor improves the H_2 generation QEs for both NRs. The relative performance of these two NRs depended on the nature of the electron donor: higher QE was observed for CdSe/CdS-Pt using MUA/methanol, while with MUA/sulfite higher QE was achieved in CdS-Pt. Using ultrafast transient absorption spectroscopy, we showed that electron transfer efficiencies to the Pt tip were near unity for both CdS and CdSe/CdS NRs. The transfer rates of holes localized at the CdS rod surface and CdSe seed were measured by time-resolved PL decay. We found a positive correlation of the observed hole transfer rates with the steady state H_2 generation quantum yields, indicating that hole transfer was a key efficiency-limiting step. Our finding suggests that the H_2 generation quantum efficiency can be further improved by using faster hole acceptors or designing nanorod structures that facilitate hole transfer.

References

(1) Alstrum-Acevedo, J. H.; Brennaman, M. K.; Meyer, T. J. *Inorg. Chem.* **2005**, *44*, 6802.

(2) Nocera, D. G. *Acc. Chem. Res.* **2012**, *45*, 767.

(3) Gust, D.; Moore, T. A.; Moore, A. L. *Acc. Chem. Res.* **2000**, *34*, 40.

(4) Liddell, P. A.; Kuciauskas, D.; Sumida, J. P.; Nash, B.; Nguyen, D.; Moore, A. L.; Moore, T. A.; Gust, D. *J. Am. Chem. Soc.* **1997**, *119*, 1400.

(5) Wasielewski, M. R. *Chem. Rev.* **1992**, *92*, 435.

(6) Habas, S. E.; Yang, P.; Mokari, T. *J. Am. Chem. Soc.* **2008**, *130*, 3294.

(7) Dukovic, G.; Merkle, M. G.; Nelson, J. H.; Hughes, S. M.; Alivisatos, A. P. *Adv. Mater.* **2008**, *20*, 4306.

(8) Shi, W.; Zeng, H.; Sahoo, Y.; Ohulchanskyy, T. Y.; Ding, Y.; Wang, Z. L.; Swihart, M.; Prasad, P. N. *Nano Lett.* **2006**, *6*, 875.

(9) Mokari, T.; Rothenberg, E.; Popov, I.; Costi, R.; Banin, U. *Science* **2004**, *304*, 1787.

(10) Tang, M. L.; Grauer, D. C.; Lassalle-Kaiser, B.; Yachandra, V. K.; Amirav, L.; Long, J. R.; Yano, J.; Alivisatos, A. P. *Angew. Chem. Int. Ed.* **2011**, *50*, 10203.

(11) Amirav, L.; Alivisatos, A. P. *J. Phys. Chem. Lett.* **2010**, *1*, 1051.

(12) Acharya, K. P.; Khnayzer, R. S.; O'Connor, T.; Diederich, G.; Kirsanova, M.; Klinkova, A.; Roth, D.; Kinder, E.; Imboden, M.; Zamkov, M. *Nano Lett.* **2011**, *11*, 2919.

(13) Kamat, P. V. *J. Phys. Chem. C* **2008**, *112*, 18737.

(14) Brus, L. E. *J. Chem. Phys.* **1983**, *79*, 5566.

(15) Berr, M.; Vaneski, A.; Susha, A. S.; Rodriguez-Fernandez, J.; Doblinger, M.; Jackel, F.; Rogach, A. L.; Feldmann, J. *Appl. Phys. Lett.* **2010**, *97*, 0931081.

(16) Berr, M. J.; Schweinberger, F. F.; Döblinger, M.; Sanwald, K. E.; Wolff, C.; Breimeier, J.; Crampton, A. S.; Ridge, C. J.; Tschurl, M.; Heiz, U.; Jäckel, F.; Feldmann, J. *Nano Lett.* **2012**, *12*, 5903.

(17) Khon, E.; Lambright, K.; Khnayzer, R. S.; Moroz, P.; Perera, D.; Butaeva, E.; Lambright, S.; Castellano, F. N.; Zamkov, M. *Nano Lett.* **2013**, *13*, 2016.

(18) Tongying, P.; Plashnitsa, V. V.; Petchsang, N.; Vietmeyer, F.; Ferraudi, G. J.; Krylova, G.; Kuno, M. *J. Phys. Chem. Lett.* **2012**, *3*, 3234.

(19) Bang, J. U.; Lee, S. J.; Jang, J. S.; Choi, W.; Song, H. *J. Phys. Chem. Lett.* **2012**, *3*, 3781.

(20) Elmalem, E.; Saunders, A. E.; Costi, R.; Salant, A.; Banin, U. *Adv. Mater.* **2008**, *20*, 4312.

(21) Ha, J. W.; Ruberu, T. P. A.; Han, R.; Dong, B.; Vela, J.; Fang, N. *J. Am. Chem. Soc.* **2014**, *136*, 1398.

(22) Tongying, P.; Vietmeyer, F.; Aleksiuk, D.; Ferraudi, G. J.; Krylova, G.; Kuno, M. *Nanoscale* **2014**, *6*, 4117.

(23) Wu, K.; Zhu, H.; Liu, Z.; Rodríguez-Córdoba, W.; Lian, T. *J. Am. Chem. Soc.* **2012**, *134*, 10337.

(24) O'Connor, T.; Panov, M. S.; Mereshchenko, A.; Tarnovsky, A. N.; Lorek, R.; Perera, D.; Diederich, G.; Lambright, S.; Moroz, P.; Zamkov, M. *Acs Nano* **2012**, *6*, 8156.

(25) Berr, M. J.; Vaneski, A.; Mauser, C.; Fischbach, S.; Susha, A. S.; Rogach, A. L.; Jäckel, F.; Feldmann, J. *Small* **2012**, *8*, 291.

(26) Lupo, M. G.; Della Sala, F.; Carbone, L.; Zavelani-Rossi, M.; Fiore, A.; Lüer, L.; Polli, D.; Cingolani, R.; Manna, L.; Lanzani, G. *Nano Lett.* **2008**, *8*, 4582.

(27) Borys, N. J.; Walter, M. J.; Huang, J.; Talapin, D. V.; Lupton, J. M. *Science* **2010**, *330*, 1371.

(28) Talapin, D. V.; Koeppe, R.; Götzinger, S.; Kornowski, A.; Lupton, J. M.; Rogach, A. L.; Benson, O.; Feldmann, J.; Weller, H. *Nano Lett.* **2003**, *3*, 1677.

(29) She, C.; Demortière, A.; Shevchenko, E. V.; Pelton, M. *J. Phys. Chem. Lett.* **2011**, *2*, 1469.

(30) Wu, K.; Rodríguez-Córdoba, W. E.; Liu, Z.; Zhu, H.; Lian, T. *ACS Nano* **2013**, *7*, 7173.

(31) She, C.; Bryant, G. W.; Demortière, A.; Shevchenko, E. V.; Pelton, M. *Phys. Rev. B* **2013**, *87*, 155427.

(32) Talapin, D. V.; Nelson, J. H.; Shevchenko, E. V.; Aloni, S.; Sadtler, B.; Alivisatos, A. P. *Nano Lett.* **2007**, *7*, 2951.

(33) Carbone, L.; Nobile, C.; De Giorgi, M.; Sala, F. D.; Morello, G.; Pompa, P.; Hytch, M.; Snoeck, E.; Fiore, A.; Franchini, I. R.; et al *Nano Lett.* **2007**, *7*, 2942.

(34) Johnson, R. C.; Li, J.; Hupp, J. T.; Schatz, G. C. *Chem. Phys. Lett.* **2002**, *356*, 534.

(35) Iwasita, T. *Electrochim. Acta* **2002**, *47*, 3663.

(36) Brown, K. A.; Wilker, M. B.; Boehm, M.; Dukovic, G.; King, P. W. *J. Am. Chem. Soc.* **2012**, *134*, 5627.

(37) Toshima, N.; Takahashi, T.; Hirai, H. *J. Macro. Sci. A Chem.* **1988**, *25*, 669.

(38) Buehler, N.; Meier, K.; Reber, J. F. *J. Phys. Chem.* **1984**, *88*, 3261.

(39) Zhu, H.; Song, N.; Lv, H.; Hill, C. L.; Lian, T. *J. Am. Chem. Soc.* **2012**, *134*, 11701.

(40) Berr, M. J.; Wagner, P.; Fischbach, S.; Vaneski, A.; Schneider, J.; Susha, A. S.; Rogach, A. L.; Jackel, F.; Feldmann, J. *Appl. Phys. Lett.* **2012**, *100*, 223903.

(41) Klimov, V. I. *J. Phys. Chem. B* **2000**, *104*, 6112.

(42) Zhu, H.; Song, N.; Rodríguez-Córdoba, W.; Lian, T. *J. Am. Chem. Soc.* **2012**, *134*, 4250.

(43) Zhu, H.; Song, N.; Lian, T. *J. Am. Chem. Soc.* **2011**, *133*, 8762.

(44) Clegg, R. M. *Curr. Opin. Chem. Biol.* **1995**, *6*, 103.

(45) Stryer, L. *Annu. Rev. Biochem.* **1978**, *47*, 819.

(46) Förster, T. *Ann. Phys. (Berlin)* **1948**, *437*, 55.

(47) Wu, K.; Rodríguez-Córdoba, W. E.; Yang, Y.; Lian, T. *Nano Lett.* **2013**, *13*, 5255.

(48) O'Connor, T.; Panov, M. S.; Mereshchenko, A.; Tarnovsky, A. N.; Lorek, R.; Perera, D.; Diederich, G.; Lambright, S.; Moroz, P.; Zamkov, M. *ACS Nano* **2012**, *6*, 8156.

(49) Song, N.; Zhu, H.; Jin, S.; Zhan, W.; Lian, T. *ACS Nano* **2010**, *5*, 613.

(50) Tvrdy, K.; Frantsuzov, P. A.; Kamat, P. V. *Proc. Natl. Acad. Sci.* **2011**, *108*, 29.

(51) Hässelbarth, A.; Eychmüller, A.; Weller, H. *Chem. Phys. Lett.* **1993**, *203*, 271.

(52) Mooney, J.; Krause, M. M.; Saari, J. I.; Kambhampati, P. *J. Chem. Phys.* **2013**, *138*, 204705.

(53) Mooney, J.; Krause, M. M.; Saari, J. I.; Kambhampati, P. *Phys. Rev. B* **2013**, *87*, 081201.

(54) Marcus, R.; Sutin, N. *Biochim. Biophys. Acta* **1985**, *811*, 265.

(55) Bao, N.; Shen, L.; Takata, T.; Domen, K. *Chem. Mat.* **2007**, *20*, 110.

(56) Liu, M.; Jing, D.; Zhou, Z.; Guo, L. *Nat Commun* **2013**, *4*, DOI: 10.1038/ncomms3278

(57) Huang, L.; Wang, X.; Yang, J.; Liu, G.; Han, J.; Li, C. *J. Phys. Chem. C* **2013**, *117*, 11584.

(58) Yan, H.; Yang, J.; Ma, G.; Wu, G.; Zong, X.; Lei, Z.; Shi, J.; Li, C. *Journal of Catalysis* **2009**, *266*, 165.

(59) Tachibana, Y.; Akiyama, H. Y.; Ohtsuka, Y.; Torimoto, T.; Kuwabata, S. *Chem. Lett.* **2007**, *36*, 88.

(60) Zhu, H.; Song, N.; Lian, T. *J. Am. Chem. Soc.* **2013**, *135*, 11461.

(61) Brown, K. A.; Dayal, S.; Ai, X.; Rumbles, G.; King, P. W. *J. Am. Chem. Soc.* **2010**, *132*, 9672.

(62) Zhang, J.; Wang, Y.; Jin, J.; Zhang, J.; Lin, Z.; Huang, F.; Yu, J. *ACS Appl. Mater. Interfaces* **2013**, *5*, 10317.

(63) Hadar, I.; Hitin, G. B.; Sitt, A.; Faust, A.; Banin, U. *J. Phys. Chem. Lett.* **2013**, 502.

(64) Sitt, A.; Sala, F. D.; Menagen, G.; Banin, U. *Nano Lett.* **2009**, *9*, 3470.

Appendix 1

Absorption spectrum of DIR-Pt

The absorption spectrum of DIR-Pt can be treated as the sum of DIR and Pt absorptions because the interaction between these two domains are not strong enough to perturb their individual electronic transitions, as shown in Figure A.5.1. Slight deviations of the fitting can be a result of dielectric changes upon mutual contact of DIR and Pt domains. The fitting also shows that at 400 nm the DIR contributes 39% of total optical density (OD) of DIR-Pt. This number will be used as the scaling factor for number of absorbed photons in DIR-Pt in order to compare with free DIR.

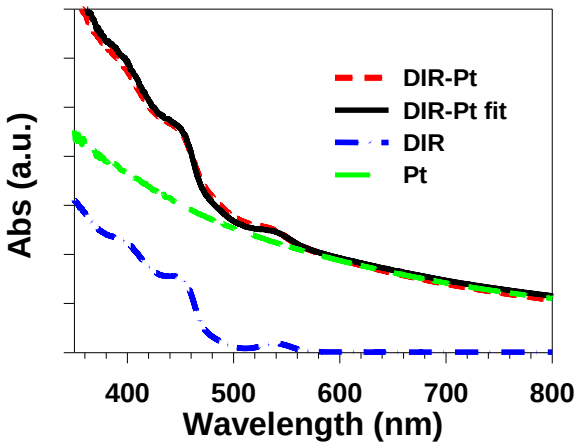

Figure A.5.1. UV-vis absorption spectrum of DIR-Pt (red dashed line) and its fit (black solid line) using sum of DIR (blue line) and Pt (green line) absorptions.

Appendix 2

Estimation of energy transfer rate between CdSe core in DIR and Pt tip

We use Forster resonant energy transfer (FRET) model to estimate energy transfer from DIR to Pt tip. Because energy transfer from the rod part to tip has been proved to be negligible compared with electron transfer, here we only need to treat FRET between CdSe core and Pt. This can be done in a standard way. The Forster radius is defined as the distance between donor and acceptor at which the fluorescence quenching efficiency is 50% and it can be calculated according to the following equation:

$$R = 0.211[\kappa^2 \Phi_D J(\lambda)/n^4]^{1/6} \qquad \text{(A.5.1)},$$

in which κ^2 is dipole orientation factor, Φ_D is emission quantum yield of donor, $J(\lambda)$ is the overlap integral between donor (DIR) emission and acceptor (Pt) absorption spectra, and n is the refractive index of dielectric medium. The overlap integral can be calculated using:

$$J(\lambda) = \frac{\int d\lambda I_D(\lambda)\varepsilon_A(\lambda)(\lambda)^4}{\int d\lambda I_D(\lambda)} \qquad \text{(A.5.2)},$$

where $I_D(\lambda)$ and $\varepsilon_A(\lambda)$ are donor emission spectrum and acceptor molar absorptivity, respectively.

$J(\lambda)$ between CdSe core and Pt is calculated to be ~1.05×10^{17} $M^{-1}cm^{-1}nm^4$. Previous studies on CdSe/CdS DIR have shown partially-polarized emission due to

electron delocalization from the core into the rod.[28,33,63] Therefore, the orientation factor κ^2 lies between 2/3 and 4/3, with the former corresponding to randomly distributed dipole orientation in CdSe core and the latter corresponding to linearly-polarized dipole along the NR. Here, we only consider the upper limit for the Forster radius, i.e. $\kappa^2 = 4/3$. The emission quantum yield of the CdSe core is measured to be 48.7%.[30] Using these values, the Forster radius R is calculated to be ~10.3 nm.

With the Foster radius, the energy transfer time constant can be calculated as:

$$\tau_{EnT} = \tau_0 (\frac{r}{R})^6 \qquad \text{(A.5.3)},$$

where τ_0 is the donor excited state lifetime in the absence of the acceptor and r is the donor-acceptor distance. The lifetime of CdSe core was previously measured to be ~13.0 ns.[30] The donor-acceptor distance is estimated to be ~12.4 nm, assuming that the CdSe core is located at the 1/4 length of DIR and the Pt particles are the end far from CdSe core. [26,64] Therefore, using Eq. S3, the energy transfer time constant can be calculated to be ~38.7 ns. Note that this value is overestimated because we are assuming the all the Pt absorption in the sampel is due to Pt tip on DIR, which is not the case, considering that there are a considerable portion of free Pt particles in the solution. Nonetheless, even this upper limit value is too slow to compete with the electron transfer rate measured in the main text. Therefore, we can conclude that the

quenching mechanism in these DIR-Pt heterostructures is almost exclusively electron transfer.

Appendix 3

TA spectra of free DIRs under 540 nm and 400 nm excitations

TA spectra of free DIRs at indicated delay times after 540 nm and 400 nm excitations are shown in Figure A.52.a and A.5.2.b, respectively. The state-filling signals are long-lived. We have previously determined the lifetimes for the excitons contributing to these signals.[30]

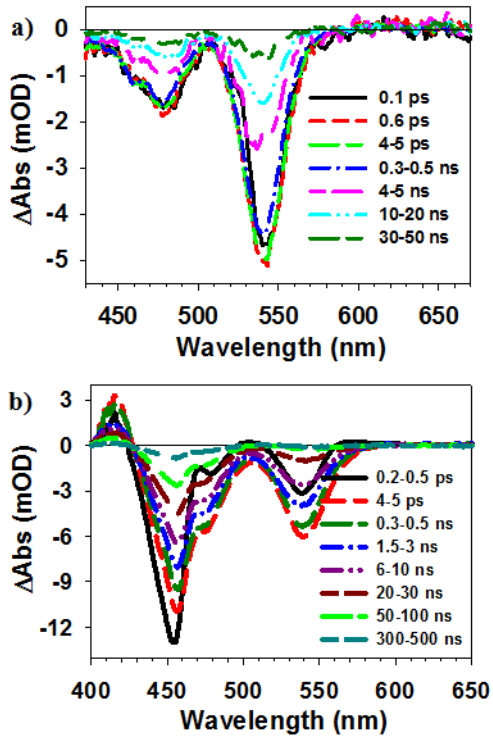

Figure A.5.2. TA spectra of free DIRs at indicated delay times after a) 540 nm and b) 400 nm excitations.

Appendix 4

Charge separation and recombination kinetics in DIR-Pt after 540 nm excitation

The TA spectra in Figure 2a were fit to the linear combinations of X3 and CS signals according to equation S4.

$$\Delta A(t) = m(t) \cdot S(X3) + n(t) \cdot S(CS)$$

(A.5.4),

$S(X3)$ and $S(CS)$ are TA spectra of X3 and CS signals, respectively, and $m(t)$ and $n(t)$ are their time-dependent coefficients. $S(X3)$ is taken from the TA spectrum of DIR-Pt at 1 ps, when all population is in the X3 exciton state, prior to dissociation. $S(CS) = S(30-50ns) * C$ where $S(30-50ns)$ is the average TA spectrum at 30 to 50 ns. The scaling factor C accounts for the fact that although at this delay time, the TA spectra contain only the CS3 state, their amplitudes are no longer 100% due to charge recombination. The scaling factor C(=1.56) as well as m(t) and n(t) were obtained by fitting TA spectra at different time delays. Fitted TA spectra at selective times between 0.4 ps and 30 ns are displayed in Figure A.5.3.

The time-dependent coefficients for X3 and CS are shown in Figure 2c and they are fitted with multiple exponential decay functions:

$$m(t) = \sum_{i=1}^{3} a_i e^{-t/\tau_i} \quad \text{(A.5.5)},$$

and $$n(t) = \sum_{i=1}^{3} a_i e^{-t/\tau_i} - m(t) \quad \text{(A.5.6)},$$

in which a_i and τ_i are the amplitude and time constant for i^{th} component of the multiexponential decay function. The second term of Eq. S6 indicates that the growth of n(t) is complementary to the decay of m(t). The fitting parameters are listed in Table S1. The amplitude-weighted average lifetime (τ_{ave}) is calculated as: $\tau_{ave} = \sum_i a_i \tau_i$ and the half life time ($\tau_{1/2}$) is the time when 50% of initial signal decays.

Table A.5.1. Fitting Parameters for Charge Separation and Recombination Kinetics of DIR-Pt under 540 nm Excitation

	τ_1/ps (a_1)	τ_2/ps (a_2)	τ_3 /ps (a_3)	τ_{ave} /ps	$\tau_{1/2}$ /ps
m(t)	5.67 ±0.52 (31.7 ±1.5%)	72.4 ±5.7 (40.8 ±1.5%)	1950 ±140 (27.4 ±0.85%)	566 ±58	43.5 ±4.7
	τ_1/ns (a_1)	τ_2/ns (a_2)	τ_3 /ns (a_3)	τ_{ave} /ns	$\tau_{1/2}$ /ns
n(t)	14.9 ±1.4 (33.7 ±3.0%)	442 ±18 (41.1 ±0.59%)	>>1000 (25.2 ±0.41%)	NA	211 ±38

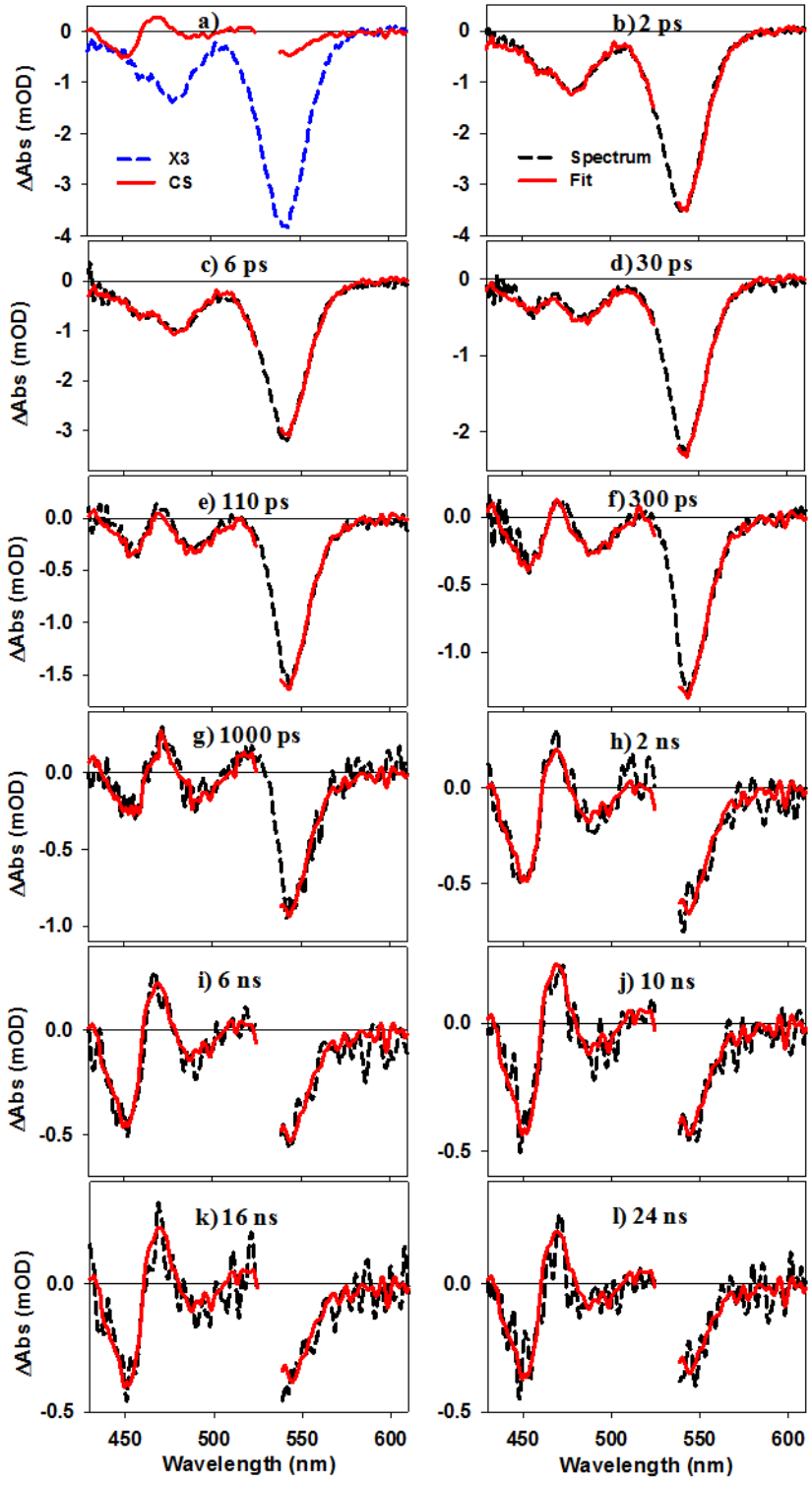

Figure A.5.3. a) TA spectra of X3 (black dashed line) and charge separated states (CS, red solid line), b-l) TA spectra (black dashed line) and their fits (red solid line) of DIR-Pt at indicated delay times after 540 nm excitation.

Appendix 5

Charge separation and recombination kinetics in DIR-Pt after 400 nm excitation

At 400 nm excitation, electron transfer from the CdS rod to Pt contains a fast component that can compete with the exciton localization within the NR. We can assume that this fast component is a single exponential process, the time constant of which (τ_{et}) can be derived in two ways. In the first way, it can be determined from the signal sizes of B2 and B3 in Figure 5.3b. We have previously determined that ~53% of total excitons are localized to the core/bulb region (X2 and X3) with a time constant of ~0.42 ps (τ_1) and the rest are localized on the rod (X1).[30] Assuming that these are parallel pathways, we can determined a time constant for the latter process of ~ 0.48 ps (τ_2). In DIR-Pt, the signal amplitudes of B2 and B3 in DIR-Pt are only ~67% those of free DIRs, indicating 36% of total excitons partition into X2 and X3. From this, the time constant of electron transfer to Pt can be calculated by:

$$\frac{1/\tau_1}{1/\tau_1+1/\tau_2+1/\tau_{et}} = 0.36$$

(A.5.7),

which gives τ_{et} of 0.47 ps.

Alternatively, τ_{et} can be obtained by fitting the kinetics of B1 (Figure 5.5b) within the first 2 ps to equation A.5.8

$$\Delta B1(t) = A \cdot [a \cdot e^{-t/\tau_0} + (1-a) - e^{-t/\tau_f}]$$

(A.5.8),

Here we have assumed a fast decay (τ_0) component of the free exciton and a slow electron transfer components of X1 exciton on the >> 2ps time scale. τ_f (0.066 ps) is the formation time constant for B1 that we have previously determined. The best of the data (shown in Figure 5.3.b) gives $\tau_0 = 0.215 \pm 0.014\, ps$ and $a = 69.5 \pm$ 3.2%. Because $\tau_0 = \frac{1}{\frac{1}{\tau_1}+\frac{1}{\tau_{et}}}$, τ_{et} can be calculated to be 0.44 ps, which agrees well with the time constant estimated above from the B2 and B3 amplitude.

Due to this fast electron transfer process, the initial amplitudes of X2 and X3, 5% and 31%, respectively, are smaller than free CdSe/CdS NRs. The fast electron transfer component comes from the dissociation of excitons before they are localized to form X1, X3 and X3. Because the free exciton spectra on the CdS rod has the same TA spectral signature as X1, we group it into X1 for simplicity. Therefore, the percentage of X1 is 64%.

The TA spectra between 2 ps and 30 ns are fitted according to equation A.5.9.

$$\Delta A(t) = m_1(t) \cdot S(X1) + n_1(t) \cdot S(CS1) + m_2(t) \cdot S(X2) + n_2(t) \cdot S(CS2) + m_3(t) \cdot S(X3) + n_3(t) \cdot S(CS3)$$

(A.5.9)

Here $(S(X1),\ m_i(t))$ and $(S(CSi),\ n_i(t))$ are the TA spectra and time-dependent coefficients for Xi and CSi, respectively. Although S(X1), S(X2), and S(X3) have been determined in previous study of free CdSe/CdS NRs, their amplitudes need to be rescaled to account for the changes in the branching ratios in CdSe/CdS-Pt due to the presence of fast electron transfer process. Specifically, branching ratios of X1, X2 and X3 are 46%, 7%, and 47%, respectively, in free CdSe/CdS and are 64%, 5%, and 31%, respectively, in CdSe/CdS-Pt. Therefore, S(X1), S(X2), and S(X3) in DIR-Pt were obtained by multiply those in free CdSe/CdS NRs by a scaling factor of 1.39, 0.70, and 0.70, respectively.

S(CS) were determined from the average TA spectra at 30-50 ns measured by 540 nm and 400 nm excitations (Figure A.5.4a). At this decay time, the TA spectra are dominated by charge separated states. As shown in Figure A.5.4b, 400 nm excitation generates a mixture of CS1, CS2, and CS3; while 540 nm excitation only generates CS3. Because CS spectra mainly depend on spatial distribution of the hole and both CS2 and CS3 have holes localized in the bulb region, we assume that the TA spectra and lifetime of CS2 and CS3 are the same. With these assumptions, the contributions of CS2 and CS3 to the total CS spectra measured at 400 nm excitation

can be subtracted to obtain CS1 spectrum. As shown in Figure A.5.4a, the CS1 TA spectrum contains a large contribution at B1 and smaller signal near B3, consistent with CdS rod localized hole (Figure A.5.4b). S(CS1), S(CS2) and S(CS3) can be obtained by scaling these average TA spectra by factors C1, C2, and C2, respectively, to account for the extent of charge recombination at 30 to 50 ns.

$m_3(t)$,$n_{3i}(t)$ and C3 are directly taken from the fitting result of A.5.4 and the same parameters are used for $m_2(t)$, $n_{2i}(t)$, and C2. The fitted spectra at selected times are shown in Figure A.5.5. The time-dependent coefficients for Xi and CSi are shown in Figure 3c. The kinetics for X2 and X3 are fitted with multi-exponentials. The kinetics for X1 is fitted with a power law: $m_1(t) = A \cdot t^{-\alpha}$.

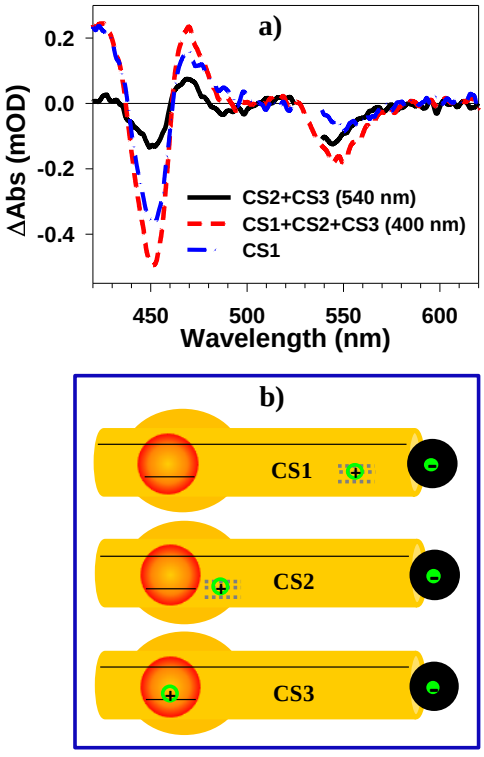

Figure A.5.4. a) Charge separated spectra obtained by 540 nm (black solid line) and 400 nm (red dashed line) excitations and derived CS1 spectrum (blue dash-dotted line). b) Scheme showing the spatial distribution of charges in charge separated states CS1, CS2, and CS3.

Table A.5.2. Fitting Parameters for Charge Separation and Recombination Kinetics of DIR-Pt under 400 nm Excitation

	τ_1/ps (a_1)	τ_2/ps (a_2)	τ_3 /ps (a_3)	τ_4 /ps (a_4)	$\tau_{1/2}$ /ps
m_1(t)	power law $(t^{-\alpha})$ with α=0.443±0.004				1.7±0.22
m_2(t)	5.59±0.40 (38.7±1.2%)	89.6±5.2 (42.3±1.1%)	1300±104 (19.0±0.92%)	NA	30.1±3.5
m_3(t)	5.67±0.52 (31.7±1.5%)	72.4±5.7 (40.8±1.5%)	1950±140 (27.4±0.85%)	NA	43.5±4.7
	τ_1/ns (a_1)	τ_2/ns (a_2)	τ_3 /ns (a_3)	τ_4 /ns (a_4)	$\tau_{1/2}$ /ns
n_1(t)	4.79±1.5 (23.6±3.1%)	39.5±5.7 (25.1±2.5%)	628±49 (24.9±0.74%)	>>1000 (26.3±0.47%)	102±29
$n_{2,3}$(t)	14.9±1.4	442±18	>>1000	NA	211±38

	(33.7 ±3.0%)	(41.1 ±0.59%)	(25.2 ±0.41%)		

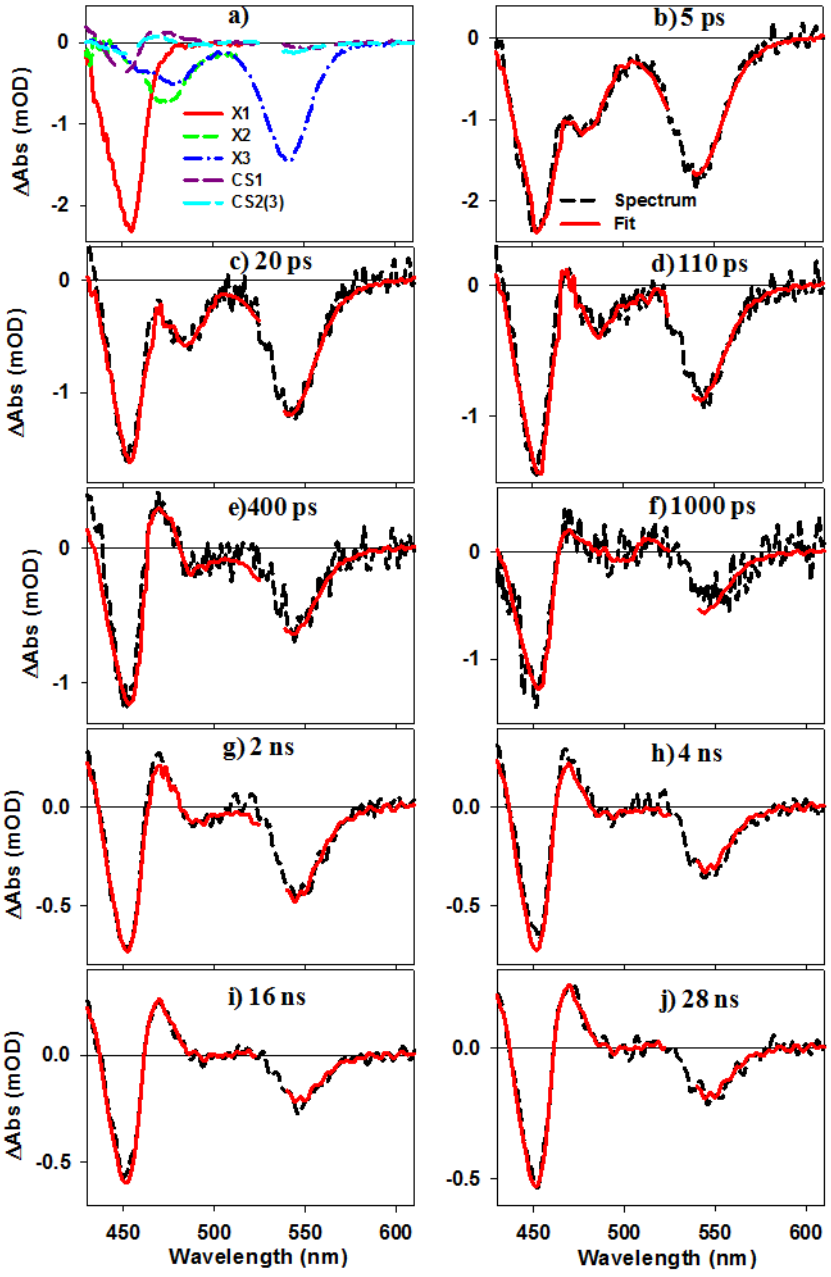

Figure A.5.5. a) TA spectra of exciton signals (X1, X2, and X3) and charge separated states signals (CS1, CS2,CS3), b-j) TA spectra of DIR-Pt (black dashed line) at indicated delay times after 400 nm excitation and their fits(red solid line).

Chapter 6. Plasmon-Induced Hot Electron Transfer from the Au Tip to CdS Rod in CdS-Au Nanoheterostructures

6.1. Introduction

Surface Plasmon Resonance (SPR), the collective oscillation of conduction band electrons, in metal nanostructures has long been a subject of intense research interests.[1-6] The SPR bands are tunable from UV to near-IR, depending sensitively on the nanostructure (materials, size and shape) and the dielectric properties of the surrounding environment, and have been widely explored for biological imaging and sensing applications.[4] In more recent years, plasmonic nanostructures have also been used to enhance the efficiency of semiconductors and/or molecular chromophore based solar energy conversion devices.[7-13] The enhancement effects in these nanostructures can generally be attributed to the following three extensively examined weak plasmon-exciton interaction mechanisms:[14] increase light absorption by

chromophore through the enhanced local field near metal nanostructures,[15-17] increase effective light path length of the absorber by the strong scattering cross sections of metal nanostructures,[16] and energy transfer from metal nanostructures to semiconductors.[18,19] In addition, strong interaction between the plasmon and exciton in plexcitonic materials has also received intense current interest.[20-22]

In the last few years, it has been shown that excitation of plasmons in metal nanostructures can lead to the injection of hot electrons into semiconductors.[23,24] This novel plasmon-exciton interaction mechanism suggests that plasmonic nanostructures can potentially function as a new class of widely tunable and robust light harvesting materials for photo-detection or solar energy conversion.[23-30] However, plasmon-induced hot electron injections from metal to semiconductor are still inefficient because hot electrons can quickly relax to lower energy levels via ultrafast electron-electron and electron-phonon scattering, [31-33] losing the energy needed to overcome the electron transfer barrier between metal and semiconductor. Because the electron-electron scattering process takes place on the several to hundreds of femtoseconds time scale,[33] electron transfer on this or faster time scales is required for the efficient utilization of plasmons. This requirement is difficult to meet in many semiconductor-metal hybrid materials in which these two domains are connected by molecular linkers[34] or insulating layers.[35,36] In this context, recently-developed colloidal semiconductor-metal nanoheterostructures, in which the metal and

semiconductor domains are connected directly by epitaxial growth, should constitute an ideal system for exploring the plasmon-induced hot electron injection phenomenon.[37-39]

In this chapter, we choose colloidal CdS nanorods (NR) with a Au nanoparticle at one end (CdS-Au) as a model system to demonstrate that the optical excitation of either the Au tip and CdS NR can lead to charge separation across the semiconductor-metal interface, as shown in Figure 6.1. CdS NRs are chosen for this study because it has well-defined excitonic transitions that are well-separated from the SPR band of Au, allowing selective excitation of the metal or semiconductor domains.[40-44] Using transient absorption spectroscopy in the visible and infrared spectral regions, we show that the photo-generated exciton in the CdS NR can dissociate by electron transfer to the Au tip; the excited plasmon in the Au tip can decay into hot electron-hole pair, followed by the injection of a hot electron into the CdS NR.

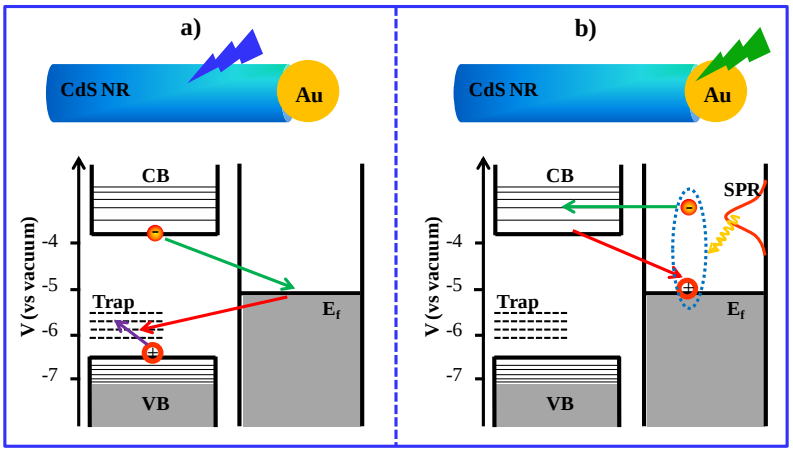

Figure 6.1. Photoinduced charge separation in CdS-Au nanoheterostructures. a) Charge separation induced by exciting the excitonic transitions in the CdS NR domain. Also shown are relevant levels in the CdS NR (conduction band (CB), valence band (VB) and hole-trap) and the Au tip (Fermi level (E_f)). The green and red arrows indicate the charge separation and recombination processes, respectively; and the purple one indicates the hole trapping process. b) Charge separation induced by plasmonic excitation in the Au tip. An excited surface plasmon in the Au tip (SP, red peak) can decay non-radiatively (yellow arrow) into a hot intraband electron-hole pair (blue dashed line), which can lead to hot electron injection into the CB of the CdS NR (green arrow) and charge recombination with the Au tip (red arrow).

6.2. Results and Discussion

6.2.1. Static absorption and emission spectra of CdS-Au

CdS NRs with an Au nanoparticle at one end (CdS-Au) were synthesized following a photo-deposition method.[37,39] We note that the absorption properties of CdS-Au depend sensitively on the preparation methods.[37,45] Thermal reduction of gold chloride under high temperature produces samples with suppressed exciton and SPR transitions;[42] photo-reduction, in contrast, yields CdS-Au with well defined exciton and SPR bands.[40,44] The details for CdS and CdS-Au NR synthesis are provided in Chapter 2. All samples were dispersed in chloroform for optical characterizations. Figure 6.2.a. and 6.2.b. show the transmission electron microscopy (TEM) images of CdS NRs before and after Au deposition. The average length and diameter (±standard deviation) of CdS NRs are 26.7(±1.7) nm and 3.6(±0.3) nm, respectively. The rod length and radius are longer and smaller, respectively, than the bulk exciton radius (2.8 nm[46]), leading to quantum confinement in the radial direction. The CdS dimensions in CdS and CdS-Au NRs are similar, indicating negligible NR etching during Au deposition and the average diameter of Au tips in CdS-Au NRs is 5.4 (±1.4) nm.

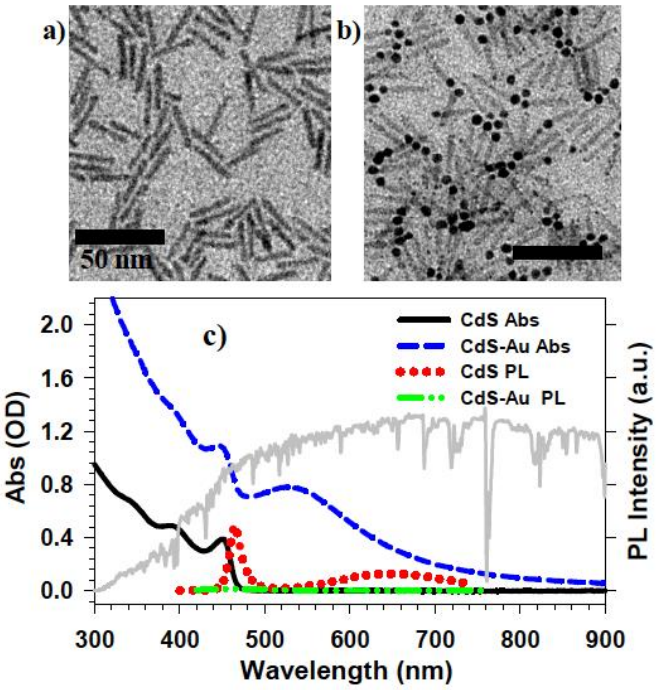

Figure 6.2. Transmission electron microscopy (TEM) image of a) CdS NRs and b) CdS-Au NRs. c) Absorption spectra of CdS NRs (black solid line) and CdS-Au NRs (blue dashed line), photoluminescence (PL) spectra of CdS NRs (red dotted line) and CdS-Au NRs (green dashed-dotted line). Also included is the AM 1.5 solar radiance spectrum (gray line).[47]

As shown in Figure 6.2.c, the absorption spectrum of CdS NRs show peaks at ~453, 401 and shorter wavelengths. The two lowest energy bands can be assigned to 1Σ ($1\sigma_e$-$1\sigma_h$) and 1Π ($1\pi_e$-$1\pi_h$) exciton transitions between discrete conduction band (CB) and valence band (VB) levels that result from quantum confinement in the radial direction.[48] The absorption spectrum of CdS-Au NRs (with the same concentration as

CdS NRs) shows CdS NR exciton bands as well as a broad feature centered at ~533 nm and enhanced absorption in the near UV region. The latter two spectral features in CdS-Au can be attributed to the Au tip. For Au nanoparticles of this small size (5.4 nm), their extinction spectrum is dominated by absorption instead of scattering,[33,49,50] consisting of a surface plasmon resonance (SPR) band centered at 533 nm (2.37 eV) and a less well resolved interband absorption feature from ~506 nm (2.45 eV) to the near UV region.[51-53] As shown in Figure A.6.1, comparing to a physical mixture of isolated Au nanoparticles of similar size and CdS NRs (prior to the growth Au tips), the 1Π and higher energy exciton bands are broadened and Au plasmon bands are broadened and red-shifted in CdS-Au NRs , indicating strong electronic interactions between the CdS and Au domains.[54] The peak shift and broadening are confirmed by fitting the absorption spectrum of CdS-Au to the sum of the contributions of the CdS exciton bands, Au SPR band and Au interband transition. The details of the fit are described in the Appendix 1 and the fitting parameters are listed in Table A.6.1 and A.6.2. The fit also reveals an enhanced absorption cross section that increases at shorter wavelengths, compared to isolated Au and CdS components. Although the exact origin of the enhanced transitions is unclear, it cannot be attributed to the enhanced CdS absorption by the Au plasmon band, which should show the largest enhancement factor at the peak of SPR band.

It is interesting to note that the absorption cross section of the Au tip (with a volume of ~82 nm^3) is stronger than that of the CdS NR (with a volume of ~280 nm^3) due to the large oscillation strength of the SPR band. Combining the absorptions of both metallic and semiconducting domains, the CdS-Au NRs are photo-active in a very broad solar spectrum window. In fact, the solar photon absorption rate, obtained by integrating the overlapping area between the CdS-Au absorption and solar irradiation spectrum, is ~6 times larger than CdS NR alone. Figure 6.2c also shows the photoluminescence (PL) spectra of the CdS NR and CdS-Au. The PL of CdS NRs is comprised of band edge and trap state emissions.[43,55,56] Both emissions are quenched in CdS-Au, similar to the emission quenching observed in CdS-Pt NRs and providing another evidence for strong CdS and Au interactions.[43]

6.2.2. Electron transfer from excited CdS NRs to Au tips

We next investigate the mechanisms of exciton and plasmon interaction in the CdS-Au heterostructure by following the dynamics of excited states in either the semiconductor or metal domains by pump-probe transient absorption (TA) spectroscopy. The set-ups of femtosecond and nanosecond visible TA, and femtosecond mid-IR TA are described in the SI. In these TA experiments, physical

mixtures of CdS NRs (prior to the growth of the Au tip) and isolated Au NPs (7 nm in diameter) are used as controls to compare with dynamics observed in CdS-Au. CdS NRs in the control samples have the same NR concentration as in CdS-Au samples. The concentrations of Au NPs were adjusted such that the optical density of the control sample is the same as the CdS-Au sample at the excitation wavelength. Under these conditions the control and the CdS-Au samples absorb the same number of excitation photons. The control samples for TA studies at 400 nm and 590 nm excitation are labeled as *control 1* and *control 2*, respectively.

The total OD (1.30) of CdS-Au at 400 nm consists of contributions of the Au SPR band (0.09), Au inter-band (0.75) and CdS NR 1Π exciton band (0.46). Therefore, 400 nm pump can excite the 1Π exciton band of CdS NRs as well as the d to sp interband transition and SPR of the Au tip. Figure 6.3 shows the TA spectra of CdS-Au NRs at 200 fs to 3000 ns after 400 nm excitation. TA spectra consist of changes in both the CdS NR and Au SPR bands at early delay times (< 4ps); at longer delay times, the latter decays almost completely and only the CdS NR TA features remain. TA spectra of *Control 1* show similar features of CdS NR and Au SPR bands. These TA features of Au nanoparticles have been extensively examined in the literature and are well understood.[33,57-61] Optical excitation of the interband transition and SPR band of Au nanoparticles leads to the generation of hot electrons, giving rise to a bleach at center and absorption features at the high and low

frequency sides of the SPR band. This TA feature decay quickly due to the electron-phonon interaction.[33,57-61] Fitting the SPR bleach center in Figure 6.4a reveals an electron-phonon scattering time of 1.23±0.12 ps (Table S3) which is nearly the same as in isolated Au NPs in *control 1*.

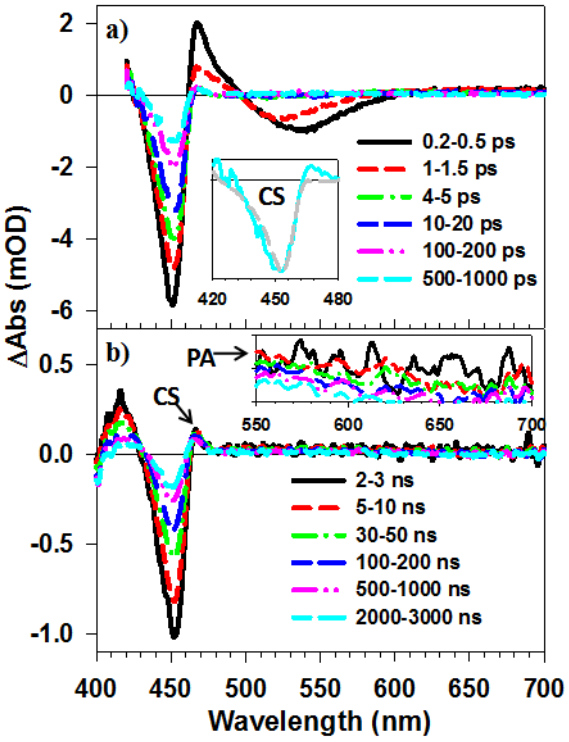

Figure 6.3. TA spectra of CdS-Au NRs at indicated delay time windows after 400 nm excitation: (a) 0.2 ps to 1000 ps and (b) 2 ns to 3000 ns. Inset in (a): a comparison of TA spectra at 1000 ps after 400 nm excitation for CdS (gray dashed line) and CdS-Au (cyan solid line) NRs, showing the presence of charge separated state (CS) absorption feature at 460 nm in the latter. Inset in the (b): an expanded view of the broad photoinduced absorption (PA) signal between 550-700 nm.

The TA spectra of CdS-Au at early delay time shows a pronounced bleach of the 1Σ exciton band at ~450 nm, which has been assigned to the filling of $1\sigma_e$ electron level in the CdS NR.[43] Similar 1Σ exciton bleach can also be seen in free CdS NRs and *control 1*. Fitting of these bleach recovery kinetics shows an average lifetime of $1\sigma_e$ electron of 38.0±1.3 ns in CdS NRs. As can be seen in Figure 6.3a and Figure 6.4a, The 1Σ exciton bleach recovery in CdS-Au NRs is much faster than CdS NRs, indicating shorter-lived $1\sigma_e$ electrons. The shortened $1\sigma_e$ electron lifetime in CdS-Au can be caused by electron or energy transfer from CdS to Au. As we have established previously in CdS-Pt, the key to distinguishing these exciton decay pathways is through the identification of both electron and hole signals.[43] Energy transfer leads to the decay of both electron and hole signals, while only the electron signal is affected in the electron transfer pathway.

The evolution of the CdS spectral features in CdS-Au NRs resembles that of CdS-Pt.[43] As shown in Figure 6.3a, 1Σ exciton bleach recovery leads to the formation of derivative like-features of 1Σ exciton band (labeled as CS) that can be attributed to Stark effect spectrum caused by the electric field of the charge separated state. In addition, there is also a broad photoinduced absorption (PA) from 550 to 700 nm that has been assigned to the absorption of holes in CdS NRs. This signal can be more readily seen in free CdS NRs and in CdS-Au at t> 5ps (Figure 6.3b inset).The average

hole PA kinetics (from 550 to 650 nm) of CdS and CdS-Au NRs are compared in Figure 6.4b, in which the signals have been scaled to correspond to the same number of absorbed photons by the CdS rod. To do this, CdS-Au and CdS NR samples were kept to the same OD (1.30) at 400 nm and the TA signal for free CdS NRs is scaled by 0.352, which is the percentage of CdS contribution to the total OD of CdS-Au, and corresponds to the fraction of the total absorbed photons by the CdS rod. A derivation of this scaling procedure is provided in the SI. For CdS NRs, the hole PA signal shows a formation time of 0.750 ± 0.045 ps and negligible decay within 1000 ps (Table S3). The same PA signal amplitude and kinetics are observed in CdS-Au, although the formation kinetics is obscured by the Au SPR TA signals in $t < 4$ps. This agreement suggests that in CdS-Au, there is negligible decay of holes in the CdS region and exciton quenching is caused by electron transfer from the excited CdS NR to Au tip. A similar ultrafast exciton quenching by electron transfer has been observed CdS-Pt NRs.[43]

It is interesting to point out that despite significant spectral overlap between CdS NR emission and Au absorption, negligible energy transfer quenching is observed. We have estimated the energy transfer rates from the CdS rod to Au tip as described in the SI. For band edge excitons, the upper limit of energy transfer rate is 4.1 ps, which is considerably slower than the hole trapping time and accounts for efficient trapping of excitons (with electrons bound to trapped holes).[62] The energy transfer

rate from the trapped exciton to Au is estimated to be 133 ns, which is significantly slower than energy transfer rate from the band edge excitons due to its much slower radiative decay rate, and is slower than the observed electron transfer rate.

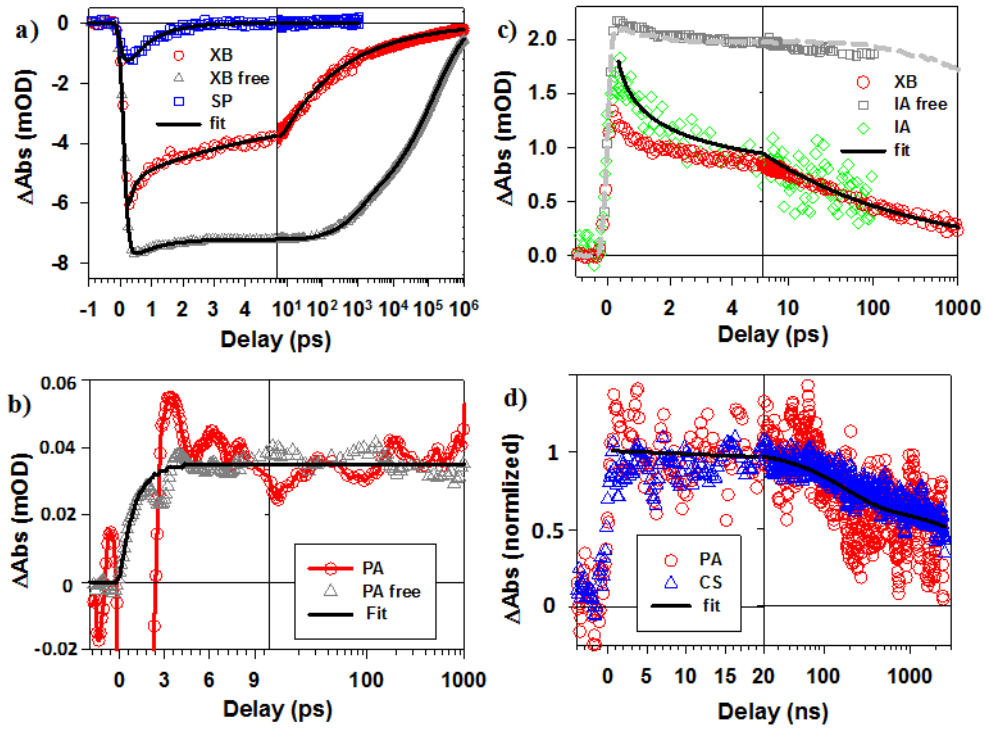

Figure 6.4. TA kinetics of CdS-Au after 400 nm excitation. a) 1Σ exciton bleach (XB) recovery kinetics of CdS-Au NRs (red circles) and free CdS NRs (gray triangles). The latter has been scaled to correspond to the same number of absorbed photons by the CdS domain in CdS-Au (see the main text for details). Also shown for comparison is the kinetics at the center of SPR bleach of the Au tip (blue squares). The black solid lines are fits to these kinetics to models described in the SI. b) Kinetics of photoinduced absorption signal (PA) for CdS-Au NRs (red circles) and free CdS NRs

(gray triangles). The black solid line is a fit to the PA kinetics of free CdS NRs. c) Kinetics of intraband absorption (IA) probed at 3000 nm for free CdS NRs (gray squares) and CdS-Au NRs (green diamond). Also shown are the 1Σ XB kinetics of free CdS NRs (gray dashed line) and CdS-Au NRs (red circles), which have been scaled to match the amplitudes of the intraband signals at 5-100 ps. The black solid line is a fit to the IA kinetics. d) Charge recombination kinetics in CdS-Au NRs probed using both charge separated state (CS, blue triangles) and photoinduced absorption (PA, red circles) signals. The black solid line is a fit to these kinetics.

In principle, electron transfer rate can be determined by fitting the 1Σ exciton bleach recovery kinetics, which unfortunately, has significant spectral overlap with the Au SPR TA signal at early delay times. SPR of Au NPs differs significantly from that of CdS-Au, which hinders a reliable subtraction of the Au contribution to the total TA signal at 1Σ band. In this report, we show that $1\sigma_e$ electrons in CdS NRs can also be followed by their intraband absorption in the mid-IR. In this spectral region, spectral overlap between the CdS and Au TA features can be avoided because Au NPs of similar sizes have no TA features.[23,63] Although it has yet to be reported, the intraband transition from $1\sigma_e$ to $1\pi_e$ CB electron levels should be optically allowed, similar to the $1S_e$ to $1P_e$ transition in quantum dots.[64-66] According to the static absorption spectrum, the energy difference between the 1Σ and 1Π excitonic levels is

0.42 eV. Considering the much denser hole levels than electron levels for CdS,[67] this difference can mostly be attributed to the difference between the $1\sigma_e$ and $1\pi_e$ CB levels, which corresponds to an estimated intraband transition at 3047 nm. As shown in Figure 6.4c, 400 nm excitation of CdS NRs generates an intraband absorption (IA) signal at 3000 nm, which shows negligible decay in 100 ps, similar to the 1Σ exciton bleach kinetics. This assignment is further supported by the study of electron transfer from CdS NRs to adsorbed methylene blue (MB^+) molecules described in Appendix 4 (Figure A.6.4).

The 1σ electron intraband absorption kinetics (at 3000 nm) of CdS and CdS-Au NRs are compared in Figure 6.4c. After correcting for the number of absorbed photons, as described above, the IA signal amplitude and the formation and decay kinetics for free CdS NRs and *control 1* (result not shown) are exactly the same. The signal in CdS-Au NRs shows a smaller initial amplitude (81%) and faster decay than CdS NRs. The smaller initial amplitude in CdS-Au indicates a smaller intraband absorption cross section and/or $1\sigma_e$ electron population. Based on the broadened 1Π transition in CdS-Au, it is possible that some of $1\pi_e$ electrons are transferred to the Au tip before they relax to $1\sigma_e$ level and the $1\sigma_e$ to $1\pi_e$ intraband transition cross section at 3000 nm is reduced, compared to CdS NR, due to a broadened $1\pi_e$ level. The decay of the IA signal reflects the electron transfer kinetics from the CdS to Au tip. Unfortunately, due to a limited length of delay stage used for this study, the IA

kinetics is limited to 100 ps, before the completion of the decay process. However, a comparison of the $1\sigma_e$ electron intraband transition with the 1Σ exciton bleach recovery kinetics in Figure 3c shows that they agree well with each other between 5 and 100 ps, suggesting that electron transfer kinetics at longer delay times can be monitored via the 1Σ exciton bleach signal. The discrepancy at < 5ps is caused by the contribution of Au SPR signal to the 1Σ exciton bleach. Therefore, the kinetics of $1\sigma_e$ electron measured by intraband absorption (<100ps) and interband bleach (5-1000 ps) can be connected to obtain the complete kinetics for $1\sigma_e$ electron decay, which is shown in Figure 6.4c. The connected kinetics follows a power law with a half-life of 4.85 (±0.46) ps. The power law kinetics indicates a very broad distribution of electron transfer rates, although the origin for which is yet to be understood in these NRs. Furthermore, as shown in Figure 6.4a, the 1Σ exciton bleach can be fit to the sum of $1\sigma_e$ electron power law decay and the contribution of the SPR band (see SI for details). The latter can be approximately described by the kinetics at the center of SPR band, even though the SPR TA signal in Au NPs is wavelength-dependent.[33] We note that a similar study on CdS-Au NRs has observed charge separation on sub-20 fs timescale [40] The reason for much slower charge separation in our system is not clear, but likely due to different dimensions (length and diameter) as well as capping ligands and dispersing solvent of CdS NRs (mercaptoundecanoic acid capped NRs in water in

their study). Moreover, the focus of our work is the plasmon-induced charge separation by Au domain excitation which will be discussed in the next session.

Charge separation between CdS and Au leads to the formation of charge separated state signal (CS), which has been attributed to the Stark effect induced exciton peak shifts by the electric field of the charge separated state.[43] This CS signal is not present in CdS NRs, which can be seen in the comparison of TA spectra of CdS and CdS-Au at 1000 ps in the inset of Figure 6.3a. Similar CS features has been reported and assigned in CdS NR-Pt and CdS NR-benzoquinone complexes, accompanying the charge separation processes in those systems.[43] As shown in Figure 6.3d lower panel, both CS and PA signals decay with the same kinetics due to charge recombination.[43] The half life of charge separated state is determined to be 1.5 (±0.6) μs. This long lifetime of the charge separated state can be attributed to hole trapping on CdS NR surfaces, consistent with previous result on CdS NR-Pt.[43]

6.2.3. Plasmon induced hot electron transfer from Au to CdS

The TA spectra of CdS-Au NRs at indicated delay times after 590 nm excitation are shown in Figure 6.5a. This excitation is below the onset of CdS and Au interband transitions. Therefore, the SPR band is selectively excited. The spectra are dominated by heating induced Au SPR spectral change as discussed above. Comparison of the

TA spectra of CdS-Au NRs and *control 2* (Figure 6.5a) under the same excitation conditions shows that the bleach of SPR signals in both samples are formed instantaneously (instrument response limited, Table S4) and decays rapidly. The formation time for the SPR TA signal is the electron-electron scattering (hot electron relaxation) time, which occurs from several to 100s of fs time scale depending on the excessive energy of the hot electron above the Fermi level, i.e. $\tau_r \propto \left(\frac{E_f}{E_i - E_f}\right)^2$ (E_i is the initial energy of the hot electron and E_f is the Fermi energy).[31,32,68] Under 590 nm excitation, the excited plasmon mostly transforms into an intraband hot electron-hole pair that has very large excessive energy and therefore fast relaxation. In contrast, 400 nm excitation creates interband electron-hole pairs that has small excessive energy and therefore a longer (0.137 ps) electron-electron scattering time. SPR kinetics at the bleach center after 590 nm excitation are fitted with two-exponential decay accounting for the electron-to-phonon and hot phonon relaxation processes.[33,59,60] From the fit, both CdS-Au and *control 2* have electron-phonon scattering time of 2.4 ps. In contrast, the hot phonon relaxation times are different in these materials: the former is 125 ps and the latter is 349 ps. The faster phonon relaxation time in CdS-Au may be attributed to higher thermal conductivity of CdS than the solvent.

The comparison between CdS-Au and *control 2* in Figure 6.5a also reveals a bleach of the 1Σ band at ~450 nm in the former that is absent in the latter. Comparison of the kinetics probed at 452 nm for CdS-Au and *control 2* in Figure 6.5b

also shows noticeable difference, consistent with the presence of a bleach of CdS 1Σ band in CdS-Au. The absence of this signal in *control 2* suggests that it cannot be attributed to direct excitation of CdS NR by two photon absorption.[69] Therefore, this bleach signal can only be attributed to plasmon induced hot electron transfer from the Au tip to CdS NR. We note that plasmon induced energy transfer from metal to semiconductor has been observed in Au/Cu_2O[18] and Ag/Cu_2O[19] core/shell structures, which is unlikely here because the energy of excited plasmon is much smaller than the absorption onset of CdS (~475 nm).

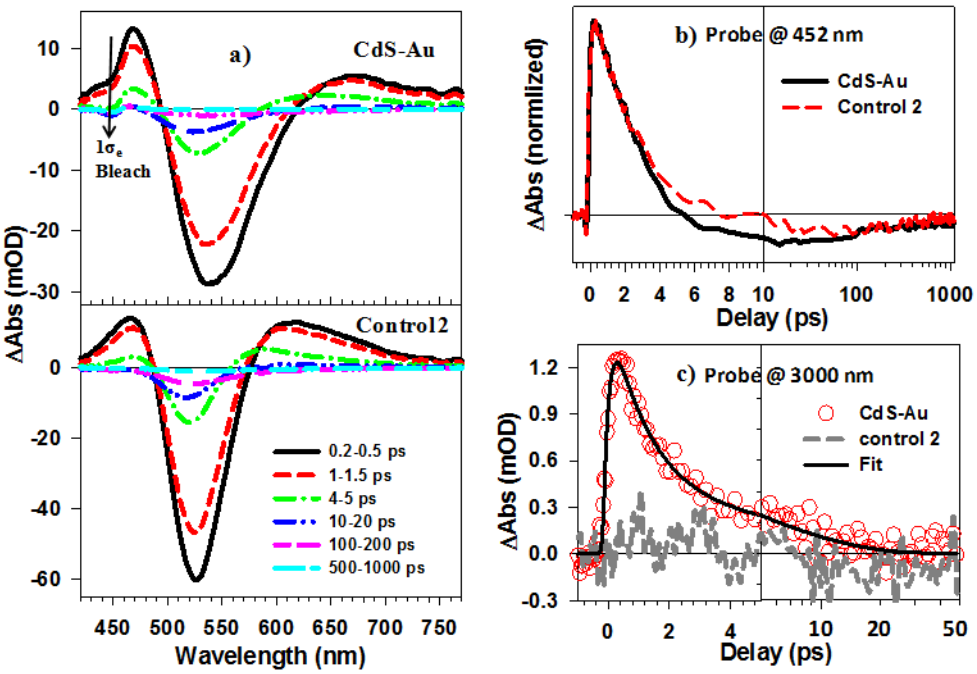

Figure 6.5. TA spectra and kinetics of CdS-Au NRs after 590 nm excitation. a) TA spectra of CdS-Au NRs (upper panel) and *control 2* (lower panel) at indicated delay time windows (from 0.2 to 1000ps). *Control 2* is a mixture of CdS NRs and Au NPs

in which the NR concentration and the sample absorbance at 590 nm are the same as the CdS-Au NR sample. b) Kinetics probed at 452 nm for CdS-Au NRs (black solid line) and *control 2* (red dashed line). c) Kinetics probed at 3000 nm for CdS-Au NRs (red circles) and *control 2* (gay dashed line). The black solid line is a fit to the kinetics of CdS-Au.

Further support for hot electron transfer can also be obtained by direct observation of 1σ electron intraband absorption at 3000 nm. Comparison of the TA kinetics at 3000 nm for both CdS-Au and *control 2* after 590 nm excitation are shown in Figure 6.5c. The intraband absorption is not observed in *control 2*, consistent with the lack of 1Σ bleach in the visible TA spectra. In CdS-Au NRs measured under the same conditions, the intraband signal can be clearly observed. It can be fit with a rise time of 0.097 ± 0.022 ps and a multi-exponential decay with a half-lifetime of 1.83 ± 0.22 ps (Table S4). The formation of this electron signal can be attributed to plasmon induced hot electron injection from the Au tip into the CdS NR. To our best knowledge, this is the first direct observation of plasmon induced hot electron transfer process in epitaxially-grown colloidal nanoheterostructures, although it has been proposed in gold-iron oxide heterostructures.[70,71] Note that the 97 fs formation time reflects the overall arrival time constant of electrons at the $1\sigma_e$ level, which includes multiple steps to be discussed later. The fast injection rate can be justified because

this process competes with ultrafast hot electron relaxation (electron-electron scattering) in Au.[31,32,68] The decay of the electron signal can be attributed to back electron transfer process from the CdS NR to Au, which can occur via the dense manifold of unfilled conduction band levels above the Fermi level of Au.

It is interesting to compare the recombination kinetics of injected hot electrons with forward electron transfer from excited CdS NR to Au because both processes involve transferring an electron from the CdS CB to the dense manifold of unfilled levels above the Fermi level of Au. As can be seen in Figure 6.6a, the former (1.83 ps half life) is faster than the latter (4.85 ps half life). More importantly, the kinetics of former can be well fitted by a two-exponential function, while the latter follows a power-law kinetics spanning 6 decades in time, indicating broadly distributed electron transfer rates. In the latter process, photogenerated excitons can localize randomly along the NR due to rapid hole trapping. The broad distributions of trapped exciton locations and possibly trap energy give rise to a broad distribution of electron transfer rates to the Au tip. Electron transfer from the Au tip to CdS NR generates an electron in the NR that is likely bound by the image charge of Au, which leads to relatively faster and more uniform recombination rates. This comparison is schematically shown in Figure 6.6b.

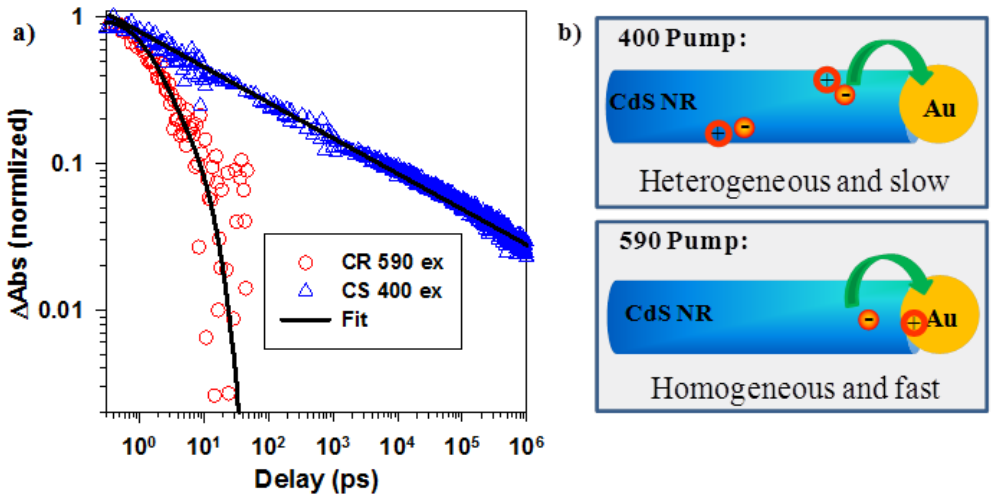

Figure 6.6. a) Comparison of 1σ electron kinetics for CdS-Au NRs after 400 nm (blue triangles) and 590 nm (red circles) excitation and their fits (black lines). b) Schematic illustration of the electron decay process: (upper panel) under 400 nm excitation of the CdS NR, excitons are randomly localized along NRs due to hole trapping, leading to a very broad distribution of electron transfer rates; (lower panel) under 590 nm excitation of the Au tip, the electron injected into CdS is attracted by the hole and image charge in Au, which gives rise to faster and less heterogeneous back electron transfer rates.

Next, we seek to quantify the quantum yield (QY) of plasmon induced hot electron transfer in CdS-Au NRs using the signal size of the intraband transition of $1\sigma_e$ electrons. In the small signal limit, where multi-exciton states are negligible, the absorbance change of $1\sigma_e$ electrons is proportional to the number of absorbed photons and the proportional factor is related to the absorption cross section and photon-to-$1\sigma_e$

electron conversion efficiency.[72] Because every absorbed 400 nm photon by free CdS NRs generates a $1\sigma_e$ electron, the QY is given by the ratio of the TA signal sizes under 590 nm($\Delta A_{(590\ nm)}$) and 400 nm ($\Delta A_{(400\ nm)}$) excitation after correcting for the numbers of absorbed photons at these wavelengths according to Eq. 1.

$$QY = \frac{\Delta A_{(590\ nm)}}{(1-10^{-OD_{(590\ nm)}})\cdot j_{(590\ nm)}} \Big/ \frac{\Delta A_{(400\ nm)}}{(1-10^{-OD_{(400\ nm)}})\cdot j_{(400\ nm)}}$$

(6.1).

Here $OD_{(590\ nm)}$ and $OD_{(400\ nm)}$ are optical densities of CdS-Au at 590 nm and free CdS NR at 400 nm, respectively; $j_{(590\ nm)}$ and $j_{(400\ nm)}$ are the photon fluxes of 590 nm and 400 nm pump beams, respectively. Realizing that the signal sizes in TA experiment is sensitive to pump/probe beam intensity attenuation along the sample path and overlap profile, we ensured the same sample ODs at the pump wavelength and similar pump beam sizes for 590 nm and 400 nm excitation(see SI for details). To improve the signal/noise ratio of the measurement, we carried out the measurement at 4 excitation pulse energies. As shown in Figure A.6.5, the TA signal amplitudes increase linearly with pump pulse energy, indicating that these experiments fall in the small signal limit. The average QY of hot electron injection is determined to be ~2.75($\pm$0.07)%. The details of the calculation can be found in Appendix 5. The low QY is a result of multiple competition energy dissipation pathways in the process of hot electron injection, which will be further discussed below.

All the elementary processes involved in plasmon-induced hot electron transfer are shown in Figure 6.7. An incident photon can be scattered by the NP or absorbed to either excite the interband transition or a plasmon. The excited plasmon has two main decay channels: radiative decay into a photon and nonradiative decay into an intraband or interband electron-hole pair. [73] The fluorescence quantum yield of metal NPs is extremely low (on the order of 10^{-10} to 10^{-5}),[74-76] indicating that the radiative decay is not a competitive plasmon deactivation pathway. Nonradiative decay of a plasmon into an electron-hole pair has been observed.[77,78] Devices based on this effect, including photodetectors,[29,79] transistors,[80] and photoelectrochemical cells,[24,25,81,82] have been demonstrated. Interestingly, the reverse process, i.e. excitation of surface plasmon by the loss of hot electron energy, has also been observed.[83,84] Finally, the plasmon generated electron-hole pairs undergo two competing pathways: relaxation through electron-electron scattering and hot electron transfer into acceptors. Therefore, the absorbed photon to hot electron transfer quantum yield (QY), is the product of the efficiencies for all elementary steps, i.e. $\mathrm{QY} = \phi_{\mathrm{ph}\rightarrow\mathrm{pl}} \times \phi_{\mathrm{pl}\rightarrow\mathrm{e-h}} \times \phi_{\mathrm{inj}}$, where $\phi_{\mathrm{ph}\rightarrow\mathrm{pl}}$, $\phi_{\mathrm{pl}\rightarrow\mathrm{e-h}}$, and ϕ_{inj} are the efficiencies for absorbed photon to plasmon conversion, excited plasmon to intraband electron-hole pair conversion and hot electron transfer from the Au tip to the CdS NR, respectively. We have assumed that hot electron transfer to CdS NR is negligible for interband electron-hole pairs due to insufficient energy of the hot electron as described below.

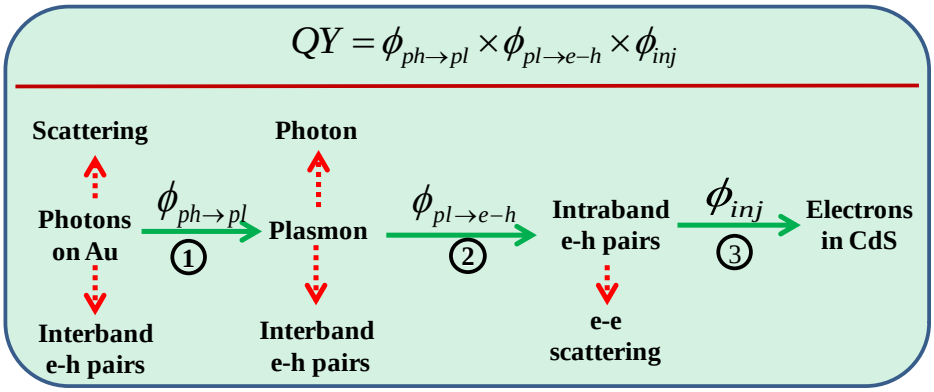

Figure 6.7. Mechanism for plasmon-induced hot electron injection process, showing all possible desirable (green arrows) and competing (red dashed arrows) elementary steps.

For selective excitation of the Au tip in CdS-Au NRs under 590 nm excitation, $\phi_{ph\rightarrow pl}$ is near-unity because scattering is negligible and the excitation is below the onset for interband absorption. $\phi_{pl\rightarrow e-h}$ is less than unity: although the radiative decay channel is negligible, the plasmon could decay into an interband electron-hole pair with a hot electron near the Fermi level and a hole in the d band of Au.[33] Because the $1\sigma_e$ level of CdS NR is about 1.1 eV above the Au Fermi level, the electron in the interband electron-hole pair has insufficient energy for injection into the CdS conduction band. On the other hand, the electron level in the intraband electron-hole pair is estimated to be at 2.10 eV above the Au Fermi level,[33] which enables the hot electron injection into the CdS NR, as indicated in Scheme 1b. ϕ_{inj} is the QY limiting step because the electron-electron scattering is a ultrafast process on the time

scale of several to 100s of fs.[33-35, 76] Because both hot electron transfer to CdS and electron-electron scattering have rate constants faster than our instument response, unambiguous determination of these two processes is not possible. We note that in addition to the aforementioned mechanism, it is also possible that the excited plasmon in the Au tip directly decays into a hot electron in the conduction band of CdS NRs through a charge-transfer type carrier scattering process.[85] The broader homogeneous linewidth in Au tips than in isolated Au NPs may indicate this possiblity.[23,86]

It is interesting to compare the hot electron injection yield and charge recombination time of this system with previous a report on Au sensitized TiO_2 nanoparticles.[23] In that work, the plasmon induced injection yield is measured to be as high as 40% and the recombination time can be as long as 100s of ps.[23] The high injection yield in Au sensitized TiO_2 is attributed to a fast electron injection rate resulted from a high density of accepting states in TiO_2.[23,87] The relatively slow recombination in Au sensitized TiO_2 can be attributed to electron diffusion inside TiO_2 nanoparticles[63] and possibly due to the formation of a Schottky barrier which expels electrons away from the semiconductor-metal interface where recombination happens.[25,29] Although the CdS-Au system shows a much lower injection yield and faster recombination, these quantum confined nanorods offer interesting opportunities for improvement because of the ability to tune their electronic properties by size and

shape.[88,89] For example, the injection yield in CdS-Au can likely be enhanced using CdS NRs with bigger diameters which lowers the band edge and increases the density of CB states.[90] Longer CdS-Au NRs may be able to slow down charge recombination by the formation of CdS-Au Schottky barrier. Furthermore, the diameter of the CdS NRs can be varied gradually along the rod axis to provide a gradient of confinement energy to drive the electron away from the interface. Alternatively, the size and shape of Au tip can be engineered to optimize the efficiency of plasmon decay into hot carriers, as predicted by recent theoretic investigations.[91]

6.3. Conclusion

In summary, we have examined the plasmon-exciton interaction mechanisms in colloidal CdS-Au NR heterostructures. compared to isolate CdS NRs and Au particles, the CdS-Au NRs show broadened exciton bands as well as broadened and red-shifted plasmon bands, indicative of strong interactions between the semiconductor and metallic domains. Excitation of either the CdS NR or Au tip can lead to charge separation across the CdS/Au interface. The exciton generated in the CdS NR (via 400 nm excitation) dissociates by electron transfer to the Au tip (with half life of 4.8 ps). Neither energy transfer or hole transfer is competitive exciton quenching pathway

because of an ultrafast hole trapping to the CdS surface (with time constant of 0.75 ps). The charge-separated state is long-lived, which decays to the CdS-Au NR ground state with a half-life of 1.5 μs. Excitation of the plasmon band in the Au tip leads to ultrafast electron injection into the CdS nanorod with a quantum yield of ~2.75%. This charge-separated state (with an electron in the CdS NR and hole in the Au tip) is relatively short-lived and recombines in 1.8 ps. To our best knowledge, this is the first demonstration of plasmon-induced hot electron transfer process in colloidal quantum confined semiconductor nanorod-metal nanoheterostructures. This finding offers a promising new approach to expand the photo-response range of current semiconductor-based devices, such as photo-detectors and solar energy conversion cells. Future work will be focused on improving both the hot electron injection yield and charge-separated state lifetime through engineering the size and shape of the colloidal structure.

References

(1) Hartland, G. V. *Chem. Rev.* **2011**, *111*, 3858.

(2) Giannini, V.; Fernández-Domínguez, A. I.; Heck, S. C.; Maier, S. A. *Chem. Rev.* **2011**, *111*, 3888.

(3) Eustis, S.; El-Sayed, M. A. *Chem. Soc. Rev.* **2006**, *35*, 209.

(4) Kelly, K. L.; Coronado, E.; Zhao, L. L.; Schatz, G. C. *J. Phys. Chem. B* **2002**, *107*, 668.

(5) Kamat, P. V. *J. Phys. Chem. B* **2002**, *106*, 7729.

(6) Halas, N. J. *Nano Lett.* **2010**, *10*, 3816.

(7) Li, P.; Wei, Z.; Wu, T.; Peng, Q.; Li, Y. *J. Am. Chem. Soc.* **2011**, *133*, 5660.

(8) Hirakawa, T.; Kamat, P. V. *J. Am. Chem. Soc.* **2005**, *127*, 3928.

(9) Thomann, I.; Pinaud, B. A.; Chen, Z.; Clemens, B. M.; Jaramillo, T. F.; Brongersma, M. L. *Nano Lett.* **2011**, *11*, 3440.

(10) Liu, Z.; Hou, W.; Pavaskar, P.; Aykol, M.; Cronin, S. B. *Nano Lett.* **2011**, *11*, 1111.

(11) Gao, H.; Liu, C.; Jeong, H. E.; Yang, P. *ACS Nano* **2011**, *6*, 234.

(12) Thimsen, E.; Le Formal, F.; Grätzel, M.; Warren, S. C. *Nano Lett.* **2010**, *11*, 35.

(13) Gomes Silva, C. u.; Juárez, R.; Marino, T.; Molinari, R.; García, H. *J. Am. Chem. Soc.* **2010**, *133*, 595.

(14) Linic, S.; Christopher, P.; Ingram, D. B. *Nat Mater* **2011**, *10*, 911.

(15) Schuller, J. A.; Barnard, E. S.; Cai, W.; Jun, Y. C.; White, J. S.; Brongersma, M. L. *Nat. Mater.* **2010**, *9*, 193.

(16) Atwater, H. A.; Polman, A. *Nat. Mater.* **2010**, *9*, 205.

(17) Alvarez-Puebla, R. n.; Liz-Marzán, L. M.; García de Abajo, F. J. *J. Phys. Chem. Lett.* **2010**, *1*, 2428.

(18) Cushing, S. K.; Li, J.; Meng, F.; Senty, T. R.; Suri, S.; Zhi, M.; Li, M.; Bristow, A. D.; Wu, N. *J. Am. Chem. Soc.* **2012**, *134*, 15033.

(19) Li, J.; Cushing, S. K.; Bright, J.; Meng, F.; Senty, T. R.; Zheng, P.; Bristow, A. D.; Wu, N. *ACS Catalysis* **2012**, *3*, 47.

(20) Fofang, N. T.; Grady, N. K.; Fan, Z.; Govorov, A. O.; Halas, N. J. *Nano Lett.* **2011**, *11*, 1556.

(21) Manjavacas, A.; Abajo, F. J. G. a. d.; Nordlander, P. *Nano Lett.* **2011**, *11*, 2318.

(22) Schlather, A. E.; Large, N.; Urban, A. S.; Nordlander, P.; Halas, N. J. *Nano Lett.* **2013**, *DOI: 10.1021/nl4014887*.

(23) Furube, A.; Du, L.; Hara, K.; Katoh, R.; Tachiya, M. *J. Am. Chem. Soc.* **2007**, *129*, 14852.

(24) Tian, Y.; Tatsuma, T. *J. Am. Chem. Soc.* **2005**, *127*, 7632.

(25) Lee, J.; Mubeen, S.; Ji, X.; Stucky, G. D.; Moskovits, M. *Nano Lett.* **2012**, *12*, 5014.

(26) Chen, H. M.; Chen, C. K.; Chen, C.-J.; Cheng, L.-C.; Wu, P. C.; Cheng, B. H.; Ho, Y. Z.; Tseng, M. L.; Hsu, Y.-Y.; Chan, T.-S.; Lee, J.-F.; Liu, R.-S.; Tsai, D. P. *ACS Nano* **2012**, *6*, 7362.

(27) Mubeen, S.; Hernandez-Sosa, G.; Moses, D.; Lee, J.; Moskovits, M. *Nano Lett.* **2011**, *11*, 5548.

(28) Lee, Y. K.; Jung, C. H.; Park, J.; Seo, H.; Somorjai, G. A.; Park, J. Y. *Nano Lett.* **2011**, *11*, 4251.

(29) Knight, M. W.; Sobhani, H.; Nordlander, P.; Halas, N. J. *Science* **2011**, *332*, 702.

(30) Wu, X.; Thrall, E. S.; Liu, H.; Steigerwald, M.; Brus, L. *J. Phys. Chem. C* **2010**, *114*, 12896.

(31) Fann, W. S.; Storz, R.; Tom, H. W. K.; Bokor, J. *Phys. Rev. B* **1992**, *46*, 13592.

(32) Hertel, T.; Knoesel, E.; Wolf, M.; Ertl, G. *Phys. Rev. Lett.* **1996**, *76*, 535.

(33) Hodak, J. H.; Martini, I.; Hartland, G. V. *J. Phys. Chem. B* **1998**, *102*, 6958.

(34) Li, M.; Cushing, S. K.; Wang, Q.; Shi, X.; Hornak, L. A.; Hong, Z.; Wu, N. *J. Phys. Chem. Lett.* **2011**, *2*, 2125.

(35) Liu, N.; Prall, B. S.; Klimov, V. I. *J. Am. Chem. Soc.* **2006**, *128*, 15362.

(36) Khanal, B. P.; Pandey, A.; Li, L.; Lin, Q.; Bae, W. K.; Luo, H.; Klimov, V. I.; Pietryga, J. M. *ACS Nano* **2012**, *6*, 3832.

(37) Menagen, G.; Macdonald, J. E.; Shemesh, Y.; Popov, I.; Banin, U. *J. Am. Chem. Soc.* **2009**, *131*, 17406.

(38) Habas, S. E.; Yang, P.; Mokari, T. *J. Am. Chem. Soc.* **2008**, *130*, 3294.

(39) Mokari, T.; Rothenberg, E.; Popov, I.; Costi, R.; Banin, U. *Science* **2004**, *304*, 1787.

(40) Mongin, D.; Shaviv, E.; Maioli, P.; Crut, A.; Banin, U.; Del Fatti, N.; Vallée, F. *ACS Nano* **2012**, *6*, 7034.

(41) Berr, M. J.; Vaneski, A.; Mauser, C.; Fischbach, S.; Susha, A. S.; Rogach, A. L.; Jäckel, F.; Feldmann, J. *Small* **2012**, *8*, 291.

(42) Khon, E.; Mereshchenko, A.; Tarnovsky, A. N.; Acharya, K.; Klinkova, A.; Hewa-Kasakarage, N. N.; Nemitz, I.; Zamkov, M. *Nano Lett.* **2011**, *11*, 1792.

(43) Wu, K.; Zhu, H.; Liu, Z.; Rodríguez-Córdoba, W.; Lian, T. *J. Am. Chem. Soc.* **2012**, *134*, 10337.

(44) Shaviv, E.; Schubert, O.; Alves-Santos, M.; Goldoni, G.; Di Felice, R.; Vallée, F.; Del Fatti, N.; Banin, U.; Sönnichsen, C. *ACS Nano* **2011**, *5*, 4712.

(45) Khon, E.; Hewa-Kasakarage, N. N.; Nemitz, I.; Acharya, K.; Zamkov, M. *Chem. Mat.* **2010**, *22*, 5929.

(46) Hoang, T. B.; Titova, L. V.; Jackson, H. E.; Smith, L. M.; Yarrison-Rice, J. M.; Lensch, J. L.; Lauhon, L. J. *Appl. Phys. Lett.* **2006**, *89*, 123123.

(47) Bird, R. E.; Hulstrom, R. L.; Lewis, L. J. *Solar Energy* **1983**, *30*, 563.

(48) Shabaev, A.; Efros, A. L. *Nano Lett.* **2004**, *4*, 1821.

(49) Mulvaney, P. *Langmuir* **1996**, *12*, 788.

(50) Link, S.; El-Sayed, M. A. *J. Phys. Chem. B* **1999**, *103*, 4212.

(51) Johnson, P. B.; Christy, R. W. *Phys. Rev. B* **1972**, *6*, 4370.

(52) Alvarez, M. M.; Khoury, J. T.; Schaaff, T. G.; Shafigullin, M. N.; Vezmar, I.; Whetten, R. L. *J. Phys. Chem. B* **1997**, *101*, 3706.

(53) Guerrisi, M.; Rosei, R.; Winsemius, P. *Phys. Rev. B* **1975**, *12*, 557.

(54) Yang, Y.; Rodríguez-Córdoba, W.; Xiang, X.; Lian, T. *Nano Lett.* **2011**, *12*, 303.

(55) Saunders, A. E.; Ghezelbash, A.; Sood, P.; Korgel, B. A. *Langmuir* **2008**, *24*, 9043.

(56) Saunders, A. E.; Popov, I.; Banin, U. *J. Phys. Chem. B* **2006**, *110*, 25421.

(57) Logunov, S. L.; Ahmadi, T. S.; El-Sayed, M. A.; Khoury, J. T.; Whetten, R. L. *J. Phys. Chem. B* **1997**, *101*, 3713.

(58) Averitt, R. D.; Westcott, S. L.; Halas, N. J. *Phys. Rev. B* **1998**, *58*, R10203.

(59) Hodak, J.; Martini, I.; Hartland, G. V. *Chem. Phys. Lett.* **1998**, *284*, 135.

(60) Link, S.; Burda, C.; Wang, Z. L.; El-Sayed, M. A. *J. Chem. Phys.* **1999**, *111*, 1255.

(61) Link, S.; El-Sayed, M. A. *J. Phys. Chem. B* **1999**, *103*, 8410.

(62) Wu, K.; Rodríguez-Córdoba, W. E.; Liu, Z.; Zhu, H.; Lian, T. *ACS Nano* **2013**, *7*, 7173.

(63) Du, L.; Furube, A.; Yamamoto, K.; Hara, K.; Katoh, R.; Tachiya, M. *J. Phys. Chem. C* **2009**, *113*, 6454.

(64) Guyot-Sionnest, P.; Hines, M. A. *Appl. Phys. Lett.* **1998**, *72*, 686.

(65) Huang, J.; Stockwell, D.; Huang, Z. Q.; Mohler, D. L.; Lian, T. Q. *J. Am. Chem. Soc.* **2008**, *130*, 5632.

(66) Yang, Y.; Rodríguez-Córdoba, W. E.; Lian, T. *J. Am. Chem. Soc.* **2011**, *133*, 9246.

(67) Klimov, V.; Bolivar, P. H.; Kurz, H. *Phys. Rev. B* **1996**, *53*, 1463.

(68) Pawlik, S.; Bauer, M.; Aeschlimann, M. *Surf. Sci.* **1997**, *377–379*, 206.

(69) Padilha, L. A.; Fu, J.; Hagan, D. J.; Van Stryland, E. W.; Cesar, C. L.; Barbosa, L. C.; Cruz, C. H. B.; Buso, D.; Martucci, A. *Phys. Rev. B* **2007**, *75*, 075325.

(70) Korobchevskaya, K.; George, C.; Manna, L.; Comin, A. *J. Phys. Chem. C* **2012**, *116*, 26924.

(71) Comin, A.; Korobchevskaya, K.; George, C.; Diaspro, A.; Manna, L. *Nano Lett.* **2012**, *12*, 921.

(72) Monti, S.; Chiorboli, C. In *The Exploration of Supramolecular Systems and Nanostructures by Photochemical Techniques*; Ceroni, P., Ed.; Springer Netherlands: 2012; Vol. 78, p 185.

(73) Sönnichsen, C.; Franzl, T.; Wilk, T.; von Plessen, G.; Feldmann, J.; Wilson, O.; Mulvaney, P. *Phys. Rev. Lett.* **2002**, *88*, 077402.

(74) Yorulmaz, M.; Khatua, S.; Zijlstra, P.; Gaiduk, A.; Orrit, M. *Nano Lett.* **2012**, *12*, 4385.

(75) Fang, Y.; Chang, W.-S.; Willingham, B.; Swanglap, P.; Dominguez-Medina, S.; Link, S. *ACS Nano* **2012**, *6*, 7177.

(76) Dulkeith, E.; Niedereichholz, T.; Klar, T. A.; Feldmann, J.; von Plessen, G.; Gittins, D. I.; Mayya, K. S.; Caruso, F. *Phys. Rev. B* **2004**, *70*, 205424.

(77) Lehmann, J.; Merschdorf, M.; Pfeiffer, W.; Thon, A.; Voll, S.; Gerber, G. *Phys. Rev. Lett.* **2000**, *85*, 2921.

(78) Endriz, J. G.; Spicer, W. E. *Phys. Rev. Lett.* **1970**, *24*, 64.

(79) Knight, M. W.; Wang, Y.; Urban, A. S.; Sobhani, A.; Zheng, B. Y.; Nordlander, P.; Halas, N. J. *Nano Lett.* **2013**, *13*, 1687.

(80) Fang, Z.; Wang, Y.; Liu, Z.; Schlather, A.; Ajayan, P. M.; Koppens, F. H. L.; Nordlander, P.; Halas, N. J. *ACS Nano* **2012**, *6*, 10222.

(81) Zhang, Z.; Zhang, L.; Hedhili, M. N.; Zhang, H.; Wang, P. *Nano Lett.* **2012**, *13*, 14.

(82) Mubeen, S.; Lee, J.; Singh, N.; Kramer, S.; Stucky, G. D.; Moskovits, M. *Nat Nano* **2013**, *8*, 247.

(83) Chu, M.-W.; Myroshnychenko, V.; Chen, C. H.; Deng, J.-P.; Mou, C.-Y.; García de Abajo, F. J. *Nano Lett.* **2008**, *9*, 399.

(84) Myroshnychenko, V.; Nelayah, J.; Adamo, G.; Geuquet, N.; Rodríguez-Fernández, J.; Pastoriza-Santos, I.; MacDonald, K. F.; Henrard, L.; Liz-Marzán, L. M.; Zheludev, N. I.; Kociak, M.; García de Abajo, F. J. *Nano Lett.* **2012**, *12*, 4172.

(85) Bauer, C.; Abid, J.-P.; Fermin, D.; Girault, H. H. *J. Chem. Phys.* **2004**, *120*, 9302.

(86) Aruda, K. O.; Tagliazucchi, M.; Sweeney, C. M.; Hannah, D. C.; Weiss, E. A. *Phys. Chem. Chem. Phys.* **2013**, *15*, 7441.

(87) Asbury, J. B.; Hao, E.; Wang, Y.; Ghosh, H. N.; Lian, T. *J. Phys. Chem. B* **2001**, *105*, 4545.

(88) Peng, X.; Manna, L.; Yang, W.; Wickham, J.; Scher, E.; Kadavanich, A.; Alivisatos, A. *Nature* **2000**, *404*, 59.

(89) Milliron, D. J.; Hughes, S. M.; Cui, Y.; Manna, L.; Li, J.; Wang, L.-W.; Paul Alivisatos, A. *Nature* **2004**, *430*, 190.

(90) Puthussery, J.; Lan, A.; Kosel, T. H.; Kuno, M. *ACS Nano* **2008**, *2*, 357.

(91) Govorov, A. O.; Zhang, H.; Gun'ko, Y. K. *J. Phys. Chem. C* **2013**, *117*, 16616.

Appendix 1

Analysis of CdS-Au absorption spectrum

Comparison between the absorption spectra of CdS-Au NRs and a physical mixture of CdS NRs with Au nanoparticles (NPs) clearly shows that the surface plasmon resonance (SPR) band in CdS-Au is significantly damped and red-shifted compared to isolated Au NPs and the excitonic bands of CdS are broadened, particularly for those bands below 400 nm, compared to free CdS NRs. In order to quantify the peak shift and broadening, we fit the CdS-Au spectrum by decomposing it into the contributions of CdS and Au domains and compare to the absorption of isolated CdS NRs and Au NPs.

The absorption spectrum of free CdS NRs can be fitted to a sum of four Gaussian bands and a continuous background feature ($\mathrm{BG(E)} \propto (\mathrm{E} - \mathrm{Eg})^3$, :

$$\mathrm{Abs_{CdS}(E)} = \mathrm{C} \cdot (\mathrm{E} - \mathrm{Eg})^3 + \sum_{\mathrm{i}=1}^{4} \frac{\mathrm{A_i}}{\sqrt{2\pi\Gamma_\mathrm{i}^2}} \cdot \exp\left[-\frac{(\mathrm{E}-\mathrm{E_{ci}})^2}{2\Gamma_\mathrm{i}^2}\right]$$

(A.6.1),

where C is a proportional constant, E is the energy, Eg is the bulk band gap for CdS (2.5 eV), and $\mathrm{A_i}$, Γ_i, and $\mathrm{E_{ci}}$ are the area, half width, and center of the ith Gaussian band. The continuous feature represents unresolved transitions and has also been included for fitting the PLE spectrum of CdSe QDs. The fit is shown in Figure S3b and the peak positions and widths are listed in Table A.6.1. Peak1 and Peak 2 are

both 1Σ exciton bands that involve the same $1\sigma_e$ electron level and different hole levels. Peak 3 and Peak 4 can be assigned to 1Π and 1Δ excitons, respectively.

For isolated Au NPs, because the interband absorption starts at ~2.45 eV, the absorption at lower energy can be attributed exclusively to the SPR band. Therefore, we first fit the SPR band for Au NPs in Figure A.6.1c to a Voigt line-shape according to Eq A.6.2.

$$\mathrm{SPR_{Au}}(\mathrm{E};\mathrm{E},\sigma,\gamma) = \int_{-\infty}^{+\infty} \mathrm{G}(\mathrm{E};\mathrm{E_c},\sigma)\mathrm{L}(\mathrm{E}-\mathrm{E}';\ \mathrm{E_c},\gamma)\mathrm{dE}'$$

(A.6.2),

where G and L are Gaussian and Lorentzian functions with their center at x_c and half widths of σ and γ, respectively. The Voigt line-shape takes into account of both intrinsic broadening (Lorentzian) and inhomogeneous broadening due to size and shape distributions (Gaussian). The fitting parameters are listed in Table A.6.2 and the fitted SPR band is shown in Figure A.6.1.c. Subtracting the SPR contribution from the total absorption spectrum gives the interband absorption profile of isolated Au NPs, which has an onset at 2.43 eV.

In principle, the absorption spectrum of CdS-Au NRs can be decomposed into the contributions of Au and CdS domains. Similar to that in isolated Au NPs, We fit the SPR band of Au tips in CdS-Au (Figure A.6.1d) to the Voigt line-shape and the fitting parameters are also listed in Table A.6.2. It is clear that compared to free Au

NPs, the peak position is red-shifted and both the Lorentzian and Gaussian widths are broadened. Thus, the broadening of SPR band cannot be accounted for by different degrees of inhomogeneous broadening in the isolated Au NPs and Au tips in CdS-Au. If we assume that the interband absorptions of Au and CdS domains are the same as those of isolated Au NPs and CdS NRs, we can add them to the SPR band of Au tip to simulate the absorption profile of CdS-Au NRs. The result is shown as fit 1 in Figure A.6.1d. The fit fails to reproduce the broadening of CdS exciton bands and also the enhanced absorption in the UV region. It should be noted that the extent of absorption enhancement increases at higher energy, suggesting that it cannot be explained by the enhanced field strength caused by the SPR band of the Au particle. The reason for this enhanced absorption in the near UV region is not clear.

Table A.6.1. Fitting parameters of CdS excitonic bands

		CdS NR	CdS-Au NR
Peak 1	Center (eV)	2.74	2.74
	Width (eV)	0.088	0.090
Peak 2	Center (eV)	2.82	2.82
	Width (eV)	0.15	0.16
Peak 3	Center (eV)	3.09	3.07

	Width (eV)	0.31	0.35
Peak 4	Center (eV)	3.60	3.61
	Width (eV)	0.65	0.81

A satisfactory fit to the absorption spectrum of CdS-Au can be obtained using a modified function to represent the interband absorption and and broadening CdS exciton bands, according to the following equation:

$$\mathrm{Abs}_{\mathrm{CdS-Au}}(\mathrm{E}) = \mathrm{SPR}_{\mathrm{Au\ tip}}(\mathrm{E}) + \mathrm{A}\cdot(\mathrm{E}-2.45\ \mathrm{eV})^{\mathrm{B}} + \mathrm{C}\cdot(\mathrm{E}-\mathrm{Eg})^{3} + \sum_{\mathrm{i}=1}^{4}\frac{\mathrm{A_i}}{\sqrt{2\pi\Gamma_\mathrm{i}^2}}\cdot \exp\left[-\frac{(\mathrm{E}-\mathrm{E_{ci}})^2}{2\Gamma_\mathrm{i}^2}\right] \quad \text{(A.6.3)},$$

where $\mathrm{SPR}_{\mathrm{Au\ tip}}(\mathrm{E})$ is the Voigt fitting to SPR band of Au tip, A and B are constants used to fit the interband absorption of Au tip, and $\mathrm{A_i}$, Γ_i, and $\mathrm{E_{ci}}$ are the area, half width, and center of the ith Gaussian band of CdS. The fitting result is shown as fit 2 in Figure A.6.1d. The fitted values of A and B are A= 1.07, B=0.822 and the Gaussian positions and widths are also listed in Table A.6.1. Compared to CdS NRs, the peak positions are almost the same but the widths are broadened in CdS-Au. The broadening becomes more pronounced for exciton bands with higher energy, suggesting it is not caused by larger heterogeneity in rod diameters in the CdS-Au sample. Therefore, we conclude that the broadened excitonic bands in CdS-Au likely indicates strong electronic coupling between the CdS and Au domains. All the

aforementioned evidence (shifted and broadened SPR band, enhanced Au interband absorption, broadened CdS exciton bands) suggests strong interactions between the Au and CdS domain in CdS-Au NRs.

Table A.6.2. Fitting parameters of SPR band

	Peak Center (eV)	Lorentzian Width (eV)	Gaussian Width (eV)
Au NPs	2.37	0.405	0.219
Au in CdS-Au	2.32	0.591	0.381

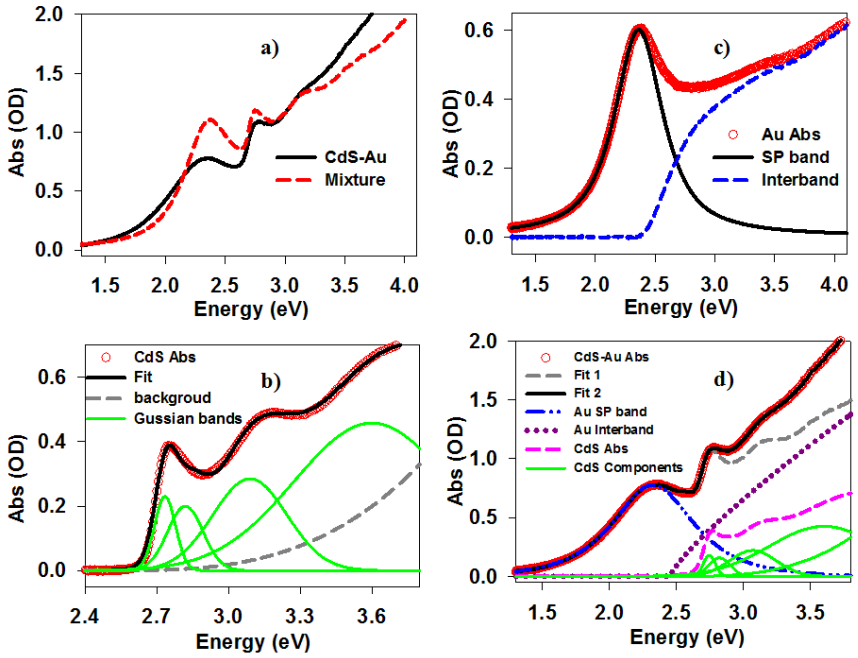

Figure A.6.1. Fit of the absorption spectra of CdS NRs, Au NPs and CdS-Au NRs. a) Comparison of the absorption spectra of CdS-Au NRs (black solid line) and a

physical mixture of isolated CdS NRs and Au NPs (red dashed line). b) Absorption spectrum of isolated CdS NRs (red circles) and its fit according to Eq. S1 (black solid line). The background function used in the fit is shown in gray dashed line and the excitonic Gaussian bands are shown in green solid lines. c) Absorption spectrum of Au NPs (red circles) and a fit to the SPR band by a Voigt line-shape function (black solid line). The difference between them is the interband absorption profile of Au NPs (blue dashed line). d) Absorption spectrum of CdS-Au NRs (red circles). The gray dashed line (fit 1) is a fit using the sum of isolated CdS NR and Au NP interband absorptions and SPR band of Au tip (blue dashed-dotted line). The black solid line (fit 2) is a fit using the sum of SPR band of Au tip, modified interband absorption of Au tip (purple dashed line) and broadened CdS absorption (pink dashed line). The green lines are the components (background function and Gaussian bands) constituting the absorption spectrum shown in pink dashed line.

Appendix 2

Estimation of energy transfer rate from CdS NR to Au tip

The estimation below is based on dipole approximation and Forster Resonant Energy Transfer (FRET) model. Previous studies have investigated the applicability of this model to these nano-objects. Specifically, based on time-dependent density functional theory, it has been shown that the dipole approximation still works when donor and/or acceptor is a spherical QD, even if two QDs are in direct connect with each other, which is in direct contrast to the breaking down of dipole approximation when distances between donor and acceptor molecules are at length scales comparable to the molecular dimensions.[8] In addition, energy transfer rates between CdSe/ZnS QD and Au NP have been measured and fitted to FRET model even when the separation between them is much smaller than the Au NP size. Therefore, the FRET model should a valid way to estimate energy transfer rates between CdS NRs and Au tips.

Since CdS NRs are susceptible to hole trapping (in ~0.7 ps), we estimate energy transfer rates both before and after the holes are trapped. The emission spectra of band edge exciton and trapped exciton are obtained by decompose the PL spectrum of CdS NR into two emission bands. Indeed, both band edge exciton emission (PL 1) and trapped exciton emission (PL2) overlap with the absorption spectrum of Au tip

(Figure A.6.2). We firstly estimate energy transfer rate from band edge exciton and then the same procedure can be applied to trapped exciton.

The Forster radius, the distance between donor and acceptor at which the fluorescence quenching efficiency is 50%, is given by the following equation:

$$R = 0.211[\kappa^2 \Phi_D J(\lambda)/n^4]^{1/6}$$

(A.6.4),

in which κ^2 is dipole orientation factor, Φ_D is emission quantum yield of donor, $J(\lambda)$ is the overlap integral between donor emission and acceptor absorption spectra, and n is the refractive index of dielectric medium. The overlap integral can be calculated using:

$$J(\lambda) = \frac{\int d\lambda I_D(\lambda)\varepsilon_A(\lambda)(\lambda)^4}{\int d\lambda I_D(\lambda)}$$

(A.6.5),

where $I_D(\lambda)$ and $\varepsilon_A(\lambda)$ are donor emission spectrum and acceptor molar absorptivity, respectively. With the Foster radius, the energy transfer time constant can be calculated as:

$$\tau_{EnT} = \tau_0(\frac{r}{R})^6$$

(A.6.6),

Where τ_0 is the donor excited state lifetime in the absence of the acceptor and r is the donor-acceptor distance.

The overlap integral between CdS band edge exciton emission and Au absorption is calculated to be 2.82×10^{17} $M^{-1}cm^{-1}nm^4$. The emission quantum yield $\Phi_D$is unknown. As an estimate of the upper limit, Φ_D is assumed to be 1 and, correspondingly, τ_0 in equation A.6.6, which is ~1ns from our previous study, can be taken as the radiative lifetime of band edge exciton. The general form for κ^2 is given by:

$$\kappa^2 = \langle(\cos\alpha - 3\cos\beta\cos\gamma)^2\rangle$$

(A.6.7),

where α is the angle between the donor and acceptor transition moments, β is the angle between the donor moment and the line joining the centers of the donor and acceptor, and γ is the angle between the acceptor moment and the line joining the centers of the donor and acceptor. For CdS-Au NR, in which the emission dipole of the 1D band edge exciton is polarized along the NR axis, we have $\alpha=\gamma$, $\beta=0$ and $\kappa^2 = \langle4(\cos\alpha)^2\rangle$. Assuming randomly-polarized Au absorption dipole (see Figure S4b for the scheme), the orientation factor κ^2 is calculated to be:

$$\kappa^2 = \langle4(\cos\alpha)^2\rangle = \frac{\int_0^{\pi}4(\cos\alpha)^2(2\pi r\sin\alpha)r d\alpha}{\int_0^{\pi}(2\pi r\sin\alpha)r d\alpha}=4/3$$

(A.6.8).

The Forster radius calculated from equation S12 is 13.7 nm, using the refractive index of chloroform (1.49). We note that this is the upper limit for Forster radius because in

CdS-Au NR donor and acceptor dipoles also interact significantly through the volume of CdS and Au which has much higher refractive index than chloroform.

The initially generated excitons are randomly distributed along the CdS rod. This corresponds to an average energy transfer time of17.9 ns. However, because the band edge exciton may move freely along the NR, the distance between its dipole and dipole of Au is not well-defined. Here, we consider the upper limit for energy transfer rate that corresponds to the closest distance between CdS and Au dipoles. Assuming the closest distance of the center of exciton from the edge of the rod is given by the bulk Bohr radius for CdS (2.8 nm), and accounting for the diameter of Au tip (5.4 nm), the closest energy transfer distance is 5.5 nm. Using equation S14, the energy transfer time constant at this distance is calculated to be ~4.1 ps, which is almost an order of magnitude slower than the hole trapping rate. Considering that this is the upper limit for energy transfer rate, we can conclude that the energy transfer from CdS band edge exciton to Au tip is not a competitive exciton quenching pathway.

Similarly, the Forster radius between trapped CdS exciton and Au tip is estimated to be 5.24 nm, using the emission QY of ~0.18%. The orientation factor is assumed to be the same as the band edge exciton, although the trapped exciton may not be polarized along the NR axis. Because of the longer lifetime of trapped excitons (~100 ns), the calculated energy transfer time (~133 ns) is much slower than band edge excitons, and much slower than the observed exciton quenching rate in CdS-Au

(with half life of 4.85 ps). Our estimate shows that, for both band edge and trapped excitons, energy transfer is not a competitive exciton quenching pathway.

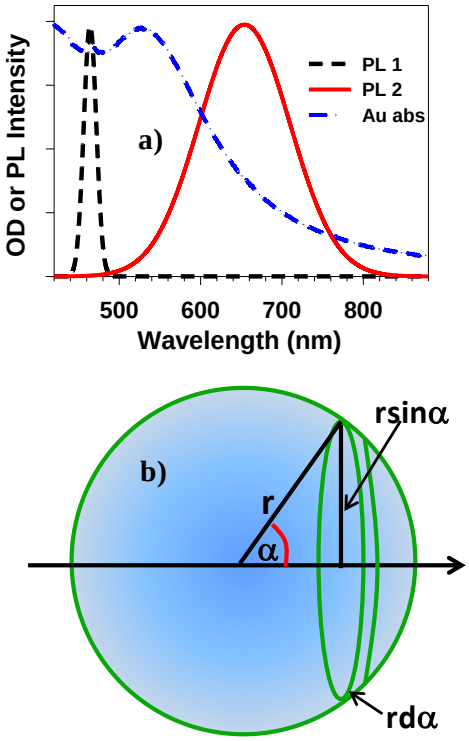

Figure A.6.2. a) Absorption spectrum of Au tip in CdS-Au (blue dashed-dotted line), and emission spectra of band edge exciton (black dashed line) and trapped exciton (red solid line) of CdS NRs. The latter spectra were obtained by decomposing the total emission spectrum of CdS NRs into two Gaussian peaks. . All the peaks are normalized to the same amplitude for better vision. b) Scheme for calculating orientation factor between CdS and Au dipoles. The axis is the line connecting the center of two dipoles and is also the direction of CdS dipole. The direction of Au dipole is randomly distributed with angle of α, and therefore the possibility of finding

an Au dipole at α is proportional to the area of the spherical shell show in the figure which is $2\pi r \sin\alpha \, r d\alpha$.

Appendix 3

TA spectra and kinetics of of free CdS Nanorod (NR) and control sample under 400 nm excitation

TA spectra of free CdS NRs at indicated delays from 0.2 ps to 500 ns after 400 nm excitation are shown in Figure A.6.3a. Figure A.6.3b shows the TA spectra for *control 1* which is a physical mixture of CdS NRs with Au NPs. The kinetics of CdS NRs and Au NPs are not affected by each other: the CdS NR 1Σ exciton (Figure A.6.3c) is long-lived as in free NR and the signal of Au NPs shows typical fast cooling kinetics (Figure A.6.3d). In Figure A.6.3c, we show the kinetics of 1Σ exciton bleach for both free CdS NRs and *control 1*. The amplitude of the former is scaled by the correction factor ($\frac{\mathrm{OD_{A1}}}{\mathrm{OD_{A1}+OD_B}} = 0.352$) and the latter is the original amplitude. Indeed, except for the early time (<4 ps) when the 1Σ exciton bleach in the control is overlapped with the positive SPR signal, both amplitude and kinetics agree in CdS NRs and *control 1*. The signals at the center of plasmon bleach in CdS NRs and *control 1* are compared in Figure A.6.3d. The electron-phonon scattering kinetics is very similar in both cases.

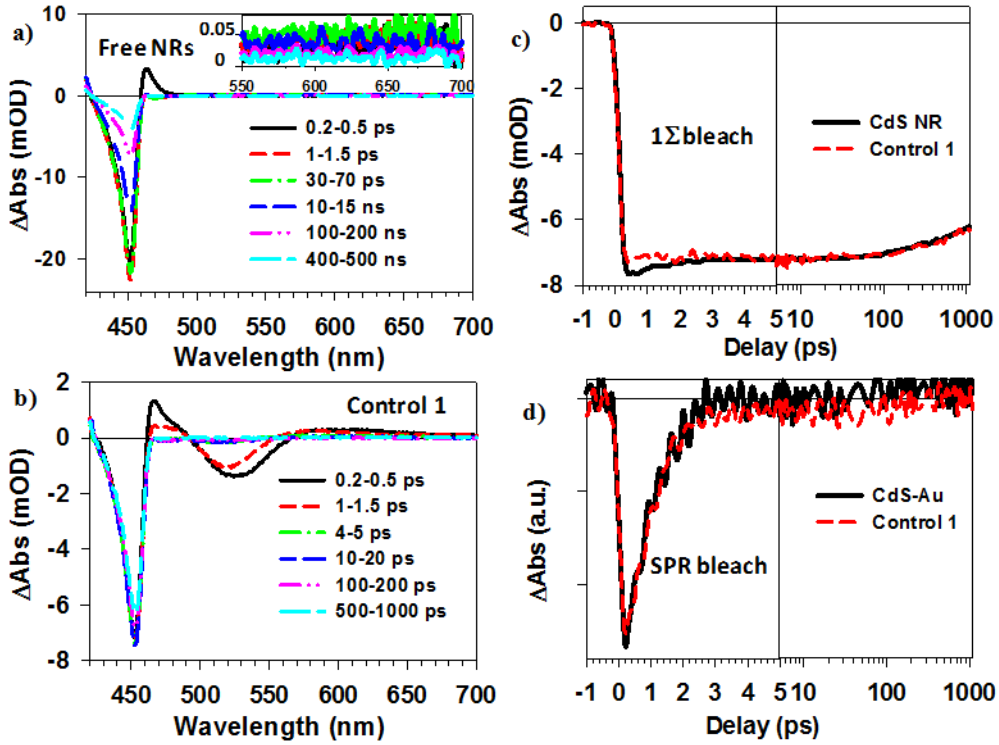

Figure A.6.3. a) TA spectra of free CdS NRs at indicated delays from 0.2 ps to 500 ns after 400 nm excitation. The inset shows the broad photoinduced absorption (PA) from 550 nm to 700 nm. b) TA spectra of *control 1* (mixture of CdS NRs with Au NPs) at indicated delays from 0.2 ps to 1000 ps after 400 nm excitation. c) Kinetics probed at 1Σ exciton bleach in free CdS NRs (black solid line) and *control 1* (red dashed line). The amplitude of the former has been scaled for number of absorbed photons. d) Kinetics probed at plasmon bleach center in CdS-Au NRs (black solid line) and *control 1*(red dashed line).

Appendix 4

Assignment of CdS NR intraband absorption at 3000 nm

The intraband absorption of NRs has not been assigned before. To ensure that the probed absorption at 3000 nm is purely contributed by $1\sigma_e$ to $1\pi_e$ transition, we carried out selective carrier removal study in CdS NR-methylene blue (MB^+) complexes. On the basis of relevant energy levels of QDs and MB^+, electron transfer from QD to MB^+ is the only exciton quenching pathway.[14] As can be seen from the visible TA spectra of this complex measured at 400 nm excitation (Figure A.6.4a), the recovery of 1Σ bleach is much faster than free CdS NRs and is accompanied by formation of MB^+ ground state bleach, indicating electron transfer from the CdS NR to MB^+. A comparison of the 1Σ bleach recovery, intraband absorption decay at 3000 nm and the growth of the MB^+ ground state bleach in Figure A.6.4b shows that the kinetics of these features agree with each other, which unambiguously confirms that that absorption at 3000 nm is due to $1\sigma_e$ to $1\pi_e$ intraband transition. Therefore, it can be used to follow the dynamics of $1\sigma_e$ electrons in CdS and CdS-Au NRs.

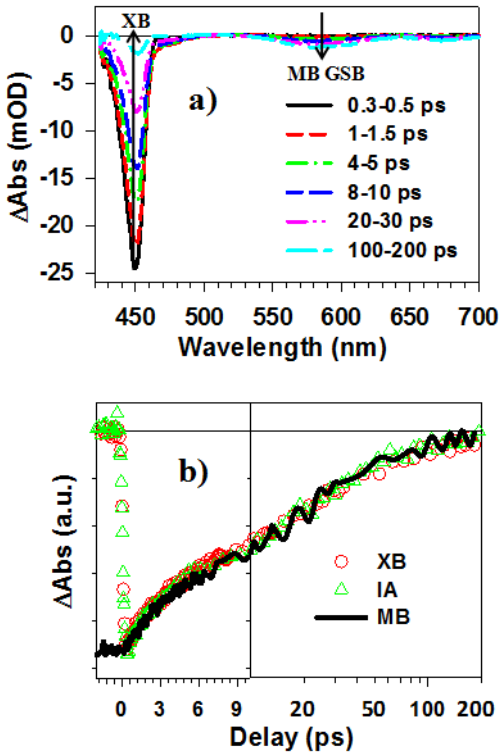

Figure A.6.4. a) TA spectra of CdS NR-methylene blue (MB) complexes at indicated delays from 0.3 ps to 200 ps after 400 nm excitation. b) Kinetics of 1Σ exciton bleach recovery (XB, red circles), intraband absorption at 3000 nm (IA, green triangles) and methylene blue ground state bleach (MB, black line). For better comparison, the MB and IA signals have been inverted and scaled.

Appendix 5

Pump fluence dependence of signal size

To quantify the plasmon-induced hot electron injection yield, we need to ensure the experiments fall into the small signal limit so that the signal size on TA spectrum is proportional to number of absorbed photons. Furthermore, measurements at multiple excitation intensities also help improve the signal-to-noise ratio of the measured value of injection quantum yield. As shown in Figure A.6.5a and A.6.5b, the TA signal amplitudes increase linearly with pump pulse energy, with slopes (in the unit of mOD/nJ) of $S_{(400\ \mathrm{nm})}$ and $S_{(590\ \mathrm{nm})}$ for 400 nm and 590 nm excitations, respectively, indicating that these experiments fall in the small signal limit. The injection quantum yield can be more conveniently calculated from the slopes and the photon flux per nJ ($j'_{(590\ \mathrm{nm},1\mathrm{nJ})}$ and $j'_{(400\ \mathrm{nm},1\mathrm{nJ})}$, at 590 and 400 nm, respectively) according to Eq. S25, which is equivalent to Eq. 1 in the main text:

$$\mathrm{QY} = \frac{S_{(590\ \mathrm{nm})}}{(1-10^{-\mathrm{OD}_{(590\ \mathrm{nm})}})\cdot j'_{(590\ \mathrm{nm},1\ \mathrm{nJ})}} \Big/ \frac{S_{(400\ \mathrm{nm})}}{(1-10^{-\mathrm{OD}_{(400\ \mathrm{nm})}})\cdot j'_{(400\ \mathrm{nm},1\ \mathrm{nJ})}} \qquad \text{(A.6.9).}$$

The parameters involved in the efficiency calculation, including pump photon energy, pump beam waist, sample OD at pump wavelengths, slope, and photon flux per nJ, are summarized in Table A.6.3.

Table A.6.3. Parameters used for QY calculation

	Photon energy (10^{-19}J)	Beam waist (μm)	Sample OD	Slope (mOD/nJ)	Flux per nJ (10^{12} • m^{-2} • s^{-1})	QY (%)

400 nm	4.97	107	0.82	0.113±0.001	5.58	100
590 nm	3.37	102	0.82	0.00925±0.00016	9.05	2.75±0.07

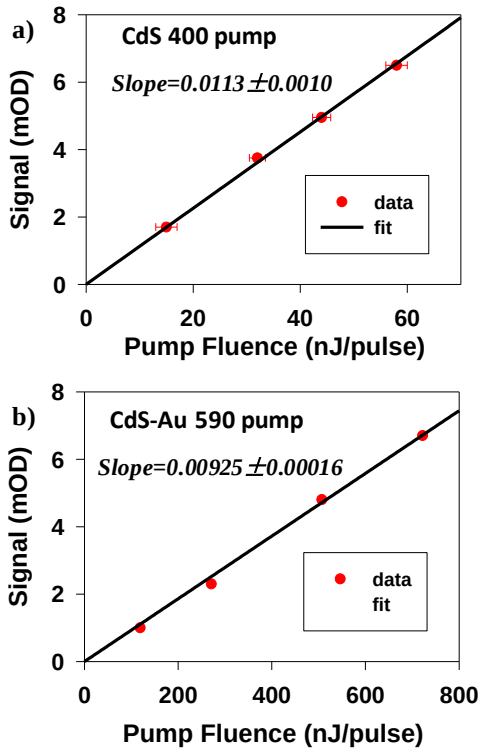

Figure A.6.5. Pump pulse energy dependence of intraband absorption signal sizes or (a) CdS-Au NRs at 590 nm excitation and (b) free CdS NRs at 400 nm excitation. The circles are data points and the lines are linear fits.

Chapter 7. Plasmon Induced Interfacial Charge Transfer Transition for Efficient Hot Electron Transfer from Metal Nanostructures

This work is submitted to *Science* and currently under revision.

7.1. Introduction

Surface plasmon resonance (SPR) of metallic nanostructures has been widely utilized to improve the efficiency of photovoltaics,[1-5] photocatalysis,[6,7] and photodetectors,[8,9] by either increasing light absorption through enhanced local fields near the metal nanostructures,[10] or by plasmon induced charge transfer from the excited metal.[11-13] The latter enhancement mechanism suggests the possibility of utilizing plasmonic metal nanostructures as a novel class of light absorbers with unique properties that include broad spectral tunability, exceptionally large absorption cross sections, superior long term stability, and low cost colloidal synthesis. [14,15] So far, all reported plasmon-induced charge separation processes are believed to go through a conventional plasmon induced hot electron transfer (PHET) mechanism (Figure 7.1.A), in which a plasmon decays into a hot electron-hole pair within the metal

through Landau Damping, followed by transfer of the hot electron into adjacent semiconductors or molecules.[16] Unfortunately, hot electron transfer competes with electron relaxation through rapid electron-electron scatterings in the conduction band (CB) of metal on the several to 10s of femtoseconds time scale.[17,18] Efficient PHET requires interfacial charge separation on an even faster time scale, which is difficult to realize in many semiconductor-metal hybrid materials. Therefore, the reported device efficiencies based on plasmon-induced charge separation concepts are still too low for practical applications. [6-8]

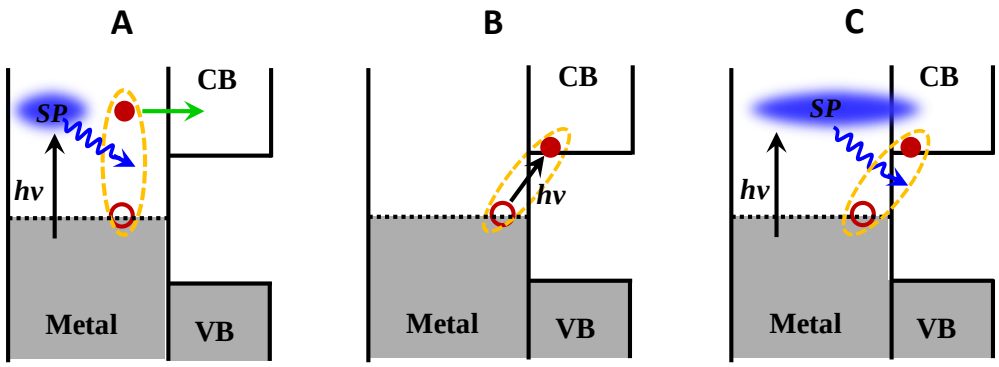

Figure 7.1. Metal to semiconductor charge separation pathways. (A) Conventional plasmon-induced hot electron transfer (PHET) mechanism in which the photoexcited plasmon in the metal decays into a hot electron-hole pair within the metal through Landau Damping, followed by injection of the hot electron into the conduction band (CB) of the semiconductor. **(B)** Optical excitation of an electron in the metal into the CB of the semiconductor through direct (metal-to-semiconductor) interfacial charge transfer transition (DICTT). **(C)** New plasmon-induced

(metal-to-semiconductor) interfacial charge transfer transition (PICTT) pathway where the plasmon decays by directly creating an electron in the CB of semiconductor and a hole in the metal.

Metal to semiconductor hot electron transfer efficiencies can be enhanced if the competition with ultrafast electron-electron scatterings in the metal can be avoided. One approach is to create a direct metal to semiconductor charge transfer transition (DICTT) that can be directly excited to promote an electron from metal into semiconductor CB, as shown in Figure 7.1.B. There have been reports of such transitions between metal adatoms and semiconductor electrodes,[19] and a metal-to-adsorbate resonance for CO adsorbed on Pt nanoparticles.[20,21] However, these interfacial transitions are too weak compared with bulk metal transitions or plasmon bands [19,22,23] and therefore cannot be an efficient light-harvesting pathway. Ideally, a desirable photoinduced hot electron transfer pathway should combine the strong light absorbing power of plasmonic transitions with superior charge separation properties of direct interfacial charge transfer transition, as shown in Figure 7.1.C. In this plasmon-induced metal-to-semiconductor interfacial charge transfer transition (PICTT) pathway, the metal plasmon serves as a light absorber, but strong inter-domain coupling and mixing of the metal and semiconductor levels leads to a new plasmon decay pathway - the direct generation of an electron in the

semiconductor and hole in the metal domains. Herein, for the first time we propose and experimentally demonstrate this new plasmon induced charge separation pathway in colloidal quantum confined CdSe-Au nanorod (NR) heterostructures. In these heterostructures, strong Au-CdSe interaction led to strong damping of the plasmon band of the Au tip through the PICTT pathway. The proposed pathway was verified by observing highly efficient plasmon induced Au-to-CdSe charge separation with > 24% quantum efficiencies upon the excitation of the Au tip. Transient absorption anisotropy measurements showed more efficient Au-to-CdSe charge transfer when exciting the plasmon along the nanorod axis, consistent with the PICTT mechanism. The charge separation efficiencies were shown to be independent of excitation photon energy, which are inconsistent with the conventional PHET mechanism and support the proposed PICTT pathway.

7.2. Results and Discussion

7.2.1. Absorption spectra of CdSe-Au

Colloidal CdSe-Au NRs was synthesized according to a published procedure [24], which is described in Chapter 2. Representative TEM images of CdSe and CdSe-Au

NRs are shown in Figure 7.2.A. These images show well-defined dumbbell-like morphologies for CdSe-Au, with two Au nanoparticles at both ends of a single crystalline CdSe NR. Static absorption spectra of CdSe and CdSe-Au NRs dispersed in chloroform are displayed in Figure 7.2.B. The discrete absorption peaks of CdSe NRs at ~480 and ~582 nm are attributed to the 1Π and 1Σ exciton bands, respectively, arising from quantum confinement in the radial direction.[25] Compared to free Au nanoparticles, the SPR band of Au tips (diameter ~4.1 nm) was strongly damped, showing a continuous absorption feature extending to the near IR, consistent with previous observations.[24,26] It has been suggested that such drastic change of the SPR band cannot be accounted for by dielectric effects alone and indicates strong electronic interactions between CdSe and Au domains through some yet to be understood mechanisms.[26] Indeed, ultrafast quenching (<100 fs) of excitons in CdSe NR by the Au tip was observed (Figure A.7.2), consistent with previous reports in related CdSe-Au NRs.[27] In contrast to the severe broadening of the Au plasmon band, changes of the CdSe excitonic bands are not apparent in Figure 7.2.B. It is important to realize that because the length of the nanorod is much longer than the strongly interacting metal/semiconductor interface region, the ends of the CdSe NR (i.e. at the CdSe/Au interface) are likely strongly perturbed, while the center is relatively un-perturbed.[28] To mimic the tip region of the CdSe-Au NRs, we synthesized CdSe QD-Au dimmers using CdSe QDs with a lowest energy exciton band similar to CdSe

NRs. In these dimmers, both excitonic peaks of QDs and the plasmon band of the Au were completely damped (Figure 7.2.B), showing a continuous absorption feature that agreed well with that in CdSe-Au NRs. Subtracting this feature from the CdSe-Au NR absorption revealed an absorption spectrum that was slightly blue-shifted from free CdSe NRs (Figure 7.2.B), which can be attributed to NR etching during the growth of the Au tips.[24] Thus, the electronic structure of CdSe-Au NRs can be viewed as a sum of the strongly interacting tip region that resembles the CdSe QD-Au dimmers (with strongly damped plasmon and exciton bands) and the center part that is similar to unperturbed CdSe NRs, as depicted in Figure 7.2.C.

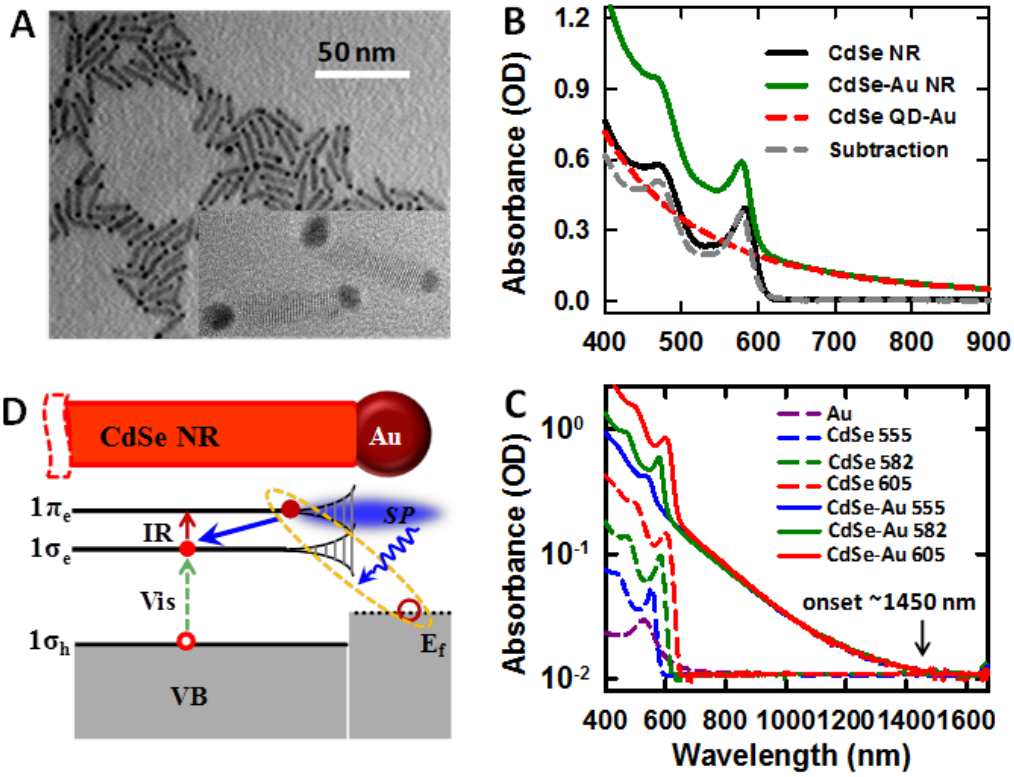

Figure 7.2. Plasmon-induced metal-to-semiconductor charge transfer transition in CdSe-Au NRs. (A) A representative TEM image of CdSe-Au NRs. Inset: a representative high resolution TEM image. **(B)** Absorption spectra of CdSe NRs (black solid line), CdSe-Au NRs (red solid line), and CdSe QD-Au dimmers (green dashed line) dispersed in chloroform. The gray dashed line is the difference spectrum between the absorptions of CdSe-Au NRs and CdSe QD-Au dimmers. **(C)** Absorption spectra (with y-axis plotted in logarithm scale and shifted by +0.01 to avoid negative values) of isolated Au nanoparticles (purple dashed line) and CdSe NRs (dashed lines) and CdSe-Au NRs (solid lines) with first excitonic peak positions at 555(blue), 582(green), 605(red) nm. The absorption spectra of CdSe-Au NRs show the same onset at ~1450 nm (0.85 eV). **(D)** Schematic electronic structure of CdSe-Au NRs, composed of strongly damped tips with broadened electronic levels and central region with relatively unperturbed discrete levels ($1\sigma_e$, $1\pi_e$…).

As shown in Figure 7.2.C, the broad feature-less near IR absorption of CdSe-Au NRs showed a clear onset at ~ 1450 nm (0.85 eV) for three NRs with 1Σ exciton bands at 555, 582 and 605 nm (with a corresponding shift of conduction band edge position of ~150 meV).[19] This result suggests that this transition cannot be attributed to direct metal-to-semiconductor optical transition (DICCT, Figure 7.1.B), which should have an onset wavelength that shifts with the CdSe CB edge. Instead, we

attribute the broad near IR absorption feature to a strongly damped Au plasmon caused by the strong mixing of Au and CdSe electronic levels. Such strong interaction introduces the PICTT pathway (Figure 7.1.C), a new plasmon decay pathway that is not present in isolated Au nanoparticles.

7.2.2. Electron transfer from excited Au to CdSe NRs

In the PICTT pathway, the damped plasmon decays *via* direct excitation of an interfacial electron-hole pair (with an electron in CdSe and a hole in Au). Direct evidence to support the proposed mechanism is provided through ultrafast transient absorption (TA) studies, in which, a pump laser with photon energy below the bandgap of CdSe was used to excite the Au tip and the electron transferred to the CdSe domain was probed through either the bleach of 1Σ exciton in the visible (caused by state filling of the $1\sigma_e$ level) and/or the $1\sigma_e - 1\pi_e$ intraband absorption in the mid-IR (Figure Figure 7.2.D).[29,30]. The assignment of these spectral signatures was confirmed by comparison transient spectra of CdSe NRs and CdSe-benzoquione (electron acceptor) complexes. As shown in Figure A.7.1, the kinetics of the 1Σ exciton bleach at ~580 nm and intraband absorption at ~3000 nm agreed with each other in free CdSe NRs and electron transfer from CdSe to adsorbed electron

acceptors led to faster decay of both spectral features in NR-electron acceptor complexes. The TA spectra of CdSe-Au NRs (Figure 7.3.A) showed a pronounced 1Σ exciton bleach feature at ~575 nm, indicating the formation of CdSe CB electrons through the excitation of the damped Au plasmon band at 800 nm. This bleach overlapped with a broad positive TA feature that was also present in the TA spectra of CdSe QD-Au dimmers (Figure A.7.3). This broad feature was subtracted from the total TA signal to obtain the TA kinetics (Figure 7.3.C) of 1Σ bleach. 800 nm excitation also generated an intraband absorption feature at 3000 nm and the formation and decay kinetics of this signal and the 1Σ bleach were in good agreement with each other (Figure 7.3.B), further confirming the presence of CB electron in CdSe. These intraband and interband signals were absent in control samples composed of a mixture of CdSe NRs and Au nanoparticles (Figure 7.3.B). Fitting these kinetics yielded a formation time of ~20±10 fs and a bi-exponential decay with a half-life of ~1.45±0.15 ps, which corresponded to plasmon-induced hot electron transfer and charge recombination times, respectively.[30] Such ultrafast charge separation time is consistent with the PICTT mechanism, according to which the decay of plasmon instantaneously generates an electron in CdSe (to give rise to the observed inter- and intra-band features) and a hole in Au near the CdSe/Au interface. The injected electron quickly relaxes back to the Au with a recombination time of

1.45 ps, which indicates negligible band bending induced recombination barrier at the CdSe/Au interface, consistent with the short rod length used in this study.

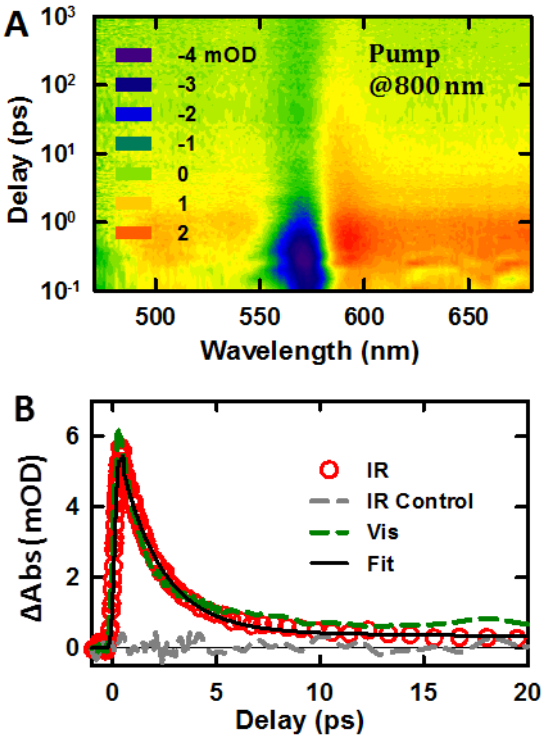

Figure 7.3. Plasmon-induced charge separation in CdSe-Au NRs. (A) Two-dimensional pseudo-color (ΔAbs) plots of TA spectra of CdSe-Au NRs at 800 nm excitation (x-axis: probe wavelength; y-axis: pump-probe delay). (B) Intraband absorption (probed at ~3000 nm, red circles) and 1Σ exciton bleach (~580 nm, green dashed line) kinetics of CdSe-Au NRs after 800 nm excitation. Negligible intraband absorption signal is observed in a control sample of a mixture of CdSe NRs and Au nanoparticles (gray dashed line). Black solid line is a multi-exponential fit of the kinetics.

7.2.3. Excitation Wavelength Independent Charge Separation Yields

The transient quantum yields (QYs) of Au-to-CdSe charge separation as a function of excitation wavelength is shown in Figure 7.4. These QYs were determined by the peak amplitude (averaged between 0.2-0.4 ps) of the CdSe intraband absorption signal (see SOM for details). The pump wavelength (energy) was tuned over a >1 eV range below the bandgap of CdSe NRs: 670 nm (1.85 eV), 710 nm (1.75 eV), and 750 nm (1.65 eV), 800 nm (1.55 eV), 1160 nm (1.07 eV), 1340 nm (0.92 eV), and 1550 nm (0.80 eV). As shown in Figure 7.4, within experimental errors, the measured QYs were constant (~24%) above ~0.85 eV, the onset of the near IR absorption feature shown in Figure 7.2.B. Below the onset, no measurable electron signals were observed due to a lack of photon absorption.

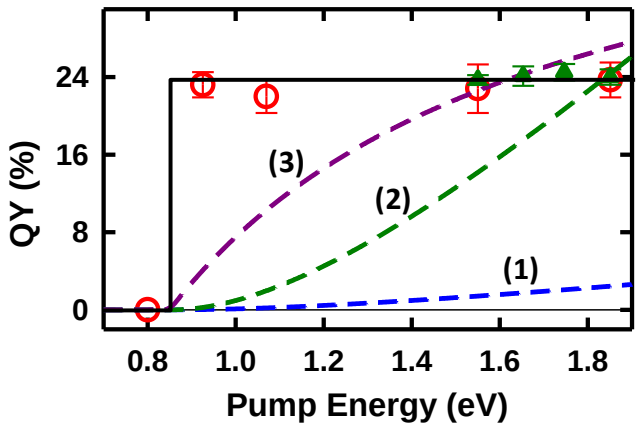

Figure 7.4. Quantum yields (QYs) of plasmon-induced charge separation as a function excitation photon energies (red open circles and green filled triangles,

measured with PbS and Cd_3P_2 QDs as calibration samples, respectively, see SOM for details) and predictions according to various Fowler models: equation 1(blue dashed line), equation 2 (green dashed line), and equation 3 (purple dashed line). The black solid line is a step-function with onset at ~0.85 eV.

In the conventional PHET mechanism (Figure 7.1.A), the excitation energy dependence of charge separation QYs can be well described by the Fowler's equation:[31]

$$QY(\omega) = \left(\hbar\omega - E_b\right)^2 / 4E_F\hbar\omega \qquad (7.1),$$

where $\hbar\omega$ is the energy of excitation photon, E_b is the barrier height between metal and semiconductor, and E_F is the Fermi energy of the metal. Indeed, most of the hot electron transfer based devices reported to date were shown to follow this model.[8,32-34] For small nanoparticles, QYs of metal-to-semiconductor photoemission generally follow the same functional form, but can be enhanced by a factor C through a geometric effect[35,36] and lowering of escape barrier[37]:

$$QY(\omega) = C \cdot \left(\hbar\omega - E_b\right)^2 / 4E_F\hbar\omega \qquad (7.2).$$

Recently, it is also found that momentum conservation requirement can be relaxed if electrons only scatter at the semiconductor/metal interface.[38] Under this condition, the QY is described by (see Appendix 4):

$$QY(\omega) = \left(\hbar\omega - E_b\right)/2\hbar\omega \qquad (7.3).$$

The predicated QYs according to eq. 7.1, 7.2 and 7.3 are shown in Figure 7.4. For eq. 7.2, we have chosen the value of C so that the predicted QY at 1.85 eV agreed with the experiment. It is clear that these Fowler type conventional hot electron transfer models predict an increasing QY at higher excitation energy (because of the increase of hot electrons with energy above the semiconductor CB edge), and are inconsistent with our experimental data.

The measured QYs are consistent with the PICTT pathway. In this pathway, the plasmon decays by direct excitation of an electron from Au to CdSe and the QY is independent of the excess energy of the electron above the CB edge. The strongly damped plasmon bandwidth is likely dominated by homogeneous broadening: as long as the excitation energy is above the absorption threshold (~0.85 eV), the same plasmon is excited and therefore the charge separation QY is independent of excitation energy. Such a homogeneous line-width (of ~1eV) would correspond to a plasmon dephasing time of ~1 fs, which is consistent with observed fast hot electron formation time. Furthermore, the observed quantum yield is about an order of magnitude higher than the reported value for CdS-Au NRs (2.75%).[30] In CdS-Au, the Au plasmon band is weakly perturbed and the plasmon induced hot electron transfer occurs through the conventional PHET mechanism (Figure 7.1.A), where the competition of hot electron transfer with ultrafast relaxation reduces its efficiency.

The observed QYs in CdSe-Au is still less than unity for at least two reasons. First, PICTT is likely not the exclusive decay channel for the strongly damped plasmon. It can also be damped in the Au domain to proceed via the much less efficient conventional PHET pathway.[30] Second, the electron generated in CdSe can either quickly relax back into the Au or escape into the center of CdSe NR (and recombine on the 1.4 ps time scale) and only the latter was detected in our measurements. Therefore, the measured QYs represent a lower limit of plasmon induced electron transfer in this system.

7.2.4. Polarization Dependent Charge Separation Yields

Further insight into the nature of the PICTT pathway can also be obtained by polarization dependent TA study. It can be expected that plasmons polarized in the direction parallel to the NR may be more strongly coupled to the CdSe than those in the direction perpendicular to the rod. Because optical transition of the CdSe is strongly polarized,[25,39] this should lead to dependence of the TA signal on the relative polarization of the pump and the probe beams. This polarization dependence can be conveniently quantified by the anisotropy of the TA signals $r=(S_{HH}-S_{HV})/(S_{HH}+2S_{HV})$, where S_{HH} and S_{HV} are TA signals with the polarizations of pump and probe beams

parallel or perpendicular, respectively, to each other. As shown in Figure 7.5.A, for band edge (590 nm) excitation of free CdSe NRs (without Au tip), 1Σ exciton bleach signal amplitude S_{HH} is larger than S_{HV}. The calculated anisotropy was 0.12 and showed negligible decay in 10 ps (Figure 7.5.A inset), which indicates that the band edge absorption transition dipole has 70% and 30% axial and radial components, respectively, consistent with previous reports (see Appendix details).[40,41] The intraband $1\sigma_e - 1\pi_e$ transition showed negligible anisotropy value. Therefore, we use 1Σ exciton bleach to probe anisotropy in CdSe-Au NRs. As shown in Figure 7.5.B, for 800 nm excitation of CdSe-Au NRs, the resulting 1Σ exciton bleach signal amplitude S_{HH} is larger than S_{HV} with an anisotropy value of 0.10. This result suggests a more efficient hot electron transfer by plasmons polarized parallel to the NR axis, consistent with the PICTT mechanism. In contrast, in CdS-Au NRs where the conventional PHET mechanism dominates,[30] we detected negligible anisotropy in the CdS 1Σ exciton bleach signal generated by exciting the Au plasmon band (Appendix).

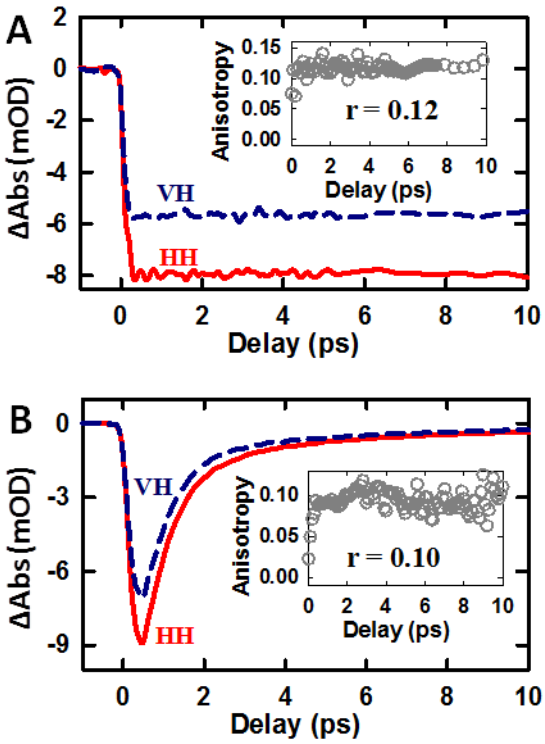

Figure 7.5. Transient Absorption anisotropy of CdSe and CdSe-Au NRs. (A) 1Σ exciton bleach kinetics (probed at ~580 nm) in free CdSe NRs after band edge (590 nm) excitation with pump and probed beams having parallel (HH, horizontal pump and horizontal probe, red solid line) and perpendicular (VH, vertical pump and horizontal probe, blue dashed line) polarizations. Inset: calculated anisotropy r as a function of pump-probe delay. **(B)** 1Σ exciton bleach kinetics (probed at ~575 nm) in CdSe-Au NRs after 800 nm excitation with pump and probed beams having parallel (HH, red solid line) and perpendicular (VH, blue dashed line) polarizations. Calculated anisotropy r is shown in the inset.

7.2.5. Reduction of methyl viologen by plasmon-generated electrons

For the cw light driven MV^{2+} reduction experiment, the concentration of aqueous CdSe-Au NRs was tuned to have an OD of 0.2 at 800 nm in a 1 cm pathlength cuvette. 1 mg methyl viologen dichloride (MV^{2+}) was added to 3 mL above solution. 1 mg sodium sulfide (Na_2S) was added as sacrificial donors. The concentration of MV^{2+} and Na_2S were kept low so that the dark reaction rate between them was slow. The reaction solution was purged with Ar for 15 min and then constantly stirred and illuminated by a red light (680±30 nm, 34.5 mW) that was produced from a Xeon lamp by applying a band pass filter. $MV^{\cdot+}$ radicals generated in the reaction were detected by measuring the absorption change of the solution. The amounts of $MV^{\cdot+}$ radicals were calculated from the difference absorbance with respect to time zero using the reported extinction coefficient.[42] The experimental scheme is shown in Figure 7.6a.

Time-dependent differential absorption spectra of the CdSe-Au-MV^{2+} system with respect to time zero are shown in Figure 7.6b, which clearly shows the accumulation of $MV^{\cdot+}$ radicals. The accumulation kinetics is plotted in Figure 7.5c. In addition, we performed a series of control experiments to investigate the role of plasmonic light absorption in radical formation. As shown in Figure 7.6.c, removing CdSe-Au NRs from the reaction solution (referred to as the blank sample) showed a much slower $MV^{+\cdot}$ radical formation rate, which can be attributed to slow reduction of MV^{2+} (-0.446 V *vs* NHE) by S^{2-} (-0.450 V *vs* NHE) in the dark. Replacing CdSe-Au

NRs by Au nanoparticles (referred to as Au sample) with the same sample absorbance at the excitation wavelength yielded similar radical generation rate as the blank sample. It implies that direct plasmon induced hot electron transfer from Au nanoparticles to MV^{2+} cannot compete with the ultrafast e-e thermalization within Au. Replacing CdSe-Au NRs by CdSe NRs (of the same concentration as CdSe-Au NRs) led to a faster radical generation rate than the blank sample (which was still much slower than the CdSe-Au-MV^{2+} system). This likely caused by imperfect filtration of lights at wavelength below the CdSe band gap.

To calculate the plasmon-induced radical generate rate $\Delta(MV^{\cdot+})$, we subtracted radical generation rate of CdSe NRs sample from that of CdSe-Au NR. Note that the reaction rate is calculated within 1 min of illumination when the radical concentration is low because the generated radicals also absorb photons around 680 ± 30 nm, as shown in Figure 7.6.b. Quantum efficiency (QE) for radical generation was calculated using: $QE = N_A \Delta(MV^{\cdot+})/ \Delta(\hbar v)$, where N_A is the Avogadro constant and $\Delta(\hbar v)$ is the number of absorbed photons per minute calculated from the excitation power and sample optical density. The plasmon enhanced QE for photo-reduction of MV^{2+} was calculated to be $0.75 \pm 0.10\%$. It should be noted that this value is likely an underestimate of the efficiency of CdSe-Au because some of the Au tips separate from the CdSe rod during the ligand exchange process and absorption by these Au tips have negligible contributions to the MV^{2+} photo-reduction.

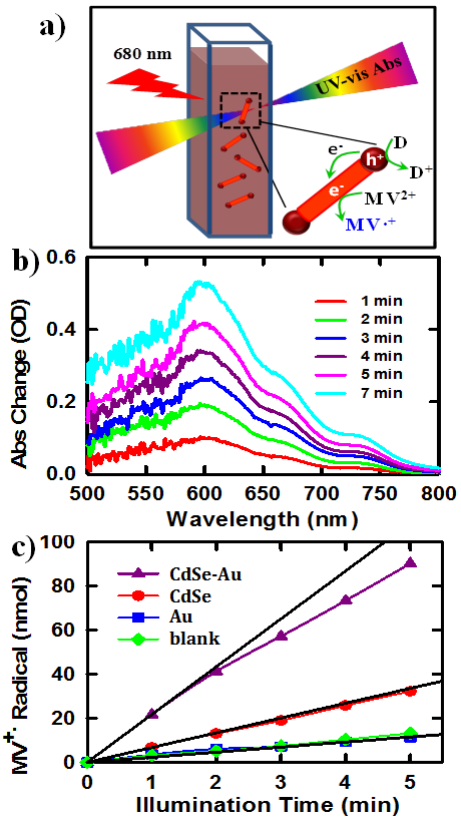

Figure 7.6. QYs for plasmon induced steady state photoreduction of MV^{2+}. a) A scheme of the plasmon-induced photocatalysis experiment. A cw light is used to excite the Au tip in CdSe-Au NRs and the plasmon-induced reduction of MV^{2+} into $MV^{+\cdot}$ radical is monitored through static absorption change. b) Difference absorption spectra of CdSe-Au NRs at indicated illumination times with respect to time zero showing accumulation of $MV^{+\cdot}$ radicals. c) $MV^{+\cdot}$ radicals as a function of illumination time for CdSe-Au NRs (purple triangles), CdSe NRs (red circles), Au nanoparticles (blue squares), and blank sample (no particles, green diamonds). The black solid lines are linear fits to extract the initial slopes of $MV^{+\cdot}$ radical generation.

7.3. Conclusion

In summary, we have proposed and demonstrated PICTT, a new mechanism for efficient plasmon induced hot electron transfer. Although the proposed mechanism has not been experimentally confirmed previously, strong mixing of Au and TiO_2 electronic levels have been reported in a recent computational study of Au cluster sensitized TiO_2 nanoparticles by Prezhdo and co-workers.[43] Strongly broadened Au plasmon band and efficient plasmon induced hot electron transfer was also observed in Au nanoparticle sensitized TiO_2 nanocrystalline thin films.[11] Therefore, the PICTT mechanism reported here is potentially a general phenomenon at metal/semiconductor and/or metal/molecule interfaces. PICTT may open an exciting new pathway to circumvent energy loss channels in metal nanostructures and drastically increase the efficiencies of devices based on plasmonic light absorption materials.

References

(1) Atwater, H. A.; Polman, A. *Nat. Mater.* **2010**, *9*, 205.

(2) Mubeen, S.; Lee, J.; Singh, N.; Kramer, S.; Stucky, G. D.; Moskovits, M. *Nat Nano* **2013**, *8*, 247.

(3) Linic, S.; Christopher, P.; Ingram, D. B. *Nat Mater* **2011**, *10*, 911.

(4) Thomann, I.; Pinaud, B. A.; Chen, Z.; Clemens, B. M.; Jaramillo, T. F.; Brongersma, M. L. *Nano Lett.* **2011**, *11*, 3440.

(5) Clavero, C. *Nat Photon* **2014**, *8*, 95.

(6) Marimuthu, A.; Zhang, J.; Linic, S. *Science* **2013**, *339*, 1590.

(7) Christopher, P.; Xin, H.; Linic, S. *Nat Chem* **2011**, *3*, 467.

(8) Knight, M. W.; Sobhani, H.; Nordlander, P.; Halas, N. J. *Science* **2011**, *332*, 702.

(9) Brongersma, M. L.; Halas, N. J.; Nordlander, P. *Nat Nano* **2015**, *10*, 25.

(10) Schuller, J. A.; Barnard, E. S.; Cai, W.; Jun, Y. C.; White, J. S.; Brongersma, M. L. *Nat. Mater.* **2010**, *9*, 193.

(11) Furube, A.; Du, L.; Hara, K.; Katoh, R.; Tachiya, M. *J. Am. Chem. Soc.* **2007**, *129*, 14852.

(12) Tian, Y.; Tatsuma, T. *J. Am. Chem. Soc.* **2005**, *127*, 7632.

(13) Li, J.; Cushing, S. K.; Zheng, P.; Senty, T.; Meng, F.; Bristow, A. D.; Manivannan, A.; Wu, N. *J. Am. Chem. Soc.* **2014**, *136*, 8438.

(14) Kelly, K. L.; Coronado, E.; Zhao, L. L.; Schatz, G. C. *J. Phys. Chem. B* **2002**, *107*, 668.

(15) Jain, P. K.; Lee, K. S.; El-Sayed, I. H.; El-Sayed, M. A. *J. Phys. Chem. B* **2006**, *110*, 7238.

(16) Govorov, A. O.; Zhang, H.; Gun'ko, Y. K. *J. Phys. Chem. C* **2013**, *117*, 16616.

(17) Fann, W. S.; Storz, R.; Tom, H. W. K.; Bokor, J. *Phys. Rev. B* **1992**, *46*, 13592.

(18) Hodak, J. H.; Martini, I.; Hartland, G. V. *J. Phys. Chem. B* **1998**, *102*, 6958.

(19) Kolb, D.; Przasnyski, M.; Gerischer, H. *Z. Phys. Chem.* **1974**, *93*, 1.

(20) Kale, M. J.; Avanesian, T.; Xin, H.; Yan, J.; Christopher, P. *Nano Lett.* **2014**, *14*, 5405.

(21) Chou, K. C.; Westerberg, S.; Shen, Y. R.; Ross, P. N.; Somorjai, G. A. *Phys. Rev. B* **2004**, *69*, 153413.

(22) Creutz, C.; Brunschwig, B. S.; Sutin, N. *J. Phys. Chem. B* **2005**, *109*, 10251.

(23) Petek, H.; Weida, M. J.; Nagano, H.; Ogawa, S. *Science* **2000**, *288*, 1402.

(24) Mokari, T.; Rothenberg, E.; Popov, I.; Costi, R.; Banin, U. *Science* **2004**, *304*, 1787.

(25) Shabaev, A.; Efros, A. L. *Nano Lett.* **2004**, *4*, 1821.

(26) Shaviv, E.; Schubert, O.; Alves-Santos, M.; Goldoni, G.; Di Felice, R.; Vallée, F.; Del Fatti, N.; Banin, U.; Sönnichsen, C. *ACS Nano* **2011**, *5*, 4712.

(27) Yu, P.; Wen, X.; Lee, Y.-C.; Lee, W.-C.; Kang, C.-C.; Tang, J. *J. Phys. Chem. Lett.* **2013**, *4*, 3596.

(28) Steiner, D.; Mokari, T.; Banin, U.; Millo, O. *Phys. Rev. Lett.* **2005**, *95*, 056805.

(29) Guyot-Sionnest, P.; Hines, M. A. *Appl. Phys. Lett.* **1998**, *72*, 686.

(30) Wu, K.; Rodríguez-Córdoba, W. E.; Yang, Y.; Lian, T. *Nano Lett.* **2013**, *13*, 5255.

(31) Fowler, R. H. *Physical Review* **1931**, *38*, 45.

(32) Li, W.; Valentine, J. G. *Nano Lett.* **2014**, *14*, 3510.

(33) Chen, H. M.; Chen, C. K.; Chen, C.-J.; Cheng, L.-C.; Wu, P. C.; Cheng, B. H.; Ho, Y. Z.; Tseng, M. L.; Hsu, Y.-Y.; Chan, T.-S.; Lee, J.-F.; Liu, R.-S.; Tsai, D. P. *ACS Nano* **2012**, *6*, 7362.

(34) Lee, Y. K.; Jung, C. H.; Park, J.; Seo, H.; Somorjai, G. A.; Park, J. Y. *Nano Lett.* **2011**, *11*, 4251.

(35) Schmidt-Ott, A.; Schurtenberger, P.; Siegmann, H. C. *Phys. Rev. Lett.* **1980**, *45*, 1284.

(36) Chen, Q. Y.; Bates, C. W. *Phys. Rev. Lett.* **1986**, *57*, 2737.

(37) Müller, U.; Burtscher, H.; Schmidt-Ott, A. *Phys. Rev. B* **1988**, *38*, 7814.

(38) GiugniA; TorreB; TomaA; FrancardiM; MalerbaM; AlabastriA; Proietti Zaccaria, R.; Stockman, M. I.; Di Fabrizio, E. *Nat Nano* **2013**, *8*, 845.

(39) Hu, J.; Li, L.-s.; Yang, W.; Manna, L.; Wang, L.-w.; Alivisatos, A. P. *Science* **2001**, *292*, 2060.

(40) Tice, D. B.; Weinberg, D. J.; Mathew, N.; Chang, R. P. H.; Weiss, E. A. *J. Phys. Chem. C* **2013**, *117*, 13289.

(41) McDonald, M. P.; Vietmeyer, F.; Kuno, M. *J. Phys. Chem. Lett.* **2012**, *3*, 2215.

(42) Watanabe, T.; Honda, K. *J. Phys. Chem.* **1982**, *86*, 2617.

(43) Long, R.; Prezhdo, O. V. *J. Am. Chem. Soc.* **2014**, *136*, 4343.

Appendix 1

Interband and intraband kinetics of free CdSe NRs and CdSe NR-BQ complexes

Interband kinetics. The vis TA spectra of free CdSe NRs at indicated delays after 400 nm excitation are shown in Figure A.7.1a. Previous TA studies on CdSe NRs have assigned the exciton bleach (XB) feature at ~580 nm to state filling of $1\sigma_e$ electronic level.[5,6] The XB kinetics is plotted in Figure A.7.1b and fitted to the following equation:

$$XB(t) = A \cdot [\sum_{i=1}^{3} a_i \cdot e^{-t/\tau_i} - e^{-t/\tau_f}] \qquad \text{(A.7.1)},$$

where A is the signal size of XB, τ_f is the formation time constants, and a_i and τ_i are amplitudes and time constants of the multi-exponential decay. The fitting parameters and errors are listed in Table A.7.1, from which the half-life of band edge electrons in CdSe NRs is determined to be 8.76±0.83 ns. In the presence of an electron acceptor, benzoquinone (BQ), XB recovery is faster due to electron transfer to BQ, as shown in Figure A.7.1c. The kinetics of XB feature in NR-BQ (Figure A.7.1d) can also be fitted to equation A.7.1 and the fitting parameters are listed in Table A.7.1. The electron transfer half-life is determined to be 70.9±2.5 ps.

Intraband kinetics. In addition to the interband XB, the dynamics of electrons in the conduction band of CdSe NRs and other quantum confined Cd chalcogenides can also be probed by intraband transition in the mid-IR regions.[7-9] Indeed, as

shown in Figure A.7.1d, in both free CdSe NRs and CdSe NR-BQ complexes, the kinetics of intraband absorption at ~3000 nm agree well with the XB feature, confirming that both signals can be used to follow band edge electron kinetics in CdSe NRs. The intraband signal provides a convenient probe to study plasmon-induced electron transfer from Au to CdSe in CdSe-Au NRs for two reasons. First, it avoids spectral overlap with plasmon signals in the visible region.[8,10] Second, it allows measurements at higher sample concentration when visible TA cannot due to strong probe absorption by the sample.

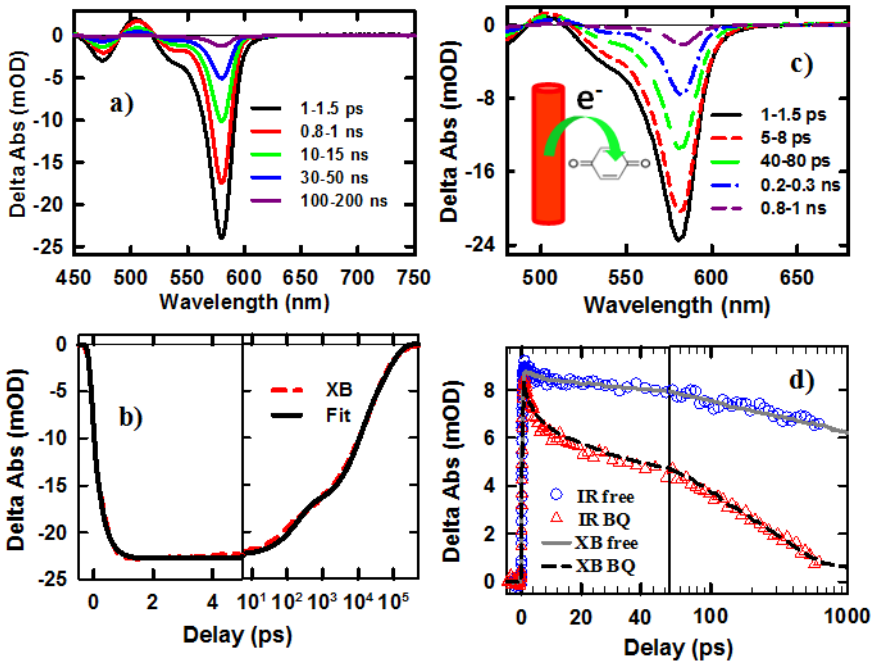

Figure A.7.1. Transient Absorption (TA) spectra and kinetics of NR and NR-acceptor complexes. a) TA spectra at indicated delays after 400 nm excitation and b) TA kinetics of exciton bleach (XB) at ~580 nm (red dashed line) and its multi-exponential fit (black solid line) of CdSe NRs. c) TA spectra of CdSe NR-BQ complexes at

indicated delay times after 400 nm excitation. The inset is a scheme of the complex. d) TA kinetics of XB (red triangles) and intraband IR transition (black dashed line) in CdSe NR-BQ complexes. Also shown for comparison are kinetics of XB (blue circles) and intraband IR transition (gray solid line) in free CdSe NRs.

Table A.7.1. XB recovery kinetics in free CdSe NRs and NR-BQ complexes

	τ_f/ps	τ_1/ns (a_1)	τ_2/ns (a_2)	τ_3/ns (a_3)	$\tau_{1/2}$/ns
NR	0.31 ±0.15	0.227 ±0.006 (22.9 ±0.2%)	11.0 ±0.2 (42.1 ±0.9%)	71.2 ±0.9 (35.0 ±0.4%)	8.8 ±0.8
	τ_f/ps	τ_1/ps (a_1)	τ_2/ps (a_2)	τ_3/ps (a_3)	$\tau_{1/2}$/ps
NR-BQ	0.31 ±0.15	3.14 ±0.09 (23.7 ±0.4%)	62.3 ±0.6 (32.1 ±0.5%)	435 ±23 (44.2 ±1.5%)	70.9 ±2.5

Appendix 2

Charge separation and recombination in 400 nm excited CdSe-Au NRs

In a previous study of electron transfer from excited CdSe NRs to Au tip, it was reported that the initial XB amplitude in CdSe-Au NRs is only 10% that of free NRs caused by ultrafast hot electron transfer to Au in <100fs. We also investigated this process in our CdSe-Au samples using 400 nm pump light, which could excite both CdSe NRs and inter-band transition of Au tips.[12] The resulting TA spectra from 0.2 ps to 1 ns (Figure A.7.2) show much smaller initial XB signal amplitude (~13.5%) in CdSe-Au compared with free CdSe NRs (after normalizing the signals to correspond to the same number of absorbed photons by CdSe) and the formation of derivative-like features within 0.2 ps that can be assigned to charge separation induced stark effect signals.[13] In addition, there is also strong broad absorption signal ranging from ~600 nm to the near IR, which is likely due to excitation of the Au tip or strongly-coupled CdSe-Au domains because a similar feature was also observed in CdSe QD-Au dimmers (see below). Because this signal is nearly constant throughout the visible spectral window, it can be subtracted from the TA spectra to reveal the kinetics of the Stark effect spectral signatures. Fitting these kinetics shows a formation time of ~46 fs (Table A.7.2) followed by multi-exponential decays with half-life of ~0.90±0.15ps. We attribute the decay to charge recombination process

(back electron transfer from Au tip to CdSe NR). The formation time (~46 fs) of charge separated states is much faster than the XB formation in free CdSe NRs (~308 fs), consistent with previous conclusion of ultrafast hot electron transfer from CdSe to Au.[11] It should be noted that although the charge separated states was observed, the charge separation yield was not determined and the possibility of ultrafast energy transfer process (which would also lead to XB recovery) can not be ruled out. Furthermore, although absorption at 400 nm is dominated by CdSe NRs, the XB bleach signal also contains contribution of Au-to-CdSe charge transfer resulted from the direct excitation of the Au tip, which can be best studied by exciting the nanorod below the CdSe band gap, as described in the main text.

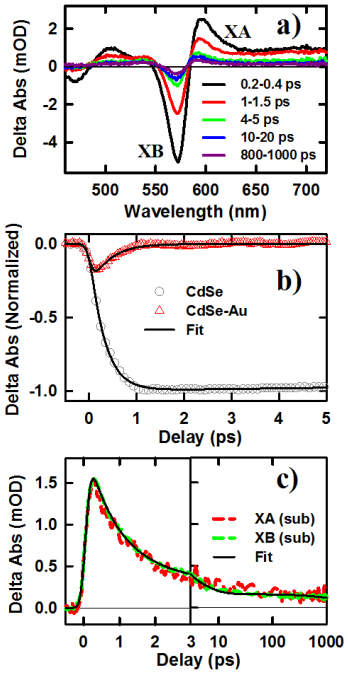

Figure A.7.2. TA spectra and kinetics of CdSe-Au at 400 nm excitation. a) TA spectra of CdSe-Au NRs at indicated delays, showing exciton absorption (XA, ~600

nm) and exciton bleach (XB, ~575 nm). b) Comparison of XB kinetics in CdSe-Au NRs (red triangles) and in free CdSe NRs (gray circles). The signals have been scaled to correspond to the same number of absorbed photons by the CdSe rod. c) Kinetics of XA (red dashed line) and XB (green dashed line, inverted) after subtraction of the broad absorption signal (averaged from 670 nm to 700 nm). The black solid line is a multi-exponential fit to these kinetics.

Table A.7.2. Charge separation and recombination in CdSe-Au NRs after 400 nm excitation

	τ_f/fs	τ_1/ps (a_1)	τ_2/ps (a_2)	τ_3/ps (a_3)	$\tau_{1/2}$/ps
CdSe-Au NRs	46 ±20	0.85 ±0.13 (72.3 ±0.9%)	4.23 ±0.16 (19.6 ±0.4%)	3105 ±100 (8.1 ±0.1%)	0.90 ±0.15

Appendix 3

Transient Absorption of CdSe QD-Au dimmers

TA spectra of CdSe QD-Au dimmers after 400 nm and 800 nm excitations are shown in Figure A.7.3a and A.7.3b, respectively. Typical TA feature of excited QDs (exciton bleach) and Au nanoparticles are absent. Instead, the TA spectral are dominated by a broad absorption feature throughout the whole probed spectral window. They are consistent with the absence of exciton bands of QDs and SPR band of Au on the static absorption spectrum of CdSe-QD dimmers in Figure 7.2A. The kinetics of this broad absorption feature (averaged from 670 to 700 nm) for CdSe QD-Au dimmers and CdSe-Au NRs are identical at both 400 nm and 800 nm excitations (Figure A.7.3c). Fitting these kinetics reveals a formation process (~118±25 fs) followed by multi-exponential decays with a halflife of 2.3±0.1 ps (Table A.7.3). This broad absorption feature is likely due to laser heating induced spectral changes of the strongly damped plasmon. In fact, the relaxation time scale (2.3 ps) is similar to previously-reported relaxation times of Au nanoparticles.[14,16,17] Quantitative understanding of this feature is beyond the scope of this work.

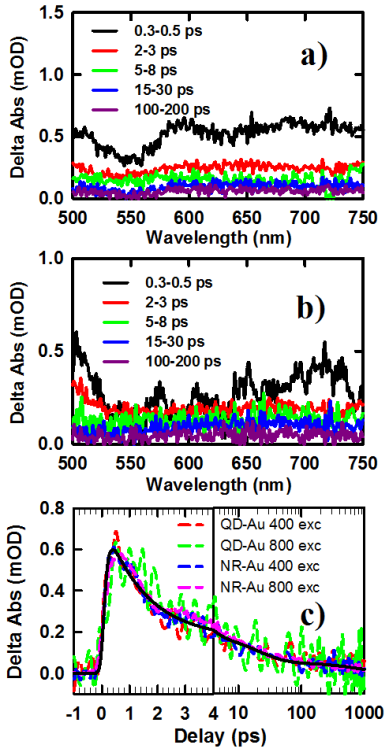

Figure A.7.3.TA spectra of CdSe QD-Au dimmers at indicated delays after a) 400 nm and b) 800 nm excitations. c) Kinetics probed at 670-700 nm for CdSe QD-Au dimmers and CdSe-Au NRs under both 400 nm and 800 nm excitations. The black solid line is a multi-exponential fit to these kinetics.

Table A.7.3. Fitting parameters for the broad-band TA absorption

	τ_f/fs	τ_1/ps (a_1)	τ_2/ps (a_2)	τ_3/ps (a_3)	$\tau_{1/2}$/ps
CdSe QD-Au	118 ±25	1.40 ±0.15 (73.6 ±1.1%)	20.3 ±0.7 (19.4 ±0.4%)	901 ±60 (7.0 ±0.1%)	2.3 ±0.1

Appendix 4

Transient Absorption Anisotropy of CdSe and CdSe-Au NRs

Theory of TA anisotropy. In TA anisotropy measurements, the polarization of the probe pulse was fixed while that of the pump pulse could be adjusted using a half-waveplate. We recorded the TA signals when the pump and probe pulses were either parallel or perpendicular to each other and corresponding anisotropy can be calculated. To help understand TA anisotropy better, we first derived the expression, adapted from commonly used fluorescence anisotropy theory,[18,19] for an anisotropic rod, which can be directly related to our CdSe and CdSe-Au NRs.

As shown in Figure A.7.4a, there are two sets of coordinates to be considered here: the laboratory coordinates (x, y, z) and the rod coordinates (a, b, c). These two are related to each other through Eulerian angles (θ, ϕ, ψ). Specifically, the rod coordinates can be transformed into the laboratory coordinates through the transformation matrix A:

$$A = \begin{pmatrix} A_{xa} & A_{xb} & A_{xc} \\ A_{ya} & A_{yb} & A_{yc} \\ A_{za} & A_{zb} & A_{zc} \end{pmatrix} \qquad \text{(A.7.3)},$$

where:

$$
\begin{aligned}
A_{xa} &= \cos\theta \\
A_{xb} &= \sin\theta\sin\psi \\
A_{xc} &= \sin\theta\cos\psi \\
A_{ya} &= \sin\theta\sin\varphi \\
A_{yb} &= \cos\psi\cos\varphi - \cos\theta\sin\psi\sin\varphi \\
A_{yc} &= -\sin\psi\cos\varphi - \cos\theta\cos\psi\sin\varphi \\
A_{za} &= -\sin\theta\cos\varphi \\
A_{zb} &= \cos\psi\sin\varphi + \cos\theta\sin\psi\cos\varphi \\
A_{zc} &= -\sin\psi\sin\varphi + \cos\theta\cos\psi\cos\varphi
\end{aligned}
\qquad \text{(A.7.4).}
$$

Assuming that the pump beam path is along x axis and it can be polarized along either y or z axis. The probabilities for absorption of the pump beam polarized along y and z axes are:

$$P_{pump,y} = p_a A_{ya}^2 + p_b A_{yb}^2 + p_c A_{yc}^2 = 0.5\cdot(1-p_c)(A_{ya}^2 + A_{yb}^2) + p_c A_{yc}^2$$

(A.7.5),

$$P_{pump,z} = p_a A_{za}^2 + p_b A_{zb}^2 + p_c A_{zc}^2 = 0.5\cdot(1-p_c)(A_{za}^2 + A_{zb}^2) + p_c A_{zc}^2$$

(A.7.6),

respectively, where p_a, p_b, and p_c are the absorption components at the pump wavelength along a, b, and c directions. They are proportional to the square of absorption dipole along each axis. For an Wurtzite CdSe nanorod, we have $p_a = p_b$ and $p_a + p_b + p_c = 1$. Assuming that the probe beam is polarized along z axis, the absorption probability of the probe beam is:

$$P_{probe,z} = q_a A_{za}^2 + q_b A_{zb}^2 + q_c A_{zc}^2 = 0.5\cdot(1-q_c)(A_{za}^2 + A_{zb}^2) + q_c A_{zc}^2$$

(A.7.7),

where q_a, q_b, and q_c are the square of absorption dipole components at the probe wavelength along a, b, and c directions.

Since the nanorods are randomly oriented, the averaged transient absorption signals for different pump polarizations can be obtained by integrating over all the possible orientations:

$$S_{zz} = \int_0^{2\pi} d\varphi \int_0^{2\pi} d\psi \int_0^{\pi} P_{pump,z} \cdot P_{probe,z} \sin\theta d\theta \qquad \text{(A.7.8)},$$

$$S_{yz} = \int_0^{2\pi} d\varphi \int_0^{2\pi} d\psi \int_0^{\pi} P_{pump,y} \cdot P_{probe,z} \sin\theta d\theta \qquad \text{(A.7.9)}.$$

The ensemble anisotropy r is defined as:

$$r = \frac{S_{zz} - S_{yz}}{S_{zz} + 2S_{yz}}$$

(A.7.10).

The calculated anisotropy as a function of both p_c and q_c is shown in Figure 9b. It shows that the anisotropy is 0 when p_c or/and q_c is 1/3, which means that there is no detectable anisotropy once pump or probe dipole is completely isotropic.

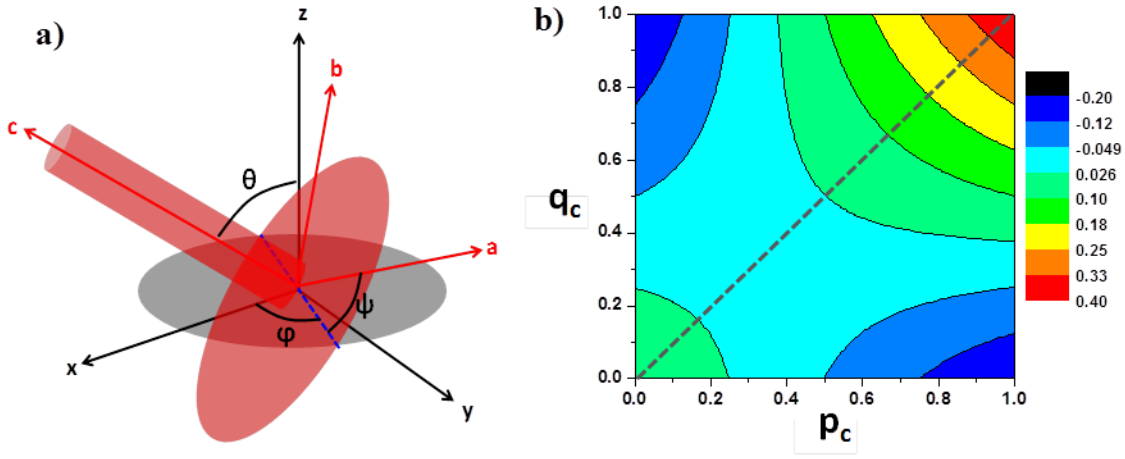

Figure A.7.4. a) A scheme of the laboratory coordinates (x, y, z) and the rod coordinates (a, b, c). Eulerian angles (θ,ϕ, ψ) are also labeled. b) 2-D contour plot of the calculated anisotropy as a function of both p_c and q_c.

TA anisotropy of CdSe NRs. For free CdSe NRs excited and probed at the band edge (590 nm) and probed at the exciton bleach (XB) signal, the transition dipoles for the pump and probe beams are the same. Therefore, $p_c = q_c$ and it corresponds to the diagonal dashed line in Figure A.7.4b. The anisotropy shown in Figure 4A is 0.12, from which we obtain: p_c=0.70. We also measured the anisotropy for the mid IR intraband TA signals after 590 excitation, which has negligible anisotropy (Figure A.7.5). Since p_c is 0.70 for the pump pulse, from Figure A.7.4b, q_c should be 1/3 for the intraband absorption. We can only probe the interband XB signal for anisotropy measurements.

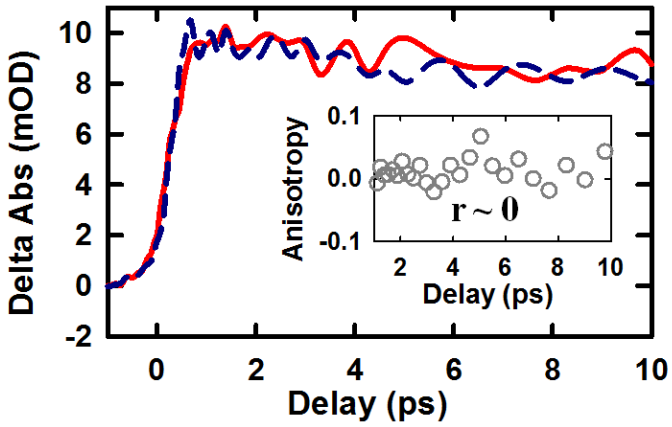

Figure A.7.5. Transient absorption anisotropy of Mid IR signals of CdSe NRs after 590 excitation. TA kinetics measured with parallel (red solid line) and perpendicular (blue dashed line) pump/probe polarizations. Inset: calculated anisotropy values.

Appendix 5

Excitation wavelength dependent QYs in the conventional mechanisms

The charge transfer QY from excited metal to semiconductor in the conventional PHET mechanism can be generally described by the Fowler's formula (equation 7.1 in the main text):[23] $QY(\hbar\omega) = (\hbar\omega - E_b)^2/4E_F\hbar\omega$, where $\hbar\omega$ is the energy of excitation photons, E_b is the barrier height between metal and semiconductor, and E_F is the Fermi energy of Au (5.5 eV). Equation 7.1 can be derived by considering both energy and momentum conservations in the hot electron transfer process.[24] As shown in Figure A.7.6a, the z-direction momentum of the hot electron has to be larger than onset momentum ($P_{on} = \sqrt{2m(E_F + E_b)}$). Therefore,

$$\sqrt{2m(E + \hbar\omega)} \cdot \cos\theta \geq \sqrt{2m(E_F + E_b)} \qquad \text{(A.7.11).}$$

According to this equation, the range of electron energy E is:

$$E_F \geq E \geq \frac{E_F + E_b}{\cos^2\theta} - \hbar\omega$$

(A.7.12),

and the range of angle θ is:

$$1 \geq \cos\theta \geq 1 - \frac{\hbar\omega - E_b}{2E_F}$$

(A.7.13).

Note that in deriving A.7.13, we have used the condition of $E_F \gg E_b$ and $\hbar\omega$. Therefore, the QY of hot electron injection is:

$$QY = \frac{1}{2N}\int_{1-\frac{\hbar\omega-E_b}{2E_F}}^{1} d\cos\theta \int_{\frac{E_F+E_b}{\cos^2\theta}-\hbar\omega}^{E_F} \rho(E)dE \qquad (A.7.14),$$

where $\rho(E)$ is the density of state (DOS) of the conduction band of metal, N is the total number of available electrons near Fermi level that can be excited and the coefficient 1/2 accounts for half of the total electrons moving towards semiconductor. Since $E_F \gg \hbar\omega$, we assume that the DOS is constant near Fermi level and therefore, $N = \hbar\omega\rho(E_F)$. With this assumption, the integral in equation A.7.14 results in: $QY(\hbar\omega) = (\hbar\omega - E_b)^2/4E_F\hbar\omega$.

It has been found that photoemission QYs from small nanoparticles are enhanced compared to planar bulk structures, possibly due to geometric effect[25,26] and lowering of escaping barrier.[27] In this case, the excitation energy dependence still follows Fowler's function form except that a scaling factor (C) is added to account for the enhancement: $QY(\hbar\omega) = C \cdot (\hbar\omega - E_b)^2/4E_F\hbar\omega$, which is the equation 7.2 used in the main text.

If electron scattering only occurs at the metal/semiconductor interface, the momentum conservation can be relaxed and electrons transfer into semiconductor as long as:

$$E + \hbar\omega \geq E_F + E_b \qquad (A.7.15).$$

In this case, the QY of hot electron injection is:

$$QY = \frac{1}{2N}\int_{E_F+E_b-\hbar\omega}^{E_F} \rho(E)dE=(\hbar\omega - E_b)/2\hbar\omega \qquad (A.7.16),$$

which is the equation 7.3 in the main text.

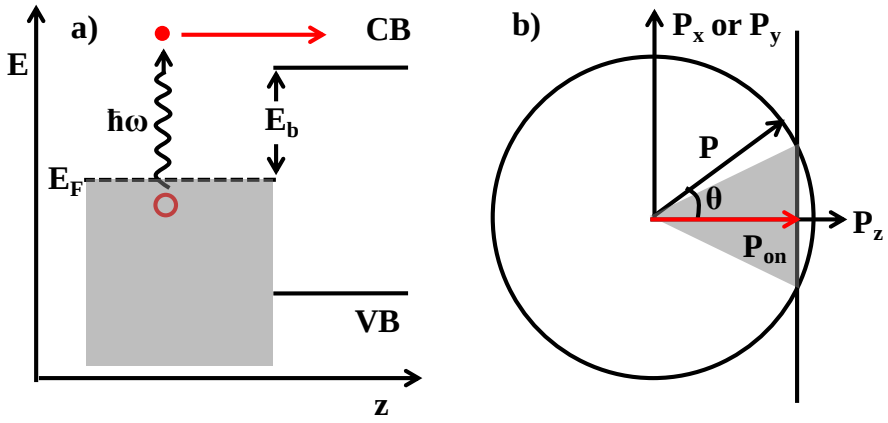

Figure A.7.6. Schematics of energy and momentum requirements in hot electron transfer a) Excitation of an electron into an energy level higher than the barrier (E_b) between Fermi energy of metal and conduction band edge of semiconductor leads to hot electron transfer into semiconductor. b) Illustration of momentum conservation in hot electron transfer process using "escaping cone" in momentum space. Z direction is perpendicular to the semiconductor/metal interface. Therefore, the projection of an electron momentum on the z axis has to be larger than an onset momentum (P_{on}) which is determined by E_b.

Chapter 8. The Competition between Band Alignment and Hole trapping in CdSe/CdS Quasi-type II Dot-in-rod Nanorods

8.1. Introduction

Recent advances in the synthesis of colloidal semiconductor heterostructures consisting of two or more material components have tremendously enriched the toolbox of semiconductor nanocrystals and produced new nanostructures with properties that cannot be achieved in single component materials.[1-8] The alignment of the conduction band (CB) and valence band (VB) positions of the components in the heterostructure can be type I, in which the CB and VB of one material are nested between those of the other ,[3,4] type II, when they are staggered with respect to each

other,[9,10] or quasi-type II, when either the CB or VB band edge positions are similar in these materials. The band alignment in core/shell quantum dots (QDs) has been shown to dictate the distribution of electrons and holes in excitonic states, which has profound effects on their properties. For example, in type I core/shell QDs such as CdSe/ZnS, both the electron and hole wavefunctions are localized in the core in the lowest energy exciton state, which reduces the effect of surface defects and improves their emission properties.[11-16] On the other hand, the spatial separation of electrons and holes in type II heterostructures can lengthen the lifetime of single and multiple exciton states and improve their charge separation properties for light harvesting applications.[10,17-19] In addition to material composition, the properties of nanoheterostructures can be further controlled by shape and size, as demonstrated in various one-dimensional (1D) colloidal nanorods (NRs).[7,20-27] Compared with QDs, these nanorods have larger absorption cross sections,[28-30] enhanced stabilities,[31,32] longer multi-exciton lifetimes,[33-36] and linearly-polarized emission[20,24,37-40] while retaining size-tunable quantum confinement effect in the radial direction,[41,42] making them promising materials for light emitting,[43,44] optical gain,[34,45,46] or solar energy conversion applications.[47-54]

Among one-dimensional heterostructures, CdSe/CdS dot-in-rod (DIR) NRs have attracted the most intense research interests.[20,23,24,47,55-78] They have been shown to enhance the charge separation efficiency in solar-to-fuel conversion systems

compared to CdS nanorods or CdSe/CdS core/shell QDs.[47-49] The VB and CB offsets between bulk wurtzite CdSe and CdS are ~ +0.5 V and -0.3 – 0 V, respectively, forming either a type I or quasi-type II heterojunction.[20,62] Despite recent investigations of this system by various techniques, including scanning tunneling spectroscopy,[62] transient absorption spectroscopy,[59,67] multi-exciton emission,[65] time-resolved fluorescence decay,[73,74] and first principle calculations,[63] the exact nature of the long-lived exciton states in the CdSe/CdS DIR structures remains a hotly debated topic. The band alignment in these materials has been reported to be type I,[62] quasi-type II,[59,74] or tunable from type I to quasi-type II depending on the core size and rod diameter,[65,73,75] as well as interfacial strain.[63] More recently, it has been suggested that even in quasi-type II DIRs, the CB electron is likely localized near the CdSe core,[75,79,80] because of the strong electron-hole coulomb attraction in one-dimensional structures.[81] Because the Bohr exciton radii of these materials (~5.4 nm in CdSe [82,83] and ~2.8 nm in CdS[84-86]) are relatively small compared to the rod length (typically 10s to 100s of nm), the fate of the initially generated electron-hole pairs depends on not only the band alignment but also their transport mechanism along the rod. The latter can be affected by deep hole traps on CdS NRs[87,88] and charge-transfer barrier at the CdSe/CdS interface.[66,89,90] Indeed, a recent study on CdSe/CdS tetrapods has demonstrated that the hole capturing efficiency by the CdSe core is not unity and there exist deep hole localized excitons on the CdS arms.[69]

In this chapter, we report a study of exciton relaxation and dissociation dynamics in CdSe/CdS DIRs by transient absorption (TA) spectroscopy. By comparing TA spectra of DIR and DIR-electron acceptor complexes, we show unambiguously that the bleaches of exciton bands in DIRs are caused by state-filling of the CB electron levels, similar to those observed in CdX (X=Te, Se, S) single component or core/shell QDs. We show that in the lowest energy band edge exciton state, the hole is confined in the CdSe core and the electron is delocalized among CdSe and CdS, consistent with a quasi-type II band alignment, although the electron wavefunction in the CdS shell is localized to regions near the CdSe core. Upon excitation of the CdS rod at 400 nm, three distinct long-lived exciton states are observed; only 46% of excitons can relax to the lowest energy band edge exciton state. Trapping of holes at the CdS rod or the CdS shell near the seed localizes excitons in those regions. Due to their distinct spatial locations, these excitons have different dissociation rates in the presence of electron acceptors. Our study suggests that in 1D heterostructures such as CdSe/CdS DIR, the fate of the exciton is determined not only by the band offset, but also by exciton trapping and localization processes that sensitively depend on the microscopic electronic and morphological heterogeneity of the materials.

8.2 Results and Discussions

8.2.1 Static Absorption and Emission Spectra.

A representative TEM image of CdSe/CdS DIRs used for this study is shown in Figure 1a, from which we determines an average length of 16.5 (±1.1) nm and diameter of 3.5 (±0.3) nm, respectively. Some of the rods show a bulb-like region with slightly large diameter near one end of the rod, similar to previous reports.[23,66] The bulb region is believed to indicate the location of the seed from which asymmetric growth along the rod (*vs* the radial direction) occurs in the growth progress.[66] Due to the presence of these bulb-structures, the diameter statistics is done at the centers of the DIRs.

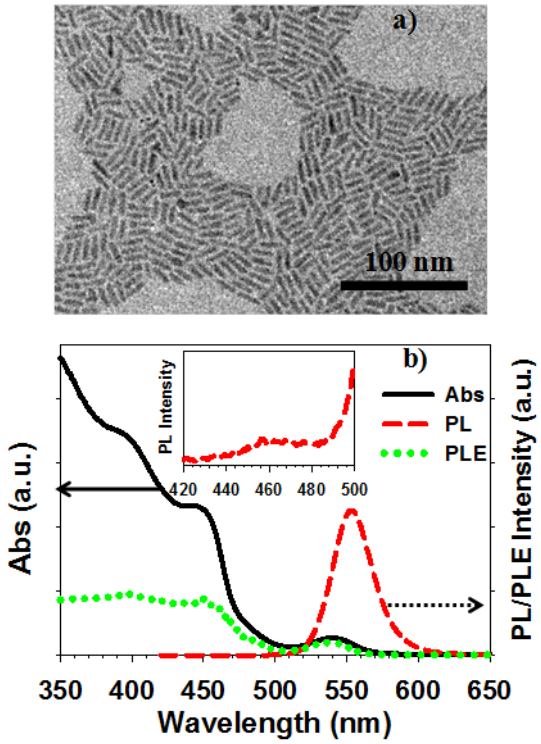

Figure 8.1. a) Representative transmission electron microscopy image of CdSe/CdS DIRs. b) UV-visible absorption spectrum (black solid line), photoluminescence (PL) spectrum measured with 400 nm excitation (red dashed line) and photoluminescence excitation (PLE) spectrum measured at 553 nm (green dashed line) of CdSe/CdS DIRs dispersed in chloroform. In the PLE spectrum, we have scaled the emission intensity to match the absorbance at 540 nm for better comparison. Inset: enlarged view of the PL spectrum between 420 and 500 nm.

The static absorption and emission spectra of DIRs are displayed in Figure 8.1b. The lowest absorption peak at ~540 nm can be assigned to the first excitonic transition, labeled as B3 in Figure 8.2b, from the valence band edge in the CdSe core to the lowest energy conduction level of the DIR, because it is close to the band edge

emission peak position (Figure 8.1b). It is below the onset of CdS absorption and red-shifted by about 0.18 eV with respect to the 1S exciton band of the starting CdSe seed. The red-shift indicates the extension of the electron wave function into the CdS shell/rod, which is indicative of a quasi-type II band alignment between CdSe and CdS and will be further discussed below. The peaks at ~400 and 450 nm can be attributed to the 1Π and 1Σ (labeled as B1 in Figure 8.2b) 1D excitonic transitions respectively, of the CdS rod in the DIR,[88] because of their resemblance to transitions in CdS NRs.[7,23,24,87,88,91] The contribution of CdSe core based transitions in this spectral region is negligible due to the much larger volume of the CdS rod.[59] In addition to these pronounced features, there exist an absorption feature near 480 nm (labeled as B2 in Figure 8.2b), which can be attributed to the lowest energy transition of the CdS in the bulb region surrounding the CdSe seed.[66] Because of the larger diameter in the bulb compared to the rod region, the carrier confinement energy is lower, which accounts for the lower transition energy. A similar CdS based absorption band has been seen in CdSe/CdS core/shell QDs of similar sizes.[92-96] In Figure A.1, we show that the absorption spectrum below 2.8 eV (440 nm) can be fit by the sum of three Gaussian peaks with centers at 2.76 eV (449 nm), 2.58 eV (480 nm), and 2.30 eV (539 nm), corresponding to B1, B2, and B3 transitions, respectively. This assignment will be supported by transient absorption study of these DIRs to be discussed below.

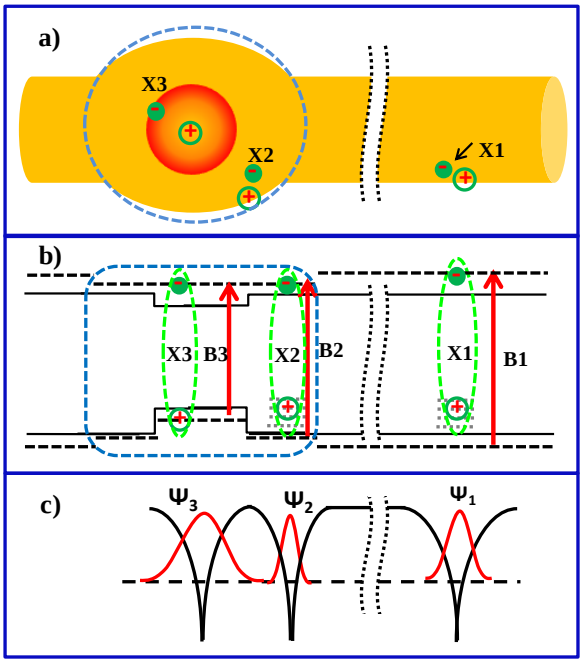

Figure 8.2. a) A schematic structure of a CdSe/CdS DIR prepared by seeded growth, showing a CdSe seed surrounded by a CdS rod and bulb-like region near the seed (blue dashed line). Also shown are the locations of three types of excitons (X1, X2, and X3). b) A schematic energy level diagram for CdSe/CdS DIR, showing bulk band edges of CdS and CdSe (black solid lines), lowest electron and hole energy levels in CdSe core, CdS bulb and CdS rod (black dashed lines) and sub-band gap hole trap states in CdS (gray dotted lines). Also shown are the electron and hole levels of the X1, X2 and X3 excitons (green dashed curves) and the three (B1, B2, B3) lowest energy optically allowed exciton absorption bands in the static absorption spectra (red arrows). c) Schematic electron wavefunctions of X1, X2 and X3 confined in the 1D Coulomb potential.

The photoluminescence (PL) of DIRs after 400 nm excitation has a peak at 553 nm, corresponding to the emission from the band edge excitonic state (X3) of the DIR.[20] An expanded view of the PL spectrum from 420-500 nm (inset in Figure 8.1b) reveals a weak yet discernible peak at ~460 nm which can be assigned to band-edge emission of CdS NRs.[88] This suggests that not all excitons generated with 400 nm excitation relax down to the band edge exciton state prior to their radiative recombination. In addition to the band edge emission, CdS rod based emission can also contain a broad trap state emission band between 500 nm and 900 nm,[88] which may be too weak to be observed in CdSe/CdS DIRs due to its overlap with the much more intense X3 exciton emission band at 553 nm.

To further investigate the fate of excitons in DIR, we have also measured photoluminescence excitation (PLE) spectrum, in which the PL intensity at 553 nm as a function of the excitation wavelength was recorded (Figure 8.1b). Accounting for the wavelength dependent absorbance, the relative emission quantum yields (QYs) at 400, 480 and 540 nm excitations are estimated to be 0.46, 0.84 and 1, respectively. The absolute QYs at 400 nm excitation (using coumarin 343 as reference[97]) and at 540 nm excitation (using rodamine 6G as reference[98]) were also determined independently to be 22.5(±1.2) % and 48.7(±2.0)%, respectively. The ratio between the QYs at these two wavelengths (0.46) agrees well with the relative QY estimated from the PLE spectrum. The smaller QY at 400 nm excitation suggests that 54% of

the excitons generated at the CdS rod do not reach the band edge (X3) exciton state. This is consistent with the observation of the CdS rod based emission at 460 nm discussed above.

8.2.2 Nature of Lowest Energy Band Edge Exciton (X3) State.

The TA spectrum of DIRs (from 0.1 ps to 50 ns) after 540 nm excitation (13 uw pump power, 0.008 excitons per DIR) is shown in Figure 8.3a. There are two main bleach features at 540 and 480 nm. Compared with the static absorption spectrum in Figure 8.1b, we can assign the feature at 540 nm to photo-induced bleach of B3 exciton band (or B3 bleach) and the feature at 480 nm to the bleach of B2 band. This feature cannot be assigned to high energy transition of CdSe seed. This is supported by a comparison with the TA spectra of a bare CdSe core-only QD with similar confinement energy, which usually shows derivative like features in this wavelength range (430-480 nm) due to the Stark effect of 1S excitons on higher energy transitions.[99]

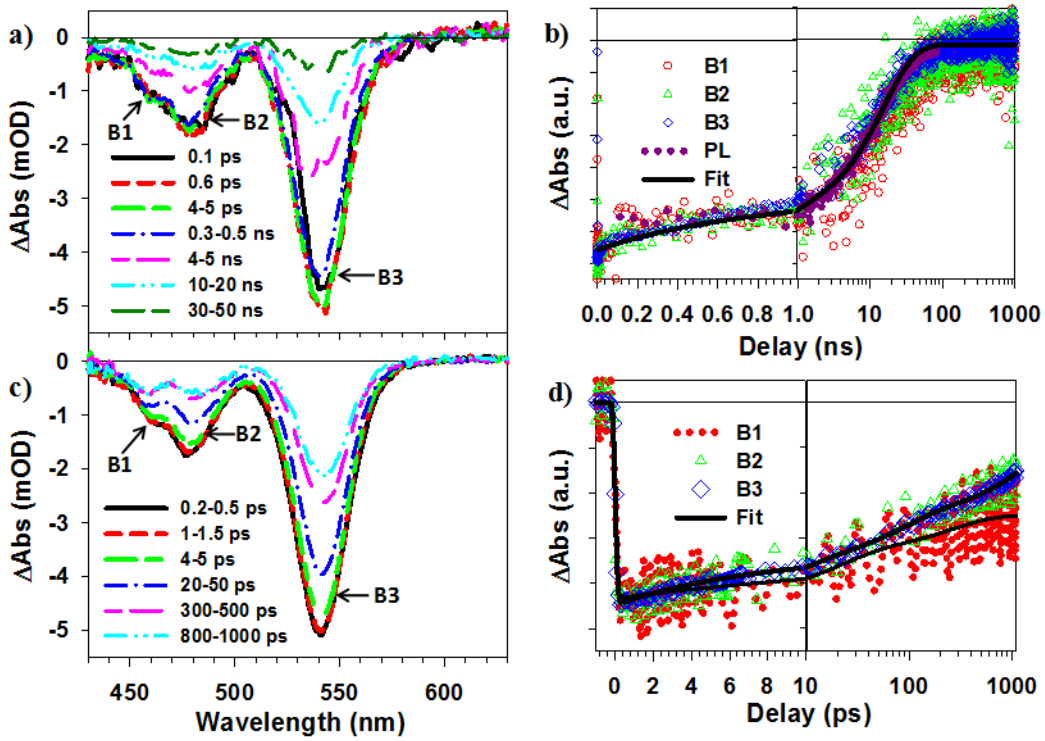

Figure 8.3. TA spectra and kinetics of DIRs (a,b) and DIR-BQ complexes (c,d). a) TA spectra of DIRs from 0.1 ps to 50 ns after 540 nm excitation. b) Kinetics of B1 (red circles), B2 (green triangles), B3 (blue diamonds) bleaches shown in panel a), time-resolved PL decay (purple dotted line, measured at 532-650 nm with 400 nm excitation) and multiple-exponential fits (black solid lines). c) TA spectra of DIR-BQ complexes from 0.2 to 1000 ps after 540 nm excitation. d) Kinetics of B1 (red dots), B2 (green triangles) and B3 (blue diamonds) bleaches shown in panel c) and multi-exponential fits (black solid lines).

Previous TA studies of group II-VI QDs[19,92,99-101] or nanorods[36,49,88,102] have shown that the bleach in exciton bands can be attributed to the state-filling of the CB electron levels with negligible contribution of VB hole-filling signals.[99,103,104] The lack of VB hole state-filling signal is generally attributed to higher density and degeneracy of the hole levels in II-VI semiconductors.[99,103,104] TA Study of DIR- methyl viologen (MV^{2+}) complexes, in which CB electrons are selective transfer to the MV^{2+} acceptor (Figure A.2a and A.2b in the Supporting Information), shows that the exciton bleach features in the DIR TA spectra are also caused exclusively by state-filling of the CB electron level associated with the transition and they can be used to follow the kinetics of CB electrons. [19,36,88,92,100,101,105] To confirm that the same assignment of exciton bleach signals applies in CdSe/CdS DIRs, we performed charge separation experiments to selectively remove CB electrons.[19,36,88,92,100,101,105] Shown in Figure A.2a and A.2b (in Appendix 2) are the TA spectra of DIR- MV^{2+} complexes at 1200 ps after 400 and 540 nm excitations, respectively. In both cases, the state-filling signals are completely removed and the remaining spectra can be attributed to the superposition of reduced $MV^{+\bullet}$ radical and charge-separation induced Stark-effect signals.[19,88,92] Therefore, the exciton bleach features in the DIR TA spectra are caused exclusively by state-filling of the CB electron level.

The kinetics of B2 and B3 after 540 nm excitation are shown in Figure 8.3b, along with the band edge exciton PL decay kinetics. It can be seen that these kinetics agree

well with each other and can be fitted by the same two-exponential decay function which gives an amplitude-weighted averaged lifetime of τ_{ave}= 13.0±0.16 ns. The agreement of the B2 and B3 kinetics indicates that these transitions involve the same electron level, which suggests that the lowest energy CB electron level in the DIR is delocalized between the CdSe core and CdS bulb, as depicted in Figure 8.2b. The observed quasi-type II band alignment is consistent with the electronic structure of CdSe/CdS core/shell QDs of similar core and shell dimensions.[92-96] The agreement of the TA and PL kinetics indicates that the lowest energy VB hole in CdSe core decays mainly through recombination with the electron, which is consistent with their spatial separation from the nanocrystal surface. Based on the average PL lifetime of 13.0±0.16 ns and the average PL QY of 48.7(±2.0) % under 540 nm excitation, an average radiative recombination time constant τ_r is estimated to be 26.7 ns using $\tau_r = \tau_{ave}/QY$. This radiative lifetime is comparable to CdSe/CdS core/shell QDs, consistent with electron delocalization into CdS and a quasi-type II band alignment in the bulb region.[106]

In addition to B2 and B3, Figure 8.3a also shows a small apparent bleach feature at ~455 nm, near the B1 transition of the CdS rod. In free QDs, B1 bleach kinetics agrees well with B2 and B3 bleach recovery. It suggests two possible origins for the small B1 feature. It may result from the state filling induced bleach of the B1 transition, which would suggests that the lowest energy CB electron level also extends

into the CdS rod. Alternatively, it may be a Stark-effect signal generated by the lowest energy exciton, which leads to derivative like features of the B1 transition.

To differentiate these two possibilities, we have also measured TA spectra in DIR-Benzoquinone (BQ) complexes (Figure 8.3c) at 540 nm excitation. BQ is chosen because it is a well-known electronic acceptor whose reduced form does not absorb in the visible region.[36,88,92,107,108] Furthermore, electron transfer rate in DIR-BQ complexes is relatively slow so that we can accurately compare the bleach recovery kinetics of B1, B2, and B3 transitions. Similar comparison is not possible in DIR-MV^{2+} complexes due to much faster ET rates. As shown in Figure 8.3c, both B2 and B3 decay much faster in DIR-BQ complexes than in free DIRs, consistent with the expected ET from DIR to BQ. Comparison of the normalized B2 and B3 kinetics (Figure 8.3d) shows that they agree well with each other, suggesting that these transitions involved the same lowest energy electron levels, consistent with the assignment above. These recovery kinetics can be fitted with the same three-exponential decay function with a half life of 312 ± 40 ps. It is also clear from Figure 8.3c and 8.3d that the B1 feature decays much less than B2 and B3 in DIR-BQ complexes. It suggest that this feature in the TA spectra of free DIR (under 540 nm excitation) can be attributed to the derivative like feature in B1 transition caused by the Stark effect of (or exciton-exciton interaction with) the lowest energy exciton.[99,104] In DIR-BQ complexes, the decay of the lowest energy electron forms

charge-separated state, which also causes Stark-effect signal of the B1 transition, leading to negligible decay of the B1 feature.[19,36,49,88,92,109] Furthermore, the TA spectrum in Figure 8.3a can be well represented by the sum of Stark effect signals in B1, B2 and B3 and state-filling signals in B2 and B3, as shown in Figure A.3, which further supports the proposed assignment.

8.2.3 Excitation Wavelength Dependent Exciton Relaxation Dynamics.

We first examine the exciton dynamics with excitation pulses centered at 480 nm (7.5 w pump power, 0.007 excitons per DIR). This pump pulse selectively excites the bulb-like CdS shell region (B2 transition) with a minor contribution by the CdS rod (B1 transition). The TA spectra within the first 2 ps after 480 nm excitation (Figure 3a) show bleach features at B1 (~ 455 nm), B2 (~ 480 nm), and B3 (~ 540 nm) transitions. The formation and decay kinetics of these features and their multiple-exponential fits are shown in Figure 8.4d.. Both B2 and B3 bleach bands contain a nearly instantaneous formation component and a smaller growth component with time constants of 0.375 ± 0.060 ps and 0.403 ± 0.069 ps, respectively. The instantaneous formation of the B3 bleach upon excitation of B2 band confirms that these transitions share the same CB electron level, consistent with the findings of 540 nm excitation discussed above. The B1 bleach shows an instrument response limited (<0.01 ps)

formation time and a fast decay component with a time constant of 0.391 ±0.051 ps that agrees well with the formation time of the second growth component of B2 and B3 bleach features. It suggests that B1 bleach is formed by the direct excitation of the B1 transition and its decay leads to the formation of the second growth component of the B2 and B3 bleach. This exciton decay kinetics is further confirmed below with 400 nm excitation.

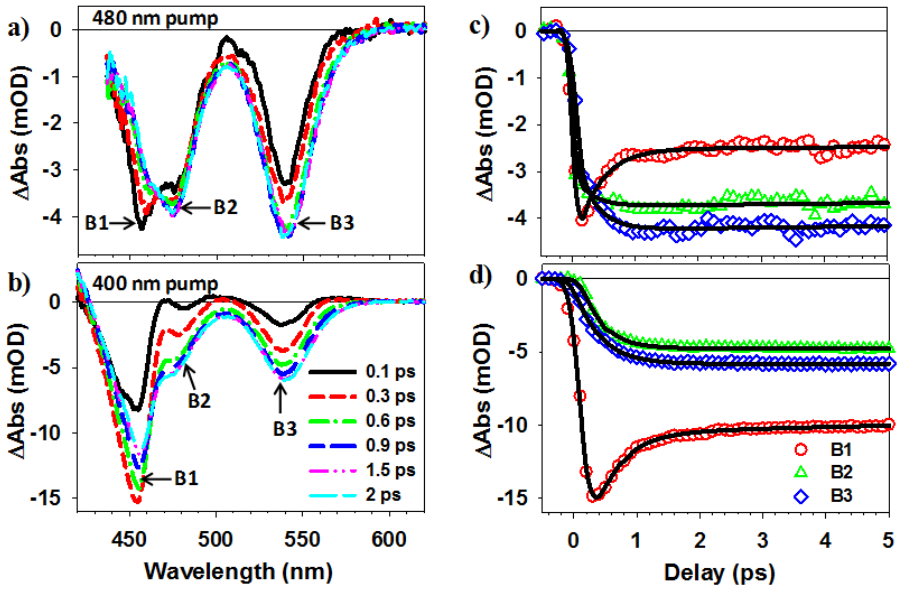

Figure 8.4. TA spectra and kinetics of DIRs at early delay time (0-5 ps) after 480 and 400 nm excitation. TA spectra at indicated delay times (a, c) and formation and decay kinetics of B1, B2 and B3 bleach (b & d) after 480 nm (a, b) and 400 nm (c, d) excitation. The black solid lines in b) and d) are multi-exponential fits according to a

model described in the supporting information and fitting parameters are listed in Appendix.

The evolution of TA spectra of DIRs within the first 2 ps after 400 nm excitation (5 uw pump power, 0.02 excitons per DIR) is shown in Figure 8.4c. Although both the CdSe seed and CdS bulb region have higher energy transitions at this excitation wavelength, the absorption is dominated by the CdS rod due to its much larger volume, leading to a selective generation of excitons in the CdS rod. The TA spectra show a partial decay of B1 bleach and the corresponding growth of B2 and B3 features. The formation and decay kinetics of these features within the first 5 ps are compared in Figure 8.4d. They can be well fit by multi-exponential functions. The B1 bleach shows a formation time of 0.066 ± 0.015 ps, which can be attributed to electron relaxation process from the initially excited 1π to the 1σ CB level within the CdS NR.[88] The decay of B1 bleach contains a fast component with 53% of its amplitude and a time constant of 0.422 ± 0.052 ps and a slow component on the ns and longer time scale (see below). B3 kinetics exhibits a single-exponential rise time constant of 0.407 ±0.041 ps. At early decay times, the signal at the B2 spectral region consists of the bleach of B2 band as well as the red-shifted absorption of B1 band that has been attributed to the effect of hot (1Π) exciton on the transition energy of 1Σ exciton. Taking both features into account, the fit reveals a B2 bleach formation time

constant of 0.387±0.057 ps. The agreement between the time constants for B1 bleach decay and B2 and B3 bleach formation suggests that 53% of the initial excitation in the CdS rod decays to form the B2 and B3 bleach features in the bulb and seed regions.

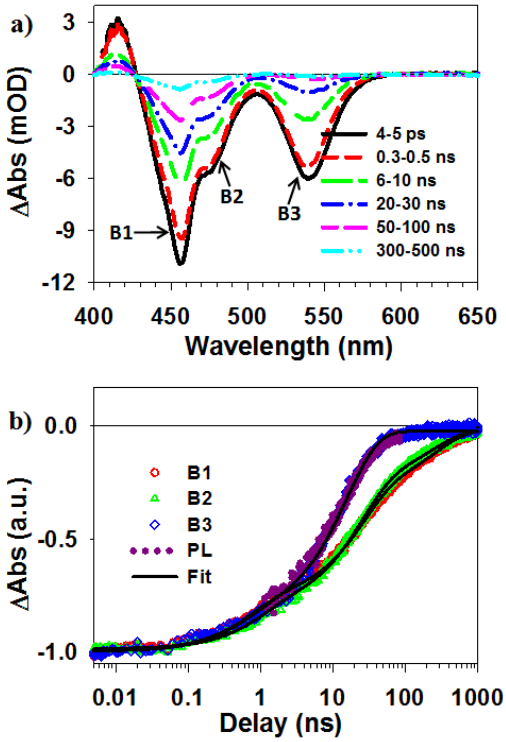

Figure 8.5. TA spectra and kinetics of DIR at 5 ps – 1 μs after 400 nm excitation. a) TA spectra of DIRs at indicated delay time windows. b) Kinetics of B1 (red circles), B2 (green triangles), B3 (blue diamonds) features shown in panel 2a, PL decay kinetics (purple dotted line) of DIRs measured at 532-675 nm after 400 nm excitation, and multi-exponential fits (black solid lines).

TA spectra and kinetics of DIRs at longer delay times (5 ps to 1 us) after 400 nm excitation are shown in Figure 8.5. There are no apparent interchanges between B1, B2 and B3 features and their decay kinetics can be well described by multi-exponential functions. B3 kinetics is the same as that measured with 540 nm excitation and can be fit by the same parameters. It suggests that the decay kinetics of excitons that are responsible for the B3 bleach feature is independent of their generation processes (*via* direct excitation or relaxation from higher energy exciton states). The half-lives are 22.5(±1.7), 21.0(±1.6), and 8.34 (±0.31) ns for B1, B2, and B3, respectively. Compared to B3 bleach, considerably longer lifetime times are observed for the B1 and B2 bleach features. The different decay times observed for these features suggest that the initial exciton generated on the CdS rod can decay into three distinct long-lived states in the DIR and these states do not convert into each other after the first ps.

8.2.4. Assignment of Three Long-Lived Exciton States.

It is clear from the TA study that the lowest energy exciton (X3) generated with 540 nm excitation involves a hole in the CdSe core and an electron that is delocalized into the CdS shell in the bulb region, which is shown in scheme 1a and 1b. As a result, the presence of this exciton leads to the bleach of both B2 and B3 transition, as shown in

Figure 8.3a. The B2 bleach amplitude in the TA spectra is smaller than B3 bleach, whereas they have comparable absorption cross sections in the static absorption spectrum. It suggests that in the X3 exciton state, despite the quasi-type II band alignment, the electron is not delocalized throughout the entire bulb and is confined in the CdS shell that is closed to the CdSe core. It should be noted that similar core localized exciton have been observed in CdSe/CdS quasi-type II core/shell QDs, in which the localization of holes to the CdSe core leads to an increase of the bleach of lowest energy transition even though the electron is directly excited to the lowest energy CB level.[92] This phenomenon is attributed Coulomb-attraction induced electron localization process to be elaborated below.

The PLE spectrum (Figure 8.1b) shows that excitation at higher energy also leads to X3 exciton emission. However, not all higher energy excitons relax to the X3 state, suggesting the presence of other exciton decay pathways. Direct excitation of the bulb region (B2 transition) leads to the bleach of B2 and B3, as shown in Figure 3a. Formation of B3 bleach is indicative of the presence of X3 excitons. The TA spectra show a larger relative amplitude of B2 than B3 bleach features compared to the TA spectrum of X3 (Figure 8.3a), suggesting that 480 nm excitation generates other species in addition to the X3 exciton. To obtain the spectrum of the yet-to-be assigned exciton feature, we can subtract the total spectrum by the contribution of X3. This subtraction procedure avoids the need to model the exact line shape of TA bleach

associated with excitons, which are often complicated due to exciton fine structure[110] and bi-exciton interaction induced spectral shifting.[99,104] In Figure 8.6a, we plotted the averaged TA spectra at 5-10 ps after 400 nm (black solid line), 480 nm (purple dashed line), and 540 nm (blue dotted line) excitation. They have been normalized at the B3 bleach peak. Because 540 nm excitation creates X3 excitons, we assign the difference spectrum between the TA spectra of 480 and 540 nm excitation (green triangles in Figure 8.6a) to X2 excitons. Similarly, the difference spectrum between 400 nm and 480 nm excited TA spectra (red circles in Figure 8.6a) is attributed to X1 excitons. We note that a small contribution of X1 exciton to the TA spectrum of 480 nm excitation has also been subtracted to yield the X2 exciton spectrum shown in Figure 8.6a.

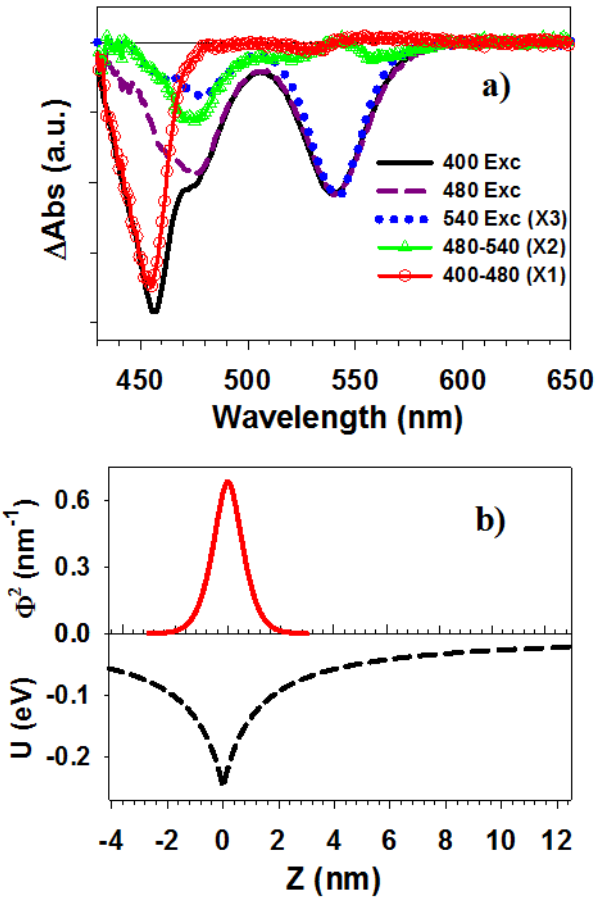

Figure 8.6. a) Averaged TA spectra of DIRs from 5 to 10 ps after 400 nm (black solid line), 480 nm (purple dashed line) and 540 nm (blue dotted line) excitations. The spectrum measured at 540 nm excitation is assigned to X3 excitons. The difference spectrum between 480 nm and 540 nm excitation (green triangles) is assigned to X2 excitons and the difference spectrum between 400 nm and 480 nm excitation (red circles) is assigned to X1 excitons. b) 1D electron-hole coulomb potential profile (black dashed line) and the corresponding electron probability density of the 1D exciton ground state (red solid line) as a function of electron-hole distance along the DIR long axis (Z). See main text for details.

As shown in Figure 8.6a, the X2 exciton spectrum shows a bleach of the B2 band with small derivative like features at B3 and B1 transitions. The latter can result from subtraction errors and/or the Stark effect of the X2 exciton on B1 and B2 transitions. In the subtraction procedure we have assumed all B3 bleach is caused by X3 exciton. According to the PLE spectrum (Figure 8.1b), the band edge emission QY at 480 nm excitation is only 84% of that at 540 nm excitation, suggesting that 84% and 16 % of the excitons generated at 480nm relax to X3 and X2 exciton states, respectively. Therefore, it is reasonable to assume that majority of the B3 bleach amplitude in Figure 8.4a is caused by the presence X3 exciton, although we cannot exclude a small contribution of the X2 exciton to B3 bleach. Despite this uncertainty, it is reasonable to conclude that the spatial distribution of the electron associated the X2 exciton is different from that of X3 exciton, such that the former does not lead to or has much smaller contribution to the state filling induced bleach in B3 transition. In light of the quasi-type II band alignment between CdSe/CdS, we propose that one way to satisfy this requirement is to have the electron strongly bound to a hole that is localized on a surface trap state, as depicted in Figure 8.2a and 8.2b. Within this model, the initial excitation at 480 nm generates delocalized electrons and holes in the CdSe/CdS bulb region, which leads to instantaneous formation of B2 and B3 bleach observed in Figure 8.4a. The localization of holes to the CdSe core, driven by large valence band

offset between CdSe and CdS, forms X3 excitons, in which the conduction band electron is also localized near the CdSe core. In competition with this process, holes can also be trapped on the surface trap states of the CdS bulb, which localizes the electrons near the trapped holes, forming the X2 exciton.

Similarly, X1 exciton spectrum is well represented by the bleach of B1 transition, with minor derivative like features at B2 and B3 transitions. Initial excitation at 400 nm generates delocalized electrons and holes on the CdS rod. Because of the smaller quantum confinement energy of both valence band holes and conduction band electrons in the bulb compared to the rod, these carriers can be transfer into the bulb region, which can then form X3 and X2 excitons similar to the dynamics observed by direct excitation at 480 nm. In competition with this process, the valence band holes can also be trapped on the CdS rod surface, which localizes the electrons and forms the X1 exciton, as depicted in Figure 8.2b. In the X1 exciton state, the electrons are located in the conduction band of the CdS rod, which accounts for the B1 bleach, but they are bound to the trapped holes. The decay of the X1 and X3 excitons can be directly monitored by B1 and B3 bleach recovery kinetics. The X2 exciton decay kinetics can be obtained by subtracting the contribution of X3 exciton to the B2 bleach. The long and uncorrelated lifetime of X1, X2 and X3 excitons and the lack of inter conversion between these species after the initial ultrafast hole localization

processes (Figure 8.5) suggests that X1 and X2 excitons are strongly bound due to either large Coulomb binding energy and/or deep hole trap energy.

It is worth noting that the TA spectra of DIR under 400 nm and 480 nm excitations show similar relative amplitudes of B2 and B3 bleach features. It implies that there is a constant partitioning factor between holes localizing in the core and on the bulb surface, regardless whether they are initially generated *via* direct excitation (in the case of 480 nm pump) or transfer from the CdS rod (in the case of 400 nm pump). This partitioning factor is determined by the relative rates of hole trapping to the shell surface and hole transfer to the core in the quasi-type II CdSe core/CdS shell structure. From the initial decay (53%) of the B1 bleach at 400 nm excitation and the yield (46%) of hole capture to CdSe core determined by PLE, the branching ratio of forming the long-lived X1, X2 and X3 exciton states at 400 nm excitation can be estimated to be 47%, 7% and 46 %, respectively. This X2:X3 branching ratio (13:87) is consistent with the value for 480 nm excitation (16:84) that we have estimated above from the PLE spectrum.

The proposed model of X1 and X2 excitons require large binding energies and spatially localized electron and hole wavefunctions, which can arise from the dielectric confinement effect in 1D nanorods. Because the motion of electrons and

holes in the radial direction of NRs are much faster than the axial direction, it is reasonable to average the electron-hole Coulomb interaction over the radial coordinates, yielding an effective 1D Coulomb potential along the axial direction.[81] Efros and co-workers have shown the enhanced 1D Coulomb interaction in CdSe NRs leads to the formation of strongly bound 1D excitons with large electron-hole binding energy of over 0.15 eV and small exciton radius of 1.6 nm.[81] According to this model, the 1D coulomb potential profile is: [81]

$$U(z) = -e^2/\kappa_m(|z| + \rho_{eff}), \qquad (8.1)$$

where e is the electron charge, κ_m is the dielectric constant of the medium, and $|z|$ is the distance between electron and hole. ρ_{eff} is the effective screening length, which is assumed to be 0.7a (a is the radius of the NR), same as the value determined for CdSe NRs.[81] At $|z| = 0$, we have $U_0 = U(0) = -e^2/\kappa_m\rho_{eff}$, the depth of the coulomb potential well. Therefore Eq. (1) can be simplified to:

$$U(z) = U_0\rho_{eff}/(|z| + \rho_{eff}). \qquad (8.2)$$

Using the κ_m (3.2) of chloroform[111] and ρ_{eff} of 1.21 nm, the depth of potential well U_0 is calculated to be 0.25 eV for CdS rod. The Coulomb potential profile as a function of e-h separation distance (z) is shown in Figure 8.6b lower panel. The wavefunctions of 1D excitons confined in this potential well are Whittaker-type functions , $\Phi(z) \propto W_{\alpha,1/2}(\bar{z})$, with $\bar{z} = 2(|z| + \rho_{eff})/(a_{1D}\alpha)$. Here $a_{1D} =$

$e^2\kappa_m/\hbar^2\mu$ and $\hbar$ is the reduced Plank constant and μ the reduced mass of electron-hole pair.[81,112] The ground state is the first even state satisfying the boundary condition: $\frac{d\Phi(z)}{dz}(z = 0) = 0$. Solving this equation gives the first root at $\alpha = 0.185$. The resulting probability density distribution is shown in Figure 5b upper panel. It shows that the excitons are highly localized with 87.6% of the total density found within ±1 nm from the hole. Although this simple calculation is for axially delocalize electrons and holes in CdS nanorod and may differ from the electrons that are bound to holes that are trapped at the CdS surface or CdSe core, their much smaller dimension compared to the rod length provides qualitative support for spatially separated and localized X1, X2 and X3 excitons in the CdSe/CdS nanorods.

8.2.5. Charge Separation from Three Types of Excitons.

To further examine the nature of X1, X2, and X3 excitons, we have also investigated charge separation properties of DIR-BQ complexes. The TA spectra of DIR-BQ complexes at indicated delay times after 400 nm excitation are shown in Figure 8.7a upper (0 -1000 ps) and lower (1 -2000 ns) panels. They show the initial formation of B1, B2 and B3 bleaches within the first ps, same as in free DIRs, indicating the formation of X1, X2 and X3 excitons. All three bleach features recover faster than

free DIRs (Figure 8.5), which can be attributed to electron transfer to BQ. The decay of the exciton bleach leads to the formation of much weaker TA features that are derivatives of the B1, B2 and B3 exciton bands and can be assigned to the TA spectrum of charge separated states (CS or DIR^{+}-BQ^{-}). Similar spectral evolution on a much faster time scale can be observed in DIR-MV^{2+} complexes and in other QD-electron acceptor complexes.[109,113,114]

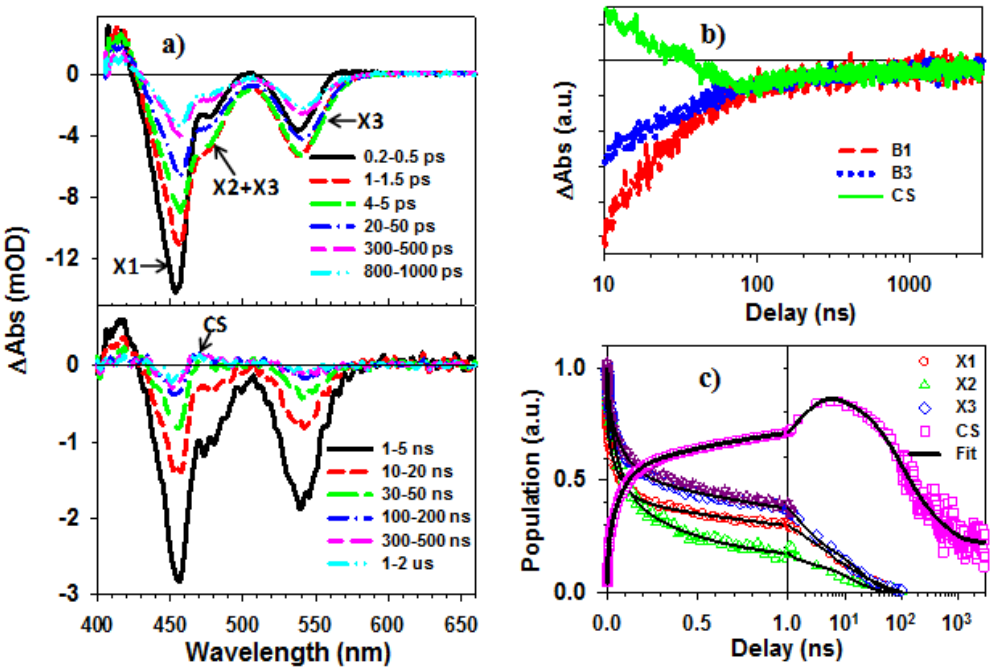

Figure 8.7. TA spectra and kinetics of DIR-BQ complexes measured at 400 nm excitation. a) TA spectra of DIR-BQ complexes at 0.2 to 1000 ps (upper panel) and 1 to 2000 ns (lower panel). b) Comparison of kinetics of B1 and B3 and CS (labeled in panel a) features from 1 to 3000 ns. CS signal has been inverted and all signals have been normalized to the same value at 100 – 3000 ns. c) Time-dependent populations of X1 (red circles), X2 (green triangles), X3 (blue diamonds) and charge separated

state (CS, pink squares) from 0 to 3000 ns and their multi-exponential fits (black lines). Also shown for comparison is the X3 exciton dissociation kinetics measured at 540 nm excitation (purple stars).

The special evolution from excited NR to CS features is completed at ~ 100 ns, indicating the completion of the exciton dissociation process. The decay of the charge separated state TA spectral features on the 100 – 3000 ns time scale can be attributed to the charge recombination process. This can be further illustrated by the comparison of normalized kinetics of B1, B3 and CS shown in Figure 8.7b. The CS kinetics reflects the TA signal between 460-470 nm, which switches from negative state filling induced bleach in the excited NR to a positive Stark-effect feature in the charge separated states.[88] The kinetics of this CS peak is inverted and scaled to compare with B1 and B3 in Figure 8.7b and all of them have been normalized to have the same value at 100 ns. Indeed, after ~100 ns, all three features decay in the same way and can be attributed to charge recombination. It should also be noted the B1 and B3 bleach decay kinetics does not agree with those in free DIRs and cannot be assigned to the presence of free DIRs in the assemble of DIR-BQ complexes. It is important to point out that the CS states resulted from the dissociation of these three excitons may have different spectra and recombination rates. However, due to their small signal amplitudes, these different charge separated states cannot be differentiated in this

measurement. As a result, we can assume that there is one CS state spectrum, whose decay reflects the average charge recombination time.

Because of the overlap of X1, X2, X3 and CS TA spectra, a quantitative extraction of charge separation and recombination kinetics requires the fitting of the TA spectra in Figure 6a by the time-dependent contributions of these spectral components. The time-dependent coefficients for the former and the latter are charge separation and recombination kinetics, respectively, which are shown in Figure 8.7c.

The kinetics of X3 exciton recovery is identical to that measured at 540 nm excitation, showing a half-life of 312±40 ps. The kinetics of X1 and X2 exciton dissociation can also be fitted to multi-exponential decays and the fitting parameters are listed in Table S5. The half-life times are 63.5(±21) ps and 112(±49) ps for X1 and X2, respectively. The exciton dissociation rates show a trend of X1> X2 > X3, showing the slowest ET rate for the X3 exciton. This is consistent with the electron distribution of X3 exciton, which is largely localized in and near the CdSe core, away from the CdS surface and reducing its electronic coupling with the acceptor. The dissociation rate for X1 is similar to that in CdS NR-BQ complexes (~90 ps),[88] although a quantitative comparison is difficult as the rate likely depends on rod length and the number of absorbed BQ molecules.

The time-dependent population of the charge separated state can be well fit to a three-exponential function, from which a half-life of 155±27 ns for charge recombination is extracted. The slow recombination in DIR-BQ complexes is a result of hole localization: they are either localized in the core (X3) or localized in the deep-trapping center on CdS surfaces (X1, X2). This is consistent with previous reported slow charge recombination in systems with core localized or surface trapped holes, such as CdSe/ZnS,[109] CdTe/CdSe,[19] CdSe/CdS[92] core/shell QDs or CdS NRs.[88]

8.3. Conclusion

In conclusion, using CdSe/CdS dot-in-rod 1D nanorods as a model system, we have studied exciton formation, relaxation and dissociation dynamics in 1D nanorod heterostructures by transient absorption spectroscopy. CdSe/CdS nanorods were prepared by a seeded growth method, consisting of a CdSe seed surrounded by a CdS shell and a CdS rod. Difference in the quantum confinement energy in the CdS shell and rod region (caused by the larger diameter in the former) and bulk band edge positions in CdSe and CdS leads to three distinct optical absorption features in the DIR with their lowest energy transitions, labeled as B1, B2 and B3 in Scheme 1b. We showed that excitation at B3 transition leads to the bleach of B2 and B3 transitions.

Because B3 transition directly generates the band edge exciton (X3) with a hole localized in CdSe valence band and electron in the lowest energy conduction band level of the DIR, the formation of B2 bleach suggests that the electron level is delocalized in the CdSe seed/CdS shell region, indicating a quasi-type II band alignment.

Excitation of B2 transition, promoting an electron from the lowest energy VB of the CdS shell to the lowest energy delocalized CB level of the CdSe seed/CdS shell region, leads to the bleach of B2 and B3 transitions and a larger amplitude of B2 bleach compared to the TA spectrum of the X3 exciton. It suggests the formation of X2 exciton (with bleach of B2 band) in addition the X3 excitons. Excitation at B1 generates excitons at the CdS rod region: 47% of the excitons relax to form X1 excitons, with electrons in the conduction band of the CdS rod (giving rise to the B1 bleach); 7% and 46%, of the remaining excitons relax to X2 and X3 states, respectively. These exciton states are long-lived, with half-lives of 22.5(±1.7) ns, 32.1(±2.2) ns, and 8.34±0.31 ns for X1, X2 and X3 excitons, respectively. The lack of inter conversion between these exciton states suggests that they are spatially separated and/or strongly bound.

We propose that in the X3 exciton state, the electron is localized in and near the CdSe seed due to strong Coulomb attraction by the CdSe confined hole, despite the quasi-type II band alignment. The formation of X2 state is driven by hole trapping on

CdS shell, which localizes the electrons to the surface-trapped holes. The hole driven localization process and strong electron-hole interaction forms spatially separated X2 and X3 excitons despite their common electron level in this 1D material with quasi-type II band alignment. Similarly, the X1 exciton state is formed by hole trapping on the CdSe rod, which localizes the electron and separates X1 from X2 and X3 excitons. The hole driven exciton localization process occurs with a time constant of ~0.4 ps, likely limited by the hole transfer/trapping rates due to their larger effective mass. The partition between these exciton states is controlled by the relative rates of hole localization and trapping. To provide further support of the proposed exciton identity, we have also study their dissociation kinetics in DIR-benzoquinone complexes. In the presence the electron acceptor, we showed that these excitons are shorter-lived due to electron transfer to the acceptors and their electron transfer rates are different. The X3 excitons show the slowest dissociation rate, consistent with the proposed structure in which the electrons are localized near the CdSe seed further away from the CdS surface compared to the X1 and X2 excitons.

Our results demonstrate that in 1D nanorod heterostructures, the fate of excitons is determined by not only the overall band alignment of the components but also the dynamics of exciton relaxation. The latter can be strongly influenced by carrier trapping induced exciton localization due to strong electron-hole interaction in 1D

materials. The distinct spatial locations of these excitons have important effect on their application as the light harvesting materials for solar energy conversion.

References

(1) Milliron, D. J.; Hughes, S. M.; Cui, Y.; Manna, L.; Li, J.; Wang, L.-W.; Paul Alivisatos, A. *Nature* **2004**, *430*, 190.

(2) Reiss, P.; Protière, M.; Li, L. *Small* **2009**, *5*, 154.

(3) Hines, M. A.; Guyot-Sionnest, P. *J. Phys. Chem.* **1996**, *100*, 468.

(4) Dabbousi, B. O.; Rodriguez-Viejo, J.; Mikulec, F. V.; Heine, J. R.; Mattoussi, H.; Ober, R.; Jensen, K. F.; Bawendi, M. G. *J. Phys. Chem. B* **1997**, *101*, 9463.

(5) Peng, X.; Schlamp, M. C.; Kadavanich, A. V.; Alivisatos, A. P. *J. Am. Chem. Soc.* **1997**, *119*, 7019.

(6) Scholes, G. D. *Adv. Funct. Mater.* **2008**, *18*, 1157.

(7) Shieh, F.; Saunders, A. E.; Korgel, B. A. *J. Phys. Chem. B* **2005**, *109*, 8538.

(8) Smith, A. M.; Nie, S. *Acc. Chem. Res.* **2009**, *43*, 190.

(9) Kim, S.; Fisher, B.; Eisler, H.-J.; Bawendi, M. *J. Am. Chem. Soc.* **2003**, *125*, 11466.

(10) Ivanov, S. A.; Piryatinski, A.; Nanda, J.; Tretiak, S.; Zavadil, K. R.; Wallace, W. O.; Werder, D.; Klimov, V. I. *J. Am. Chem. Soc.* **2007**, *129*, 11708.

(11) Alivisatos, P. *Nat. Biotech.* **2004**, *22*, 47.

(12) Xing, Y.; Chaudry, Q.; Shen, C.; Kong, K. Y.; Zhau, H. E.; Chung, L. W.; Petros, J. A.; O'Regan, R. M.; Yezhelyev, M. V.; Simons, J. W.; Wang, M. D.; Nie, S. *Nat. Protocols* **2007**, *2*, 1152.

(13) Michalet, X.; Pinaud, F.; Bentolila, L.; Tsay, J.; Doose, S.; Li, J.; Sundaresan, G.; Wu, A.; Gambhir, S.; Weiss, S. *Science* **2005**, *307*, 538.

(14) Chan, W. C. W.; Nie, S. *Science* **1998**, *281*, 2016.

(15) Tessler, N.; Medvedev, V.; Kazes, M.; Kan, S.; Banin, U. *Science* **2002**, *295*, 1506.

(16) Coe, S.; Woo, W.-K.; Bawendi, M.; Bulovic, V. *Nature* **2002**, *420*, 800.

(17) Oron, D.; Kazes, M.; Banin, U. *Phys. Rev. B* **2007**, *75*, 035330.

(18) Klimov, V. I.; Ivanov, S. A.; Nanda, J.; Achermann, M.; Bezel, I.; McGuire, J. A.; Piryatinski, A. *Nature* **2007**, *447*, 441.

(19) Zhu, H.; Song, N.; Lian, T. *J. Am. Chem. Soc.* **2011**, *133*, 8762.

(20) Talapin, D. V.; Koeppe, R.; Götzinger, S.; Kornowski, A.; Lupton, J. M.; Rogach, A. L.; Benson, O.; Feldmann, J.; Weller, H. *Nano Lett.* **2003**, *3*, 1677.

(21) Halpert, J. E.; Porter, V. J.; Zimmer, J. P.; Bawendi, M. G. *J. Am. Chem. Soc.* **2006**, *128*, 12590.

(22) Kudera, S.; Carbone, L.; Casula, M. F.; Cingolani, R.; Falqui, A.; Snoeck, E.; Parak, W. J.; Manna, L. *Nano Lett.* **2005**, *5*, 445.

(23) Talapin, D. V.; Nelson, J. H.; Shevchenko, E. V.; Aloni, S.; Sadtler, B.; Alivisatos, A. P. *Nano Lett.* **2007**, *7*, 2951.

(24) Carbone, L.; Nobile, C.; De Giorgi, M.; Sala, F. D.; Morello, G.; Pompa, P.; Hytch, M.; Snoeck, E.; Fiore, A.; Franchini, I. R.; et al *Nano Lett.* **2007**, *7*, 2942.

(25) Kirsanova, M.; Nemchinov, A.; Hewa-Kasakarage, N. N.; Schmall, N.; Zamkov, M. *Chem. Mat.* **2009**, *21*, 4305.

(26) Koo, B.; Korgel, B. A. *Nano Lett.* **2008**, *8*, 2490.

(27) Kumar, S.; Jones, M.; Lo, S. S.; Scholes, G. D. *Small* **2007**, *3*, 1633.

(28) Giblin, J.; Kuno, M. *J. Phys. Chem. Lett.* **2010**, *1*, 3340.

(29) Giblin, J.; Syed, M.; Banning, M. T.; Kuno, M.; Hartland, G. *ACS Nano* **2010**, *4*, 358.

(30) Carey, C. R.; LeBel, T.; Crisostomo, D.; Giblin, J.; Kuno, M.; Hartland, G. V. *J. Phys. Chem. C* **2010**, *114*, 16029.

(31) Manna, L.; Scher, E. C.; Li, L.-S.; Alivisatos, A. P. *J. Am. Chem. Soc.* **2002**, *124*, 7136.

(32) Mokari, T.; Banin, U. *Chem. Mat.* **2003**, *15*, 3955.

(33) Htoon, H.; Hollingsworth, J. A.; Dickerson, R.; Klimov, V. I. *Phys. Rev. Lett.* **2003**, *91*, 227401.

(34) Htoon, H.; Hollingworth, J.; Malko, A.; Dickerson, R.; Klimov, V. *Appl. Phys. Lett.* **2003**, *82*, 4776.

(35) Robel, I.; Bunker, B. A.; Kamat, P. V.; Kuno, M. *Nano Lett.* **2006**, *6*, 1344.

(36) Zhu, H.; Lian, T. *J. Am. Chem. Soc.* **2012**, *134*, 11289.

(37) Hu, J.; Li, L.-s.; Yang, W.; Manna, L.; Wang, L.-w.; Alivisatos, A. P. *Science* **2001**, *292*, 2060.

(38) Hadar, I.; Hitin, G. B.; Sitt, A.; Faust, A.; Banin, U. *J. Phys. Chem. Lett.* **2013**, 502.

(39) Sitt, A.; Salant, A.; Menagen, G.; Banin, U. *Nano Lett.* **2011**, *11*, 2054.

(40) Wang, J.; Gudiksen, M. S.; Duan, X.; Cui, Y.; Lieber, C. M. *Science* **2001**, *293*, 1455.

(41) Katz, D.; Wizansky, T.; Millo, O.; Rothenberg, E.; Mokari, T.; Banin, U. *Phys. Rev. Lett.* **2002**, *89*, 086801.

(42) Li, L.-s.; Hu, J.; Yang, W.; Alivisatos, A. P. *Nano Lett.* **2001**, *1*, 349.

(43) Deka, S.; Quarta, A.; Lupo, M. G.; Falqui, A.; Boninelli, S.; Giannini, C.; Morello, G.; De Giorgi, M.; Lanzani, G.; Spinella, C.; et al *J. Am. Chem. Soc.* **2009**, *131*, 2948.

(44) Pisanello, F.; Martiradonna, L.; Spinicelli, P.; Fiore, A.; Hermier, J. P.; Manna, L.; Cingolani, R.; Giacobino, E.; De Vittorio, M.; Bramati, A. *Superlattices Microstruct.* **2010**, *47*, 165.

(45) Huang, M. H.; Mao, S.; Feick, H.; Yan, H.; Wu, Y.; Kind, H.; Weber, E.; Russo, R.; Yang, P. *Science* **2001**, *292*, 1897.

(46) Kazes, M.; Lewis, D. Y.; Ebenstein, Y.; Mokari, T.; Banin, U. *Adv. Mater.* **2002**, *14*, 317.

(47) Tang, M. L.; Grauer, D. C.; Lassalle-Kaiser, B.; Yachandra, V. K.; Amirav, L.; Long, J. R.; Yano, J.; Alivisatos, A. P. *Angew. Chem. Int. Ed.* **2011**, *50*, 10203.

(48) Amirav, L.; Alivisatos, A. P. *J. Phys. Chem. Lett.* **2010**, *1*, 1051.

(49) Zhu, H.; Song, N.; Lv, H.; Hill, C. L.; Lian, T. *J. Am. Chem. Soc.* **2012**, *134*, 11701.

(50) Acharya, K. P.; Khnayzer, R. S.; O'Connor, T.; Diederich, G.; Kirsanova, M.; Klinkova, A.; Roth, D.; Kinder, E.; Imboden, M.; Zamkov, M. *Nano Lett.* **2011**, *11*, 2919.

(51) Berr, M.; Vaneski, A.; Susha, A. S.; Rodriguez-Fernandez, J.; Doblinger, M.; Jackel, F.; Rogach, A. L.; Feldmann, J. *Appl. Phys. Lett.* **2010**, *97*, 0931081.

(52) Brown, K. A.; Wilker, M. B.; Boehm, M.; Dukovic, G.; King, P. W. *J. Am. Chem. Soc.* **2012**, *134*, 5627.

(53) Tongying, P.; Plashnitsa, V. V.; Petchsang, N.; Vietmeyer, F.; Ferraudi, G. J.; Krylova, G.; Kuno, M. *J. Phys. Chem. Lett.* **2012**, *3*, 3234.

(54) Bang, J. U.; Lee, S. J.; Jang, J. S.; Choi, W.; Song, H. *J. Phys. Chem. Lett.* **2012**, *3*, 3781.

(55) Müller, J.; Lupton, J. M.; Rogach, A. L.; Feldmann, J.; Talapin, D. V.; Weller, H. *Phys. Rev. Lett.* **2004**, *93*, 167402.

(56) Müller, J.; Lupton, J. M.; Lagoudakis, P. G.; Schindler, F.; Koeppe, R.; Rogach, A. L.; Feldmann, J.; Talapin, D. V.; Weller, H. *Nano Lett.* **2005**, *5*, 2044.

(57) Müller, J.; Lupton, J. M.; Rogach, A. L.; Feldmann, J.; Talapin, D. V.; Weller, H. *Phys. Rev. B* **2005**, *72*, 205339.

(58) Kraus, R. M.; Lagoudakis, P. G.; Rogach, A. L.; Talapin, D. V.; Weller, H.; Lupton, J. M.; Feldmann, J. *Phys. Rev. Lett.* **2007**, *98*, 017401.

(59) Lupo, M. G.; Della Sala, F.; Carbone, L.; Zavelani-Rossi, M.; Fiore, A.; Lüer, L.; Polli, D.; Cingolani, R.; Manna, L.; Lanzani, G. *Nano Lett.* **2008**, *8*, 4582.

(60) Mauser, C.; Limmer, T.; Da Como, E.; Becker, K.; Rogach, A. L.; Feldmann, J.; Talapin, D. V. *Phys. Rev. B* **2008**, *77*, 153303.

(61) Morello, G.; Della Sala, F.; Carbone, L.; Manna, L.; Maruccio, G.; Cingolani, R.; De Giorgi, M. *Phys. Rev. B* **2008**, *78*, 195313.

(62) Steiner, D.; Dorfs, D.; Banin, U.; Della Sala, F.; Manna, L.; Millo, O. *Nano Lett.* **2008**, *8*, 2954.

(63) Luo, Y.; Wang, L.-W. *ACS Nano* **2009**, *4*, 91.

(64) Saba, M.; Minniberger, S.; Quochi, F.; Roither, J.; Marceddu, M.; Gocalinska, A.; Kovalenko, M. V.; Talapin, D. V.; Heiss, W.; Mura, A. *Adv. Mater* **2009**, *21*, 4942.

(65) Sitt, A.; Sala, F. D.; Menagen, G.; Banin, U. *Nano Lett.* **2009**, *9*, 3470.

(66) Borys, N. J.; Walter, M. J.; Huang, J.; Talapin, D. V.; Lupton, J. M. *Science* **2010**, *330*, 1371.

(67) Lupo, M. G.; Zavelani-Rossi, M.; Fiore, A.; Polli, D.; Carbone, L.; Cingolani, R.; Manna, L.; Lanzani, G. *Superlattices Microstruct.* **2010**, *47*, 170.

(68) Lutich, A. A.; Mauser, C.; Da Como, E.; Huang, J.; Vaneski, A.; Talapin, D. V.; Rogach, A. L.; Feldmann, J. *Nano Lett.* **2010**, *10*, 4646.

(69) Mauser, C.; Da Como, E.; Baldauf, J.; Rogach, A. L.; Huang, J.; Talapin, D. V.; Feldmann, J. *Phys. Rev. B* **2010**, *82*, 0813061.

(70) Morello, G.; Della Sala, F.; Carbone, L.; Manna, L.; Cingolani, R.; De Giorgi, M. *Superlattices Microstruct.* **2010**, *47*, 174.

(71) Zavelani-Rossi, M.; Lupo, M. G.; Tassone, F.; Manna, L.; Lanzani, G. *Nano Lett.* **2010**, *10*, 3142.

(72) Krahne, R.; Morello, G.; Figuerola, A.; George, C.; Deka, S.; Manna, L. *Phys. Rep.* **2011**, *501*, 75.

(73) Rainò, G.; Stöferle, T.; Moreels, I.; Gomes, R.; Kamal, J. S.; Hens, Z.; Mahrt, R. F. *ACS Nano* **2011**, *5*, 4031.

(74) She, C.; Demortière, A.; Shevchenko, E. V.; Pelton, M. *J. Phys. Chem. Lett.* **2011**, *2*, 1469.

(75) Smith, E. R.; Luther, J. M.; Johnson, J. C. *Nano Lett.* **2011**, *11*, 4923.

(76) Xing, G.; Chakrabortty, S.; Ngiam, S. W.; Chan, Y.; Sum, T. C. *J. Phys. Chem. C* **2011**, *115*, 17711.

(77) Rainò, G.; Stöferle, T.; Moreels, I.; Gomes, R.; Hens, Z.; Mahrt, R. F. *ACS Nano* **2012**, *6*, 1979.

(78) Chakrabortty, S.; Xing, G.; Xu, Y.; Ngiam, S. W.; Mishra, N.; Sum, T. C.; Chan, Y. *Small* **2011**, *7*, 2847.

(79) Yoskovitz, E.; Menagen, G.; Sitt, A.; Lachman, E.; Banin, U. *Nano Lett.* **2010**, *10*, 3068.

(80) Kunneman, L. T.; Zanella, M.; Manna, L.; Siebbeles, L. D. A.; Schins, J. M. *J. Phys. Chem. C* **2013**, *117*, 3146.

(81) Shabaev, A.; Efros, A. L. *Nano Lett.* **2004**, *4*, 1821.

(82) Ekimov, A. I.; Hache, F.; Schanne-Klein, M. C.; Ricard, D.; Flytzanis, C.; Kudryavtsev, I. A.; Yazeva, T. V.; Rodina, A. V.; Efros, A. L. *J. Opt. Soc. Am. B* **1993**, *10*, 100.

(83) Norris, D. J.; Sacra, A.; Murray, C. B.; Bawendi, M. G. *Phys. Rev. Lett.* **1994**, *72*, 2612.

(84) Puthussery, J.; Lan, A.; Kosel, T. H.; Kuno, M. *ACS Nano* **2008**, *2*, 357.

(85) Xu, X.; Zhao, Y.; Sie, E. J.; Lu, Y.; Liu, B.; Ekahana, S. A.; Ju, X.; Jiang, Q.; Wang, J.; Sun, H.; et al *ACS Nano* **2011**, *5*, 3660.

(86) Hoang, T. B.; Titova, L. V.; Jackson, H. E.; Smith, L. M.; Yarrison-Rice, J. M.; Lensch, J. L.; Lauhon, L. J. *Appl. Phys. Lett.* **2006**, *89*, 123123.

(87) Saunders, A. E.; Ghezelbash, A.; Sood, P.; Korgel, B. A. *Langmuir* **2008**, *24*, 9043.

(88) Wu, K.; Zhu, H.; Liu, Z.; Rodríguez-Córdoba, W.; Lian, T. *J. Am. Chem. Soc.* **2012**, *134*, 10337.

(89) Shafran, E.; Borys, N. J.; Huang, J.; Talapin, D. V.; Lupton, J. M. *J. Phys. Chem. Lett.* **2013**, 691.

(90) Choi, C. L.; Li, H.; Olson, A. C. K.; Jain, P. K.; Sivasankar, S.; Alivisatos, A. P. *Nano Lett.* **2011**, *11*, 2358.

(91) Saunders, A. E.; Popov, I.; Banin, U. *J. Phys. Chem. B* **2006**, *110*, 25421.

(92) Zhu, H.; Song, N.; Rodríguez-Córdoba, W.; Lian, T. *J. Am. Chem. Soc.* **2012**, *134*, 4250.

(93) García-Santamaría, F.; Brovelli, S.; Viswanatha, R.; Hollingsworth, J. A.; Htoon, H.; Crooker, S. A.; Klimov, V. I. *Nano Lett.* **2011**, *11*, 687.

(94) Brovelli, S.; Schaller, R. D.; Crooker, S. A.; García-Santamaría, F.; Chen, Y.; Viswanatha, R.; Hollingsworth, J. A.; Htoon, H.; Klimov, V. I. *Nat Commun* **2011**, *2*, 280.

(95) Htoon, H.; Malko, A. V.; Bussian, D.; Vela, J.; Chen, Y.; Hollingsworth, J. A.; Klimov, V. I. *Nano Lett.* **2010**, *10*, 2401.

(96) Garcia-Santamaria, F.; Chen, Y. F.; Vela, J.; Schaller, R. D.; Hollingsworth, J. A.; Klimov, V. I. *Nano Lett.* **2009**, *9*, 3482.

(97) Reynolds, G. A.; Drexhage, K. H. *Opt. Commun.* **1975**, *13*, 222.

(98) Kubin, R. F.; Fletcher, A. N. *J. Lumin.* **1982**, *27*, 455.

(99) Klimov, V. I. *J. Phys. Chem. B* **2000**, *104*, 6112.

(100) Huang, J. E.; Huang, Z. Q.; Jin, S. Y.; Lian, T. Q. *J. Phys. Chem. C* **2008**, *112*, 19734.

(101) Huang, J.; Stockwell, D.; Huang, Z. Q.; Mohler, D. L.; Lian, T. Q. *J. Am. Chem. Soc.* **2008**, *130*, 5632.

(102) Jiang, Z.-J.; Kelley, D. F. *J. Phys. Chem. C* **2011**, *115*, 4594.

(103) Srivastava, A.; Htoon, H.; Klimov, V. I.; Kono, J. *Phys. Rev. Lett.* **2008**, *101*.

(104) Klimov, V. I. *Annu. Rev. Phys. Chem.* **2007**, *58*, 635.

(105) Yang, Y.; Rodríguez-Córdoba, W. E.; Lian, T. *J. Am. Chem. Soc.* **2011**, *133*, 9246.

(106) Chen, O.; Zhao, J.; Chauhan, V. P.; Cui, J.; Wong, C.; Harris, D. K.; Wei, H.; Han, H.-S.; Fukumura, D.; Jain, R. K.; Bawendi, M. G. *Nat Mater* **2013**, *12*, 445.

(107) Burda, C.; Green, T. C.; Link, S.; El-Sayed, M. A. *J. Phys. Chem. B* **1999**, *103*, 1783.

(108) McArthur, E. A.; Morris-Cohen, A. J.; Knowles, K. E.; Weiss, E. A. *J. Phys. Chem. B* **2010**, *114*, 14514.

(109) Zhu, H. M.; Song, N. H.; Lian, T. Q. *J. Am. Chem. Soc.* **2010**, *132*, 15038.

(110) Norris, D. J.; Efros, A. L.; Rosen, M.; Bawendi, M. G. *Phys. Rev. B* **1996**, *53*, 16347.

(111) Goss, F. R. *J. Chem. Soc.* **1940**, *0*, 888.

(112) Loudon, R. *Am. J. Phys.* **1959**, *27*, 649.

(113) Wu, K.; Liu, Z.; Zhu, H.; Lian, T. *J. Phys. Chem. A* **2013**, DOI: 10.1021/jp402511m.

(114) Wu, K.; Song, N.; Liu, Z.; Zhu, H.; Rodr ́guez-C ́rdoba, W. E.; Lian, T. *J. Phys. Chem. A* **2013**, DOI: 10.1021/jp402425w.

Appendix 1

Fitting of Static Absorption Spectrum

To qualitatively show transitions B1, B2 and B3 in the static absorption spectrum of DIRs, we fit the spectrum below 2.8 eV with three Gaussians. The higher energy transitions are not included into the fitting. As shown in Figure A.8.1, the transitions below 2.8 eV can indeed be fitted to sum of three Gaussian peaks with their centers at 2.76 eV (449 nm), 2.58 eV (480 nm), and 2.30 eV (539 nm). The fitting parameters (peak center, width and height) are listed in Table A.8.1. The obtained transition wavelengths of B1, B2, and B3 agree well with those observed on TA spectra of DIRs in the main text.

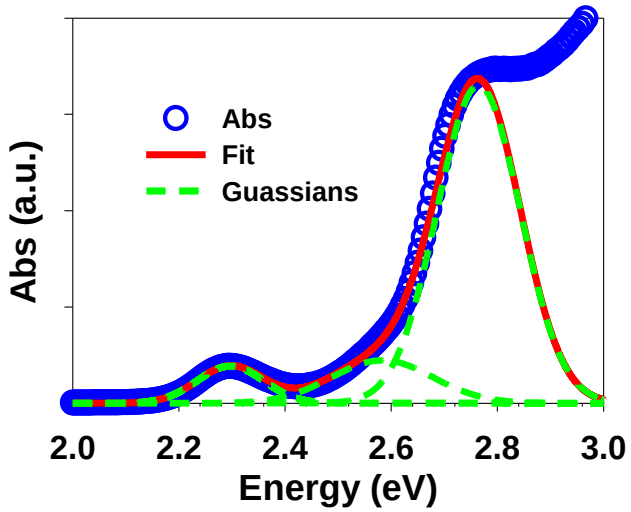

Figure A.8.1. Multi-peak fit(red dashed lines) to the static absorption spectrum (blue circles) of DIRs below 2.8 eV. The fit consists of three Gaussian bands(dashed lines) with peak positions and widths listed in Table S1.

Table A.8.1. Fitting Parameters for Static Absorption Spectrum

	B3	B2	B1
Center (eV)	2.297	2.583	2.765
Width (eV)	0.125	0.190	0.157
Height (a.u.)	0.077	0.089	0.66

Appendix 2

Assignment of Exciton Bleach Features Using DIR-MV^{2+} Complexes

To confirm the assignment of exciton bleach signals in CdSe/CdS DIRs, we performed charge separation experiments to selectively remove CB electrons. Shown in Figure A.8.2a and A.8.2b are the TA spectra of DIR- MV^{2+} complexes at 1200 ps after 400 and 540 nm excitations, respectively. In both cases, the state-filling induced exciton bleach signals are completely removed and the remaining spectra can be attributed to the superposition of reduced $MV^{+\bullet}$ radical and charge-separation induced Stark-effect signals. Therefore, the exciton bleach features in the DIR TA spectra are dominated by state-filling of the CB electron level with negligible contribution of the hole level.

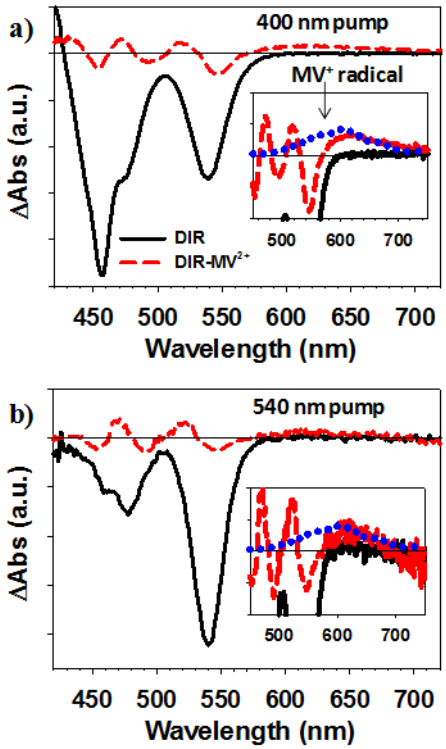

Figure A.8.2. TA spectra of DIRs (black solid line) and DIR-MV^{2+} complexes (red dashed line) at 1200 ps (a) after 400 nm and (b) and 540 nm excitation. Insets in a) and b) are the expanded view of the spectrum along with the spectrum of the reduced $MV^{+\bullet}$ radical signal (blue dotted line).

Appendix 3

Simulation of DIR TA spectrum under 540 nm excitation

To confirm that the small B1 feature in Figure 8.3a is due to Stark effect spectrum of B1 transition induced by electron-hole pair in the CdSe core/bulb region, we simulate the TA spectrum by the sum of Stark effect signals in B1, B2 and B3 and state-filling signals in B2 and B3. The Stark effect spectrum(S_{stark}) is obtained by subtraction of $MV^{+\bullet}$ radical signal from the TA spectrum of the charge-separated state of DIR-MV^{2+} complexes shown in Figure A.8.2b. Although S_{stark} is the Stark effect spectrum of DIRs resulting from dipolar fields of separated charge pairs (DIR^{+}-$MV^{+\bullet}$), we assume that it provides a reasonable approximation for the Stark effect spectrum of free DIRs caused by the presence of lowest energy exciton. With this assumption, the spectrum in Figure A.8.3 can be fitted by the sum of two Gaussians and Stark effect signals:

$$S(\omega) = S_{stark}(\omega) + \sum_{i=1}^{2} \frac{a_i}{\sqrt{2\pi}\Gamma_i} \exp\left[-\frac{(\hbar\omega - E_i)^2}{2\Gamma_i^{\,2}} \right] \qquad \text{(A.8.1).}$$

In equation A.8.1, a_i, E_i and Γ_i are the amplitude, peak position and width, respectively, of the Gaussian functions. They represent the state filling induced bleach

of the B2 and B3 transitions. Because the S_{stark} is obtained in DIR-MV^{2+} complexes with the same nanorod concentration and excitation power as in the free DIR sample, it is used in the simulation without any scaling factors. Figure A.8.3 shows that the TA spectrum can indeed be well reproduced by this simulation. The fitting parameters

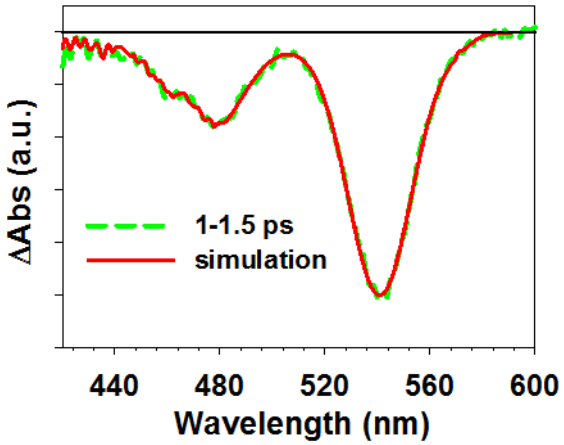

Figure A.8.3. Comparison of average TA spectrum (green dashed line) of free DIR at 1 to 1.5 ps after 540 nm excitation and the simulated spectrum (red solid line).

Table A.8.2. Fitting Parameters for the TA spectrum

	Gaussian 1	Gaussian 2	S_{stark}
E_i (eV)	2.2951(±0.0005)	2.6107(±0.0012)	NA
Γ_i (eV)	0.0538(±0.0004)	0.0855(±0.0015)	

Chapter 9. Universal Length-Dependence of Rod-to-Seed Exciton Localization Efficiency in CdSe/CdS Dot-in-rod Nanorods

9.1. Introduction

CdSe/CdS dot-in-rod NRs (CdSe/CdS hereafter for simplicity), with a CdS NR grown from a CdSe QD seed, is one of the most intensely-studied 1D heterostructure.[15,16,29,36-41] Due to the large valence band (VB) offset (>0.45 eV) and small conduction band (CB) offset (<0.3 eV) between bulk wurtzite CdSe and CdS,[15,38] the band alignment of these CdSe/CdS NRs can be tuned by the seed size and rod diameter from type I (with the lowest energy electron and hole levels confined in the CdSe seed) to quasi-type II (with the lowest energy hole confined in CdSe seed and the lowest energy electron level degenerate in CdSe and CdS).[37-48] While it is clear that in Type I NRs, the lowest energy exciton is confined in the CdSe seed, extensive recent studies have revealed that in quasi type II NRs, the electron in the lowest energy exciton state is also localized at and near the CdSe seed,[41,42,49] due

to strong electron-hole bindings in 1D nanostructures.[50] Therefore, in these heterostructures, the CdS rod acts as nanoscale light harvesting antennas and the photogenerated excitons in the rod can be transported and localized to the CdSe seed,[40] mimicking natural light harvesting complexes.[51,52] For this reason, CdSe/CdS NRs have been applied to solar-to-fuel conversion,[23,27,53] luminescent solar concentrators,[54] and optical gains.[28,29,55] These applications all take advantage of the large volume of CdS rods for efficient light absorption and funnel photogenerated excitons into CdSe seeds where chemical reactions or light emissions occur.

Exciton transport from the CdS rod to CdSe seed in CdSe/CdS NRs involves not only energy relaxation from higher to lower energy exciton states but also charge transport over a length scale of 10-1000 nm. Such long distance exciton transport is susceptible to energetic disorder along the length of the rod caused by diameter variations and trap states.[40] In last chapter, we show that the rod-to-seed exciton localization efficiency is not unity and there exist long-lived excitons trapped on the CdS rod in addition to localized excitons at the CdSe seed.[46,56,57] But it remains unclear how these excitons are transported along the rods and how the branching ratio of the aforementioned pathways depends on the length of the rods and the seed/rod band alignment. In this chapter, we report a study of the rod length dependence of exciton localization efficiency in CdSe/CdS NRs with both type I and quasi-type II band alignments. By photoluminescence excitation (PLE) spectroscopy and transient

absorption (TA) spectroscopy, we observed that the exciton localization efficiency was independent of the band alignment but decreased at longer rod length. We showed that this universal length-dependence could be accounted for by the competition between 1D exciton diffusion from the rod to the seed and exciton trapping at the rod. We believe that the proposed model is generally applicable to other 1D nanoheterostructures, providing guidance for a rational design of NR morphology for their many applications.

9.2 Results and Discussions

9.2.1. Preparation and Morphological Characterization of CdSe/CdS NRs.

CdSe/CdS NRs of varying dimensions were synthesized using modified approaches from the method of Manna and coworkers,[16, 37, 58,59] where CdSe QDs of different sizes were used as seeds to prepare CdS NRs. Synthetic details can be found in Chapter 2. An attractive feature of these heterostructures is the ability to prepare NRs of uniform length and diameter by controlling the ratio of CdSe QD seeds to CdS NR precursors. In this chapter, seven NR samples were prepared using three CdSe seed

sizes (diameter=2.5 nm, 2.7 nm, and 3.8 nm): three NRs of different lengths were grown with 2.7 nm and 3.8 nm CdSe seeds and one NR was grown for 2.5 nm seeds. For convenience we labeled them by their seed diameters and rod lengths. For example, $CdSe_{2.5}/CdS_{36}$ has a seed diameter of 2.5 nm and rod length of 36 nm. Representative transmission electron microscopy (TEM) images of NRs grown from 2.7 nm and 3.8 nm seeds are shown in Column 1 of Figure 9.1 and Figure 9.2, respectively. These seeded NRs exhibit relatively uniform diameter without the incidence of geometric, or morphological defects along the 1-D CdS phase.[36,40] In addition, we observed that increasing rod length was accompanied by a slight decrease in the average rod diameter from 5.6 ±0.7 nm in $CdSe_{2.7}/CdS_{29}$ to 4.9±0.6 nm in CdSe2.7/CdS_{117}. Similarly, for 3.8 nm seed, the average rod diameter decreased from 5.9 ± 0.6 nm in $CdSe_{3.8}/CdS_{31}$ to 4.8 ± 0.7 nm in $CdSe_{3.8}/CdS_{116}$. In general, the morphology of these nanorods can be approximately represented by a uniform CdS nanorod with an enclosed CdSe seed as depicted in Figure 9.3a.

Energy dispersive X-ray spectroscopy (EDX) was used to analyze the element distribution along the NRs and to identify the position of the CdSe seed for the series of NRs investigated in this study. These seed positions are crucial when determining rod-to-seed exciton transport distances. As shown in the insets of Column 1 of Figure 9.1, the CdSe seeds can be traced by the green Se regions, from which average seed positions were determined. Roughly, the seeds were located at ~1/2, 1/3, and 1/5 of

the total rod lengths of $CdSe_{2.7}/CdS_{29}$, $CdSe_{2.7}/CdS_{47}$ and $CdSe_{2.7}/CdS_{117}$, respectively. Similar trends were observed for NRs with 2.5 nm and 3.8 nm seeds. It has often been assumed that the seed is located at 1/4 of the rod length due to different growth rates of the two terminating facets of CdS NRs.[16,37] Our result indicates that the seed is close to the center of short rods but deviates gradually from the center for longer rods. The detailed morphological parameters (including seed size, seed position, rod length and rod diameter) for all investigated NRs are summarized in Table 9.1.

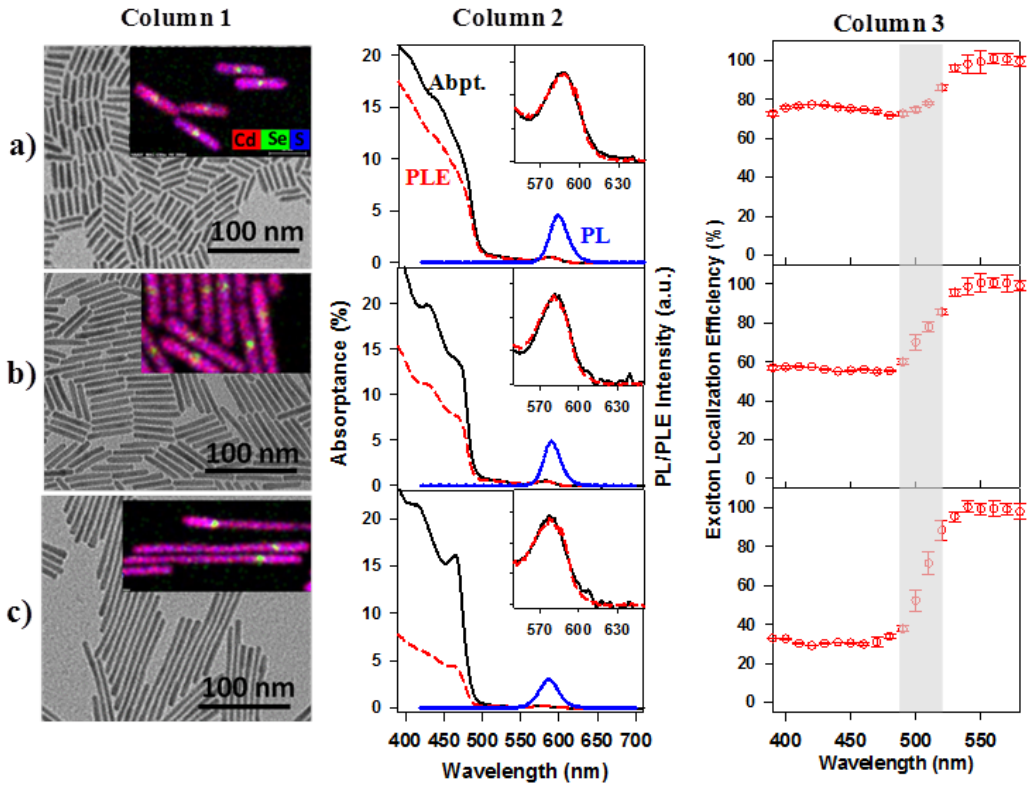

Figure 9.1. Quasi-type II CdSe/CdS NRs (2.7 nm seed). (Column 1) Representative TEM images, (Column 2) Absorptance (black solid line), Photoluminescence (PL, blue solid line) and Photoluminescence excitation (PLE, red

dashed line) spectra and (Column 3) Wavelength-dependent relative PL QYs of a) $CdSe_{2.7}/CdS_{29}$, b) $CdSe_{2.7}/CdS_{47}$, and c) $CdSe_{2.7}/CdS_{117}$ NRs. Column 1 insets: colored coded EDX elemental maps of Se (green, indicating location of CdSe seed), Cd (red) and S (blue). Note that they are arbitrarily enlarged and do not share the same scale bar as the TEM images. The PLE and absorptance spectra in Column 2 have been normalized at the lowest energy exciton peak (an expanded view is shown in the inset). The shaded areas in Column 3: regions of gradual decrease of relative PL QYs.

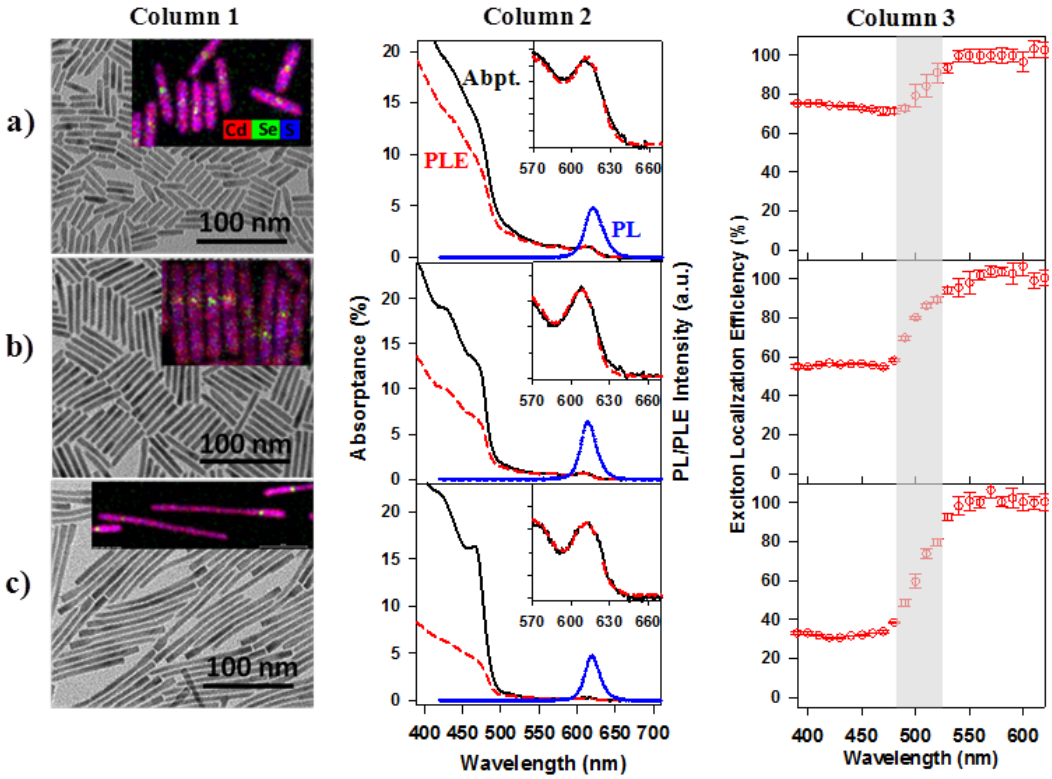

Figure 9.2. Type-I CdSe/CdS NRs (3.8 nm seed). (Column 1) Representative TEM images, (Column 2) Absorptance (black solid line), Photoluminescence (PL, blue solid line) and Photoluminescence excitation (PLE, red dashed line) spectra and (Column 3) Wavelength-dependent relative PL QYs of a) $CdSe_{3.8}/CdS_{31}$, b) $CdSe_{3.8}/CdS_{48}$, and c) $CdSe_{3.8}/CdS_{116}$ NRs. Column 1 insets: colored coded EDX elemental maps of Se (green, indicating location of CdSe seed), Cd (red) and S (blue). Note that they are arbitrarily enlarged and do not share the same scale bar as the TEM images. The PLE and absorptance spectra in Column 2 have been normalized at the lowest energy exciton peak (an expanded view is shown in the inset). The shaded areas in Column 3: regions of gradual decrease of relative PL QYs.

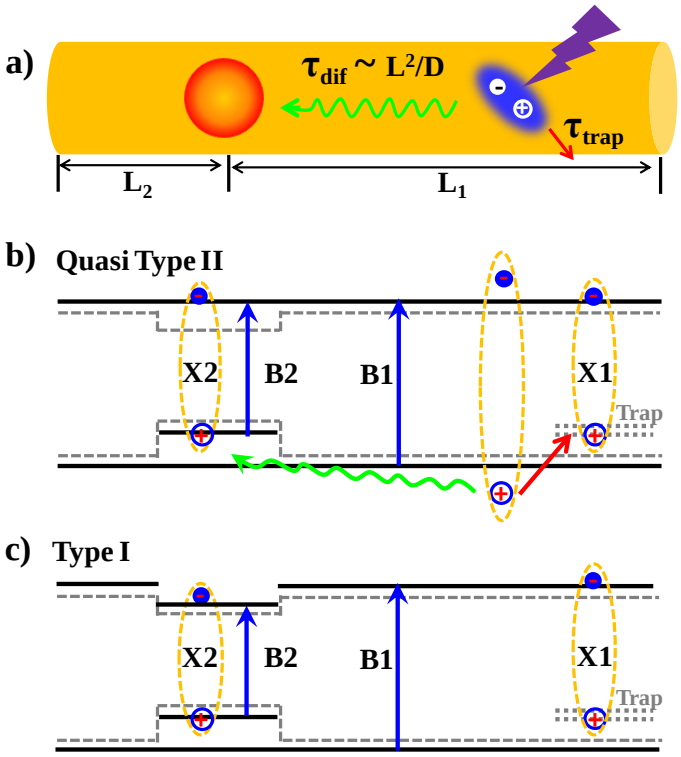

Figure 9.3. Electronic structure and exciton dynamics in type I and quasi-type II CdSe/CdS NRs. a) Schematic illustration of a CdSe/CdS seeded NR and the relaxation processes (localizing to the CdSe seed or trapping at the CdS rod) of an exciton generated at the CdS rod. Schematic energy level diagrams of (b) quasi-type II (2.7 and 2.5 nm seeds) and (c) type I (3.8 nm seeds) CdSe/CdS NRs, showing bulk band edges of CdS and CdSe (gray dotted lines) and lowest electron and hole energy levels in CdSe seed and CdS rod (black solid lines) and sub-band gap hole trapping states on CdS rod (black dotted lines). Also labeled are excitons trapped on CdS rod (X1) and localized at CdSe seed (X2) as well as lowest energy transitions in the CdS rod (B1) and the CdSe seed (B2).

Table 9.1. Tabulated nanorod lengths, diameters and seed positions

Sample	Length (nm)	Diameter (nm)	Seed position (nm)
$CdSe_{2.5}@CdS_{36}$	35.9 ±2.4	5.11 ±0.57	14.9 ±1.7
$CdSe_{2.7}@CdS_{29}$	28.6 ±2.1	5.57 ±0.71	13.4 ±1.1
$CdSe_{2.7}@CdS_{47}$	46.7 ±3.6	5.66 ±0.63	16.1 ±1.4
$CdSe_{2.7}@CdS_{117}$	116.6 ±13.1	4.89 ±0.61	23.1 ±2.1
$CdS_{3.8}@CdS_{31}$	30.6 ± 1.7	5.87 ± 0.61	15.5 ±1.4

$CdSe_{3.8}@CdS_{48}$	48.2 ± 5.2	5.58 ±0.56	16.9 ±1.7
$CdSe_{3.8}@CdS_{116}$	115.7 ±11.8	4.83 ± 0.68	22.5 ±1.5

9.2.2. Electronic structure of type I and quasi-type II CdSe/CdS NRs.

The optical absorption and emission spectra of these NRs confirmed that the band alignment of CdSe and CdS can be tuned from type I to quasi-type II by decreasing the CdSe seed sizes. The absorptance, photoluminescence (PL), and photoluminescence excitation (PLE) spectra of NRs with 2.7 nm and 3.8 nm seeds and different lengths are shown in Column 2 of Figure 9.1 and Figure 9.2, respectively. For a better comparison with PLE spectra (PL intensity as a function of excitation wavelength), we have shown the absorptance spectra (absorptance = $1\text{-}10^{-OD}$, where OD was optical density, representing the percentages of absorbed photons as a function of wavelength) instead of the absorption spectra in Figure 9.1 and 9.2. Extensive studies of related CdSe/CdS NRs have shown that their electronic structure can be described by the schematic energy level diagrams depicted in Figure 9.3b and 9.3c.[37,39,40,44,46,47,56,57] Because of the large valence band (VB) and small conduction band (CB) offsets between CdSe and CdS, CdSe/CdS NRs can exhibit band alignments of either quasi type II for small CdSe seeds[37] (Scheme 1b) or type I for large CdSe seeds[38] (Figure 9.3c) depending on the extent of quantum confinement

in the seed.[39] Quantum confinement in the radial direction leads to discrete electron and hole energy levels in the CdS rod and excitonic transitions between these levels give rise to the 1D exciton bands at < 480nm in the absorption spectra. [37,56] As shown in Column 2 of Figure 9.1 and Figure 9.2, the absorption bands at ~ 475 and 420 nm can be attributed to the lowest energy 1Σ (or B1) and 1Π excitonic bands of CdS rods, respectively. In addition, the absorption spectra showed excitonic features >512 nm (smaller than the CdS bulk band gap of 2.42 eV[60]) that can be associated with transitions from the CdSe seed. The transition energies of CdSe features depend sensitively on the size of CdSe seeds, with the lowest excitonic band at ~580 nm and ~610 nm for NRs with 2.7 nm and 3.8 nm seeds, respectively. We labeled this transition as B2 in Figure 9.3b and 9.3c. With increasing rod length, the relative amplitude of the CdS absorption (B1) became larger because of its increasing volume. For both NRs with the 2.7 and 3.8 nm seed, the B1 exciton peak positions are blue-shifted with increasing rod length, reflecting decreasing diameters at longer rod lengths. Interestingly, the same length dependent was observed in B2 transition for NRs with a 2.7 nm seed, but not for NRs with a 3.8 nm seed. This result suggests that B2 transition energy of NRs with a 2.7 nm seed is sensitive to the energy level of the CdS rod, consistent with a quasi-type II band alignment (scheme 1b) and the B2 transition energy of NRs with a 3.8 nm seed is insensitive to the energy level of CdS rod, exhibiting a type I band alignment (Figure 9.3c).

To further confirm the band alignment in these NRs, we carried out transient absorption (TA) study following previous works.[37,56,61] In these measurements, we selectively excited these samples at 575 nm, the lowest energy transition (B2), to generate an X2 exciton (see Figure 9.3b and 9.3c) in the seed. The resulting TA spectra (averaged between 1-2 ps delay) for NRs with 2.7 nm and 3.8 nm seeds are shown in Figure 9.4a and 9.4b, respectively. Their kinetics show that these spectral features form instantaneously (<10 fs) and only slightly decay (<15%) within 1 ns, indicating dominant single-exciton conditions.[29] For NRs with a 2.7 nm seed (Figure 9.4a), 575 nm excitation led to both a strong bleach of the B2 band of the CdSe seed (~580 nm) and the B1 band of the CdS rod (~475 nm). Since these bleaches are caused by the state filling of the CB electron level,[56] the instantaneous formation of both B1 and B2 bleach indicates that the electron wavefunction of the X2 exciton extends from the CdSe seed into the CdS rod, consistent with a quasi-type II electronic structure (Figure 9.3b).[41,56] A similar electron wavefunction delocalization and quasi type II band alignment was observed for $CdSe_{2.5}/CdS_{36}$ NR. In contrast, for NRs with a 3.8 nm seed (Figure 9.4b), 575 nm excitation led to a strong B2 bleach and negligible B1 bleach, indicating that the electron wavefunction of X2 exciton has negligible amplitude at the CdS rod, consistent with a type I electronic structure (Figure 9.3c). There exist a derivative-like feature near B1 (Figure 9.4b), which is also observed in CdSe QDs of similar confinement energy (Figure 9.4b) and can be

attributed to the effect of the lowest energy exciton on the higher energy transitions (i.e. bi-exciton interaction) of the CdSe seed.[62]

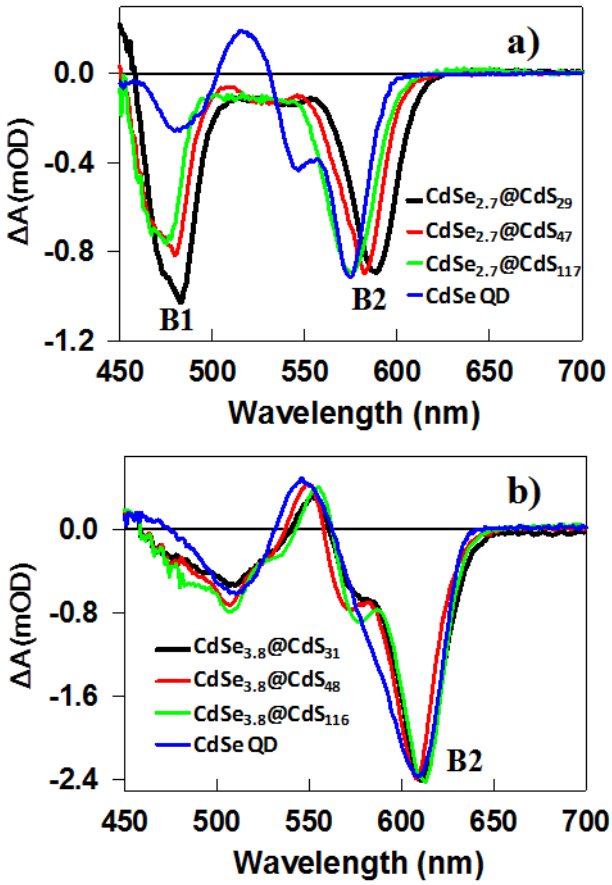

Figure 9.4. Averaged Transient Absorption (TA) spectra of NRs with a 2.7 nm (a) and 3.8 nm (b) seed measured at 1-2 ps after 575 nm excitation. For comparison, TA spectra of corresponding CdSe QDs with similar confinement energies are also shown.

9.2.3. Length-dependent exciton localization efficiency.

PL spectra of all NRs studied in this work (column 2 of Figure 9.1 and 9.2) showed pronounced X2 exciton emission that was slightly red-shifted from the B2 absorption band of the seed and negligible emission from the CdS rod, consistent with previous reports.[16,36] PLE spectra shown in Figure 9.1 and 9.2 were acquired by monitoring the emission at the PL peak (with a detection bandwidth of 2 nm) and have been normalized to the same amplitude as the absorptance spectra at the B2 band. The ratio of normalized PLE over absorptance yields relative PL quantum yields (QYs), which is also the efficiency of converting (localizing) the initial photogenerated exciton on the rod to X2 exciton in the seed (with the localization efficiency for excitation at the B2 band set to 1).[56] As shown in column 3 of Figure 9.1 and 9.2, for all these NRs, the exciton localization efficiencies were constant (unity) at wavelength longer than 520 nm where light absorption occurs at the CdSe seed; decreased gradually at 480-520 nm when the absorption of CdS rods increased; and leveled off at wavelengths shorter than 480 nm to ~75.7±1.5% (74.2±1.2%), 55.9±1.6% (55.8±0.7%), and 30.5±2.6% (31.3±3.0%), for $CdSe_{2.7}/CdS_{29}$ ($CdSe_{3.8}/CdS_{31}$), $CdSe_{2.7}/CdS_{47}$ ($CdSe_{3.8}/CdS_{48}$), and $CdSe_{2.7}/CdS_{117}$ ($CdSe_{3.8}/CdS_{116}$), respectively. At < 480 nm (above the CdS rod band gap), the absorption is dominated by CdS rods due to its much larger volume than CdSe seeds and the measured exciton localization efficiency reflects the localization of excitons generated at the CdS rod to (near) CdSe seed in these NRs, driven by the

large VB offset (>0.45 eV).[53,56] Similar measurements were performed on the $CdSe_{2.5}CdS_{36}$ sample and the rod-to-seed exciton localization efficiency was determined to be 64.6±2.8%. These results, plotted in Figure 9.5, showed that the rod-to-seed exciton localization efficiency for these NRs was independent of the seed size but decreased with rod length. Since the NRs with 2.5 nm and 2.7 nm seeds have quasi type II band alignments different from the type I band alignment in NRs with a 3.8 nm seeds, the seed size independence indicates that the band alignment does not affect the exciton localization process in these NRs.

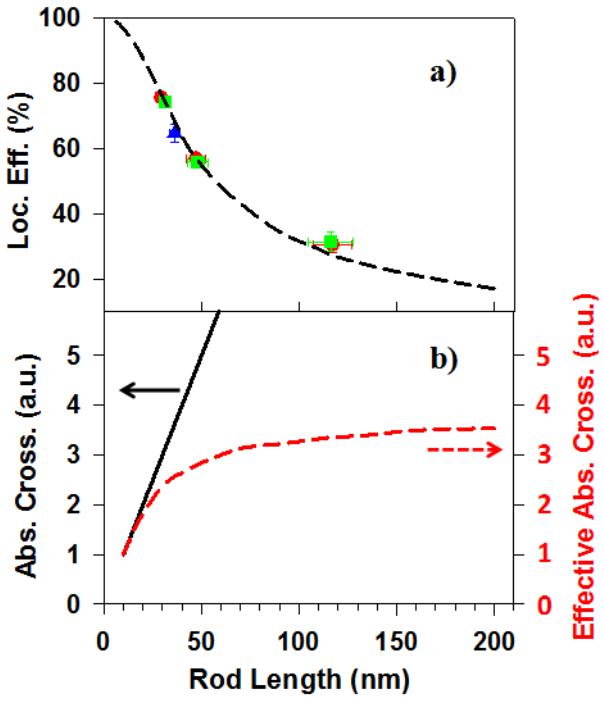

Figure 9.5. Universal length dependence of exciton localization. a) Measured (symbols) and simulated (dashed line) exciton localization efficiencies in CdSe/CdS NRs with 2.5 nm (blue triangles), 2.7 nm (red circles) and 3.8 nm (green squares)

seeds. b) CdS rod absorption cross-section (black solid line) and effective CdSe seed absorption cross-section (red dashed line) as a function of rod length.

9.2.4. Exciton Trapping on Nanorods.

The observed non-unity rod-to-seed exciton localization efficiencies and their rod length dependence suggest the presence of other exciton localization pathways that compete with exciton transport to the CdSe seed. Through studies of related CdSe/CdS NRs and CdS NRs, we have previously attributed this competition process to hole trapping induced exciton localization on CdS NRs.[56] Although the hole trapping time constant was reported to be ~0.7 ps for CdS NRs with an average length of 29 nm,[63] the length dependence of this process remains unknown. To this end, we have measured the hole trapping time for NRs used in this study by TA spectroscopy. Representative average TA spectra at 5-10 ps after 400 nm excitation for $CdSe_{2.7}/CdS_{117}$ and $CdSe_{3.8}/CdS_{116}$ are shown in Figure 9.6a. These spectra exhibited a small and broad photoinduced absorption (PA) signature at wavelengths longer than the B2 exciton band, which has been assigned to trapped holes on the surfaces of CdS rods (by selective removal of electrons from the rods in the presence of electron acceptors).[63] Comparison of NRs with 2.7 nm and 3.8 nm seeds of different lengths (Figure 9.6b) showed that the formation kinetics of the PA signal was independent of the rod length or seed size. Single exponential fit to these kinetics revealed a hole

trapping time of τ_{Trap} = 0.78±0.13 ps, similar to our previous result of CdS NRs.[63] Although the reason for the lack of length dependence in the hole trapping rate is unclear, it may indicate that the hole trap density is independent of rod length. We speculate that they are likely associated with defects on the rod surfaces, such as the unpassivated sulfur anions,[64] that increase proportionally with the rod length.

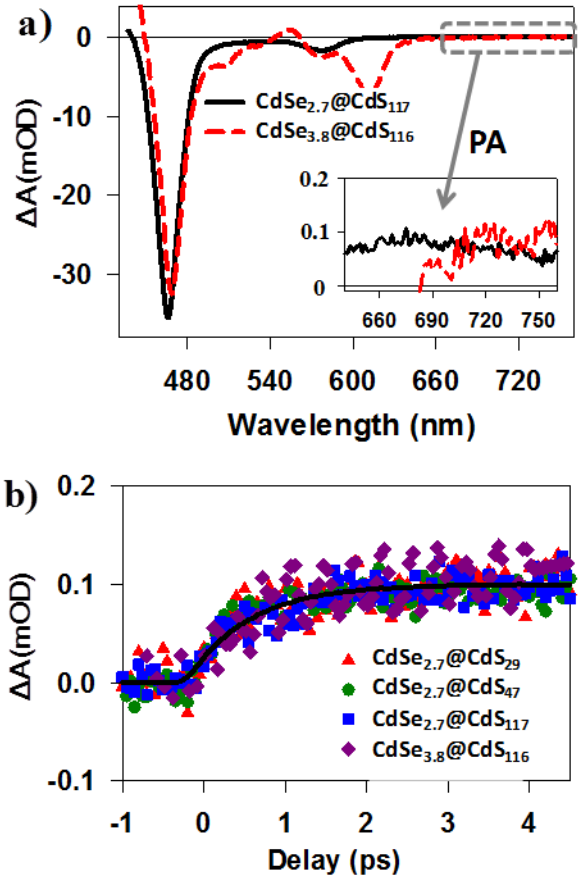

Figure 9.6. a) TA spectra of $CdSe_{2.7}/CdS_{117}$ (black solid line) and $CdSe_{3.8}/CdS_{116}$ (red dashed line) averaged between 5-10 ps after 400 nm excitation. The inset is the expanded view of the photoinduced absorption (PA) signal from 640 nm to 760 nm. b) Formation kinetics of PA signal for $CdSe_{2.7}/CdS_{29}$ (red triangles), $CdSe_{2.7}/CdS_{47}$

(green circles), $CdSe_{2.7}/CdS_{117}$ (blue squares), and $CdSe_{3.8}/CdS_{116}$ (purple diamonds). The black solid line is a fit using single exponential formation.

9.2.5. Mechanism of universal length-dependent exciton localization efficiency.

In the following, we consider three possible mechanisms of exciton localization from the CdS rod to the CdSe seed: energy transfer, ballistic exciton transport, and exciton diffusion.[65] These mechanisms can be differentiated by their dependence on the rod length. Energy transfer time constant is proportional to the sixth power of donor-acceptor distance according to the Foster Resonant Energy Transfer (FRET) theory.[66] Therefore, the length dependence of energy transfer rate can be readily calculated, even though reliable estimates of the absolute energy transfer rate, requiring the information of absorption and emission cross sections, are difficult for these NRs. The simulated results in Figure A.9.1 showed that the FRET mechanism led to a much stronger distance dependence of the exciton localization efficiency than the measured trend shown in Figure 9.5. Further details of the simulation can be found in Appendix 1.

Ballistic transport occurs within the carrier mean free path (L_{mfp}). L_{mfp} in CdS NRs is related to product of scattering time constant, τ_c, and thermal velocity at room temperature (RT), v_{th}, through $L_{mfp} \sim \tau_c \cdot v_{th}$.[67] τ_c can be calculated from the

reported carrier mobility (μ) through $\tau_c = \mu m^*/q$,[67] where m* and q are effective mass and charge of the particle, respectively. The reported upper limit of electron (hole) mobility in bulk single CdS at room temperature is ~400 (~48) $cm^2 s^{-1} V^{-1}$, [68-72] which corresponds to an upper limit of mean free path of ~4 (1.6) nm. The short carrier mean free path in CdS has been attributed to their strong interactions with phonons, through Frohlich, deformation potential, or piezoelectric scatterings.[73] Therefore, in our NRs with lengths of 10s to 100s of nanometers, exciton and carrier transport should proceed through diffusion.

We then model the exciton localization process by accounting for the competition between exciton diffusion and exciton trapping. As shown in Figure 9.3, the CdSe seed divides CdS NR into two segments with length of L_1 and L_2. We solve the exciton localization problem within L_1 and L_2 using the modified 1-D diffusion equation:

$$\frac{\partial N(x,t)}{\partial t} = D\frac{\partial^2 N(x,t)}{\partial^2 x} - \frac{N(x,t)}{\tau_{Trap}} \qquad (9.1),$$

where D is the exciton diffusion constant and $N(x,t)$ is the concentration of excitons at distance x from the seed at time t. The second part on the right-hand side of equation (1) accounts for depopulation of CdS band edge excitons due to trapping. The boundary conditions for this equation are: $N(x,t=0) = N_0$, $N(x=0,t) = 0$, and $J\left(x = L_{1(2)}, t\right) = \frac{\partial N(x=L_{1(2)},t)}{\partial x} = 0$. The first boundary condition indicates

randomly generated excitons along the rod; the second one assumes that exciton transfer across the CdS/CdSe interface (i.e. capture by the CdSe seed) is much faster than the diffusion process within the CdS rod; the third one indicates that the fluxes cross the NR ends are zero. Using these boundary conditions, equation (1) is analytically solvable and the details are shown in Appendix 2. With the solution of N(x,t), the ensemble-averaged exciton population on the rod, S(t), is obtained by integrating N(x,t) over the rod length:

$$S_{L_1}(t) \propto \int_0^{L_1} N(x,t)dx \propto \sum_{n=1}^{\infty} \frac{1}{n^2} e^{-\left[D(\frac{n\pi}{2L_1})^2+\frac{1}{\tau_{Trap}}\right]t} \quad (9.2),$$

where n is an odd integer 1, 3, 5…. The exponents in equation (9.2) reflects the competition between carrier trapping, with time constant of τ_{Trap}, and diffusion, whose characteristic time scale is proportional to the square of the diffusion length.[74] The efficiency of exciton localization to the seed within L_1 is calculated as:

$$\Phi(L_1) = \sum_{n=1}^{\infty} \frac{1}{n^2} \frac{D(\frac{n\pi}{2L_1})^2}{D(\frac{n\pi}{2L_1})^2+\frac{1}{\tau_{Trap}}} \Big/ \sum_{n=1}^{\infty} \frac{1}{n^2} \quad (9.3).$$

$\Phi(L_2)$ can be calculated in the same way and the overall localization efficiency $\Phi(L)$ is obtained by length weighted average of $\Phi(L_2)$ and $\Phi(L_2)$:

$$\Phi(L) = \frac{L_1 \cdot \Phi(L_1) + L_2 \cdot \Phi(L_2)}{L_1 + L_2} \quad (9.4).$$

With the exciton diffusion constant D as the only fitting parameter, we simultaneously fit the localization efficiency for all NRs, as shown in Figure 9.5a. From the best fit,

we obtained a diffusion constant D of 2.3×10^{-4} m^2/s. The electron (D_e) and hole (D_h) diffusion constants in bulk CdS, calculated from their mobilities, are $\sim10\times10^{-4}$ and 1.2×10^{-4} m^2/s, respectively. The exciton center of mass diffusion constant (D_X) can be calculated to be 3.2×10^{-4} m^2/s. Our fitted exciton diffusion constant in CdS NRs is slightly smaller than the bulk value, which is reasonable considering additional scattering channels due to the presence of large surface areas in NRs.[75] Our simulation result confirms that the rod-to-seed exciton localization efficiency is controlled by the competition of exciton diffusion and exciton trapping, which is independent of the rod/seed band alignment, and is dependent on the rod length in a predictable manner.

CdSe/CdS NRs have been used as light absorbing materials in luminescent solar concentrators in which the large CdS rod absorption, efficient rod-to-seed exciton localization and small CdSe seed reabsorption loss enable the concentration of absorbed solar flux by the rod into the emission at the seed.[54] Although the requirement of large rod absorption and small seed reabsorption can be realized by increasing the rod length, there exists an optimal rod length because the rod-to-seed localization efficiency decreases at longer rod length. Thus it is useful to define an effective light harvesting power (or effective absorption cross-section) for these CdSe/CdS NRs as a product of the absorption cross-section of the rod and the rod-to-seed exciton localization efficiency. This quantity represents the effective cross section for creating excitons in the seed through absorption at the rod. The fit to the

measured data discussed above gives a prediction of exciton localization efficiencies of all NRs in the length ranges of 10 nm to 200 nm, as shown in Figure 9.5a. In this calculation, we have assumed that the seed positions followed the trend observed for the NRs we studied and the absorption cross-section of the rod increases linearly with the rod length. The calculated effective seed absorption cross-section (Figure 9.5b) initially increases with the rod length and levels off at a rod length of ~100 nm. In this calculation, we have set the cross sections to one for NRs of 10 nm in length. The effective seed absorption cross section levels off at a value that is 3.5 times of a 10 nm rod, despite a factor 10 and higher total absorption cross section of the CdS rod at a rod length exceeding 100 nm. Further increase in the rod length does not lead to enhanced ability of creating excitons at the seed because of the reduced rod-to-seed exciton localization efficiency. This result confirms the existence of an optimal rod length for light harvesting applications.

9.3. Conclusion

In conclusion, we have examined the mechanism of rod–to-seed exciton localization in CdSe/CdS dot-in-rod NR heterostructures with both type I or quasi-type II band alignments. We observed a universal rod length dependent exciton localization efficiency that decreased with the rod length (~75.7±1.5% in a ~29 nm rod to

30.5±2.6% in a 117 nm rod) and was independent of the CdSe/CdS band alignment. We showed that this universal length dependence could be reproduced by a model that accounted for the competition between ultrafast 1-D exciton diffusion and ultrafast exciton trapping (τ_{Trap} = 0.78±0.13 ps) on the CdS NR. Best fit to the measured results revealed an exciton diffusion constant of 2.3×10^{-4} m^2/s that is slightly smaller than the reported value in bulk CdS. The proposed model can be used to predict the exciton localization efficiency in CdSe/CdS of any length and should be applicable to other NRs, providing a rational approach for optimizing NR morphologies for efficient yet cost-effective 1D heterostructure based devices.

References

(1) Peng, X. G.; Manna, L.; Yang, W. D.; Wickham, J.; Scher, E.; Kadavanich, A.; Alivisatos, A. P. *Nature* **2000**, *404*, 59.

(2) Milliron, D. J.; Hughes, S. M.; Cui, Y.; Manna, L.; Li, J.; Wang, L.-W.; Paul Alivisatos, A. *Nature* **2004**, *430*, 190.

(3) Li, H.; Kanaras, A. G.; Manna, L. *Acc. Chem. Res.* **2013**, *46*, 1387.

(4) Shieh, F.; Saunders, A. E.; Korgel, B. A. *J. Phys. Chem. B* **2005**, *109*, 8538.

(5) Giblin, J.; Kuno, M. *J. Phys. Chem. Lett.* **2010**, *1*, 3340.

(6) Giblin, J.; Syed, M.; Banning, M. T.; Kuno, M.; Hartland, G. *ACS Nano* **2010**, *4*, 358.

(7) Carey, C. R.; LeBel, T.; Crisostomo, D.; Giblin, J.; Kuno, M.; Hartland, G. V. *J. Phys. Chem. C* **2010**, *114*, 16029.

(8) Manna, L.; Scher, E. C.; Li, L.-S.; Alivisatos, A. P. *J. Am. Chem. Soc.* **2002**, *124*, 7136.

(9) Mokari, T.; Banin, U. *Chem. Mat.* **2003**, *15*, 3955.

(10) Htoon, H.; Hollingsworth, J. A.; Dickerson, R.; Klimov, V. I. *Phys. Rev. Lett.* **2003**, *91*, 227401.

(11) Htoon, H.; Hollingworth, J.; Malko, A.; Dickerson, R.; Klimov, V. *Appl. Phys. Lett.* **2003**, *82*, 4776.

(12) Robel, I.; Bunker, B. A.; Kamat, P. V.; Kuno, M. *Nano Lett.* **2006**, *6*, 1344.

(13) Zhu, H.; Lian, T. *J. Am. Chem. Soc.* **2012**, *134*, 11289.

(14) Hu, J.; Li, L.-s.; Yang, W.; Manna, L.; Wang, L.-w.; Alivisatos, A. P. *Science* **2001**, *292*, 2060.

(15) Talapin, D. V.; Koeppe, R.; Götzinger, S.; Kornowski, A.; Lupton, J. M.; Rogach, A. L.; Benson, O.; Feldmann, J.; Weller, H. *Nano Lett.* **2003**, *3*, 1677.

(16) Carbone, L.; Nobile, C.; De Giorgi, M.; Sala, F. D.; Morello, G.; Pompa, P.; Hytch, M.; Snoeck, E.; Fiore, A.; Franchini, I. R.; et al *Nano Lett.* **2007**, *7*, 2942.

(17) Hadar, I.; Hitin, G. B.; Sitt, A.; Faust, A.; Banin, U. *J. Phys. Chem. Lett.* **2013**, 502.

(18) Sitt, A.; Salant, A.; Menagen, G.; Banin, U. *Nano Lett.* **2011**, *11*, 2054.

(19) Wang, J.; Gudiksen, M. S.; Duan, X.; Cui, Y.; Lieber, C. M. *Science* **2001**, *293*, 1455.

(20) Deka, S.; Quarta, A.; Lupo, M. G.; Falqui, A.; Boninelli, S.; Giannini, C.; Morello, G.; De Giorgi, M.; Lanzani, G.; Spinella, C.; et al *J. Am. Chem. Soc.* **2009**, *131*, 2948.

(21) Pisanello, F.; Martiradonna, L.; Spinicelli, P.; Fiore, A.; Hermier, J. P.; Manna, L.; Cingolani, R.; Giacobino, E.; De Vittorio, M.; Bramati, A. *Superlattices Microstruct.* **2010**, *47*, 165.

(22) Kazes, M.; Lewis, D. Y.; Ebenstein, Y.; Mokari, T.; Banin, U. *Adv. Mater.* **2002**, *14*, 317.

(23) Amirav, L.; Alivisatos, A. P. *J. Phys. Chem. Lett.* **2010**, *1*, 1051.

(24) Berr, M.; Vaneski, A.; Susha, A. S.; Rodriguez-Fernandez, J.; Doblinger, M.; Jackel, F.; Rogach, A. L.; Feldmann, J. *Appl. Phys. Lett.* **2010**, *97*, 0931081.

(25) Brown, K. A.; Wilker, M. B.; Boehm, M.; Dukovic, G.; King, P. W. *J. Am. Chem. Soc.* **2012**, *134*, 5627.

(26) Bang, J. U.; Lee, S. J.; Jang, J. S.; Choi, W.; Song, H. *J. Phys. Chem. Lett.* **2012**, *3*, 3781.

(27) Khon, E.; Lambright, K.; Khnayzer, R. S.; Moroz, P.; Perera, D.; Butaeva, E.; Lambright, S.; Castellano, F. N.; Zamkov, M. *Nano Lett.* **2013**, *13*, 2016.

(28) Xing, G.; Liao, Y.; Wu, X.; Chakrabortty, S.; Liu, X.; Yeow, E. K. L.; Chan, Y.; Sum, T. C. *ACS Nano* **2012**, *6*, 10835.

(29) Saba, M.; Minniberger, S.; Quochi, F.; Roither, J.; Marceddu, M.; Gocalinska, A.; Kovalenko, M. V.; Talapin, D. V.; Heiss, W.; Mura, A. *Adv. Mater* **2009**, *21*, 4942.

(30) Reiss, P.; Protière, M.; Li, L. *Small* **2009**, *5*, 154.

(31) Hines, M. A.; Guyot-Sionnest, P. *J. Phys. Chem.* **1996**, *100*, 468.

(32) Dabbousi, B. O.; Rodriguez-Viejo, J.; Mikulec, F. V.; Heine, J. R.; Mattoussi, H.; Ober, R.; Jensen, K. F.; Bawendi, M. G. *J. Phys. Chem. B* **1997**, *101*, 9463.

(33) Peng, X.; Schlamp, M. C.; Kadavanich, A. V.; Alivisatos, A. P. *J. Am. Chem. Soc.* **1997**, *119*, 7019.

(34) Scholes, G. D. *Adv. Funct. Mater.* **2008**, *18*, 1157.

(35) Smith, A. M.; Nie, S. *Acc. Chem. Res.* **2009**, *43*, 190.

(36) Talapin, D. V.; Nelson, J. H.; Shevchenko, E. V.; Aloni, S.; Sadtler, B.; Alivisatos, A. P. *Nano Lett.* **2007**, *7*, 2951.

(37) Lupo, M. G.; Della Sala, F.; Carbone, L.; Zavelani-Rossi, M.; Fiore, A.; Lüer, L.; Polli, D.; Cingolani, R.; Manna, L.; Lanzani, G. *Nano Lett.* **2008**, *8*, 4582.

(38) Steiner, D.; Dorfs, D.; Banin, U.; Della Sala, F.; Manna, L.; Millo, O. *Nano Lett.* **2008**, *8*, 2954.

(39) Sitt, A.; Sala, F. D.; Menagen, G.; Banin, U. *Nano Lett.* **2009**, *9*, 3470.

(40) Borys, N. J.; Walter, M. J.; Huang, J.; Talapin, D. V.; Lupton, J. M. *Science* **2010**, *330*, 1371.

(41) Smith, E. R.; Luther, J. M.; Johnson, J. C. *Nano Lett.* **2011**, *11*, 4923.

(42) Kunneman, L. T.; Zanella, M.; Manna, L.; Siebbeles, L. D. A.; Schins, J. M. *J. Phys. Chem. C* **2013**, *117*, 3146.

(43) Eshet, H.; Grünwald, M.; Rabani, E. *Nano Lett.* **2013**, *13*, 5880.

(44) She, C.; Demortière, A.; Shevchenko, E. V.; Pelton, M. *J. Phys. Chem. Lett.* **2011**, *2*, 1469.

(45) Rainò, G.; Stöferle, T.; Moreels, I.; Gomes, R.; Kamal, J. S.; Hens, Z.; Mahrt, R. F. *ACS Nano* **2011**, *5*, 4031.

(46) Mauser, C.; Da Como, E.; Baldauf, J.; Rogach, A. L.; Huang, J.; Talapin, D. V.; Feldmann, J. *Phys. Rev. B* **2010**, *82*, 0813061.

(47) Lutich, A. A.; Mauser, C.; Da Como, E.; Huang, J.; Vaneski, A.; Talapin, D. V.; Rogach, A. L.; Feldmann, J. *Nano Lett.* **2010**, *10*, 4646.

(48) Luo, Y.; Wang, L.-W. *ACS Nano* **2009**, *4*, 91.

(49) Yoskovitz, E.; Menagen, G.; Sitt, A.; Lachman, E.; Banin, U. *Nano Lett.* **2010**, *10*, 3068.

(50) Shabaev, A.; Efros, A. L. *Nano Lett.* **2004**, *4*, 1821.

(51) Scholes, G. D.; Rumbles, G. *Nat. Mater.* **2006**, *5*, 683.

(52) Scholes, G. D.; Fleming, G. R.; Olaya-Castro, A.; van Grondelle, R. *Nat Chem* **2011**, *3*, 763.

(53) Wu, K.; Chen, Z.; Lv, H.; Zhu, H.; Hill, C. L.; Lian, T. *J. Am. Chem. Soc.* **2014**, *136*, 7708.

(54) Bronstein, N. D.; Li, L.; Xu, L.; Yao, Y.; Ferry, V. E.; Alivisatos, A. P.; Nuzzo, R. G. *ACS Nano* **2013**, *8*, 44.

(55) Kelestemur, Y.; Cihan, A. F.; Guzelturk, B.; Demir, H. V. *Nanoscale* **2014**, *6*, 8509.

(56) Wu, K.; Rodríguez-Córdoba, W. E.; Liu, Z.; Zhu, H.; Lian, T. *ACS Nano* **2013**, *7*, 7173.

(57) She, C.; Bryant, G. W.; Demortière, A.; Shevchenko, E. V.; Pelton, M. *Phys. Rev. B* **2013**, *87*, 155427.

(58) Hill, L. J.; Richey, N. E.; Sung, Y.; Dirlam, P. T.; Griebel, J. J.; Lavoie-Higgins, E.; Shim, I.-B.; Pinna, N.; Willinger, M.-G.; Vogel, W.; et al *ACS Nano* **2014**, *8*, 3272.

(59) Hill, L. J.; Bull, M. M.; Sung, Y.; Simmonds, A. G.; Dirlam, P. T.; Richey, N. E.; DeRosa, S. E.; Shim, I.-B.; Guin, D.; et al *ACS Nano* **2012**, *6*, 8632.

(60) Peter, Y. Y.; Cardona, M. *Fundamentals of Semiconductors: Physics and Materials Properties*; Springer, 2010.

(61) Lupo, M. G.; Zavelani-Rossi, M.; Fiore, A.; Polli, D.; Carbone, L.; Cingolani, R.; Manna, L.; Lanzani, G. *Superlattices Microstruct.* **2010**, *47*, 170.

(62) Klimov, V. I. *J. Phys. Chem. B* **2000**, *104*, 6112.

(63) Wu, K.; Zhu, H.; Liu, Z.; Rodríguez-Córdoba, W.; Lian, T. *J. Am. Chem. Soc.* **2012**, *134*, 10337.

(64) Wei, H. H.-Y.; Evans, C. M.; Swartz, B. D.; Neukirch, A. J.; Young, J.; Prezhdo, O. V.; Krauss, T. D. *Nano Lett.* **2012**, *12*, 4465.

(65) Wu, K.; Rodríguez-Córdoba, W.; Lian, T. *J. Phys. Chem. B* **2014**, *118*, 14062.

(66) Stryer, L. *Annu. Rev. Biochem.* **1978**, *47*, 819.

(67) Van Zeghbroeck, B. *Colarado University* **2004**.

(68) Warman, J. M.; De Haas, M. P.; Van Hovell tot Westerflier, S. W. F. M.; Binsma, J. J. M.; Kolar, Z. I. *J. Phys. Chem.* **1989**, *93*, 5895.

(69) Islam, M. N.; Woods, J. *J. Phys. D: Appl. Phys.* **1970**, *3*, 1297.

(70) Spear, W. E.; Mort, J. *Proc. Phys. Soc.* **1963**, *81*, 130.

(71) Mort, J.; Spear, W. E. *Phys. Rev. Lett.* **1962**, *8*, 314.

(72) Islam, M. N.; Woods, J. *Solid State Commun.* **1969**, *7*, 1457.

(73) Khandros, L. I.; Pekar, G. S.; Sheinkman, M. K.; Shtrum, E. L. *Phys. Status Solidi (a)* **1976**, *33*, 765.

(74) Houston, P. L. *Chemical Kinetics and Reaction Dynamics*; Courier Dover Publications, 2012.

(75) Joyce, H. J.; Wong-Leung, J.; Yong, C.-K.; Docherty, C. J.; Paiman, S.; Gao, Q.; Tan, H. H.; Jagadish, C.; Lloyd-Hughes, J.; Herz, L. M.; Johnston, M. B. *Nano Lett.* **2012**, *12*, 5325.

Appendix 1

Simulating Exciton Localization with FRET Model

In the Forster resonant energy transfer (FRET) theory, the energy transfer time constant can be calculated as:

$$\tau_{EnT} = \tau_0 (\frac{L}{R})^6 \quad \text{(A.9.1)},$$

where τ_0 is the donor excited state lifetime in the absence of the acceptor, L is the donor-acceptor distance, and R is the Forster radius, defined as the distance between donor and acceptor at which the fluorescence quenching efficiency is 50% . As shown in Figure A.9.1a, we use τ_0/R^6 as a fitting parameter C to simulate the exciton localization process. At distance L_i from the seed, the energy transfer time is $\tau_{EnT,i} = C \cdot L_i^6$. Due to competition with exciton trapping process, the efficiency of exciton generated at L_i being localized is: $\Phi_i = \tau_{Trap}/(\tau_{Trap}+\tau_{EnT,i})$.We average over all the possible L_i to obtain the ensemble exciton localization efficiency:

$$\Phi_{Loc} = \frac{1}{N} \cdot \sum_{i=1}^{N} \tau_{Trap}/(\tau_{Trap} + \tau_{EnT,i}) \quad \text{(A.9.2)}.$$

To obtain the localization efficiency of 75% for DIRs with a length of ~30 nm ($CdSe_{2.7}/CdSe_{29}$ and $CdSe_{3.9}/CdS_{31}$), the fitting parameter C is ~10^{-6} ps nm^{-6}. Using this parameter, the localization efficiency for 48 nm and 116 nm NRs are estimated to be 40.4% and 17.5%, respectively. As shown in Figure A.9.1b, they are considerably

lower than the experimental values. This is because the sixth power dependence on rod length is too drastic so that exciton localization efficiency quickly vanishes as distance increases. Therefore, the FRET model is not an appropriate description for exciton localization process due to its sixth power dependence on rod length. Since excitons are free to move along the NRs, it is natural to consider that exciton can diffuse to core location, which is modeled in the main text.

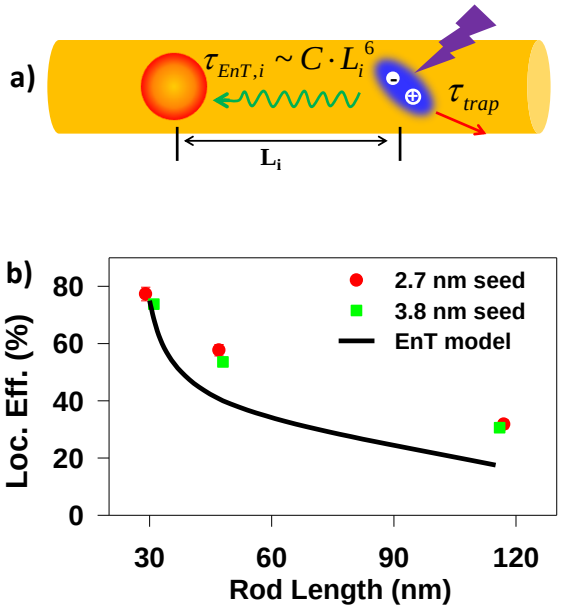

Figure A.9.1. a) A scheme showing the competition between exciton energy transfer and exciton trapping. The localization efficiency is an average over all the excitons generated randomly along the rod. b) Measured and simulated exciton localization efficiencies. The 2.7 nm and 3.8 nm seeded NRs with different lengths are shown in red circles and green squares, respectively. The black solid line is simulated exciton localization efficiency using FRET model.

Appendix 2

Analytic solution of exciton diffusion and trapping in NRs

Differential Equation (9.1) in the main text can be solved using Variable Separable Method by assuming:

$$N(x,t) = X(x) \cdot T(t) \qquad \text{(A.9.3).}$$

Consequently, we have:

$$\frac{dT(t)}{DT(t)dt} = \frac{d^2X(x)}{X(x)\,d^2x} - \frac{1}{\tau_{Trap}D} = C \qquad \text{(A.9.4).}$$

We further introduce a parameter k so that:

$$\frac{d^2X(x)}{X(x)\,d^2x} = C + \frac{1}{\tau_{Trap}D} = -k^2 \qquad \text{(A.9.5).}$$

Therefore,

$$\frac{dT(t)}{DT(t)dt} = C = -(k^2 + \frac{1}{\tau_{Trap}D}) \qquad \text{(A.9.6).}$$

Solving equation A.9.6 gives:

$$T(t) = e^{-\left(Dk^2 + \frac{1}{\tau_{Trap}}\right)t} \qquad \text{(A.9.7).}$$

Equation A.9.5 can be solved using Fourier series accounting for the boundary conditions in the main text, which result in:

$$X(x) = \sum_{n=1}^{\infty} \frac{2N_0}{n\pi} \mathrm{Sin}\frac{n\pi}{2L}x \qquad \text{(A.9.8),}$$

where n is an odd integer 1,3,5…

Therefore,

$$N(x,t) = X(x) = \sum_{n=1}^{\infty} \frac{2N_0}{n\pi} \mathrm{Sin} \frac{n\pi}{2L} x \cdot e^{-\left(D(\frac{n\pi}{2L})^2 + \frac{1}{\tau_{Trap}}\right)t}$$

(A.9.9).

Integration of N(x,t) over length L gives equation (9.2) in the main text.

Chapter 10. Unity Efficiency Formation of Charge-transfer Exciton State in Atomically-thin CdSe/CdTe Type-II Heteronanosheets

10.1. Introduction

Colloidal 2-D CdX (X=S, Se, Te) nano-platelets (NPLs), or nanosheets (NSs), with atomically precise thickness of 1-2 nanometers have been reported recently.[1-6] The precise and strong quantum confinement in the thickness direction gives rise to uniform band edge positions and exciton energy across the NSs of 10s-100s nm in length and width. This enables rapid in-plane exciton and carrier motion, in addition to precise tuning of energetics (by thickness). Unfortunately, similar to other 2-dimensional (2D) materials (such as transition metal dichalcogenides[7,8]), strong electron-hole Coulomb interaction and large exposed surface leads to fast exciton radiative and nonradiative decay,[3] hindering their applications as light harvesting materials for solar energy conversion. It has been well demonstrated that in 0D

quantum dots and 1D nanorods, type-II heterostructures (with conduction band minimum and valence band maximum residing in two different domains) can prolong exciton lifetime by increasing the spatial separation of the electron and hole. [9-16] [17-23] Although several type I heteronanosheets, such as CdSe/CdS or CdSe/CdZnS core/shell[24,25] and CdSe/CdS core/crown,[26,27] have been synthesized and studied, the preparation of type-II heteronanosheets has only been reported very recently.[28] This study demonstrates that excited state lifetime can also be extended in CdSe/CdTe core/crown type-II heteronanosheets, similar to type-II quantum dots and nanorods. Our studies in previous two chapters have shown that of in CdSe/CdS dot-in-rod heteronanorods, due to large electron-hole binding energy and presence of defects, ultrafast trapping of excitons on CdS rod reduces the efficiency of exciton localization to the CdSe core.[29-32] Because similar trapping processes should also exist in type II heteronanosheets, it is important to investigate how they may compete with the exciton localization process and whether the larger in-plane exciton mobility can reduce the effect of the undesirable exciton trapping pathways.[33]

In this chapter, we report the first ultrafast spectroscopic study of exciton localization and interfacial separation process in CdSe/CdTe core/crown type-II nanosheets (with a CdTe NS crown laterally extending on a CdSe NS core, Figure 10.1.a). The structure was confirmed by electron microscopy, elemental analysis, and static and time-resolved optical spectroscopy. The formation of CdSe/CdTe type II

heterojunctions led to charge transfer (CT) absorption and emission features. Photoluminescence excitation measurements showed that excitons from CdTe and CdSe domains were localized to and separated across the CdSe/CdTe heterojunction to form CT excitons with near unity efficiency. The CT exciton formation process was shown to occur with a time constant of 0.64±0.07 ps by transient absorption studies. The spatial separation of electrons and holes across the heterojunction reduced their radiative and nonradiative recombination rates, leading to long-lived CT excitons with a half-life of 41.7±2.5 ns, ~30 times longer than core-only CdSe NSs.

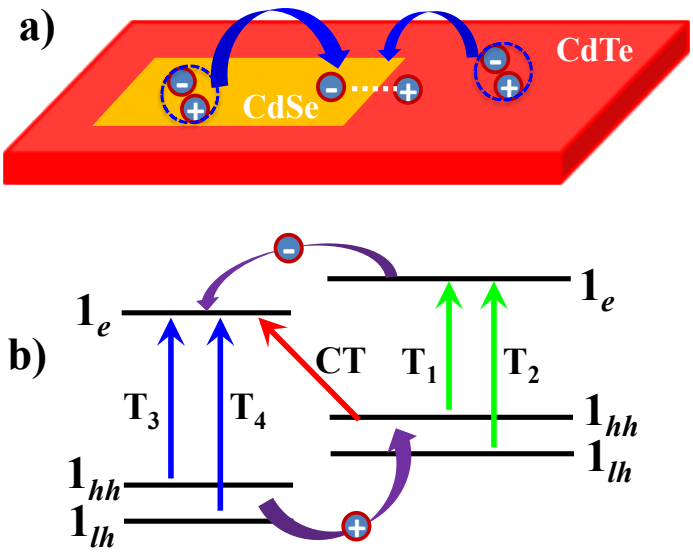

Figure 10.1. a) A schematic depiction of charge transfer exciton formation in Type-II CdSe/CdTe nanosheets. Photo-generated excitons in both CdSe and CdTe localize to the interface to form charge transfer excitons with electrons in CdSe and holes in CdTe. b) Energy level diagram in Type-II CdSe/CdTe nanosheets. T1 (T3) and T2 (T4) are lowest energy heavy (1_{hh}) and light (1_{lh}) hole to electron (1_e) transitions,

respectively, in CdTe (CdSe) and the charge transfer (CT) band corresponds to transition between heavy hole in CdTe and electron in CdSe. The charge separation processes are also indicated

10.2 Results and Discussions

10.2.1. Sample Preparations and Characterizations.

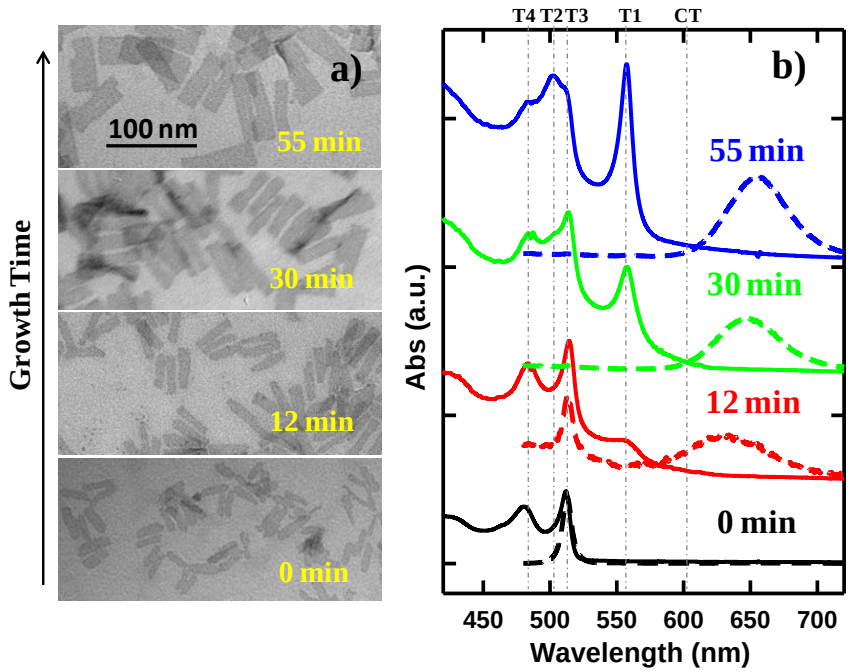

Figure 10.2. a) TEM images and b) absorption (solid line) and Photoluminescence (PL, dashed lines) spectra of CdSe/CdTe NSs at indicated growth times (starting with CdSe NSs at 0 min.).

CdSe NSs were synthesized according to literature procedures.[1-3] Lateral extension of CdTe on CdSe NSs was achieved following a reported synthetic procedures for CdTe NSs with a slight modification.[34] By injecting Te precursors at a lower rate and lower temperature than those reported for CdTe synthesis, CdTe heterogeneous nucleation on CdSe NSs can dominate over homogeneous nucleation in solution.[26,27] Detailed synthetic method and conditions can be found in the Chapter 2 and are similar to a recent independent report by Dubertret and coworkers.[28] Transmission Electron Microscopy (TEM) images of CdSe/CdTe nanosheets at different times after Te precursor injection (Figure 10.2.a) clearly shows a gradual increase of NS lateral dimension. The starting CdSe NSs (0 min) exhibited rectangular morphology with an average length and width of 28.0 (±2.5) nm×7.0 (±1.0) nm, respectively. After 55 minutes of Te precursor injection, the NSs maintained their rectangular morphology but the average size increased to 71.0 (±7.7) nm×21.3 (±3.7) nm, corresponding to ~8 fold increase in surface area.

The absorption spectra (Figure 10.2b) showed three features that are consistent with the lateral extension of CdTe on CdSe. The exciton peak positions of NSs are determined by their thickness. The CdSe NS peaks, centered at ~512 nm (T3, n=1

heavy hole to n=1 electron, or 1_{hh}-1_e[1]) and ~480 nm (T4, n=1 light hole to n=1 electron, or 1_{lh}-1_e), remained unchanged during CdTe growth, indicating negligible change of CdSe thickness (~1.2 nm). [27] The amplitudes of two new peaks centered at ~556 nm (T1) and ~501 nm (T2) and a broad absorption tail from ~650 nm (CT) increased with growth time. The former (T1 and T2) matches the 1_{hh}-1_e and 1_{lh}-1_e transitions of CdTe NSs with a thickness of ~1.3 nm.[28,34] The CT band is energetically lower than both the lowest energy exciton transitions in CdSe (T3) and CdTe (T1) NSs and can be attributed to the charge transfer (CT) transition from the CdTe valance band (VB) edge to CdSe conduction band (CB) edge (Figure 10.1b), a characteristic feature of type II heterostructures.[9] Photoluminescence (PL) spectra of these samples (Figure 10.2b, exciting at 400 nm) showed that upon CdTe growth, the PL of CdSe at ~512 nm was gradually replaced by CT emission centered at ~650 nm, showing negligible emission of CdTe NS (expected at ~556nm).[34] These results confirm that the observed morphological changes are due to formation of CdSe/CdTe heteronanosheets instead of homogeneous nucleation of CdTe NS. In the following, we will focus on the 55 min sample for structural and spectroscopic characterizations.

High-angle annular dark-field (HAADF) scanning TEM (STEM) combined with energy-dispersive X-ray spectroscopy (EDX) was used to provide direct evidence for heterostructure formation. For the selected area in the HAADF image of Figure 10.3a,

elemental maps for Cd, Se, and Te are shown in Figure 10.3c, d, and f, respectively. The Cd map matched well with TEM image; Se was only present in the center of nanosheets; and the Te map showed holes in the center, complementary to the Se map. The overlaid map, shown in Figure 10.3b, confirms that in these heterostructure, the CdTe NS laterally extends on CdSe seed, as illustrated in Figure 10.1a.

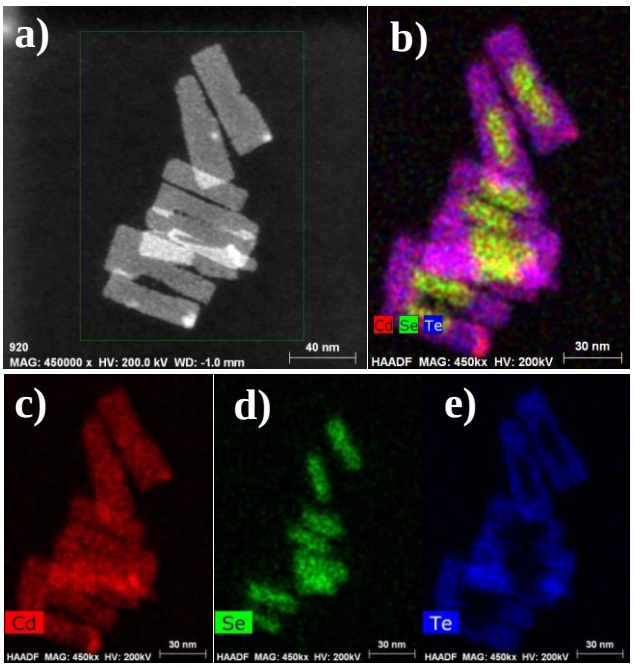

Figure 10.3. a) HAADF STEM image of CdSe/CdTe nanosheet. b) Overlaid elemental maps of Cd (red), Se (green), and Te (blue). Elemental maps of c) Cd, d) Se and e) Te.

10.2.2. Efficiency of Charge Transfer Exciton formation.

In Figure 10.4.a, we compare the Photoluminescence Excitation (PLE, monitoring emission at 653±1 nm) spectrum of CdSe/CdTe NSs with their absorptance spectrum. The latter represents the percentage of absorbed photons (i.e. $1\text{-}10^{-OD}$, OD=optical density). By normalizing PLE and absorptance at the CT band, as done in Figure 10.4a, the ratios of these curves represent the relative emission QYs as a function of excitation wavelength (with QY at CT band excitation set to 1). As shown in Figure 10.4b, the relative QYs are near unity from 450 to 650 nm, indicating that all the photo-generated excitons can move to the CdSe/CdTe interface to form the CT excitons.

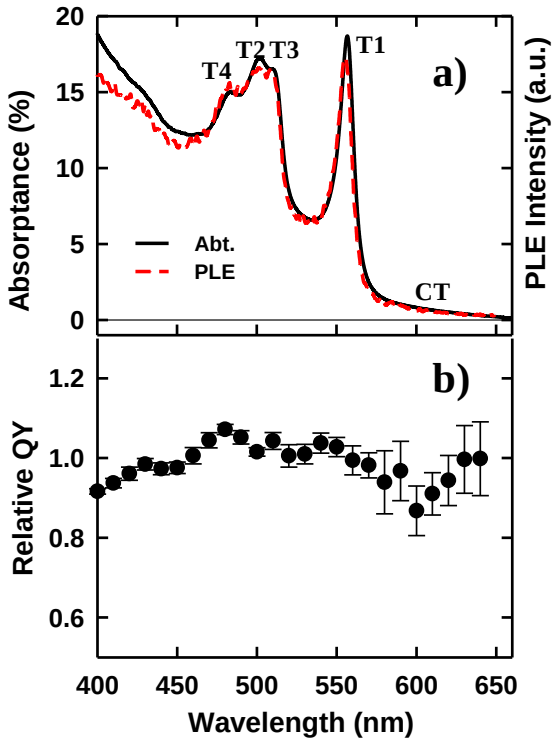

Figure 10.4. a) Photoluminescence Excitation (PLE, red dashed line) and absorptance (Abt, black solid line) spectra of CdSe/CdTe NSs. These curves are normalized at the

CT band. b) Relative emission QYs (the ratio between absorptance and PLE) as a function of excitation wavelength. The relative QY was set to 1 at the CT band.

There are two implications from the near unity formation efficiency of the CT exciton. First, the exciton transport through CdTe and CdSe domains is fast enough to reach the CdSe/CdTe interface prior to their radiative and nonradiative decay. Secondly, the initial photogenerated excitons in both CdTe and CdSe domains can be dissociated across the CdSe/CdTe interface, in spite of the large exciton binding energy (~ 100s of meV) in these 2D nanosheets.[35,36] Similar processes have been observed in type-II single layer transition metal dichalcogenide heterojunctions[8,37] and can be explained by the fact that the energy required for exciton dissociation is compensated by the binding energy of the CT exciton.[8]

10.2.3. Ultrafast Charge Separation and Recombination Dynamics

The exciton localization and separation dynamics implied by the PLE result can be directly probed by transient absorption (TA) spectroscopy. In these measurements, we have used low excitation flux to ensure that the signal was dominated by single excitons (see Figure A.10.1), excluding the complications of multi-exciton annihilation dynamics.[38,39] We first examined the CdSe/CdTe NSs with 625 nm excitation, where the CT band was selectively excited according to the

absorption spectrum in Figure 10.2b. The resultant TA spectra and kinetics (Figure 10.5a and b) showed instantaneous bleach of T3 (~511 nm), T4 (~480 nm) and CT (~630 nm) bands and negligible subsequent changes of these TA features within the first nanosecond. Although part of the CT bleach was obscured by the scattered pump beam at 625 nm, it was fully observed with 400 nm excitation (see below). We have shown recently that the bleaches of exciton bands of Cd chalcogenide NSs were caused by state-filling of the CB electron level,[40] similar to Cd chalcogenide quantum dots and nanorods.[41-44] [3]The observed TA features indicate the direct generation of electrons in CdSe CB edge, consistent with the nature of the CT band (see Figure 10.1b). The CT transition should also directly generate VB holes in CdTe. The presence of holes has been shown to shift the exciton peak position, giving rise to derivative like charge separated states (CS) features in TA spectrum.[20,40,43,45-48] Indeed, CS feature of T1 band was observed at 520-570 nm (see inset of Figure 10.5a and 10.5b). Therefore, these TA features confirm the proposed type II electronic structure in Figure 10.1.

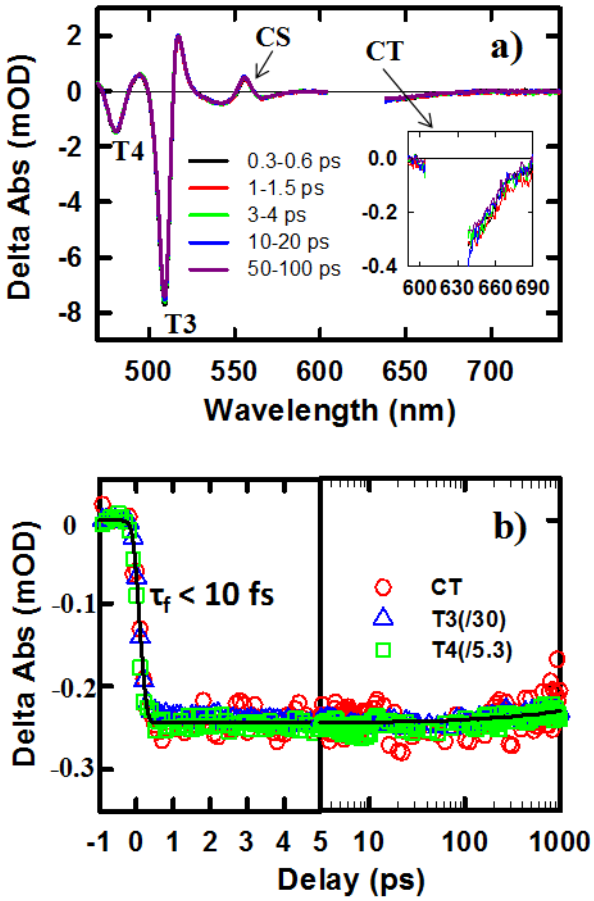

Figure 10.5. TA spectra of CdSe/CdTe heteronanosheets measured at 625 nm excitation of the CT band. a) TA spectra at indicated delays (up to 100 ps). b) Normalized comparison of TA Kinetics of CT (red circles), T3 (blue triangles), and T4 (green squares) features and their fit (black solid line). The fit shows an instantaneous formation (< 10 fs) and negligible decay in 1000 ps. The x-axis is in linear scale from -1 to 5 ps and logarithmic scale from 5 to 1000 ns.

We next investigated how the excitons generated at the CdTe crown can be localized to the CdSe/CdTe interface. In this experiment the CdSe/CdTe NSs were excited at

400 nm, where the CdSe and CdTe domains contributed to 16.8% and 83.2 %, respectively, of the total absorption. The larger CdTe absorption is consistent with the ~7 fold larger surface area of CdTe than CdSe domain. The TA spectra (Figure 10.6a) showed ultrafast decay of T1 and T2 bleach and concomitant formation of the bleach of T3, T4 and the CT bands, consistent with electron transfer from CdTe to CdSe CB. After ~100 ps, T1 and T2 features completely disappeared and the resulting spectra were identical to the TA spectra measured with 625 nm excitation, as shown in Figure 10.6b, indicating complete conversion of excitons at CdSe and CdTe sheets to CT excitons across the CdTe/CdSe interface. This is consistent with the near unity CT band formation efficiency determined from the PLE measurement. Interestingly, the excitation wavelength independent final TA spectra in Figure 5b are in sharp contrast with previously-examined CdSe/CdS heteronanorods, in which the competition of rapid exciton trapping on the CdS nanorod and localization to the CdSe core lead to excitation wavelength dependent branching ratio of long lived exciton states. [29,30]

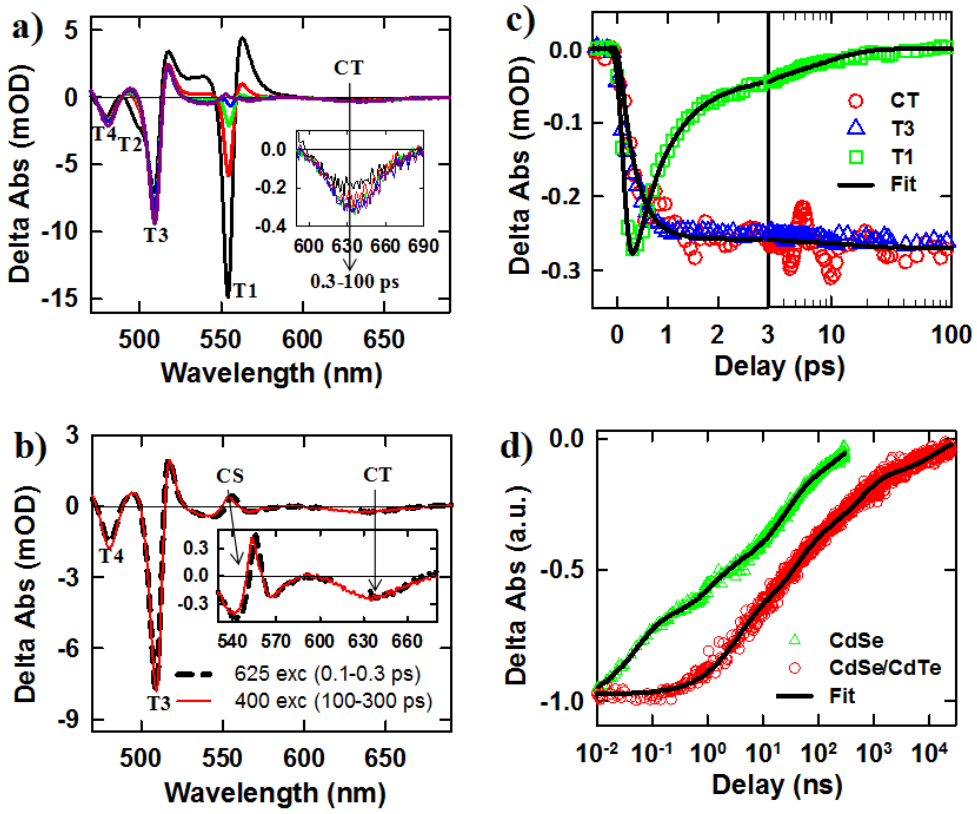

Figure 10.6. TA spectra and kinetics of CdSe/CdTe NSs. a) TA spectra at 0.3-0.4 ps (black), 1-1.5 ps (red), 3-4 ps (green), 10-20 ps (blue), and 50-100 ps (purple) after 400 nm excitation. Inset: expanded view of the CT feature. b) Comparison of TA spectra measured with 625 nm (at 0.1-0.3 ps, black dashed line) and 400 nm (at 100-300 ps, red solid line) excitation. Inset: expanded view of CS feature of T1 from 530 to 580 nm and CT band bleach from 590 to 690 nm. c) TA kinetics of CT (610-650 nm, red circles), T3 (511 nm, blue triangles), and T1 (555 nm, green squares) in CdSe/CdTe NSs measured with 400 nm excitation and their multi-exponential fits (black solid lines). d) Comparison of electron lifetime (T3 exciton bleach recovery) in

core-only CdSe (red circles) and CdSe/CdTe (green squares) NSs. The black solid lines are multi-exponential fits.

As shown in Figure 10.6c, the formation of CT and T3 bleach (electrons in CdSe 1_e level) and the recovery of T1 bleach (electrons in CdTe 1_e level) could be fitted with the same sets of parameters, confirming electron transfer from CdTe to CdSe. According to the fit, electron transfer kinetics from CdTe to CdSe was described as a bi-exponential process with time constants of 0.48±0.09 ps (90.4±0.4%) and 9.50±0.85 ps (9.6±0.3%). Electron transfer from CdTe to CdSe domains contains the contribution of exciton transport to the CdSe/CdTe interface and interfacial electron transfer across the heterojunction driven by the conduction band offset. A previous study on CdSe/CdTe core/shell QDs reported an electron transfer time of ~0.8 ps from CdTe to CdSe.[20] The main electron transfer component in our heteronanosheets is faster than the CdTe/CdSe core/shell QDs, which indicates that the intra-nanosheet exciton transport time is extremely fast, if not negligible, caused by the large in-plane exciton mobility. This observation is also consistent with our previous finding of ultrafast exciton quenching of CdSe NSs by decorated Pt nanoparticles.[40] In addition, the laterally extended 2D sheets might have smaller interfacial strain than curved core/shell QDs, which may reduce the possible interfacial charge transfer barrier.[49] The minor slow electron transfer component is likely caused by trapped excitons at hole traps, which slows down their in-plane transport and interfacial separation.[31,40,50]

[50]400 nm excitation should also generate excitons at CdSe core, which would separate at the interface by hole transfer to CdTe. This process should lead to derivative like features in the CdTe bands (Figure 10.5a and 10.6b). Unfortunately, the transient absorption signals at CdTe exciton bands were dominated by much larger state filling induced bleach and the smaller hole transfer induced change could not be independently probed. Furthermore, because of the spectral overlap of CdSe with CdTe transitions, selective excitation of the CdSe sheet was not experimentally feasible.

The electrons in the CT states were long-lived. The kinetics of T3 recovery (Figure 10.6d) was fitted by multi-exponential decay with a half-life of 41.7±2.5 ns. As a comparison, the T3 exciton bleach kinetics of CdSe only NSs (Figure 10.6d) showed a half-life of 1.4±0.2 ns. Therefore, the CB electron life-time was prolonged by ~30-fold in type-II NSs. Because T3 exciton bleach only reflected the CB electron population, we turned to PL decay (depending on both CB electrons and VB holes) to probe the effect of CT exciton formation on VB holes. The time-resolved PL decay and T3 exciton bleach kinetics of CdSe/CdTe NSs were compared in Figure 10.7. The PL decay matched well with the T3 bleach recovery between 5 -1000 ns, confirming that the spatial separation of electrons and holes across the CdTe/CdSe interface gave rise to long-lived CT excitons. This is consistent with a recent report by Dubertret and coworkers.[28] Interestingly, the PL decay showed a fast component (with 50.2±1.7%

amplitude and a time constant of 1.2±0.1 ns) that was not present in the T3 bleach recovery, which can only be assigned to the trapping of VB holes in the CdTe domain. [50]Because this hole trapping process does not lead to the decay of the CB electron, it indicates that the spatial separation of electrons and holes across the heterojunction also slows down their nonradiative recombination at trapped sites.

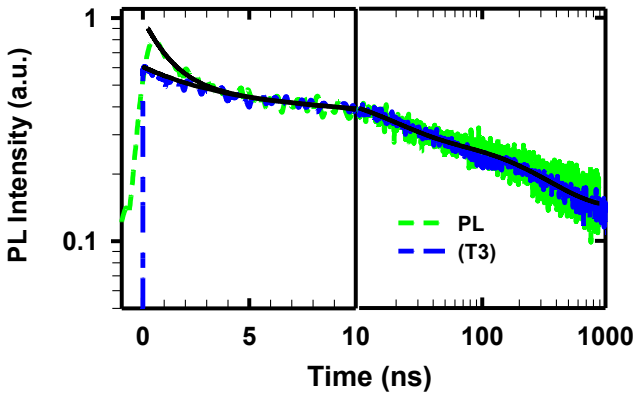

Figure 10.7. Comparison of time-resolved PL decay (green dashed line) and TA T3 (CT) bleach recovery kinetics of (blue dashed line) in CdSe/CdTe type II NSs measured with 400 nm excitation. The black solid lines are multi-exponential fits and fitting parameters are listed in Table S2.

It should be noted that similar efficient exciton localization was observed in Type I CdSe/CdS core/crown nanosheets.[27] These efficient in-plane exciton transports are in contrast to 1-D CdSe/CdS NR heterostructures, in which the localization efficiency is significantly less than unity due to hole-trap induced exciton trapping on the CdS

rod.[29,30] We tentatively attribute the efficient exciton localization in NSs to large exciton and carrier mobility in these atomically flat materials.[39] It is also interesting to compare the CdSe/CdTe heterostructure to MoS_2/WS_2 van der Waals heterostructures at which a ~50 fs hole transfer time was reported.[8] Although the covalent/ionic bonding at our CdSe/CdTe interface is much stronger than van der Waals interactions per unit area,[8] the smaller total interfacial area in the core/crown structure than the stacked structure might lead to weaker total electronic coupling and therefore slower charge separation. Nonetheless, the charge separation rate in these CdSe/CdTe core/crown heterostructure is still much faster than excited state lifetime of NSs (on the order of ns[51]), which gives rise to unity yield for forming the long-lived CT exciton states. The efficient exciton localization in CdSe/CdTe nanosheets may offer a new class of materials for constructing triadic nanosheet heterostructures (such as CdSe/CdTe/Pt) for light-driven H_2 generation. Our recent study suggests that in CdSe NS-Pt heterostructures, the ultrafast exciton mobility leads to efficient quenching of excitons by energy transfer, which limits the utility of such structure of solar-driven H_2 generation.[40] The ability to form long-lived charge transfer excitons at CdSe/CdTe interface may allow efficient electron transfer to Pt in CdSe/CdTe/Pt triadic structures.

10.3. Conclusion

In conclusion, we have studied the ultrafast exciton dynamics in colloidal type-II CdSe/CdTe core/crown heteronanosheets. The formation of the heterostructure was confirmed by absorption, emission, electron microscopy and element analysis. By PLE measurements, we showed that excitons generated in CdSe and CdTe domains could be localized to the CdSe/CdTe heterojunction to form charge transfer excitons with unity efficiency. Using transient absorption spectroscopy, we showed that these charge transfer excitons were formed on the ultrafast time scale (half-life ~0.64±0.07 ps) due to facile in-plane exciton motion and interfacial electron transfer. The spatial separation of electrons and holes at the CT states effectively suppressed radiative and nonradiative recombination, leading to long-lived charge transfer exciton state (half-life ~41.7±2.5 ns). Therefore, these 2D type II heteronanosheets are promising materials for efficient light harvesting and charge separation and transport in solar energy conversion applications.

References

(1) Ithurria, S.; Dubertret, B. *J. Am. Chem. Soc.* **2008**, *130*, 16504.
(2) Ithurria, S.; Bousquet, G.; Dubertret, B. *J. Am. Chem. Soc.* **2011**, *133*, 3070.
(3) Ithurria, S.; Tessier, M. D.; Mahler, B.; Lobo, R. P. S. M.; Dubertret, B.; Efros, A. L. *Nat Mater* **2011**, *10*, 936.

(4) Joo, J.; Son, J. S.; Kwon, S. G.; Yu, J. H.; Hyeon, T. *J. Am. Chem. Soc.* **2006**, *128*, 5632.

(5) Son, J. S.; Wen, X.-D.; Joo, J.; Chae, J.; Baek, S.-i.; Park, K.; Kim, J. H.; An, K.; Yu, J. H.; Kwon, S. G.; Choi, S.-H.; Wang, Z.; Kim, Y.-W.; Kuk, Y.; Hoffmann, R.; Hyeon, T. *Angew. Chem. Int. Ed.* **2009**, *48*, 6861.

(6) Son, J. S.; Yu, J. H.; Kwon, S. G.; Lee, J.; Joo, J.; Hyeon, T. *Adv. Mater.* **2011**, *23*, 3214.

(7) Geim, A. K.; Grigorieva, I. V. *Nature* **2013**, *499*, 419.

(8) Hong, X.; Kim, J.; Shi, S.-F.; Zhang, Y.; Jin, C.; Sun, Y.; Tongay, S.; Wu, J.; Zhang, Y.; Wang, F. *Nat Nano* **2014**, *9*, 682.

(9) Kim, S.; Fisher, B.; Eisler, H.-J.; Bawendi, M. *J. Am. Chem. Soc.* **2003**, *125*, 11466.

(10) Halpert, J. E.; Porter, V. J.; Zimmer, J. P.; Bawendi, M. G. *J. Am. Chem. Soc.* **2006**, *128*, 12590.

(11) Kumar, S.; Jones, M.; Lo, S. S.; Scholes, G. D. *Small* **2007**, *3*, 1633.

(12) Zhong, H. Z.; Scholes, G. D. *J. Am. Chem. Soc.* **2009**, *131*, 9170.

(13) Kirsanova, M.; Nemchinov, A.; Hewa-Kasakarage, N. N.; Schmall, N.; Zamkov, M. *Chem. Mat.* **2009**, *21*, 4305.

(14) Dorfs, D.; Salant, A.; Popov, I.; Banin, U. *Small* **2008**, *4*, 1319.

(15) Balet, L. P.; Ivanov, S. A.; Piryatinski, A.; Achermann, M.; Klimov, V. I. *Nano Lett.* **2004**, *4*, 1485.

(16) Milliron, D. J.; Hughes, S. M.; Cui, Y.; Manna, L.; Li, J.; Wang, L.-W.; Paul Alivisatos, A. *Nature* **2004**, *430*, 190.

(17) Peng, P.; Milliron, D. J.; Hughes, S. M.; Johnson, J. C.; Alivisatos, A. P.; Saykally, R. J. *Nano Lett.* **2005**, *5*, 1809.

(18) Jones, M.; Kumar, S.; Lo, S. S.; Scholes, G. D. *J. Phys. Chem. C* **2008**, *112*, 5423.

(19) Hewa-Kasakarage, N. N.; El-Khoury, P. Z.; Tarnovsky, A. N.; Kirsanova, M.; Nemitz, I.; Nemchinov, A.; Zamkov, M. *ACS Nano* **2010**, *4*, 1837.

(20) Zhu, H.; Song, N.; Lian, T. *J. Am. Chem. Soc.* **2011**, *133*, 8762.

(21) Jin, S.; Zhang, J.; Schaller, R. D.; Rajh, T.; Wiederrecht, G. P. *J. Phys. Chem. Lett.* **2012**, *3*, 2052.

(22) Ivanov, S. A.; Piryatinski, A.; Nanda, J.; Tretiak, S.; Zavadil, K. R.; Wallace, W. O.; Werder, D.; Klimov, V. I. *J. Am. Chem. Soc.* **2007**, *129*, 11708.

(23) Zhu, H.; Chen, Z.; Wu, K.; Lian, T. *Chemical Science* **2014**, *5*, 3905.

(24) Mahler, B.; Nadal, B.; Bouet, C.; Patriarche, G.; Dubertret, B. *J. Am. Chem. Soc.* **2012**, *134*, 18591.

(25) Ithurria, S.; Talapin, D. V. *J. Am. Chem. Soc.* **2012**, *134*, 18585.

(26) Prudnikau, A.; Chuvilin, A.; Artemyev, M. *J. Am. Chem. Soc.* **2013**, *135*, 14476.

(27) Tessier, M. D.; Spinicelli, P.; Dupont, D.; Patriarche, G.; Ithurria, S.; Dubertret, B. *Nano Lett.* **2013**, *14*, 207.

(28) Pedetti, S.; Ithurria, S.; Heuclin, H.; Patriarche, G.; Dubertret, B. *J. Am. Chem. Soc.* **2014**, *136*, 16430.

(29) Wu, K.; Rodríguez-Córdoba, W. E.; Liu, Z.; Zhu, H.; Lian, T. *ACS Nano* **2013**, *7*, 7173.

(30) She, C.; Bryant, G. W.; Demortière, A.; Shevchenko, E. V.; Pelton, M. *Phys. Rev. B* **2013**, *87*, 155427.

(31) Mauser, C.; Da Como, E.; Baldauf, J.; Rogach, A. L.; Huang, J.; Talapin, D. V.; Feldmann, J. *Phys. Rev. B* **2010**, *82*, 0813061.

(32) Kunneman, L. T.; Zanella, M.; Manna, L.; Siebbeles, L. D. A.; Schins, J. M. *J. Phys. Chem. C* **2013**, *117*, 3146.

(33) Coleman, J. N.; Lotya, M.; O'Neill, A.; Bergin, S. D.; King, P. J.; Khan, U.; Young, K.; Gaucher, A.; De, S.; Smith, R. J.; Shvets, I. V.; Arora, S. K.; Stanton, G.; Kim, H.-Y.; Lee, K.; Kim, G. T.; Duesberg, G. S.; Hallam, T.; Boland, J. J.; Wang, J. J.; Donegan, J. F.; Grunlan, J. C.; Moriarty, G.; Shmeliov, A.; Nicholls, R. J.; Perkins, J. M.; Grieveson, E. M.; Theuwissen, K.; McComb, D. W.; Nellist, P. D.; Nicolosi, V. *Science* **2011**, *331*, 568.

(34) Pedetti, S.; Nadal, B.; Lhuillier, E.; Mahler, B.; Bouet, C.; Abécassis, B.; Xu, X.; Dubertret, B. *Chem. Mat.* **2013**, *25*, 2455.

(35) Grim, J. Q.; Christodoulou, S.; Di Stasio, F.; Krahne, R.; Cingolani, R.; Manna, L.; Moreels, I. *Nat Nano* **2014**, *9*, 891.

(36) Benchamekh, R.; Gippius, N. A.; Even, J.; Nestoklon, M. O.; Jancu, J. M.; Ithurria, S.; Dubertret, B.; Efros, A. L.; Voisin, P. *Phys. Rev. B* **2014**, *89*, 035307.

(37) Ceballos, F.; Bellus, M. Z.; Chiu, H.-Y.; Zhao, H. *ACS Nano* **2014**, *DOI: 10.1021/nn505736z*.

(38) Pelton, M.; Ithurria, S.; Schaller, R. D.; Dolzhnikov, D. S.; Talapin, D. V. *Nano Lett.* **2012**, *12*, 6158.

(39) Kunneman, L. T.; Tessier, M. D.; Heuclin, H.; Dubertret, B.; Aulin, Y. V.; Grozema, F. C.; Schins, J. M.; Siebbeles, L. D. A. *J. Phys. Chem. Lett.* **2013**, *4*, 3574.

(40) Wu, K.; Li, Q.; Du, y.; Chen, Z.; Lian, T. *Chemical Science* **2015**, *6*, 1049.

(41) Klimov, V. I. *J. Phys. Chem. B* **2000**, *104*, 6112.

(42) Zhu, H.; Lian, T. *J. Am. Chem. Soc.* **2012**, *134*, 11289.

(43) Wu, K.; Zhu, H.; Liu, Z.; Rodríguez-Córdoba, W.; Lian, T. *J. Am. Chem. Soc.* **2012**, *134*, 10337.

(44) Huang, J.; Stockwell, D.; Huang, Z. Q.; Mohler, D. L.; Lian, T. Q. *J. Am. Chem. Soc.* **2008**, *130*, 5632.

(45) Wu, K.; Chen, Z.; Lv, H.; Zhu, H.; Hill, C. L.; Lian, T. *J. Am. Chem. Soc.* **2014**, *136*, 7708.

(46) Wu, K.; Song, N.; Liu, Z.; Zhu, H.; Rodríguez-Córdoba, W.; Lian, T. *J. Phys. Chem. A* **2013**, *117*, 7561.

(47) Wu, K.; Liu, Z.; Zhu, H.; Lian, T. *J. Phys. Chem. A* **2013**, *117*, 6362.

(48) Zhu, H. M.; Song, N. H.; Lian, T. Q. *J. Am. Chem. Soc.* **2010**, *132*, 15038.

(49) Smith, A. M.; Nie, S. *Acc. Chem. Res.* **2009**, *43*, 190.

(50) Kunneman, L. T.; Schins, J. M.; Pedetti, S.; Heuclin, H.; Grozema, F. C.; Houtepen, A. J.; Dubertret, B.; Siebbeles, L. D. A. *Nano Lett.* **2014**, *14*, 7039.

(51) Biadala, L.; Liu, F.; Tessier, M. D.; Yakovlev, D. R.; Dubertret, B.; Bayer, M. *Nano Lett.* **2014**, *14*, 1134.

Appendix 1

Single exciton experimental conditions

Estimating average number of photo-generated excitons on each NS requires absorption cross section of these CdSe/CdTe NSs, which is not measured in this work. However, to ensure that our experiments were performed under single exciton conditions, i.e. each NS has either one or zero exciton, we measured power-dependent exciton kinetics for these NSs, for both 625 nm and 400 nm excitations. Figure A.10.1.a shows the kinetics of T3 at three indicated 625 nm pump powers and they agree well with each other after scaling. Also, the initial signal amplitudes are proportional to excitation powers (inset). Figure A.10.1.b shows the kinetics of T1 at three indicated 400 nm pump powers and they also agree well\after scaling Therefore, these experiments were in the linear regime, or single exciton excitation conditions. The data shown in the main text all correspond to the second powers, i.e. 160 uW for 625 nm and 25 uW for 400 nm.

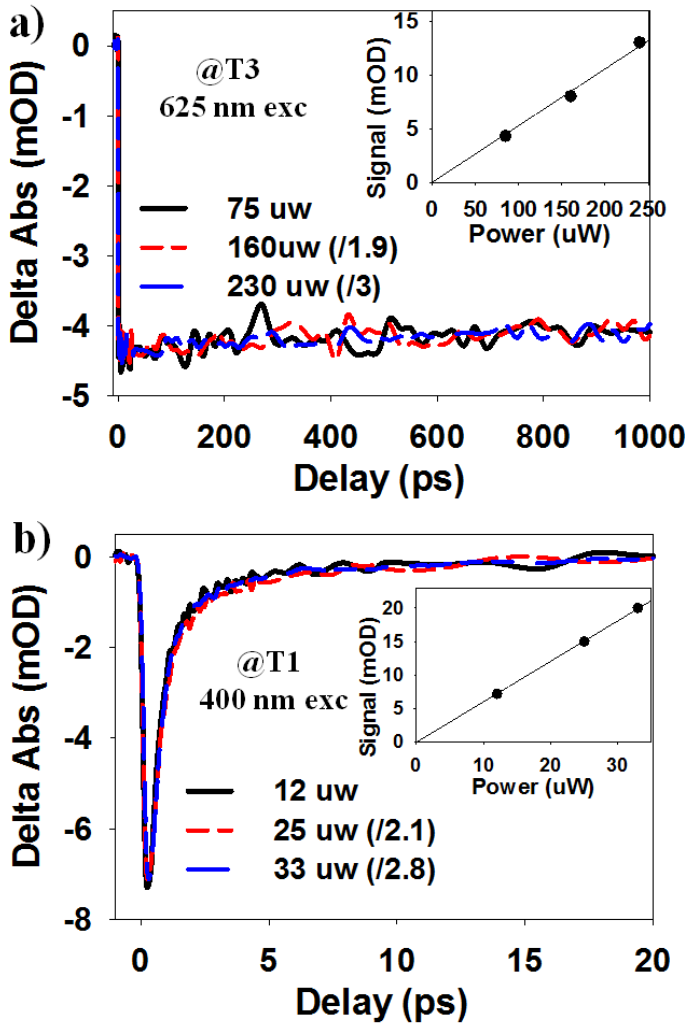

Figure A.10.1. T3 kinetics at different powers of 625 nm excitation (a) and T1 kinetics at different powers of 400 nm excitation, respectively. They are scaled for better comparison and the scaling factors are labeled. The insets are plots of initial signal amplitudes as a function of excitation powers.